Titre: Title:	The Structural and Magnetic Properties of MnP Films and Nanocrystals
Auteur: Author:	Seyyed Nima Nateghi
Date:	2014
Type:	Mémoire ou thèse / Dissertation or Thesis
Référence: Citation:	Nateghi, S. N. (2014). The Structural and Magnetic Properties of MnP Films and Nanocrystals [Thèse de doctorat, École Polytechnique de Montréal]. PolyPublie. https://publications.polymtl.ca/1427/

UNIVERSITÉ DE MONTRÉAL

THE STRUCTURAL AND MAGNETIC PROPERTIES OF MNP FILMS AND NANOCRYSTALS

SEYYED NIMA NATEGHI
DÉPARTEMENT DE GÉNIE PHYSIQUE
ÉCOLE POLYTECHNIQUE DE MONTRÉAL

THÈSE PRÉSENTÉE EN VUE DE L'OBTENTION
DU DIPLÔME DE PHILOSOPHIÆ DOCTOR
(GÉNIE PHYSIQUE)
MAI 2014

UNIVERSITÉ DE MONTRÉAL

ÉCOLE POLYTECHNIQUE DE MONTRÉAL

Cette thèse intitulée :

THE STRUCTURAL AND MAGNETIC PROPERTIES OF MNP FILMS AND NANOCRYSTALS

présentée par : NATEGHI Seyyed Nima
en vue de l'obtention du diplôme de : Philosophiæ Doctor
a été dûment acceptée par le jury d'examen constitué de :

M. MEUNIER Michel, Ph.D., président
M. MÉNARD David, Ph.D., membre et directeur de recherche
M. MASUT Remo A., Ph.D., membre et codirecteur de recherche
M. MOUTANABBIR Oussama, Ph.D., membre
M. TRUDEAU Michel Laurent, Ph.D., membre

To my parents

ACKNOWLEDGMENT

I would like to thank my advisers, David Ménard and Remo Masut, for their consistent support and inspiration. It was a pleasure working with these two brilliant scientists.

I would also like to thank Arthur Yelon and Patrick Desjardins for fruitful discussions and helpful suggestions.

I thank the members of the jury, Michel Trudeau, Michel Meunier, and Oussama Moutanabbir for evaluating this thesis and for their constructive comments.

I would like to thank Samuel Lambert-Milot for training me to use MOCVD and for providing samples, which have been studied in this thesis.

I would like to thank Jelle Demeulemeester and Annie Lévesque for texture measurements of my samples.

I thank Jöel Bouchard for his wonderful job in maintaining the MOCVD lab, and Jean-Phillipe Masse for his help in TEM imaging and sample preparation. I also thank Nicole MacDonal, Martin Chicoine, and Louis Godbout for helping me in TEM sample preparation.

I thank all my colleagues and friends, especially Christian Lacroix, Gabriel Monette, Elyse Adam, Louis-Phillipe Carignan, Nicolas Schmidt, Amir Roohi, Saman Choubak, and Foad Mehdizadeh for their support and helpful discussions.

And finally I thanks my wonderful parents, my brother and sister, and Debbie, my lovely girlfriend for their continuous support and endless love.

RÉSUMÉ

Les semi-conducteurs magnétiques hétérogènes constitués de nano-aimants de pnictures de manganèse incorporés dans des matrices de semi-conducteurs ont des applications magnéto-électroniques et magnéto-optoélectroniques potentielles tel que la magnétorésistance géante et les effets magnétooptiques géants en raison de leurs fonctionnalités magnétiques. Parmi ces matériaux, les systèmes hétérogènes avec des températures de Curie élevées, comme MnSb, MnAs et MnP, ont fait l'objet de nombreuses études.

Étant donné que la texture des nanoagrégats affecte fortement les fonctionnalités magnétiques des semi-conducteurs hétérogènes, nous devons avoir un contrôle sur la structure et la texture du système afin de réaliser les fonctions magnétiques souhaitées. Par conséquent, il est nécessaire de comprendre les propriétés de l'hétérostructure en fonction de sa structure.

Les nanoparticules de MnP ferromagnétiques encastrées dans une matrice de phosphure de gallium (GaP), GaP:MnP, crues par épitaxie en phase vapeur (MOVPE) ont été étudiées comme un système modèle pour vérifier à quel niveau la texture pouvait être pré-conditionnée par synthèse. Malgré les études détaillées sur la façon dont certains éléments structuraux (par exemple la taille des nanoparticules) peuvent être contrôlés par les paramètres de croissance (par exemple la température de croissance), la complexité de ces systèmes n'a pas permis de résoudre cette dépendance.

L'objectif général de ce travail est de comprendre le mécanisme de la croissance, de sélection de la texture du MnP dans le GaP et comment la texture pourrait être conditionnée par les paramètres de croissance. Pour atteindre notre objectif, nous avons choisi d'étudier un système moins complexe, des couches minces de MnP crues sur substrat de GaP, afin d'approfondir notre compréhension du mécanisme de croissance et d'évolution de la texture des hétérostructures. La comparaison de l'évolution de la texture de couches minces et de celle des hétérostructures nous aide à comprendre le rôle de la matrice de GaP, ce qui pourrait conduire à la conception de structures avec les propriétés souhaitées.

Un autre objectif de ce travail est de développer une méthode simple pour déterminer la taille magnétique des nanoparticules de MnP ainsi que leur distribution. Puisque notre sujet d'intérêt porte sur la texture et la structure magnétique des nanoparticules, la taille magnétique, par opposition à la taille physique, des nanoparticules est la composante structurale pertinente à étudier. Il n'existe pas dans la littérature de modèle cohérent pour déterminer la distribution de la taille d'un ensemble de nanoparticules dont certaines sont superparamagnétiques et d'autres ferromagnétiques, tel que les nanoparticules de MnP dans le GaP.

Pour analyser la texture des couches de MnP, nous avons utilisé la diffraction des rayons-

X (XRD) et la microscopie électronique (EM). Nous avons montré que la combinaison des figures de pôles depuis l'XRD et des diagrammes de diffraction des électrons obtenus à partir de la microscopie électronique est avantageuse pour analyser la texture, comparé à chacune des techniques prise individuellement.

L'étude de la durée de la croissance et de l'évolution de la température de la texture des couches de MnP nous a permis d'observer que : (1) les grains de MnP croissent partiellement à l'intérieur du GaP, un phénomène connu sous le nom de croissance endotaxiale, (2) le GaP a souvent une surface convexe entre deux grains endotaxiaux de MnP, (3) les grains de MnP se forment dans un certain nombre d'orientations cristallographiques (épitaxiales et axiotaxiales), (4) les grains MnP avec différentes orientations cristallographiques ont différentes facettes de la surface libre et différentes profondeurs de diffusion, (5) la texture axiotaxiale domine à des températures de croissance plus élevées.

Ces observations nous amènent à développer un modèle semi-quantitatif pour décrire la croissance endotaxiale de grains de MnP. La surface convexe entre deux grains endotaxiaux suggère que la croissance se produit à travers la diffusion externe (out-diffusion) des atomes de gallium à l'interface GaP/MnP, qui pourrait recristalliser par recombinaison avec les atomes de phosphore fournis en phase vapeur au cours de la croissance. La recristallisation d'élément diffusé de la colonne III a été observée dans des systèmes similaires (MnSb sur GaSb et MnSb sur InP). Les atomes de manganèse remplacent les atomes de gallium diffusés et le MnP croit endotaxialement.

Compte tenu de l'énergie du système pendant la croissance de la couche mince (énergie libre de surface, l'énergie de l'interface, et l'énergie de contrainte), la croissance endotaxiale des grains de MnP forme des configurations où la surface de contact entre GaP et MnP tend à augmenter. Ceci favorise l'énergie de contrainte et d'interface du système par rapport à l'augmentation de la surface libre du MnP.

À partir de l'étude de la durée de la croissance et de l'évolution des profondeurs endotaxiales de grains MnP de différentes orientations cristallographiques en fonction de la température, nous avons extrait les coefficients de diffusion (de l'ordre de $10^{-14} cm^2/s$) et l'énergie d'activation ($0,6 \pm 0,2$ eV) du processus de diffusion externe mentionnée ci-dessus (dans la gamme de température $550 - 650\,^{\circ}\mathrm{C}$). La valeur des coefficients de diffusion est au moins trois ordres de grandeur supérieure à celle de la diffusion volumique du manganèse dans le GaP et l'énergie d'activation est un ordre de grandeur plus petite. Comme il n'y a pas de dislocations observées dans nos échantillons, nous avons proposé que ce processus de diffusion se produit par diffusion externe du Ga à l'interface MnP/GaP à travers des sites vacants qui pourraient exister en raison de la différente structure cristalline du MnP et du GaP.

En comparant la texture des couches minces de MnP aux épicouches de GaP:MnP, nous avons réalisé qu'il y a davantage de familles d'orientation épitaxiales et axiotaxiales pour le MnP dans les couches minces que dans les épicouches. Compte tenu de la maturation des nanoparticules (qui n'a pas été considérées initialement dans l'analyse du développement de la texture) en conséquence à la diffusion du manganèse dans le GaP, nous avons suggéré que la texture selectionnée dans les épicouches est similaire à celle des couches minces de MnP au stade précoce de la croissance. Certaines familles d'orientations épitaxiales et axiotaxiales, qui ont été observées dans les couches minces, disparaissent éventuellement dans les épicouches pendant le processus de maturation. Ceci a été attribué à l'excès d'énergie d'interface et de contrainte gardé au sein des cristaux (les nanoagrégats), ce qui limite la poursuite de la croissance de ces familles d'orientation et de la texture axiotaxiale.

L'importance de la diffusion du manganèse dans le GaP a été révélée par l'étude des hétérostructures de GaP/MnP/GaP et GaP/GaP:MnP/GaP. Le coefficient de diffusion du manganèse dans le GaP a été estimé à $4,0 \pm 0,3 \times 10^{-15}$ (cm^2/s) à 650 °C, ce qui est de deux ordres de grandeur plus grand que la valeur répertoriée pour la diffusion du manganèse dans le GaP. La diffusion accrue a été attribuée à la concentration de défauts de structure dans les couches de GaP.

L'analyse de ces observations nous amène une compréhension accrue des phénomènes inhérents aux processus de croissance comme la sélection et le développement de la texture dans les semi-conducteurs magnétiques hétérogènes. Cependant, ces mêmes observations confirment combien il est difficile de contrôler la texture de l'hétérostructure.

Enfin, en utilisant le concept de processus de renversement de l'aimantation thermiquement activé, nous avons développé une méthode simple pour déterminer la taille magnétique des nanoparticules de MnP ainsi que leur distribution. Notre méthode permet de construire l'histogramme de la taille magnétique des nanoparticules à partir de la mesure d'aimantation isorémanente, et par conséquent de trouver la distribution de la taille magnétique d'un ensemble de nanoparticules. Nos résultats montrent que la taille magnétique des nanoparticules est de façon significative (20 à 50 %) plus petite que la taille physique apparente obtenue à partir de l'analyse d'image EM. Cela pourrait être dû à des déficiences des techniques électromagnétiques dans la détermination de la taille des nanoparticules non sphériques, à une possible couche morte magnétique recouvrant les nanoparticules, ou encore à la sur-simplification du modèle magnétique dans l'extraction de la distribution de la taille.

ABSTRACT

Heterogeneous magnetic semiconductors consisting manganese pnictide nanomagnets embedded in semiconductor matrices have potential magnetoelectronic and magnetooptoelectronic applications due to their enhanced magnetic functionalities, such as Giant Magneto-Resistance (GMR) and Giant Magneto-Optical (GMO) Kerr and Faraday effects. Among these, heterogeneous systems with higher Curie temperatures, such as manganese antimonide, manganese arsenide, and manganese phosphide (MnP) have been the focus of many studies.

Since the texture of the nanoclusters highly affects the magnetic functionalities of the heterogeneous semiconductors, in order to achieve the desired magnetic functionalities we need to have a control over the structure and texture of the system. Hence, it is necessary to understand the properties of the heterostructure in relation to its structure.

Ferromagnetic MnP nanoclusters embedded in gallium phosphide (GaP) matrix, GaP:MnP, grown by Metal-Organic Vapor Phase Epitaxy (MOVPE) has been studied as a model system to verify to what level the texture could be pre-conditioned by synthesis. Despite the valuable achievements of the studies on how some structural components (e.g. size of nanoclusters) can be controlled by growth parameters (e.g. growth temperature), the complexity of the structure did not allow to fully exploit this matter.

The general objective of this work is to understand the growth mechanism and texture selection of MnP on GaP and how the texture could be pre-conditioned by growth. To achieve our goal we chose to study a less complex system, MnP thin films grown on GaP, in order to expand the limits of our understanding on the growth mechanism and texture evolution of the heterostructure systems. Comparing the texture evolution of thin films and heterostructures helps us understand the role of the surrounding GaP matrix on texture, which may potentially lead to designing structures with desired properties.

Another objective of this work is to develop a simple method to determine the magnetic size distribution and magnetic size of MnP nanoclusters. Since our topic of interest deals with the texture and structure of magnetic nanoparticles, the magnetic size of the nanoparticles is the relevant structural component to study, rather than their apparent physical size. However, there is a lack of a consistent model to determine the magnetic size distribution of an assembly of superparamagnetic and ferromagnetic nanoparticles (such as MnP nanoclusters in GaP:MnP) in the literature.

To analyze the texture of MnP films we have used X-ray diffraction (XRD) and electron microscopy (EM) techniques. We have shown that combining the XRD pole figures and electron diffraction patterns obtained from EM makes a much stronger tool to analyze the

texture compared to each of the techniques applied alone.

Studying the growth time and temperature evolution of the texture of MnP thin films we observed: (1) MnP grains partially grow inside GaP, a phenomenon known as endotaxial growth, (2) GaP often has a convex surface between two endotaxial MnP grain, (3) MnP grains form in a specific number of crystallographic orientations (epitaxial and axiotaxial), (4) MnP grains with different crystallographic orientations have different free surface facets and different diffusion depths, (5) the axiotaxial texture dominates at higher growth temperatures.

These observations lead us to develop a semi-quantitative model to describe the endotaxial growth of MnP grains. Convex GaP surface between two endotaxial grains suggest that the endotaxial growth occurs through the out-diffusion of Ga atoms at GaP/MnP interface, which could recrystallize at the surface through recombination with P atoms provided during the growth. The recrystallization of the out-diffused element III has been observed in similar systems (MnSb on GaSb and MnSb on InP), as well. Mn atoms replace the out-diffused Ga atoms and MnP grows endotaxially.

Considering the energy of the system as the film grows (free surface energy, interface energy, and strain energy), the endotaxial growth of MnP grains indicates that increasing the contact surface area between GaP and MnP, which enhances the interface and strain energy of the system is favored over increasing the free surface area of MnP.

Studying the growth time and temperature evolution of the endotaxial depths of MnP grains with different crystallographic orientations, we have extracted the diffusion coefficients (order of $10^{-14} cm^2/s$) and the activation energy (0.6 ± 0.2 eV) of the above mentioned diffusion process (in the temperature range $550-650\,^{\circ}$C). The values of diffusion coefficients are at least three orders of magnitude larger than those of Mn bulk diffusion in GaP and the activation energy is one order of magnitude smaller. Since there are no dislocations observed in our samples, we suggested this large diffusion process to occur through Ga self-diffusion at the MnP/GaP interface through vacant sites that could exist due to different crystal structure of MnP and GaP.

By comparing the texture of MnP films and GaP:MnP epilayers, we realized that there are more epitaxial orientation families and axiotaxial textures in the films than in the epilayares. Considering the ripening of the nanoclusters (which was not considered initially in the texture development analysis) due to diffusion of Mn in GaP, we suggested that the texture selection in the GaP:MnP epilayers is similar to that of MnP thin films at the early stage of growth. Some epitaxial orientation families and axiotaxial textures, which have been observed in thin films disapper in the epilayers during the ripening process. This has been attributed to the excess interface/strain energies in the buried crystals (nanoclusters), which limits the further growth of those orientation families and axiotaxial features.

The significance of Mn diffusion in GaP has been revealed by studying the GaP/MnP/GaP and GaP/GaP:MnP/GaP heterostructures. The diffusion coefficient of Mn inside GaP has been estimated to be $4.0 \pm 0.3 \times 10^{-15}$ (cm^2/s) at 650 °C, which is two orders of magnitude larger than the reported value for Mn diffusion in bulk GaP. The enhanced diffusion has been attributed to large concentration of structural defects in GaP layers.

These observations brought us one step closer to understand the texture selection and development in heterogeneous magnetic semiconductors. However, they clarified how challenging it is to control the texture of the heterostructure.

Finally, using the concept of thermally activated magnetization reversal process, we have developed a method to extract the magnetic size distribution and magnetic size of MnP nanoclusters in GaP:MnP. Our method enables us to build the magnetic size histogram of the nanoclusters from the isoremanent magnetization measurements, and consequently find the magnetic size distribution and magnetic size by fitting the histogram using known mathematical functions. Our results show that the magnetic size of the nanoclusters is significantly (20-50%) smaller than their apparent physical size obtained from EM image analysis. This could be attributed to deficiencies of EM techniques in determining the size of the non-spherical nanoparticles from their projected area, possible magnetic dead layer covering the nanoclusters, or the over simplification of the magnetic model in extracting the size distribution.

TABLE OF CONTENTS

DEDICATION iii

ACKNOWLEDGMENT iv

RÉSUMÉ v

ABSTRACT viii

TABLE OF CONTENTS xi

LIST OF TABLES xiv

LIST OF FIGURES xvi

LIST OF APPENDICES xxvii

NOMENCLATURE xxviii

CHAPTER 1 INTRODUCTION 1
1.1 Magnetic semiconductors 1
1.2 Growth techniques 2
1.3 Effect of texture on GMO and GMR responses 2
1.4 Motivation, general objective, and choice of material 3
1.5 Organization of the thesis 5

CHAPTER 2 Texture evolution in polycrystalline thin films 6
2.1 Different types of texture 7
2.2 Texture development in polycrystalline thin films 7
2.2.1 Pre-coalescence texture development 9
2.2.2 Texture development during coalescence 11
2.2.3 Time and Temperature evolution of the texture of thin films 12
2.3 Endotaxial growth 14

CHAPTER 3 Experimental techniques 18
3.1 MOVPE growth of MnP and GaP:MnP films and multilayers 18
3.2 Electron microscopy 20

3.2.1 Transmission electron microscopy . . . 21
3.2.2 Dislocation imaging . . . 23
3.2.3 TEM sample preparation . . . 24
3.2.4 Scanning electron microscopy . . . 26
3.3 X-ray diffraction pole figures . . . 27
3.4 Vibrating sample magnetometer (VSM) . . . 33

CHAPTER 4 Texture evolution of polycrystalline MnP films grown on GaP (100) . . . 36
4.1 Introduction . . . 36
4.2 Growth time evolution of MnP films grown on GaP (100) . . . 38
4.2.1 MnP films grown at 550 °C . . . 38
4.2.2 MnP films grown at 650 °C . . . 45
4.3 Growth temperature evolution of MnP films grown on GaP (100) . . . 51
4.4 Discussion . . . 58
4.4.1 Crystallographic orientation of MnP grains grown on GaP (100) . . . 60
4.4.2 Free surface facets of MnP grains . . . 62
4.4.3 Endotaxial growth of MnP grains on GaP . . . 62
4.4.4 Could endotaxial growth favor axiotaxial texture ? . . . 63
4.4.5 Growth rates . . . 64
4.5 Endotaxial growth model . . . 65

CHAPTER 5 Texture of MnP films vs. MnP nanoclusters . . . 69
5.1 Texture of GaP:MnP epilayers . . . 69
5.1.1 GaP:MnP epilayers grown at **550** °C . . . 70
5.1.2 GaP:MnP epilayer and MnP film grown at **600** °C . . . 70
5.1.3 GaP:MnP epilayers and MnP films grown at **650** °C . . . 71
5.1.4 Samples grown at **700** °C . . . 74
5.2 Multilayer samples . . . 74
5.2.1 GMP-M10 (GaP/GaP:MnP/GaP (period =10)) . . . 74
5.2.2 MnP-M17 (GaP/MnP/GaP (period = 17)) . . . 76
5.3 Discussion . . . 78
5.4 Summary . . . 83

CHAPTER 6 Extracting the magnetic size distribution of an assembly of ferromagnetic/superparamagnetic nanoparticles using magnetometry . . . 85
6.1 Introduction . . . 85
6.2 Theoretical background . . . 87

6.2.1 Demagnetization in the absence of applied magnetic field 87
6.2.2 Remagnetization in the presence of applied magnetic field 89
6.2.3 Volume distribution of particles 91
6.3 Description of the method 95
6.4 Application of the method to GaP:MnP 99
6.4.1 Magnetic size distribution of GaP:MnP 99
6.4.2 Validation of the method 103
6.4.3 Magnetic size distribution of GaP:MnP grown at different temperatures 105
6.4.4 Discussion 107

CHAPTER 7 Conclusion 111
7.1 Summary of the work and principal contributions 111
7.1.1 Texture selection in MnP films, nanocrystals, and multilayers 111
7.1.2 Magnetic size distribution of MnP nanoclusters in GaP:MnP 113
7.2 Suggestions for future work 114
7.2.1 Energy terms and enhanced diffusion of Mn in GaP 114
7.2.2 Controlling the texture 114
7.2.3 Magnetic properties of an individual MnP nanocluster studied by electron holography 116

REFERENCES 117

ANNEXES 122

LIST OF TABLES

Table 1.1 Influence of the structure and texture of nanoclusters on MO and MR responses. . . . 3

Table 3.1 List of samples grown on GaP (100) substrates by the procedure described in the text. . . . 20

Table 3.2 List of MnP films grown on glass substrates. The growth procedure is described in the text. . . . 20

Table 3.3 List of parameters used for the growth of samples studied in this thesis, as well as their range of values. . . . 21

Table 4.1 Average effective diameter and mean effective diameter of MnP crystals grown at 550 °C for different growth times, as well as their standard deviations and aspect ratios. . . . 38

Table 4.2 Average normal growth rate of the samples grown at 550 °C compared to their lateral growth rates. . . . 41

Table 4.3 Epitaxial alignments of MnP grains in MnP-550-15 obtained from pole figure analysis by decreasing order of population weight. The last columns indicate the least value of strain, respectively calculated for each alignment using equation 4.2, as well as the integers m and n (described in the text). . . . 45

Table 4.4 Average effective diameter of primary MnP grains grown at 650 °C for different growth times, as well as their standard deviations and aspect ratios. . . . 46

Table 4.5 Average normal growth rate of the primary grains grown at 650 °C compared to their lateral growth rates. . . . 47

Table 4.6 Observed epitaxial alignments of the MnP grains for the three samples grown at 650 °C for the growth times indicated in the table. These orientations are obtained from FFT (MnP-650-5) and SAED patterns (MnP-650-15 and MnP-650-30). . . . 50

Table 4.7 Average effective diameters of the grains in MnP films grown for 15 minutes at different temperatures. . . . 51

Table 4.8 Average normal growth rate of the primary grains grown at different temperatures compared to their lateral growth rates. The sample MnP-750-15 was not available to determine its effective diameter and lateral growth rate from SEM micrographs. . . . 51

Table 4.9 Epitaxial alignments of MnP grains in MnP-550, MnP-600, and MnP-650. 58
Table 4.10 The angles between MnP [020] with GaP [-11-1] (α_1), MnP [-11-1] with GaP [11-1] (α_2), and MnP [-13-1] with GaP [02-2] (α_3) directions in three MnP grains of MnP-600-15. 60
Table 5.1 List of all orientation families (mostly alignments with low-index GaP planes) in the GaP:MnP epilayers and MnP film grown at 650 °C. . . . 73
Table 6.1 Anisotropy fields and saturation magnetization of GaP:MnP at different temperatures Lacroix (2010). 93
Table 6.2 The angles θ_{ci} and ϕ_{ci} for orientations O_3 to O_6 Lacroix (2010). 102
Table 6.3 Extracted parameters from the lognormal fit of magnetic size histogram of GMP-650-45 obtained at 240, 260, and 280 K. 104
Table 6.4 Mean effective diameter (m) and standard deviation (s) extracted from the lognormal fit of the magnetic size histogram and TEM size histogram. 106
Table A.1 Average maximum depth of Mn diffusion in GaP <11-1>, d<111>, for MnP grains grown at 550 °C with MnP {121} || GaP {100}. 123
Table A.2 $d_{<111>}$ (nm) and the obtained diffusion coefficients ($D_{<111>}$) of Mn in GaP. The data presented without error are obtained from only one grain. The diffusion coefficient for MnP {111} || GaP (100) is obtained from four grains of MnP-650-15, using the diffusion equation $d = \sqrt{Dt}$, where d is the average in-diffusion depth of Mn and t is the growth time. 124
Table A.3 Diffusion coefficient of Mn in GaP along <111> at different growth temperatures below the congruent temperature of GaP. 124
Table A.4 Average maximum endotaxial depth of MnP in GaP along GaP [100], d, for MnP grains grown at 550 °C and 650 °C. 127
Table A.5 Portion of the GaP substrate, which is covered by MnP films grown at different temperatures for 15 minutes. 128

LIST OF FIGURES

Figure 2.1 Schematic representation of the interface of axiotaxial alignments of NiSi film grown on Si (110), as reported in Ref. (Detavernier *et al.*, 2003). The d-spacings of the four planes shown in the figure at the interface (d_{int}) almost match the d-spacing of Si (220) (d) at the interface. However, only NiSi (211) and (202) || Si (220) are axiotaxy axes, since the normals to their planes make the same angle (χ) with the interface as the normal to Si (220) plane does ($\chi = 45\,^{\circ}$), thus creating a periodic interface. 8

Figure 2.2 Growth stages of a polycrystalline film on a polycrystalline or amorphous buffer layer : a) nucleation, b) crystal growth, c, d) coalescence and grain growth to form a continuous film, e) thickening of the continuous film. In the image the light circles are the adatoms and the dark circles are impurity atoms. This schematic representation is adapted from Ref. (Barna et Adamik, 1995). 9

Figure 2.3 Hemispherical cap shape particle that partially wets the substrate. γ_f, γ_s, and γ_i are the surface energy of the particle (J/m^2), surface energy of the substrate (J/m^2), and the particle-substrate interface energy (J/m^2), respectively. α, β, and δ are the possible axes of rotation of the particle. θ_c is the contact angle and $r^{\star}$ is the critical radius for the nucleus formation. This schematic representation is adapted from Ref. (Thompson et Carel, 1995). 10

Figure 2.4 Basic structure zone model describing the temperature evolution of the texture of thin films. T_s and T_m in the horizontal axis represent the temperature of the substrate and the melting point of the bulk film. The figure is taken from Ref. (Barna et Adamik, 1995). 13

Figure 2.5 Real structure zone model that considers the level of impurity, as well as growth temperature to describe the texture evolution of thin films : a) Low impurity ($C_{imp} < 0.5\%$), b) medium impurity ($C_{imp} \approx 1\%$), and c) high impurity ($C_{imp} > 10$ %) level (Barna et Adamik, 1995). 14

Figure 2.6 Cross-sectional TEM images revealing the endotaxial growth of MnSb on GaSb at a) 380 ± 10°C and b) 465 ± 10°C. The images are taken from Ref. (Braun *et al.*, 2007). 16

Figure 2.7 a) Braun's proposed mechanism for endotaxial growth of MnSb on GaSb, and b) similar growth mechanism proposed for endotaxial growth of MnSb on InP. Dashed arrows indicate elemental fluxes, while solid arrows show the growth direction. The figure is taken from S. Hatfield's thesis (Hatfield, 2006). 17
Figure 3.1 Schematics of the MOVPE reactor dedicated to the growth of compounds containing transition metals, such as Mn. The image is taken from Ref. (Lambert-Milot, 2012). 18
Figure 3.2 Schematic representation of a TEM. The figure is taken from Ref. Lambert-Milot (2012). 22
Figure 3.3 a) Cross-sectional TEM image of a MnP grain grown at 600 °C on GaP, b) the SAED pattern of GaP substrate and MnP grain, and c) determined normal direction to GaP and MnP planes. The diameter of the aperture hole to obtain the SAED pattern is 120 nm. According to (c), we assigned the alignment MnP [-13-1] || GaP [02-2] to this grain. . 24
Figure 3.4 a) Cross-sectional TEM image of MnP-650-15 taken at GaP [011] zone axis along g [200]. b) The diffraction condition, where only GaP {200} planes diffract. 25
Figure 3.5 Few steps of TEM sample preparation using FIB technique. a) Sandwich of two samples and the tungsten layer deposited on the surface, b) ion milling, lamella preparation, and microprobe welding, c) transferring the lamella to copper grid. 26
Figure 3.6 Schematic representation of an SEM. The image is taken from Ref. Egerton (2005). 27
Figure 3.7 Plan view SEM image of MnP film grown on GaP (100) at 600 °C showing polycrystalline MnP grains on the surface. 28
Figure 3.8 Definition of reciprocal space coordinates $1/\ d_{hkl}$, ψ and ϕ associated to a crystalline material sample. 29
Figure 3.9 Configuration of XRD pole figure measurement. a) Incident (S_0) and diffracted (S_1) beam and their angle with sample's plane, b) geometry of the sample holder and illustration of angles, c) experimental setup to obtain reciprocal space map with a synchrotron source, and d) different types of detectors and their corresponding scan modes. 30
Figure 3.10 Different types of texture and their corresponding pole figures. This figure is taken from (Gaudet, 2011). 31

Figure 3.11 Position of different planes normal on the reciprocal space map of GaP. This reciprocal space map is obtained by a projection of a surface in 3D to a plane. The image is taken from (Lambert-Milot, 2012). 31
Figure 3.12 MnP (111) Pole figure of MnP-650-15. The blue color shows the lowest intensity and the red shows the highest. The spots with higher intensity correspond to epitaxial grains, while the arc corresponds to axiotaxial grains. The dark blue color on the right side of the pole figure corresponds to the angular portion that has not been measured. 32
Figure 3.13 Schematic representation of a VSM measurement. 34
Figure 3.14 The IRM response of GMP-650-45 to the magnetic field (in-plane) applied at $T = 280$ K. 35
Figure 4.1 a) Cross-sectional TEM micrograph of GMP-650-5, showing the formation of GaP (111) facets. White arrows show the MnP nanoclusters that form on GaP (111) facets. 36
Figure 4.2 Schematic representation of the growth model describing the time evolution of the texture of GaP:MnP epilayers. Symbols with different colors inside the nanoclusters correspond to a specific family of orientation, described in Refs. (Lambert-Milot, 2012),(Lambert-Milot *et al.*, 2012). The image is taken from Ref. (Lambert-Milot, 2012). 37
Figure 4.3 Plan view SEM micrographs of a) MnP-550-1.5, b) MnP-550-5, and c) MnP-550-15 showing formation of polycrystalline films. The sample grown for 1.5 min appears to be in the pre-coalescence stage, while the crystals of the samples grown for longer times are in contact with each other and most likely are in the coalescence stage. 39
Figure 4.4 Size histogram of a) MnP-550-1.5, b) MnP-550-5, and c) MnP-550-15. The size distribution of MnP-550-1.5 looks unimodal, which is not the case for MnP-550-5 and MnP-550-15, as a comparison with the best lognormal fit (obtained from Igor pro software) indicates. 40
Figure 4.5 Cross-sectional TEM images of a) MnP-550-1.5, b) MnP-550-5, and c) MnP-550-15. The white line in (a) shows the GaP buffer layer/substrate interface. MnP grows endotaxially on GaP, even at an early stage of growth, as shown in (a). We also observe that samples with longer growth times have larger endotaxial depths. 40

Figure 4.6 a) HR-TEM image of a MnP crystal in MnP-550-1.5 and b) its FFT pattern. Analyzing the FFT pattern (shown in (b)), we assigned the MnP {121} || GaP (200) the alignment to this grains. Moreover, we determined MnP (010), (111), and (101) surface facets, as shown in the HR-TEM image. The long white line shows the surface of the GaP buffer layer (≈ 200 nm thick). We also observe that this crystal partly grew inside the GaP buffer layer. 41

Figure 4.7 HR-TEM image of five MnP grains in MnP-550-1.5. We could not determine the orientation of grain A, since it completely grew inside GaP and we do not clearly observe its planes. Grains D and E have the same alignment, namely MnP {121} || GaP (200). 42

Figure 4.8 a) A trapezoidal crystal in MnP-550-5 with MnP {121} || GaP (200), and b) an elongated crystal in MnP-550-5 with MnP {110} || GaP (200). The two crystals have different surface facets (except for MnP {111} facet). 42

Figure 4.9 Pole figures of MnP-550-15 obtained using a planar detector a) MnP {020}, b) MnP {101}, and c) MnP {211}. The bright spots indicate epitaxial alignments, while partial arcs/lines indicate partial axiotaxy. 44

Figure 4.10 Plan view SEM micrographs of a) MnP-650-5, b) MnP-650-15, c) MnP-650-30 show the formation of polycrystalline films, the grains of which grow larger in time. In (c) we observe the formation of long rods (≈ 2 μm) on top of primary grains. 46

Figure 4.11 Lateral size histograms of primary MnP grains of a) MnP-650-5, b) MnP-650-15, and c) MnP-650-30 show a multimodal distribution. . . . 47

Figure 4.12 Cross-sectional TEM images of a) MnP-650-5, b) MnP-650-15, and c) MnP-650-30, showing the endotaxial growth of the grains. Grains with longer growth times have a larger endotaxial depths. Nucleation and growth of secondary grains is observed in (b) and (c). We infer that secondary grains have a tendency to grow as long rods, as observed in MnP-650-30. 48

Figure 4.13 TEM micrograph of three nanorods in MnP-650-30 and their corresponding SAED patterns. Two of the nanorods are growing faster in [002] direction, while the other one is elongated along [101]. 49

Figure 4.14 Plan view SEM images of MnP films grown at a) 550 °C, b) 600 °C, c) 650 °C, and d) 700 °C. e) Larger area of MnP-700-15, showing formation of very long nanorods. 52

Figure 4.15 Bright field cross-sectional TEM images of MnP films grown for 15 min at a) 550 °C, b) 600 °C, c) 650 °C, and d) 700 °C, and e) 700 °C. The white line in b) shows the GaP substrate/buffer layer interface. Formation of new grains on top of endotaxial primary grains is observed in (c), (d), and (e). 53

Figure 4.16 MnP 020 pole figure of MnP-650-15. The white arrows show the bright spots located at $\psi = 64$ and $\phi = 0\,^{\circ}$, $90\,^{\circ}$, $180\,^{\circ}$, and $270\,^{\circ}$. These are the angular positions where we expect GaP {233} planes. This pole figure has been obtained using a linear detector. 54

Figure 4.17 MnP {101} and b) MnP {211} pole figures of MnP-650-15. In these pole figures we observe bright spots and bright arcs/line segments that indicate epitaxial and partial axiotaxial alignments. These pole figures have been obtained using a planar detector. 55

Figure 4.18 MnP {211} pole figures of a) MnP-550-15, b) MnP-600-15, c) MnP-650-15, d) MnP-700-15, e) MnP-750-15. The white arrows show the bright spots due to the artifacts of the experiment. For MnP-700-15 and MnP-750-15 we only see bright arcs and lines that indicate axiotaxial texture, while the other samples have epitaxial and partial axiotaxial textures. The pole figures have been obtained using a planar detector. 56

Figure 4.19 MnP (020) pole figures of a) MnP-600-15 and b) MnP-650-15, as well as MnP (111) pole figures of c) MnP-600-15 and d) MnP-650-15. We observe more features on the pole figures of MnP-650-15 than MnP-600-15. The pole figures have been obtained using a linear detector. . . 59

Figure 4.20 Axiotaxial features on a) MnP (020) and b) MnP (111) pole figures of MnP-650-15. The purple/green arcs on MnP (111) pole figure appear as lines on MnP (020) pole figure. As it is described in the text, we do not show the purple/green line in the MnP (020) pole figure. 59

Figure 4.21 SAED pattern of MnP grains with a) MnP (-13-1) || GaP (02-2), b) MnP (-1-1-1) || GaP (200), and c) MnP (-11-1) || GaP (11-1) alignments are shown below their TEM micrographs. 61

Figure 4.22 Small bright spots that are very close to each other on the MnP (020) of MnP-600-15. The region in the box is enlarged and presented on the right. The black arrows point to some of the bright spots on the seemingly axiotaxial line. This pole figure is obtained by a linear detector. 62

Figure 4.23 Schematic side view of GaP/MnP contact area in a) MnP crystal growing on top of GaP and b) MnP crystal growing partially inside GaP. Red lines show the portion of MnP that is in contact with GaP. This indicates the larger contact area in the case of endotaxial growth. . . . 63

Figure 4.24 Two grains of MnP-650-15 with different orientation that have different facets and different endotaxial depth. a) MnP {121} || GaP (200), endotaxial depth along GaP <111> = 57 nm, and b) MnP {110} || GaP (200) endotaxial depth along GaP <111> = 27 nm. The long white lines show the approximate position of where the surface of GaP buffer layer is deduced to be. 64

Figure 4.25 a) Initial stage of nucleation of MnP on GaP, b) Mn atoms replacing the Ga atoms that are diffused to the surface, and c) endotaxial growth of MnP crystal and formation of a GaP bump at the surface. 65

Figure 4.26 Recrystallization of GaP at the surface, possibly from out-diffused Ga atoms in MnP-600-15. 66

Figure 4.27 Semi-logarithmic graph of the diffusion coefficient (D) as a function of ($1000/T$) for our samples (average of all orientation families) and their corresponding linear fits, compared to Mn bulk diffusion reported in Ref. Kirillov *et al.* (1980). The extracted activation energy (ΔE) and the pre-exponential factor (D_0) in our samples are 0.45 ± 0.14 (eV) and $1.03 \pm 0.99 \times 10^{-11} (cm^2/s)$, respectively, compared to 4.7 (eV) and $2.1 \times 10^9 (cm^2/s)$ reported in Ref. Kirillov *et al.* (1980). The interface and bulk diffusion coefficients of Mn in GaAs are also presented in the graph for comparison. 67

Figure 4.28 Cross-sectional TEM image of MnP-650-15 taken at GaP [1-12] zone axis along g [1-11] and its corresponding diffraction paatern. No dislocations are observed in this image. 67

Figure 5.1 a) Plan-view SEM image of GaP grown at 600 °C shows its poor surface quality. b) Presence of many structural defects revealed from the cross-sectional TEM micrograph of GMP-600-45. 71

Figure 5.2 a) MnP (020) and b) MnP (101) pole figures of GMP-650-15 (top) compared to c) MnP (020) and d) MnP (101) pole figures of MnP-650-15 (bottom). More bright spots and partial arcs are observed in the pole figures of MnP-650-15, which indicates that there are more epitaxial and partial axiotaxial orientations in this sample compared to GMP-650-15. These pole figures are obtained using a linear detector. 72

Figure 5.3 Cross-sectional TEM images of GMP-M10. In (a) we see that the spacing between the first few layers is much less than that of the last layers, which indicates more Mn diffusion in GaP for the first few layers. In (b), at higher resolution, we highlight a 80 nm thick layer containing MnP nanoclusters, while the growth time should contain the nanoclusters to a 30 ± 5 nm thick layer. 75

Figure 5.4 Square of the diffusion length as a function of time in GMP-M10. The slope of the line represents the diffusion coefficient of Mn in GaP to be $4.0 \pm 0.3 \times 10^{-15}$ (cm^2/s). The error bars are roughly estimated. 76

Figure 5.5 Plan-view SEM image of a GaP layer (60 nm) grown at 650 °C that has been grown on a 30 nm GaP:MnP layer (grown at 650 °C). The dark spots are the GaP surface pits. These pits are also observed in cross-sectional TEM images of GMP-650-1.5 in (Lambert-Milot, 2012),(Lambert-Milot *et al.*, 2012). 77

Figure 5.6 Cross-sectional TEM images of MnP-M17, a sample grown at 650 °C (GaP) and 550 °C (MnP) to nominally have 17 periods of 3 nm MnP and 50 nm GaP. We observe formation of larger nanoclusters close to the buffer layer/epilayer interface. We also observe formation of GaP with different crystallographic orientations and structural defects in this sample. 78

Figure 5.7 a) ED pattern, b) GaP (111), and c) GaP (200) pole figures of MnP-M17. The presence of many bright spots on the ED pattern and pole figures suggest that in this sample GaP crystals grow with different crystallographic orientations. The yellow arrows show the expected angular positions of GaP (111) and (200) planes of the substrate. The red and white arrows correspond to angular positions of GaP (111) and (200) planes of some GaP crystals that are differently oriented than the substrate, on which MnP nanoclusters nucleate (will be presented in figure 6.11). These pole figures are obtained using a linear detector. 79

Figure 5.8 a) MnP (020) and b) MnP (101) pole figures of MnP-M17. The white and red arrows in a) correspond to MnP {020} || GaP {100} (red circle) and MnP {020} || GaP {111} (lines) alignments for the nanoclusters that form on GaP crystals with different orientation than the substrate. The pole figures are obtained using a linear detector. 80

Figure 5.9 a) MnP nanoclusters embedded in GaP (GMP-650-1.5) compared to b) MnP crystal grown endotaxially on GaP (GMP-650-1.5). 80
Figure 5.10 Schematic representation of the ripening process in GaP:MnP. a) Initial stage of nucleation of a nanocluster. b) As the nanocluster grows, it ends up surrounded by GaP due to larger growth rate of GaP. c) When this nanocluster is completely buried in GaP, Mn atoms of this nanocluster may diffuse towards a neighboring nanocluster with lower energy (shown by the block arrow). In this representation we do not show the P atoms. 81
Figure 5.11 Schematic representation of nucleation of MnP nanocluster in MnP-M17 (only three MnP layers are shown). The arrows show the direction of Mn diffusion from the crystals to the nanoclusters, that potentially occurs through structural defects present in this sample. 83
Figure 6.1 Magnetic energy of the system (vertical) as a function of the angle with respect to the z-axis (horizontal). The minima of magnetic energy in the absence of external magnetic field ($H_0 = 0$) are at -180° and 0°, corresponding to (↓) and (↑), respectively. 87
Figure 6.2 Schematic diagrams of the magnetic energy and its deep and shallow minima in applied field H_0. The figure shows the change in populations of (↑) and (↓) a) right after the field is applied and b) some time (t_0) after it is applied. 90
Figure 6.3 a) Rapid variation of $\tau(V)$ as a function of the diameter of MnP nanoclusters in GMP-650-45 and b) rapid variation of the exponential term in Eq. (6.22) as a function of the diameter of the nanoclusters, for different time constants (t = 1 s, 90 s, and 1 day). The exponential term could be fairly approximated with a step function. The energy barrier density of the clusters has been calculated at 260 K at zero applied field. The diameter has been calculated assuming spherical nanoclusters. . . 92
Figure 6.4 Isoremanent magnetization, temperature of experiment, and applied magnetic field as a function of time during ZFC process and IRM measurement. 96
Figure 6.5 Bright field cross-sectional TEM image of GaP:MnP grown at 650°C. . 99
Figure 6.6 Easy axes of magnetization (c-axis) of MnP nanoclusters with respect to GaP [100]. 100

Figure 6.7 Magnetic field H_0 applied at an arbitrary angle θ_H with respect to GaP [100]. The Hard (a-axis of MnP) and intermediate (b-axis of MnP) anisotropy fields of a MnP (orthorhombic with convention a > b > c) nanocluster are also shown in the figure. 101

Figure 6.8 a) 3D representation of the magnetic energy density of GaP:MnP at $H_0 = 0$. Points A, D, B, and C represent local minima, saddle point, and maximum of the energy density, respectively. b) Contour graph of the magnetic energy density of GaP:MnP at $H_0 = 0$. The points A, B, C, D are the same as shown in part (a). The blue color represents the lowest and the red color indicates the highest value of the energy density. 102

Figure 6.9 3D representation of the magnetic energy density of GaP:MnP at $H_0 = 159kA/m(2000Oe)$. Points A, D, B, and C represent the local minima, saddle point, and maximum of the energy density, respectively. b) Same graph as in (a), but from a different point of view. c) Contour graph of the magnetic energy density of GaP:MnP at $H_0 = 159kA/m(2000Oe)$. . 103

Figure 6.10 The IRM response of GMP-650-45 at T = 280 K. 104

Figure 6.11 The magnetic size histogram of GMP-650-45 and its lognormal fit obtained at a) 240 K, b) 260 K, and c) 280 K. 105

Figure 6.12 Magnetic hysteresis curve of GMP-650-45 obtained at 240 K, while the magnetic field was applied parallel to sample's normal (GaP [100]). The blue dots show the experimental data and the red line shows the result of simulation using the parameters presented in Table 6.3. 106

Figure 6.13 Magnetic size histogram obtained at T = 280 K (left) vs. physical size histogram (right) of a) GMP-600-45, b) GMP-650-45, and c) GMP-700-45. 107

Figure A.1 A grain in MnP-600 with MnP {131} || GaP (111) alignment. The long white line shows the expected GaP surface prior to growth of MnP. For this grain we measured $d_{[100]} = 43$ nm and $d_{[-11-1]} = 76$ nm. 123

Figure A.2 Square of the diffusion depth ($d^2_{<111>}$) of MnP grains grown at with MnP {121} || GaP (100) in GaP along <111> direction as a function of growth time (t). The slope of the line reveals the diffusion coefficient of $D_{<111>} = 1.31 \pm 0.012 \times 10^{-14}(cm^2/s)$. 124

Figure A.3 $d_{<111>}$ as a function of growth time for a) MnP {010} || GaP (111) ($D_{<111>} = 1.4 \times 10^{-14} \pm 8.4 \times 10^{-16}(cm^2/s)$), b) MnP {110} || GaP (200) ($D_{<111>} = 2.6 \times 10^{-14} \pm 1.7 \times 10^{-15}(cm^2/s)$), and c) MnP {121} || GaP (200) ($D_{<111>} = 3.8 \times 10^{-14} \pm 2.6 \times 10^{-15}(cm^2/s)$). Since we only had two data points, we added the point (0, 0) and assured the fitted line, the slope of which represents $D_{<111>}$, is passing through the origin. The data points that are presented with no error bars are obtained from only one grain. 125

Figure A.4 Semi-logarithmic graph of D as a function of $(1/T)$. The extracted activation energy and pre-exponential factor from the linear fit are $(\Delta E_{Diff}) = 0.6 \pm 0.2$ (eV) and $(D_0 = 2.7 \pm 2.6) \times 10^{-10}(cm^2/s)$. 126

Figure A.5 The square of endotaxial depths as a function of growth time for MnP grains grown at 550 °C and 650 °C. The linear behavior confirms that endotaxial growth is a diffusion-controlled process. The slope of the lines provide the diffusion coefficients to be $4.4 \pm 0.04 \times 10^{-15}(cm^2/s)$ and $8.9 \pm 0.47 \times 10^{-15}(cm^2/s)$ for the growth temperatures 550 °C and 650 °C, respectively. 126

Figure A.6 Semi-logarithmic graph of the diffusion coefficient (D) as a function of $(1000/T)$ for our samples and their corresponding linear fits, compared to Mn bulk diffusion reported in Ref. Kirillov *et al.* (1980). The extracted activation energy (ΔE) and the pre-exponential factor (D_0) in our samples are 0.45 ± 0.14 (eV) and $1.03 \pm 0.99 \times 10^{-11}(cm^2/s)$, respectively, compared to 0.45 (eV) and $2.1 \times 10^{9}(cm^2/s)$ reported in Ref. Kirillov *et al.* (1980). The interface and bulk diffusion coefficients of Mn in GaAs are also presented in the graph for comparison. 128

Figure A.7 Image analysis of the plan-view SEM micrograph of MnP-550-15. Dark shows the deposited film, while bright represents the substrate. For this sample the film covers 72% of the substrate. 128

Figure B.1 Plan-view SEM images of MnP films grown on glass at a) MnP-G550-15 and b) MnP-G550-60 show formation of polycrystalline films. 130

Figure B.2 Cross-sectional SEM image of MnP-G550-60 showing the thickness of the film to be 410 nm. The growth rate has been calculated to be almost 7 nm/min. 130

Figure B.3 a) Plan view SEM image of the MnP-G600-60 and b) Plan view TEM micrograph of the powder obtained from this sample. 131

Figure B.4 Plan view TEM image of an elongated MnP nanoparticle obtained from MnP-G600-60 powder and its SAED pattern. It shows that MnP grows faster in [001] direction. We also observe (110) and (111) surface facets. 131

Figure B.5 a) Magnetic hysteresis curve of MnP-G600-60 at 240 K indicating ferromagnetic ordering. b) Temperature evolution of the IRM signal of MnP-G600-60 indicating a Curie temperature of 292 ± 1 K. 132

Figure B.6 a) Faraday rotation θ_f of MnP-G550-15 at 1.89 eV as a function of magnetic field at different temperatures. b) Magnetic hysteresis curve of MnP-G550-15 at different temperatures. 133

LIST OF APPENDICES

Annexe A Mn diffusion in GaP 122
Annexe B Structural, magnetic, and magneto-optical properties of MnP films grown on glass substrate 129

NOMENCLATURE

Abreviations

MOVPE	Metal-organic chemical vapor deposition
TEM	Transmission electron microscopy
HR-TEM	High-resolution transmission electron microscopy
SEM	Scanning electron microscopy
XRD	X-ray diffraction
VSM	Vibrating sample magnetometer
sccm	Standard cubic centimeter per minute
ED	Electron diffraction
SAED	Selected area electron diffraction
FTED	Fourier transform electron diffraction
FIB	Focused ion beam
NSLS	National Synchrotron Light Source
RT	Room temperature
AR	Aspect ratio

Symbols

T_s	Temperature of substrate
T_m	Melting temperature of the deposited film
α, β, δ	Axes of rotation of the crystal
γ_f	Surface energy of the film
γ_s	Surface energy of the substrate
γ_i	Film-substrate interfacial energy
θ_c	the contact angle
$r^\star$	Critical radius for the nucleus formation
C_{imp}	Level of impurity
D_o	Diameter of an object
M_m	Magnification of the microscope
d_{hkl}	Interplanar spacing of hklplanes
λ	Wavelength of X-ray
θ	Angle of incidence with the normal to the scattering planes (hkl)
g	Diffraction vector

ψ	Angle between the sample's surface normal and $1/d_{hkl}$ in the reciprocal space map
ϕ	Angle between the projection of $1/d_{hkl}$ and one of sample's in-plane principal axes in the reciprocal space map
χ	Tilt angle of the sample in Schultz geometry
S_0	Incident beam of X-ray
S_1	Diffracted beam of X-ray
σ_M	Mass magnetization of the sample
m	Magnetic moment of the sample
M_s	Saturation magnetization of the sample
M	Magnetization (magnetic moment per unit volume)
IRM	Isoremanent magnetization
TRM	Thermoremanent magnetization
T_c	Curie temperature
T	Absolute temperature
H	Applied magnetic field
t	time
H_k	Anisotropy field
$R_\parallel$	Average lateral growth rate
$R_\perp$	Average normal growth rate
$\alpha_{a,b,c}$	Thermal expansion coefficients of a, b, and c-axes of MnP
α_{GaP}	Thermal expansion coefficient of GaP
$e(\%)$	Strain percent
$\alpha_{1,2,3}$	Angles between three different MnP and GaP plane normals
N	Number of non-interacting single domain nanoparticles in a system
V	Volume of the nanoparticles
ΔE	Energy barrier for magnetization reversal
n^+	Number of nanoparticles in the up-state
n^-	Number of nanoparticles in the down-state
τ	Relaxation time
k_B	Boltzmann's constant
n	Difference in the number of nanoparticles in the up-state and down-state
f_0	Reversal attempt frequency
μ_0	Permeability of free space
K	Magnetic anisotropy constant

H_a	Magnetic anisotropy field
O	Magnetic orientation family
m_p	Mean size of the nanoparticles
s	Standard deviation
d_p	Diameter of the nanoparticles
d	Diffusion depth (length)
D	Diffusion coefficient
ΔE_{Diff}	Activation energy of diffusion
θ_f	Faraday rotation angle

CHAPTER 1

INTRODUCTION

1.1 Magnetic semiconductors

Materials scientists' long time dream of combining the semiconducting and ferromagnetic properties in one material system came true by observing ferromagnetic ordering in europium chalcogenides and semiconducting spinels with a periodic array of magnetic atoms in the 1960s and early 1970s (Mauger et Godart, 1986). However, these materials could not be easily adopted in technological applications due to their different crystal structures compared to silicon and gallium arsenide, and also because of their complex and time consuming growth procedure (Ohno, 1998).

One strategy to create a system with potential industrial applications, which combines ferromagnetism and semiconductivity, is to introduce local magnetic moments into a semiconductor matrix with proven industrial applications Ohno (1998), Gaj *et al.* (1978), Jaczyński *et al.* (1978). Introducing small quantities of transitional metals (Fe, Mn, Co, ...) into Si, Ge, II-VI (ZnO, CdTe, ZnSe,...) (Furdyna (1988), Dietl (1994)) and III-V (GaAs, InSb, AlAs,...) (Ohno (1999), MacDonald *et al.* (2005)) compound semiconductors has been reported to result in ferromagnetic behavior. These new materials, known as magnetic semiconductors, have shown promising magneto-active functionalities, which along with the simplicity of their fabrication make them potential candidates for magneto-optical (Akinaga *et al.* (2000), Shimizu *et al.* (2001)) and magneto-electronic devices (Ohno (1998), Thio et Solin (1998), Yuldashev *et al.* (2001)).

An important challenge to fulfill the industrial requirements is to grow homogeneous ferromagnetic semiconductors, which maintain their ferromagnetic ordering above room temperature. In other words, for industrial applications the Curie temperature, T_c, of the material needs to be well above room temperature. High T_c requires a strong exchange interaction between the magnetic ions. However, since the solubility of the magnetic atoms into the semiconductor matrix is limited, their density is too low to provide an effective interaction (the exchange interaction is short range). The Curie temperatures obtained so far for dilute homogeneous materials are thus far from the application range.

Increasing T_c requires increasing the amount of transitional metal ions over the solubility limit, which results in the segregation of the metal ions, resulting in the formation of ferromagnetic metallic inclusions. The presence of metallic inclusions usually increases

the Curie temperature to the desired range, but lowers the possibility of employing these materials in spintronics, since the mobile carriers rapidly lose their spin polarity due to scattering from these inclusions. However, the observed giant magneto-optical (GMO) and giant magneto-resistance (GMR) responses of some of these hybrid structures make them potential candidates for magneto-optical and magneto-electronic devices, such as optical isolators and magneto-resistive sensors. Such magnetic functionalities depend on the texture of these heterostructure magnetic semiconductors (Akinaga *et al.* (2000), Shimizu *et al.* (2001), Thio et Solin (1998), Yuldashev *et al.* (2001)).

1.2 Growth techniques

The most common techniques to fabricate heterogeneous magnetic semiconductors (embedded nanoclusters in semiconductors) are : 1) post-growth thermal annealing of metastable diluted magnetic semiconductors (DMS) grown by molecular beam epitaxy (MBE) (De Boeck *et al.* (1996), Akinaga *et al.* (1998), Moreno *et al.* (2002)), 2) post-growth thermal annealing of semiconductors implanted by magnetic ions (Wellmann *et al.* (1997), Ando *et al.* (1998), Couto *et al.* (2005), Bucsa *et al.* (2009)), and 3) one step growth of nanoclusters embedded in semiconductor matrices by metal-organic vapor phase epitaxy (MOVPE) (Hartmann *et al.* (2002), Lampalzer *et al.* (2003), Lambert-Milot *et al.* (2008), Pristovsek *et al.* (2008)).

MOVPE and MBE are the two most common epitaxial growth techniques of semiconductors. In MOVPE the heterostructure is grown by chemical reactions of the molecules of the decomposed metal-organic precursors from the gaseous phase on a heated substrate surface. On the other hand, in MBE the structure is grown from the molecular beam of elemental sources under ultra high vacuum. Costly ultra high vacuum requirements for MBE growth makes it less attractive for high throughput production of semiconductors for technological applications.

1.3 Effect of texture on GMO and GMR responses

The texture of the nanoclusters (size and crystallographic orientation) strongly affects the magnetic functionalities of the system. For example, the GMR and GMO effects strongly depend on the size and orientation of the nanoclusters. Heterostructures containing larger nanoclusters show smaller GMO and GMR responses (Akinaga *et al.* (2000), Shimizu *et al.* (2001), Ye (2005), Heimbrodt et Klar (2005)). On the other hand, the maximum GMR and GMO responses are obtained when the magnetic moment of all nanoclusters are aligned in the direction of the current (usually in-plane of the sample) Ye *et al.* (2003), Wellmann *et al.* (1998) and in the direction of light propagation Monette *et al.* (2010), respectively. Table 1.1

summarizes the effect of texture on GMO and GMR responses.

Table 1.1 Influence of the structure and texture of nanoclusters on MO and MR responses.

Texture/structure component	**MO**	**MR**
Size	**Yes** (larger clusters, smaller MO response) (Akinaga *et al.* (2000), Shimizu *et al.* (2001))	**Yes** (larger clusters, smaller MR response) (Ye (2005), Heimbrodt et Klar (2005))
Orientation	**Expected** (Clusters magnetically oriented perpendicular to light propagation increase the MO response) (Monette *et al.* (2010))	**Expected** (Clusters magnetically oriented parallel to the direction of current increase the MR response) (Ye *et al.* (2003), Wellmann *et al.* (1998))

1.4 Motivation, general objective, and choice of material

In order to optimize the GMO, GMR or any properties related to the magnetization of the system, it is imperative that the conditions influencing the structure and texture be well understood. Hence, the model systems manganese phosphide (MnP) nanoclusters embedded in gallium phosphide (GaP) matrix and MnP films grown on GaP substrate are chosen to further understand how the texture is preconditioned by synthesis, and how it impacts the properties (in particular magnetic). Near room temperature T_c of MnP (291 K) and very similar lattice constants of GaP and silicon (5.45 Å for GaP and 5.43 Å for silicon) and its wide band gap ($E_g = 2.26$ eV) make this heterogeneous semiconductor an interesting model system.

Samuel Lambert-Milot *et al.* have shown one-step MOVPE growth of MnP nanoclusters embedded in GaP matrix, GaP:MnP, without further need for post-growth annealing (Lambert-Milot *et al.* (2008)). They studied the effect of MOVPE growth parameters such as growth temperature, growth time, and Mn/Ga flow ratio on phase, size, and orientation of MnP nanoclusters (Lambert-Milot (2012)).

Lambert-Milot's PhD work showed that larger nanoclusters form at higher growth temperatures and higher Mn/Ga flow ratios. He also showed that at higher growth temperatures (above 600 °C), in addition to MnP nanoclusters, antiferromagnetic Mn_2P (Néel temperature of 100 K) is observed, the relative concentration of which increases with increasing the growth temperature (Lambert-Milot (2012), Lambert-Milot *et al.* (2012)). This information suggests that in order to boost the magnetic functionality of the system (according to table

1.1) one needs to lower the growth temperature in order to obtain only ferromagnetic MnP nanoclusters (no antiferromagnetic Mn_2P) with smaller sizes. However, due to many structural defects observed at lower growth temperatures (Lambert-Milot (2012), Lambert-Milot *et al.* (2012)) the quality of the epilayer would not meet the industrial requirements. This is an example of how challenging it could be to fabricate heterogeneous semiconductors that meet the technological requirements.

The magnetic properties of GaP:MnP epilayers in relation to the texture have been studied by C. Lacroix in his PhD thesis (Lacroix (2010)). A controversial result of his study is the significant difference (50%) between the extracted magnetic size (Lacroix (2010)) and the physical size of MnP nanoclusters obtained from the TEM image analysis (Lambert-Milot (2012)).

The common method to find the mean size of nanoparticles is to build the size histogram by measuring the size of a large number of nanoparticles in a TEM image. The mean size and standard deviation of the nanoparticles are then found by fitting the size histogram with the aid of known mathematical functions. Due to the lack of a well-formulated technique in the literature to obtain the magnetic size histogram of an assembly of ferromagnetic and superparamagnetic nanoparticles, C. Lacroix extracted the magnetic size of the nanoclusters by modeling the magnetic hysteresis curve of GaP:MnP, based on a simple model of coherent reversal of magnetization, and fitting it to the experimental data (Lacroix (2010)). The effect of size of the nanoclusters on the reversal magnetic fields (coercive fields in the magnetic hysteresis) has been considered by introducing the thermally activated magnetization reversal process in the model (Lacroix (2010)). The lognormal size distribution has been assumed and the mean magnetic size and standard deviation of the nanoclusters have been extracted by trying different fitting parameters to the hysteresis curve (Lacroix (2010)). One of the objectives of this work is to develop a viable technique to determine the magnetic size distribution of the magnetic nanoparticles, from which the mean magnetic size and standard deviation could be extracted.

Besides the phase and size of the nanoclusters, their crystallographic orientation is an important factor that affects magnetic properties of the system. Moreover, it is more challenging to control. MnP nanoclusters in heterogeneous GaP:MnP epilayers show a limited number of specific cluster orientations with respect to the GaP matrix, whose population depend on the growth temperature and growth time Lambert-Milot (2012), Lambert-Milot *et al.* (2012). By studying the time evolution of the texture of GaP:MnP heterostructures using X-ray diffraction (XRD) pole figures and TEM image analysis, Lambert Milot *et al.* proposed a growth model, in which they suggested that presence of MnP nanoclusters inside GaP matrix leads to formation of different GaP facets after a specific thickness of the epi-

layer, which in turn affects the crystallographic orientation of nanoclusters forming at later growth times (Lambert-Milot (2012), Lambert-Milot *et al.* (2012)). Therefore, longer growth times create more variety of cluster orientations. Thus, due to the anisotropy of the magnetic functionality (orientation dependence in Table 1.1) it is highly challenging to meet industrial requirements.

In order to lessen the complexity of the structure and to have a better understanding of the formation of MnP nanoclusters in GaP matrix we chose to study the texture of a simpler geometry, MnP films grown on GaP, at different growth temperatures and growth times. This helps us to determine the most favorable orientations of MnP growing on GaP and study the texture evolution in time and temperature without any contribution from the substrate (GaP facets and structural defects).

The next step would be to use the information obtained from MnP films to design structures such as GaP/GaP:MnP/GaP and GaP/MnP/GaP to obtain the desired phase, size, and orientation of nanoclusters by eliminating the undesired factors, such as GaP facets or structural defects.

1.5 Organization of the thesis

In the next chapter nucleation and growth of thin films, different types of texture, and driving forces for texture selection will be reviewed. Chapter 3 is devoted to describe the experimental techniques, including the growth technique and analyses tools. Chapter 4 presents the results of time and temperature evolution of the texture of MnP thin films on GaP (100). The texture of MnP thin films will be compared to MnP nanoclusters in GaP:MnP, as well as GaP/MnP/GaP multilayers in Chapter 5. In Chapter 6, a methodology will be presented to extract the size distribution of magnetic nanoparticles. The results of this work will be summarized in chapter seven and conclusions will be drawn.

CHAPTER 2

Texture evolution in polycrystalline thin films

As it is mentioned in Chapter 1, we have chosen to study the texture of MnP thin films grown on GaP substrate to further understand the formation of MnP nanoclusters in a simpler system than GaP:MnP, which will hopefully provide a basis to understand and control growth in GaP:MnP epilayers. Since the effect of growth parameters on the size of nanoclusters has been studied in S. Lambert-Milot's PhD thesis (larger nanoclusters form at higher growth temperatures or larger Mn/Ga flow ratios) (Lambert-Milot, 2012), the main focus of this chapter will be on the texture selection and development of thin films.

Since MnP forms as a polycrystalline film on GaP (see Chapter 4), in this chapter we first review different types of texture, which have been observed in polycrystalline thin films. Then, we briefly discuss the effect of growth time and temperature on the texture, as well as the driving forces for texture selection, as described in the literature. At the end of this chapter we briefly review the endotaxial growth mode, as MnP grows endotaxially on GaP (Chapter 4).

It should be mentioned that in order to provide a general overview of texture selection and development in polycrystalline thin films, we have chosen to review the texture of the most studied systems in the literature, polycrystalline metallic thin films grown on polycrystalline or amorphous substrates. As the fundamentals of texture selection and development in thin films are fairly the same (for example see Ref. (Däweritz, 2006) and references therein, which discuss the texture selection and development of low temperature MBE grown MnAs on GaAs, based on the same concepts), the general concepts presented in this chapter can be applied to discuss the texture of MnP films grown on single crystalline GaP substrates.

In this thesis we use the terms "crystal", "grain", and "nanocluster". The small individual islands of the film that form at the initial stage of growth on the substrate are referred to as "crystals" in this thesis. When two or more crystals coalesce they form a larger crystal with usually the same orientation, namely "grain". The grains themselves could be considered as single crystals. In a polycrystalline film, the single crystals (grains) with different orientations are separated by grain boundaries. The term "nanoclusters" will be left for nano-sized crystals that form inside a matrix, e.g. MnP nanoclusters embedded in GaP matrix (GaP:MnP) as studied in Ref. (Lambert-Milot, 2012). Another term that is used in this thesis is the "energy" of the system, which is the Gibbs free energy of the system.

2.1 Different types of texture

Texture of a polycrystalline film is the distribution of its grains' crystallographic orientations. Four types of texture have been found and recognized in the literature : random, fiber, axiotaxial, and epitaxial (Detavernier *et al.*, 2003).

The grains in a film with random texture do not have any preferential crystallographic orientation. Hence, all possible grain orientations are equally populated, or uniformly distributed at random.

In a fiber texture the grains have a 1D alignment with the substrate in such a way that a specific family of planes {hkl} of the grains lie parallel to the surface, while their other families of planes can take any orientation (randomly distributed). The normal to the specific plane (hkl) that is parallel to the surface is called the fiber axis. In a fiber texture, the grains keep their 1D alignment and have a rotational degree of freedom about the fiber axis.

Axiotaxy is an off-normal fiber texture, in which a family of {hkl} planes of the grains align with $\{h'k'l'\}$ of the substrate (not the surface normal), while other families of planes are randomly distributed. Similar to the fiber texture, keeping their 1D alignment ([hkl] || $[h'k'l']$) the grains have a rotational degree of freedom about the axiotaxy axis to select an orientation, which is off-normal in contrast to fiber axis. As mentioned in Ref. (Detavernier *et al.*, 2003), formation of an axiotaxial texture requires two conditions. One is that the planes (hkl) of the film and $(h'k'l')$ of the substrate have a very similar d-spacing at the interface. This means that the strain in that specific plane should be very small (no limits for the strain has been mentioned in Ref. (Detavernier *et al.*, 2003). The other is that the planes (hkl) of the film and $(h'k'l')$ of the substrate remain periodic at the interface. This is schematically shown in figure 2.1 for two axiotaxy axes NiSi (211) || Si (220) and NiSi (202) || Si (220). Periodic interface possibly has a lower-energy bond configuration (Detavernier *et al.*, 2003), thus a lower interfacial energy.

Finally, the 2D alignment of a family of grains with the substrate results in obtaining epitaxial texture. The grains in a polycrystalline film may have several epitaxial alignments with the substrate.

2.2 Texture development in polycrystalline thin films

In this section, we review the texture development of thin films deposited from the vapor phase, which do not fully wet the substrate. In this case, the film grows as individual heterogeneous nucleated crystals that eventually coalesce to form a continuous film that thickens. Figure 2.2 shows growth stages, which have been recognized in a polycrystalline film grown on polycrystalline or amorphous substrates, presented by Barna and Adamik (Barna et Ada-

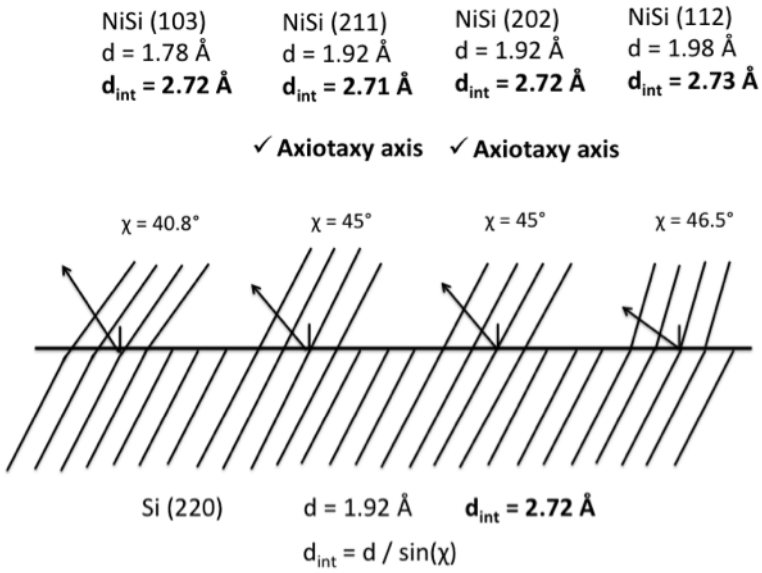

Figure 2.1 Schematic representation of the interface of axiotaxial alignments of NiSi film grown on Si (110), as reported in Ref. (Detavernier *et al.*, 2003). The d-spacings of the four planes shown in the figure at the interface (d_{int}) almost match the d-spacing of Si (220) (d) at the interface. However, only NiSi (211) and (202) || Si (220) are axiotaxy axes, since the normals to their planes make the same angle (χ) with the interface as the normal to Si (220) plane does ($\chi = 45\,^{\circ}$), thus creating a periodic interface.

mik, 1995). This growth model basically describes the texture development in metallic thin films (one component or alloy, homogeneous or heterogeneous). Yet, it can be applied to the growth of compound thin films, such as MnP on single crystalline GaP. The fundamentals of the growth of these systems and the corresponding growth stages are the same. However, some modifications need to be applied, which will be discussed throughout the text in this chapter.

According to this growth model, the texture of a polycrystalline film develops during : (1) pre-coalescence (figure 2.2(b)), (2) coalescence (figure 2.2(c,d)), and (3) thickening of continuous film (Barna et Adamik, 1995). Texture development during post-growth treatment is possible as well (Thompson et Carel, 1995), but since it is not relevant to the context of this thesis it is not considered in this chapter.

The growth stages presented in figure 2.2 are valid for $T_s \geq 0.3\ T_m$ for growth of metallic films, where T_s is the substrate temperature (growth temperature) and T_m is the melting point of the deposited film (Barna et Adamik, 1995). The growth temperature limit, $T_s \geq 0.3\ T_m$, assures the sufficient bulk and surface diffusion of adatoms, such that the material exchange between the two (or more) crystals takes place. This temperature limit may not

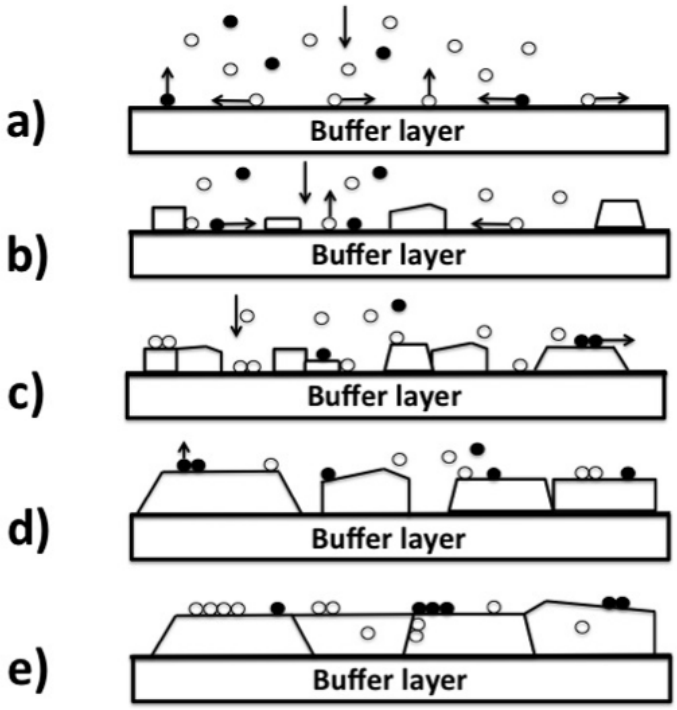

Figure 2.2 Growth stages of a polycrystalline film on a polycrystalline or amorphous buffer layer : a) nucleation, b) crystal growth, c, d) coalescence and grain growth to form a continuous film, e) thickening of the continuous film. In the image the light circles are the adatoms and the dark circles are impurity atoms. This schematic representation is adapted from Ref. (Barna et Adamik, 1995).

necessarily be valid for growth of compound materials, such as MnP on GaP. We will further discuss the effect of growth temperature on material exchange between the grains in the following sections.

2.2.1 Pre-coalescence texture development

Thompson and Carel presented a model that describes the pre-coalescence orientation selection in heterogeneous crystals that partially wet the substrate (Thompson et Carel, 1995). Orientation selection of the crystal refers to the favorable crystallographic orientations of the crystals with respect to the substrate to nucleate on the substrate. Figure 2.3 shows a heterogeneous nucleated island and the corresponding surface and interface energies. For growth on amorphous substrates, the interface energy, γ_i, is invariant for rotations about α, but not about β and δ axes. α, β, and δ are the axes of rotation of the crystal presented in figure 2.3. In this case, minimization of γ_i could lead to formation of fiber texture (Thompson et Carel, 1995).

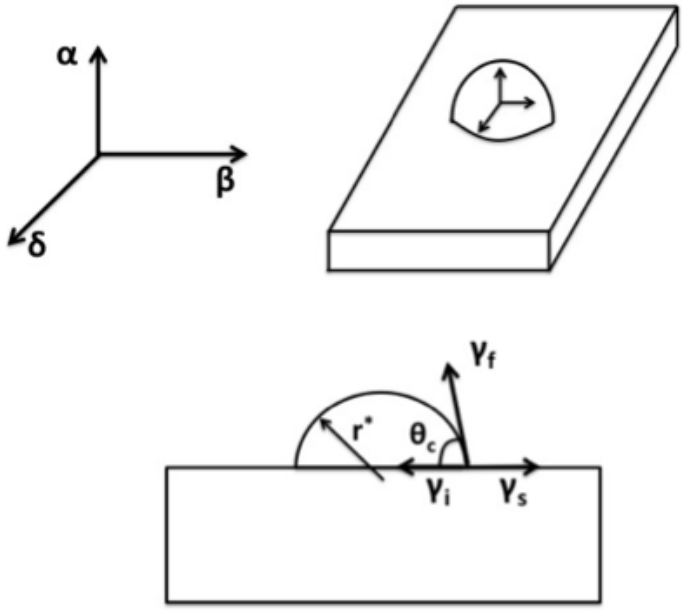

Figure 2.3 Hemispherical cap shape particle that partially wets the substrate. γ_f, γ_s, and γ_i are the surface energy of the particle (J/m^2), surface energy of the substrate (J/m^2), and the particle-substrate interface energy (J/m^2), respectively. α, β, and δ are the possible axes of rotation of the particle. θ_c is the contact angle and $r^\star$ is the critical radius for the nucleus formation. This schematic representation is adapted from Ref. (Thompson et Carel, 1995).

On the other hand, for growth on single crystalline substrates, γ_i depends on β, δ, and α. In this case, the polycrystalline film may develop restricted in-plane textures. (This is the case for the growth of MnP films on single crystalline GaP substrate.)

The growth rate of crystals with different crystallographic orientations (initially formed on the substrate) depends on γ_f, γ_s, and γ_i in such a way that the crystals with minimum surface and interface energies grow slightly faster than other crystals with the same volume. Hence, specific orientations will have a slight growth advantage and will have stronger presence in the texture of the thin film.

In addition to minimizing the surface/interface energy of the system, minimizing the strain energy during the grain growth affects the development of the texture. The competition between these various driving forces may result in developing a different type of texture (Thompson et Carel, 1995). For example, in f.c.c. metals minimizing the surface/interface energy favors the (111) texture formation, while minimizing the strain energy, which becomes more significant as the grains grow larger (later growth times), favors the formation of (100) texture (Thompson et Carel, 1995). As a result we observe a time evolution in texture of

f.c.c. metals from (111) to (100) fiber texture.

2.2.2 Texture development during coalescence

The texture development continues as the crystals grow larger and touch each other. This stage of texture development, coalescence, takes place at sufficiently high growth temperatures, where the exchange of material between different crystals occurs through surface diffusion. If the coalescence process is complete the thin film grows to become a single crystal, otherwise a polycrystalline thin film will form.

Depending on the growth temperature, this stage can be divided into two regimes : (1) the surface diffusion rate of the adatoms is high enough for the crystals to go through re-structuration. This means that adatoms migrate from a crystal that has a higher energy to a crystals with a lower energy. As the energy of a crystal depends on its crystallographic orientation, during this process crystals with some specific orientations grow at the expense of the others. This process is thermodynamically controlled and is not kinetically limited (the surface diffusion is large enough for mass transfer).

(2) The surface diffusion rate of adatoms is not sufficiently large to allow the re-structuration, and the adatoms are limited to transfer from one crystal to the neighboring crystals. This is a kinetically limited mass transfer process, during which the crystals that have higher energy surface facets grow faster than their neighboring crystal. Higher energy surface facets have larger perpendicular growth rates, since they either have more dangling bonds or more nearest neighbors (Hartman et Perdok, 1955). According to Ref. (Hartman et Perdok, 1955) the sticking coefficient of adatoms on surfaces with higher energies is larger, which results in a faster perpendicular growth rate. Thus at this stage of growth the driving force for competitive growth of neighboring crystals can be attributed to surface energy.

Coalescence occurs above a certain growth temperature, which has been determined experimentally to be $T_s \geq 0.3\ T_m$ for metallic thin films. At this growth temperature range the mobility of adatoms at the surface assures material exchange between the crystals. For the growth of a compound thin film such as MnP on GaP, the surface diffusion rate of Mn adatoms on GaP will determine the rate of material exchange between two (or more) MnP crystals, since growth conditions assure that P atoms are abundant at the surface (ratio of P/Mn $\approx$ 300). Surface diffusion of Mn adatoms could correspond to : (1) surface diffusion of Mn adatoms that arrive at the surface from the vapor phase, and (2) surface diffusion of Mn adatoms that leave a MnP crystal and diffuse at the surface. Case (2) becomes more important during the coalescence stage, where the atoms of a crystal with higher energy leave to support the growth of a crystal that has a lower energy. At this stage, the congruent temperature of MnP may become more important than its melting point, when considering

the rate of material exchange between crystals. The congruent temperature of a compound is the temperature, above which the compound decomposes. In the case of MnP the more volatile P atoms leave the MnP crystal, facilitating the Mn adatoms diffusion at the substrate. Thus the congruent temperature may be more relevant to consider. However this cannot be justified, since the congruent temperature of MnP is not reported in the literature.

In the growth temperature range of MnP films studied in this thesis, the surface diffusion rate of Mn on GaP is large enough for the coalescence stage to take place, as confirmed by the SEM and TEM micrographs of all of our MnP films grown on GaP (Chapter 4).

The coalescence process is present for a long time during the growth, after which the film becomes continuous. During this stage, nucleation and growth of secondary crystals on the substrate is present, as well. The texture development during thickening of continuous films is not observed in MnP films grown on GaP, thus will not be reviewed here. The details of this growth stage can be found in Ref. (Barna et Adamik, 1995).

2.2.3 Time and Temperature evolution of the texture of thin films

The temperature evolution of the texture of thin films at high purity conditions, proposed as the basic structural zone model presented in figure 2.4, has been reviewed by Barna and Adamik (Barna et Adamik, 1995). We briefly review this model, which essentially targets the metallic thin films on amorphous substrates. However, it could be applied to compound films such as MnP grown on single crystalline GaP substrate, since the essence of texture evolution is based on diffusion rates. In both metallic films (one component or alloy) and compound film (such as MnP) the surface and bulk diffusion rates are governed by the growth temperature (temperature of the substrate.

At low temperatures, in zone I ($T_s < 0.2\ T_m$), the surface diffusion is limited and bulk diffusion does not exist. Randomly oriented crystals form in this temperature zone and grow as fibers (columnar growth), the size of which increases by increasing the growth temperature (Barna et Adamik, 1995). This is true for growth on amorphous substrates. Crystals with specific orientations could form on crystalline substrates and grow individually (columnar growth) due to the absence of coalescence at this growth temperature range.

At moderate temperatures, in zone T ($0.2\ T_m < T_s < 0.3\ T_m$), surface diffusion becomes effective, allowing the competitive growth of randomly oriented primary islands. This is the early stage of coalescence in metallic thin films grown on amorphous substrates. In this zone the driving force for crystal growth is the difference in the surface energy of neighboring crystals. First, primary crystals with random orientations form and then, due to the competitive growth, crystals that have higher growth rates develop into cone like grains as the film thickens (Barna et Adamik, 1995). For compound films grown on crystalline substrates, since

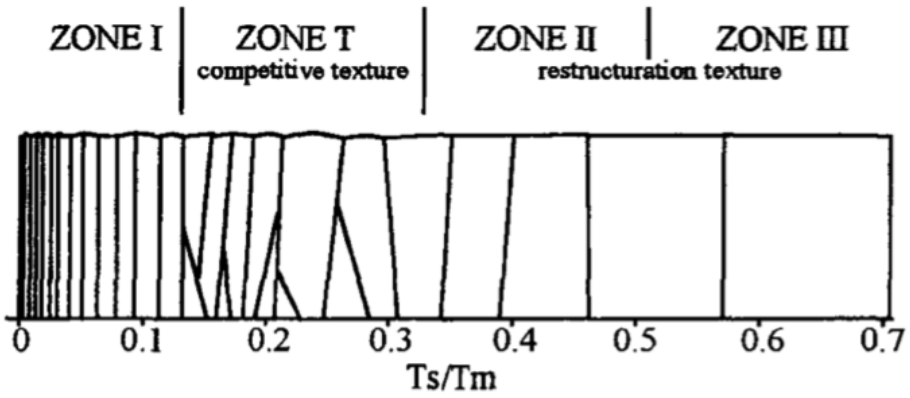

Figure 2.4 Basic structure zone model describing the temperature evolution of the texture of thin films. T_s and T_m in the horizontal axis represent the temperature of the substrate and the melting point of the bulk film. The figure is taken from Ref. (Barna et Adamik, 1995).

the mass transfer is kinetically limited in this growth zone, the crystals that have surface facets with larger growth rates are expected to grow faster than their neighboring crystals.

At higher temperatures, in zones II ($0.3\ T_m < T_s < 0.5\ T_m$) and III ($0.5\ T_m < T_s < 0.7\ T_m$), the texture is controlled by coalescence. The film is composed of single crystalline columns, the diameter of which increases with increasing temperature. The driving force that determines the texture of metallic films (on amorphous substrates) is minimizing the surface energy of the crystals (Barna et Adamik, 1995). For growth of compound films on crystalline substrate, since the growth is not kinetically limited the driving force that determines the texture is minimizing the energy of the system (the sum of its surface, interface, and strain energies).

Considering the level of impurity during thin film growth, Barna and Adamik presented the real structure zone model, which describes the time and temperature evolution of the texture of thin films (Barna et Adamik, 1995). The schematics of the real structure zone model is presented in figure 2.5.

In their model, Barna and Adamik argued that segregation of impurities, which mainly occurs at the grain boundaries, could affect the texture. This process increases the density of nucleation and consequently decreases the size of grains and the diameter of fibers, as the level of impurity and growth temperature increase. At higher growth temperatures and higher levels of impurities a contamination layer can develop, which completely covers the surface of the crystals. This contamination layer acts as new nucleation sites and new crystals will nucleated on top of the primary ones. Thus, repeated nucleation can occur during growth (Barna et Adamik, 1995). Hence, the presence of impurity can highly affect the consecutive coalescence of the primary and secondary grains, and consequently affect the time and

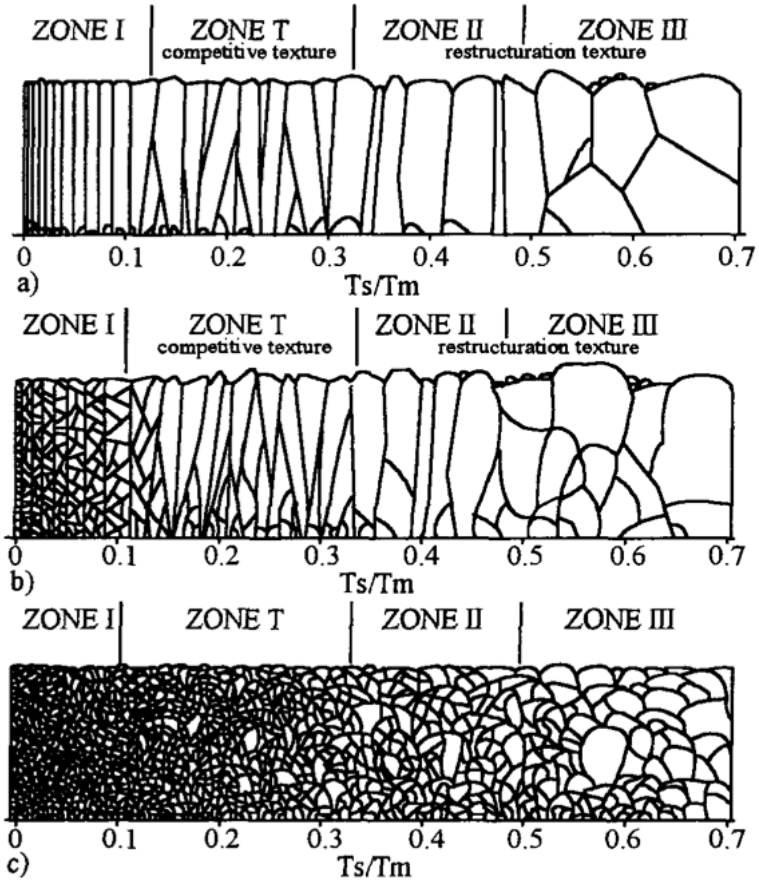

Figure 2.5 Real structure zone model that considers the level of impurity, as well as growth temperature to describe the texture evolution of thin films : a) Low impurity ($C_{imp} < 0.5\%$), b) medium impurity ($C_{imp} \approx 1\%$), and c) high impurity ($C_{imp} > 10$ %) level (Barna et Adamik, 1995).

temperature evolution of thin films. Secondary MnP grains growing on top of the primary ones have been observed in MnP films and will be discussed in Chapter 4.

2.3 Endotaxial growth

As the present models that describe the texture development in thin films do not mention the nucleation and growth of the crystals that partially or completely grow inside the substrate, in this section we briefly review this growth mode, the endotaxial growth (Bonev, 1972). Endotaxial growth has been observed in several systems, such as : buried $CoSi_2$ single crystals in Si grown by MBE (Fathauer *et al.*, 1992), silicide nanowires grown on Si as reviewed in Ref. (Bennett *et al.*, 2011), MnSb films grown on GaSb (Braun *et al.*, 2007) and InP Hatfield (2006), MnAs grown on GaAs (Yatago *et al.*, 2012) and GaInAs/InP (Iguchi

et al., 2008) grown by MOVPE.

Fathauer *et al.* observed the formation of buried single crystals of $CoSi_2$ in Si substrate (Fathauer *et al.*, 1992). In their MBE chamber, first they grew $CoSi_2$ columns on Si. After, they grew Si layers with different thicknesses on top of these columns, as cap layers. Then they deposited Co on the Si cap layer. They observed the oriented growth of buried $CoSi_2$ single crystals (on $CoSi_2$ columns) rather than expected growth of $CoSi_2$ at the surface. They also observed that this endotaxial growth depends on the thickness of the Si cap layer, such that for thicknesses higher than a critical value there was no endotaxial growth and $CoSi_2$ formed as faceted crystals on top of the Si cap layer.

They provided a qualitative description of the endotaxial growth in their system. The Co atoms hop on the surface until they find a nucleation site. With each hop there is a probability that the Co atom enters the Si cap layer. If there are not sufficient nucleation sites on the surface, they diffuse into the Si cap layer until they recombine at the surface or find a subsurface nucleation sites. In their system, the subsurface nucleation sites are the buried $CoSi_2$ columns (Fathauer *et al.*, 1992).

They have also commented on the effect of cap layer thickness on endotaxial growth, suggesting that the diffusion of Co in Si towards the $CoSi_2$ columns might be mediated by the strain in the very thin Si cap layers (Fathauer *et al.*, 1992). Hence, as the thickness of the cap layer increases and the strain is relieved, there is no endotaxial growth.

They consider the minimization of the energy of the system as the driving force for endotaxial growth. They consider two situations : (1) $CoSi_2$ crystals form on top of the Si cap layer (no endotaxy), and (2) the $CoSi_2$ crystals form on top of the $CoSi_2$ columns (buried inside Si). They argue that formation of $CoSi_2$ in case (1) has a lower energy than case (2). As the buried crystals have a lower energy than the crystals forming at the surface, then the sum of interface energy and the strain energy of $CoSi_2$ should be smaller than its free surface energy (Fathauer *et al.*, 1992).

Mahato *et al.* report the shape transition of endotaxial $CoSi_2$ nanodots to $CoSi_2$ nanowires grown on Si (100) (Mahato *et al.*, 2012). They observed formation of small square shape islands that grow up to a critical size, after which the shape transition to rectangular islands occurs. They attribute this shape transition to be strain driven as proposed by Tersoff and Tromp (Tersoff et Tromp, 1993). Moreover, they suggested that minimizing the interface energy is the driving force for the endotaxial growth on Si (100). They argued that the epitaxial growth of $CoSi_2$ on Si (100) is far more difficult than the growth on Si (111), since $CoSi_2$ (100) || Si (100) has a very high interfacial energy. Hence, it prevents the growth of islands above the surface. Thus, the endotaxial growth that leads to formation of the lowest possible interface energy, $CoSi_2$ (111) || Si (111), is favored in this system (Mahato *et al.*,

2012).

In a similar system to our MnP films grown on GaP, Braun *et al.* observed the formation of MnSb single crystals that partially grow inside a GaSb matrix (Braun *et al.*, 2007). Unlike the growth of $CoSi_2$ crystals in Si, they did not use any buried columns (as growth seeds) and directly introduced Mn and Sb on GaSb in their MBE chamber. They did not discuss the driving force for the endotaxial growth, but they argued that the observed endotaxial orientation relationship between MnSb and GaSb matrix minimizes the strain energy of the crystals. This is a comment on why a specific orientation might be observed, but does not provide any information on why the grains are forming through endotaxy.

However, by studying the in situ XRD spectra during the growth they provided useful information regarding the endotaxial growth mechanism. New peaks appeared in their spectra during growth, which correspond to formation of new GaSb orientation. They attributed this recrystallization to be due to the combination of the out-diffused Ga atoms from under the MnSb crystals with incoming Sb atoms at the surface (Braun *et al.*, 2007).

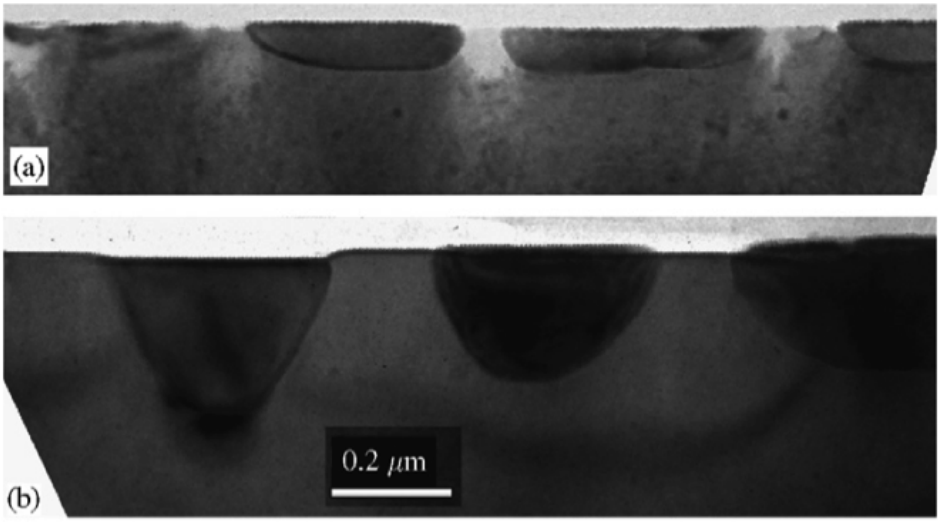

Figure 2.6 Cross-sectional TEM images revealing the endotaxial growth of MnSb on GaSb at a) 380 ± 10°C and b) 465 ± 10°C. The images are taken from Ref. (Braun *et al.*, 2007).

Hatfield *et al.* observed a similar behavior in endotaxial growth of MnSb on InP (Hatfield, 2006). In their case, the out-diffused In atoms of the substrate combined with incoming Sb to form InSb at the surface. Formation of InSb on InP substrate further confirms the endotaxial growth process proposed by Braun *et al.* (Braun *et al.*, 2007). Figures 2.6 and 2.7 show the endotaxial growth of MnSb in GaSb and the proposed endotaxial growth model, respectively.

In conclusion of these two studies, there is no information regarding the potential driving force for endotaxial growth, while the growth mechanism is observed to occur through out-

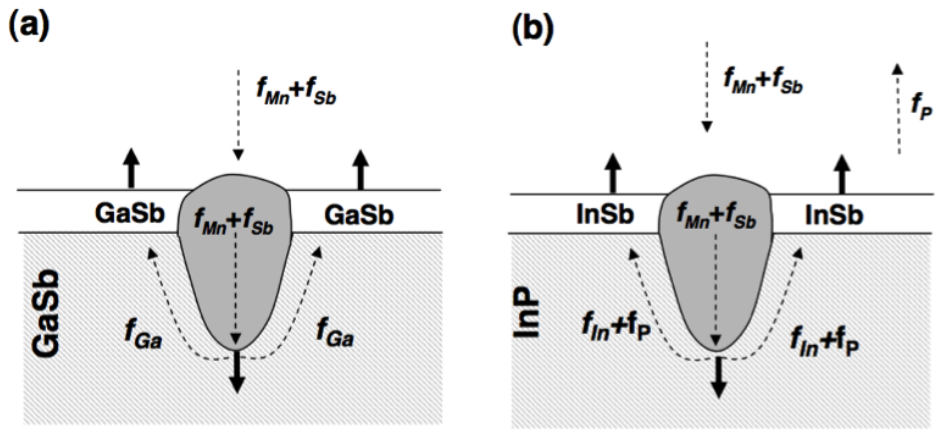

Figure 2.7 a) Braun's proposed mechanism for endotaxial growth of MnSb on GaSb, and b) similar growth mechanism proposed for endotaxial growth of MnSb on InP. Dashed arrows indicate elemental fluxes, while solid arrows show the growth direction. The figure is taken from S. Hatfield's thesis (Hatfield, 2006).

diffusion of Ga (Braun *et al.*, 2007) or In (Hatfield, 2006) atoms of the substrate.

In summary, minimizing the energy of the system, either the surface energy (Fathauer *et al.*, 1992) or the interface energy (Mahato *et al.*, 2012) could lead to endotaxial growth of the crystals. None of these studies provide a quantitative or semi-quantitative comparison between different energy terms (surface energy, interface energy, and strain energy), since values of some of the properties (such as surface energy per area) are missing in the literature.

By comparing with these systems we realize that contrary to what has been proposed by Fathauer *et al.* (Fathauer *et al.*, 1992), subsurface nucleation sites are not essential for endotaxial growth. Moreover, in none of the studies the diffusion rate of the atoms of the deposited film into the substrate (endotaxial growth) has been compared to the bulk diffusion of such atoms into the corresponding substrates.

Despite a small number of studies on the endotaxial growth mechanism, there is lack of a systematic study and solid evidence that correlates the endotaxial growth and the diffusion process, the knowledge of which may lead to a better understanding of this little-known growth mode.

In Chapter 4 of this thesis we report the endotaxial growth of MnP grains on GaP (100) substrate and provide a semi-quantitative picture for endotaxial growth. Moreover, we determine the diffusion coefficient and activation energy of the diffusion process that is suggested to take place at the GaP/MnP interface. Our results show a much larger diffusion coefficient for the interface diffusion of Mn in GaP compared to its bulk diffusion.

CHAPTER 3

Experimental techniques

In this chapter the experimental techniques that have been used to grow and characterize the samples are briefly described. We have used metal-organic vapor phase epitaxy (MOVPE) to grow all our samples, GaP, GaP:MnP and MnP from the vapor phase. The samples were then characterized by transmission electron microscopy (TEM), scanning electron microscopy (SEM), X-ray diffraction (XRD) pole figures, and vibrating sample magnetometer (VSM).

3.1 MOVPE growth of MnP and GaP:MnP films and multilayers

The samples have been grown in a horizontal low-pressure cold-wall MOVPE quartz reactor at the Polytechnique Montreal, which is schematically illustrated in figure 3.1 (Cova *et al.*, 1991). Trimethyl-gallim (TMGa), trimethyl-indium (TMIn), tertiarybutylphosphine (TBP), and methyl cyclopentadienyl manganese tricarbonyl (MCTMn) have been used as organometallic precursors, with high-purity hydrogen as the carrier gas.

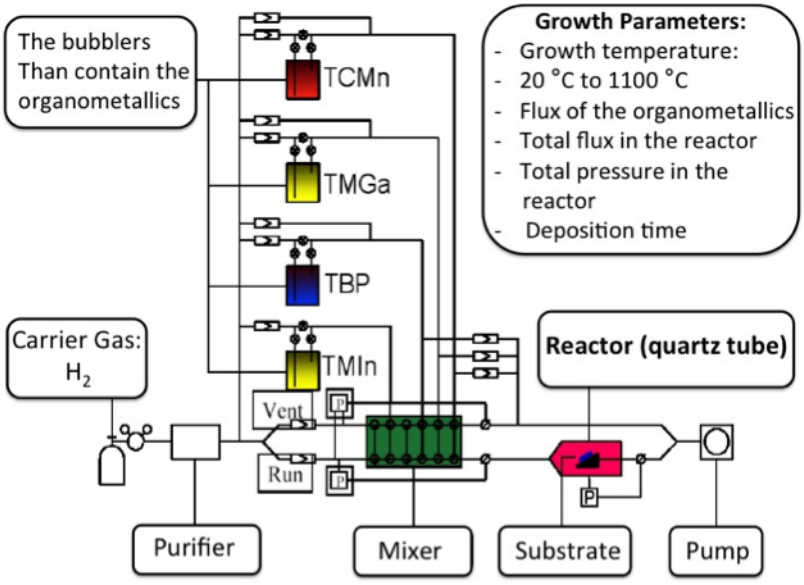

Figure 3.1 Schematics of the MOVPE reactor dedicated to the growth of compounds containing transition metals, such as Mn. The image is taken from Ref. (Lambert-Milot, 2012).

Prior to growth, the substrates (GaP and glass (microscope slides)) have been cleaned in

acetone (about 40 °C), iso-propanol (about 40 °C), and de-ionized water [H_2O (DI)] (room temperature), each step for 10 minutes. The substrates were then chemically etched in a $HNO_3 : HCl : H_2O$ (DI) (1 :2 :2) solution at 60 °C for 2 minutes. They were then rinsed with H_2O (DI) and dried with a nitrogen gun for 5 minutes and, immediately after, transferred into the MOVPE reactor. The substrates were placed on a graphite susceptor approximately located at the center of the reactor. A thermocouple was inserted into the susceptor ensuring intimate thermal contact to continuously monitor the growth temperature.

The growth parameters have been set by independently adjusting the growth temperature, the gas flow of the organometallic precursors and carrier gas, the total pressure in the reactor, and the growth time. The total pressure of the reactor has been set to 40 Torr with total gas flow of 4000 sccm (standard cubic centimeter per minute) for growth on GaP and 2000 sccm for glass substrates. The flow of TMGa has been fixed to 8.6 μmole/min, which gives a reasonable ($\approx$1.2 μm/h) growth rate for GaP at 650 °C. TBP flow has been set to 670 μmole/min to fix the ratio of element V to element III (J_V/J_III) to 78, which was found necessary to avoid surface morphology degradation The flow of MCTMn has been set to 2.46 μmole/min to grow MnP films (on GaP and glass substrates) and GaP/MnP/GaP multilayers and 0.98 μmole/min for GaP:MnP and GaP/GaP:MnP/GaP multilayers.

After insertion into the reactor, the substrates have been heated for 10 minutes at 700 °C (GaP) and 600 °C (glass) under the TBP flow in order to remove the oxides from their surfaces, and to avoid substrate surface degradation in the case of GaP. Then nominally 200 nm of GaP has been grown at 700 °C as a buffer layer for samples grown on GaP. No buffer layers were introduced for the growth of MnP on glass.

The growth of the GaP:MnP heterogeneous films starts after the buffer layer deposition by adjusting the growth temperature to the desired value and introducing the MCTMn precursor to the quartz reaction chamber. To grow the GaP/GaP:MnP/GaP multilayers (10 periods) after buffer layer deposition we have decreased the temperature to 650 °C and introduced MCTMn for 90 seconds (about 30 nm of GaP:MnP) and then re-introduced it after 3 minutes. During this 3 minutes GaP has been grown for about 60 nm. This procedure was repeated 9 times and the growth has been ended by the 10^{th} layer of GaP:MnP.

To grow the GaP/MnP/GaP multilayer (17 periods) after the buffer layer growth we decreased the temperature to 550 °C, switched the TMGa flow to vent, and introduced the MCTMn precursor for 54 seconds ($\approx$3 nm of MnP). Then we switched the MCTMn flow to vent, increased the temperature to 650 °C (no growth during temperature raise) and then introduced TMGa for 2.5 minutes (50 nm of GaP). We repeated this procedure 16 times and finished the growth by the 17^{th} layer of MnP. Tables 3.1 and 3.3 summarize the list of samples studied in this thesis and their growth parameters.

Table 3.1 List of samples grown on GaP (100) substrates by the procedure described in the text.

Sample	**Structure**	**Growth T** °C	**Growth time (s)**
MnP-550-1.5	MnP Thin film	550	90
MnP-550-5	MnP Thin film	550	300
MnP-550-15	MnP Thin film	550	900
MnP-650-5	MnP Thin film	650	300
MnP-650-15	MnP Thin film	650	900
MnP-650-30	MnP Thin film	650	1800
MnP-600-15	MnP Thin film	600	900
MnP-700-15	MnP Thin film	700	900
MnP-750-15	MnP Thin film	750	900
GMP-550-45	GaP : MnP	550	2700
GMP-600-45	GaP : MnP	600	2700
GMP-650-1.5	GaP : MnP	650	90
GMP-650-5	GaP : MnP	650	300
GMP-650-15	GaP : MnP	650	900
GMP-650-45	GaP : MnP	650	2700
GMP-700-45	GaP : MnP	700	2700
GMP-750-45	GaP : MnP	750	2700
MnP-M17	GaP/MnP/GaP	650 (GaP) / 550 (MnP)	150 (Ga) / 54 (MnP) (1 period)
GMP-M10	GaP/GaP:MnP/GaP	650	180 (Ga) / 90 (MnP) (1 period)

Table 3.2 List of MnP films grown on glass substrates. The growth procedure is described in the text.

Sample	**Growth T** °C	**Growth time (min)**
MnP-G550-15	550	15
MnP-G550-60	550	60
MnP-G600-15	600	60

All the GaP:MnP epilayers and the MnP films (except for MnP-550-1.5 and MnP-550-5) have been grown by Samuel Lambert-Milot. The MnP films grown on glass, the multilayer samples, as well as MnP-550-1.5 and MnP-550-5 have been grown by myself.

3.2 Electron microscopy

The angular resolution of 3×10^{-4} rad and the focusing distance of 25 cm for human eye's retina gives the diameter of the smallest distinguishable particle to be about $75\mu m$. To study the vast interesting world below this spatial resolution, we need a tool to magnify the images, a microscope. The minimum magnification that is required to observe an object with diameter D_o is $M_m = (75\mu m)$ / D_o. For example to observe a DNA molecule with $D_o = 2$ nm

Table 3.3 List of parameters used for the growth of samples studied in this thesis, as well as their range of values.

Sample	GaP:MnP, MnP films, GaP/GaP:MnP/GaP, GaP/MnP/GaP
Substrates	GaP and glass (microscope slide)
Growth temperature	Range : $550 - 750\,^{\circ}\mathrm{C}$
Growth time	Range : 1.5-60 min
Total flow in reactor	4000 sccm (GaP) / 2000 sccm (Glass)
Flow of TMGa	8.6 $\mu mole/min$ (≈ 1.2 $\mu mole/h$ of GaP)
Flow of MCTMn	0.98 $\mu mole/min$ (GaP:MnP epilayers and GMP-M10) 2.46 $\mu mole/min$ (MnP films and MnP-M17)
Flow of TBP	670 $\mu mole/min$

we need a minimum magnification of 40,000. But of course to study this molecule we need a much larger magnification coupled with a very high resolution (Egerton, 2005).

The resolution of an optical microscope is limited by the wavelength of light and numerical aperture of the objective lens. If we take the shortest visible wavelength of 400 nm and the best available numeric aperture of 1.4 we obtain the resolution of 200 nm for the best optical microscope, which certainly is not sufficient to study small molecules or atoms (Egerton, 2005).

In early 20^{th} century scientists discovered the wave-like behavior of small particles, such as electrons and realized that the wavelength of these small particles can be controlled by an accelerating voltage. A relatively small potential difference of 50 V applied to electrons gives them the energy that is equivalent to a wave packet with the wavelength of 0.17 nm. This wavelength is comparable to atomic dimensions. Increasing the voltage to 50 kV decreases the wavelength of electrons to 5 pm. These high-energy electrons will also penetrate several microns into the material. If theses electrons pass through a very thin crystalline solid, they diffract from atomic planes. By focusing these diffracted electrons, one can form the image of the material with a very high resolution (Egerton, 2005).

3.2.1 Transmission electron microscopy

In a TEM, a beam of electrons transmits through a very thin specimen ($\approx$100 nm), interacts with the atomic planes and is focused by appropriate lenses to form the image. The magnification of TEMs is typically in the range of 10^3 to 10^6. Moreover, the instrument provides the possibility of forming electron diffraction patterns and chemical analysis (Egerton, 2005). Figure 3.2 is a schematics representation of a TEM.

We can divide a TEM into three sections : the illumination system, the specimen stage, and the imaging system. The illumination system consists of an electron gun and two or

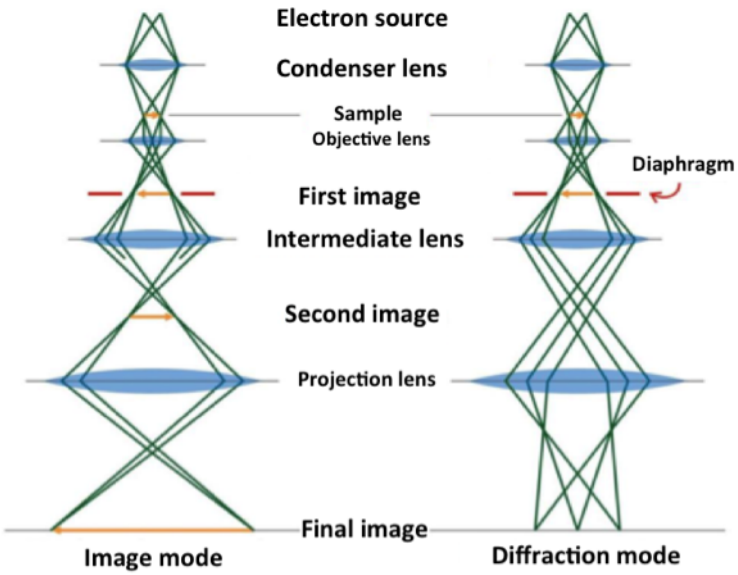

Figure 3.2 Schematic representation of a TEM. The figure is taken from Ref. Lambert-Milot (2012).

more condenser lenses. The electrons are generated from an element that is connected to a high voltage source. The element is usually tungsten or lanthanum hexaboride (LaB_6) (In JOEL 2100F the element is ZrO/W). By applying a high voltage (typically 100-300 kV), the element will emit electrons through thermionic or field emission. The generated beam of electrons is then focused into a very thin beam by electromagnetic lenses (condenser lenses) before passing through the specimen. The specimen is placed on a stage that allows it to be held stationary or move (or tilt). The mechanical stability of the stage is an important factor that affects the spatial resolution of the image (Egerton, 2005).

The transmitted beam of electrons pass through few electromagnetic lenses (objective lenses) and the magnified image (or the diffraction pattern) is formed on a fluorescent screen, a photographic film, or on the screen of an electronic camera. The configuration of the lenses determines the magnification of the image, while the design of the lenses determines the spatial resolution of the image.

To produce the SAED pattern, a parallel beam of electrons are shone to the specimen and the transmitted electrons are passing through a thin strip of metal, which is the selected area aperture. This aperture has holes with different sizes that allow the electrons to pass through. Hence, we have the possibility to block the transmitted electrons from everywhere in the sample, except for the region of interest. The diameter of the smallest aperture used in this thesis is 120 nm.

Due to the very small size of some of our MnP grains we were not able to obtain their ED patterns using SAED. For these grains we produced the ED patterns using the Fast Fourier transform of the high-resolution TEM (HR-TEM) images. This Fourier transform to obtain the reciprocal space of a lattice has been performed using the Digital Micrograph software at CM^2 of Polytechnique Montreal.

Figure 3.3 shows the cross sectional image of a MnP grain grown at 600 °C on GaP and its SAED pattern. From the electron diffraction (ED) pattern (obtained from SAED or FFT) we can determine the directions of the normal to the GaP and MnP planes. On the ED pattern the central bright spot is the transmitted beam and the other bright spots are the diffracted electron beams from different planes. The separation between a bright spot and the central bright spot is the inverse of the interplanar spacing (d-spacing) of a specific plane. For example, if the distance between a bright spot and the central spot is measured to be 0.19 nm^{-1}, it corresponds to MnP (010) plane with d-spacing of 5.26 Å. The White and yellow arrows in figure 3.3 show different crystallographic directions of MnP and GaP, respectively. The pattern allows us to determine the crystallographic orientation of MnP with respect to GaP. The grain shown in figure 3.3 has the orientation relation MnP [-13-1] || GaP [02-2], since the angle between these two directions is almost zero (0.3 °). In the SAED pattern shown n figure 3.3, the out of plane directions are MnP [10-1] and GaP [011]. Hence this grain has the epitaxial relation : MnP [-13-1] || GaP [02-2] and MnP [10-1] and GaP [011]. The selected area aperture used for this SAED pattern has been selected such that we obtain the diffracted electrons from both GaP buffer layer and MnP grain.

In this thesis, we have used the TEM imaging, selected area electron diffraction (SAED) and Fast Fourier transform (FFT) of MnP grains in JEOL 2100F microscope equipped with a field-emission electron source at the CM^2 of Polytechnique Montreal. All the cross-sectional TEM images presented in this thesis are bright field images taken at the [011] zone axis of GaP, unless otherwise mentioned. By GaP [011] zone axis we mean that the transmitted electron beam is parallel to GaP [011].

3.2.2 Dislocation imaging

To verify whether there is any dislocations in the GaP buffer layer in our MnP films, we studied the bright field TEM cross-sectional images of our samples taken at two different zone axes GaP [011] and GaP [1-12], along three different g vectors [200], [1-11], and [0-22]. A TEM image taken along g[200] corresponds to an imaging condition, in which the sample is tilted in such a way that only the transmitted beam and the diffracted beam from GaP {200} planes are allowed to reach the detector. This condition provides a contrast that allows one to detect potential dislocations in the sample. Figure 3.4 shows an TEM image of MnP-

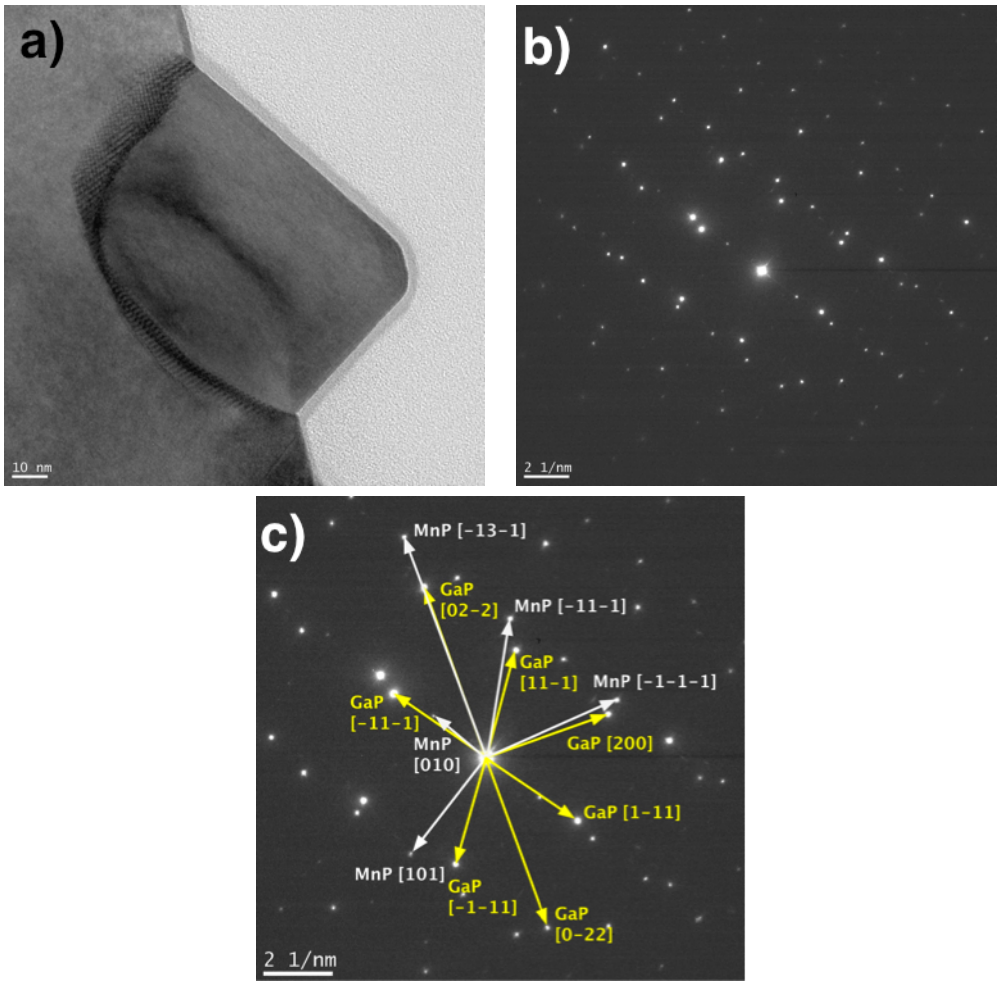

Figure 3.3 a) Cross-sectional TEM image of a MnP grain grown at 600 °C on GaP, b) the SAED pattern of GaP substrate and MnP grain, and c) determined normal direction to GaP and MnP planes. The diameter of the aperture hole to obtain the SAED pattern is 120 nm. According to (c), we assigned the alignment MnP [-13-1] || GaP [02-2] to this grain.

650-15 taken at GaP [011] zone axes along g [200]. Since we do not observe any sharp lines in the TEM micrograph, it seems safe to conclude that there is no dislocations observed in the image.

3.2.3 TEM sample preparation

The samples studied in this thesis have been prepared for cross sectional TEM imaging, either by the conventional mechanical polishing or using focused ion beam (FIB) technique. The samples MnP-550-15, MnP-600-15, MnP-650-15, MnP-700-15, and MnP-750-15 have been prepared for cross-sectional TEM imaging by Samuel Lambert-Milot and the sample GMP-M17 by myself using conventional mechanical polishing technique. In this technique, a

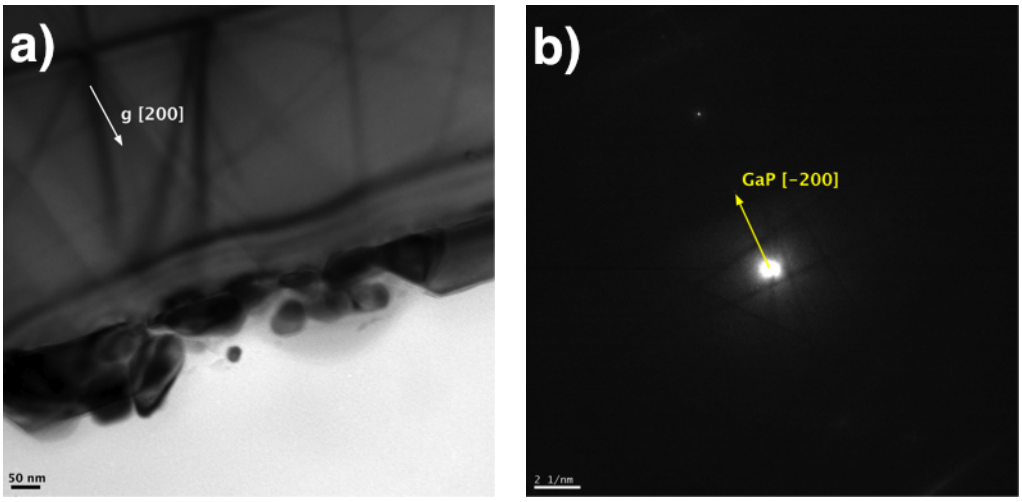

Figure 3.4 a) Cross-sectional TEM image of MnP-650-15 taken at GaP [011] zone axis along g [200]. b) The diffraction condition, where only GaP {200} planes diffract.

stack of sample and silicon substrates were epoxied together, in such a way that the center-piece was two samples epoxied face to face. Then a thin slice was cut from the stack cross section, mechanically polished, dimpled and ion milled until a small hole appeared at the center of the sample. The region around the hole was thin enough (about 100 nm) for cross sectional TEM observations. The details of this technique are presented in Ref. (Lambert-Milot, 2012). The rest of the samples have been prepared using FIB technique by Jean Philippe Masse and Nicole MacDonald in CM^2 center at Polytechnique Montreal. Here, we briefly describe the FIB technique to prepare the samples for cross sectional TEM imaging.

FIB functions in a very similar fashion to scanning electron microscope (see next section), except that in SEM a focused beam of electrons is used for imaging, while in FIB a focused beam of ions (usually gallium) is used for imaging (low beam current) or milling and sputtering (high beam current).

Two samples have been prepared at a time using the FIB technique. Figure 3.5 shows few steps of FIB sample preparation. First, the two samples were epoxied together face to face. Then due to the size limitation of the FIB machine, they were polished to a size of 3-4 mm by 1.5-2 mm. Then a 2 μm $\times$ 15 μm protective tungsten (W) layer has been deposited at the center of the sandwich. After, by ion milling (30 kV) the surrounding of the tungsten layer, all parts of the sample were removed except for a small piece that connected the thin specimen (lamella) to the bulk (the small piece acts as a bridge). Then a microprobe was welded to the free side of lamella to remove it from the bulk and glue it on a TEM copper grid. The microprobe was removed after. In the final stage of sample preparation, the lamella was thinned from both sides using a low current beam to about 60-100 nm.

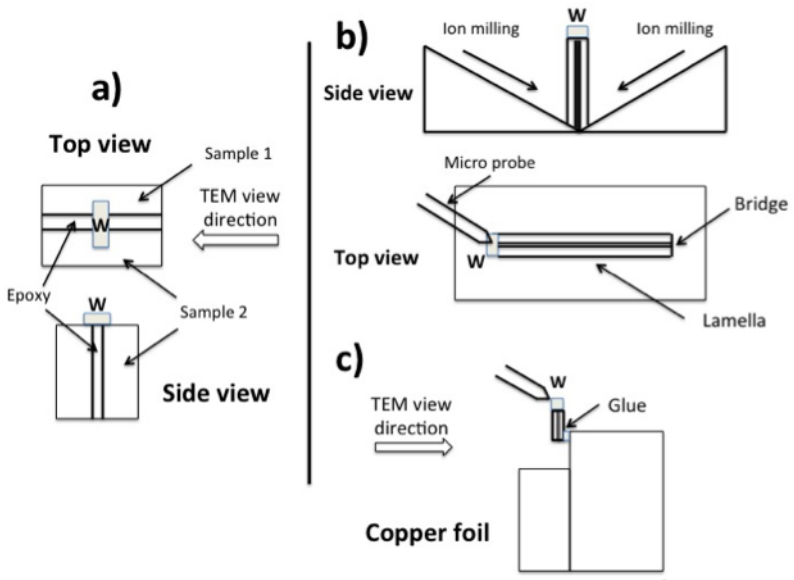

Figure 3.5 Few steps of TEM sample preparation using FIB technique. a) Sandwich of two samples and the tungsten layer deposited on the surface, b) ion milling, lamella preparation, and microprobe welding, c) transferring the lamella to copper grid.

3.2.4 Scanning electron microscopy

For the samples studied in this thesis plan-view and cross-sectional SEM images have been carried out in Hitachi S-4700 system.

Scanning Electron Microscope is an electron microscope that creates the image of the sample through scanning the surface by an electron beam. There are three main components in an SEM : electron column, specimen chamber, and appropriate electronics (Egerton, 2005). Figure 3.6 is a schematic representation of an SEM.

Similar to TEM, in the electron column, a beam of electrons is created through thermal or field emission. Tungsten or lanthanum hexaboride (LaB_6) are usually used as the filament of the electron source. Since the spatial resolution of the instrument is critically dependent on the electron beam diameter, before reaching the specimen the electron beam passes through two or three condenser lenses and finally through an objective lens. The final diameter of the beam can be as narrow as 1 nm (Egerton, 2005).

The specimen chamber is located below the electron gun and is held under vacuum. It contains a moving stage for the specimen and detectors. The focused electron beam scans the specimen's surface horizontally in two perpendicular directions, x and y. This process is known as raster scanning and the beam covers a rectangular area on the specimen. Various forms of radiation such as secondary electrons, back scattered electrons, and X-rays are generated

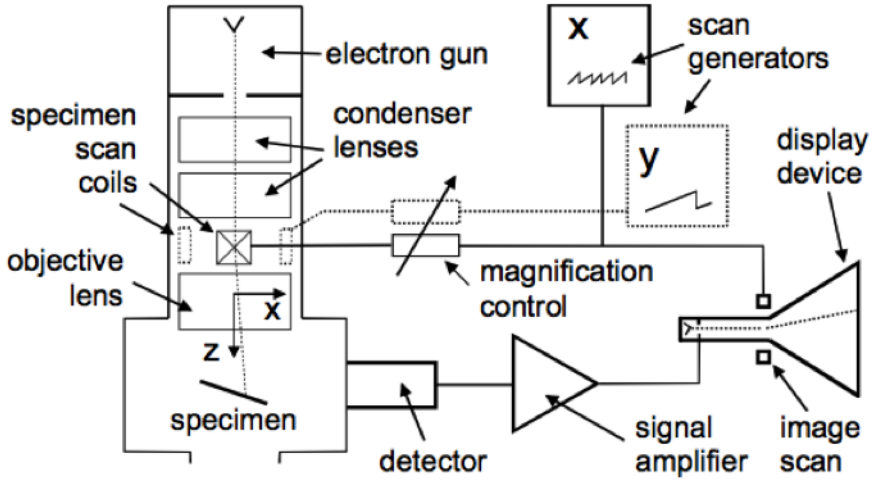

Figure 3.6 Schematic representation of an SEM. The image is taken from Ref. Egerton (2005).

through the interaction between the beam and the specimen (Egerton, 2005).

The most common mode of scanning electron imaging is through detecting secondary electrons. The generated secondary electrons are accelerated through a scintillator and as a result, visible light is emitted. This light is detected by a photomultiplier and converted to an amplified current signal. In traditional SEM this signal is further amplified by a cathode ray tube, but in modern SEMs the current signal from the detector is digitized and a computer is used to analyze the image.

Figure 3.7 shows a plan view SEM image of MnP-600-15. From this image we realize the MnP grows as a polycrystalline film on GaP. Moreover, we extracted the grain size distribution and the aspect ratio of the elongated grains in this sample (Chapter 4), using Fiji software.

3.3 X-ray diffraction pole figures

The details of X-ray diffraction pole figure measurements and analysis are provided in Refs. (Lambert-Milot, 2012) and (Gaudet, 2011). In this section we give a brief background on X-ray pole figure measurements and analysis.

X-ray diffraction is a powerful technique to study the structure of crystalline materials. In a typical X-ray diffraction measurement the specimen is mounted on a goniometer that is rotated, while being irradiated by the X-ray beam and the diffracted X-ray will be detected. The interaction of the X-ray beam with the crystallographic planes (hkl) of the specimen with inter-planar spacing d_{hkl} creates an interference pattern, in which the constructive interference

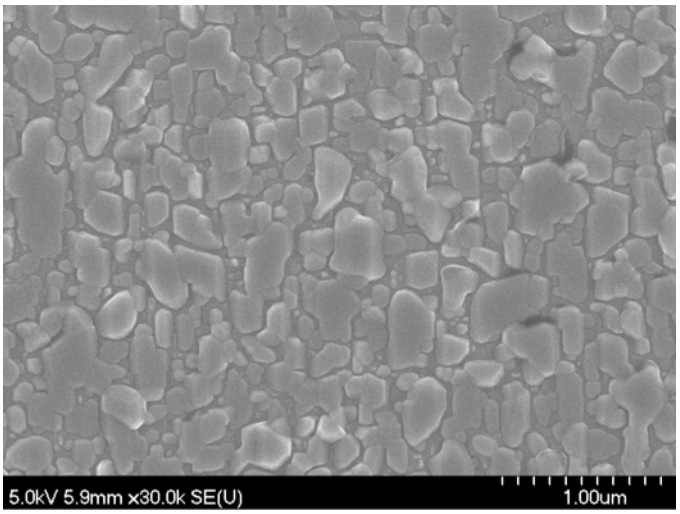

Figure 3.7 Plan view SEM image of MnP film grown on GaP (100) at 600 °C showing polycrystalline MnP grains on the surface.

satisfies Bragg's equation :

$$n\lambda = 2d_{hkl}sin\theta \tag{3.1}$$

In Eq. 3.1, λ is the wavelength of the incident X-ray, θ is the angle of incidence with the normal to the scattering planes (hkl), and n is a positive integer (n = 0, 1, 2, ...).

To systematically study the texture of a crystalline material it is best to create a three-dimensional (3D) reciprocal space map of the specimen, which has become possible with X-ray sources of high photon flux. In the reciprocal space map of a material, we scan a large number of points, the position of which are determined by the inter-planar spacing, d_{hkl}, the θ angle according to Eq. 3.1, and the position of the normal to the sample surface, which is defined by angles ψ and ϕ in figures 3.8, and 3.9.

To create a 3D reciprocal space map of a crystalline material we need to measure the intensity of the diffracted X-rays as a function of angles ψ and ϕ, as well as inter-planar spacing, d_{hkl}, which is related to angle θ by Eq. 3.1. Figure 3.9 schematically shows the measurement configuration, as carried out at the National Synchrotron Light Source (NSLS) (Brookhaven National Laboratory).

A beam of X-rays from a synchrotron source, S_0, is shone to the specimen that is mounted on a four-circle diffractometer (Schultz geometry) and the intensity of the diffracted X-rays, S_1, is measured using different types of detectors, which are presented in figure 3.9 (d). In a conventional measurement with a point detector, set of {hkl} planes with inter-planar spacing d_{hkl} are selected by setting the angles of incidence equal to the angle of diffraction ($\omega = \theta$). By moving the goniometer to scan all χ (0 ° to 90 °, χ = 90 ° - ψ) and ϕ (0 ° to 360 °) angles,

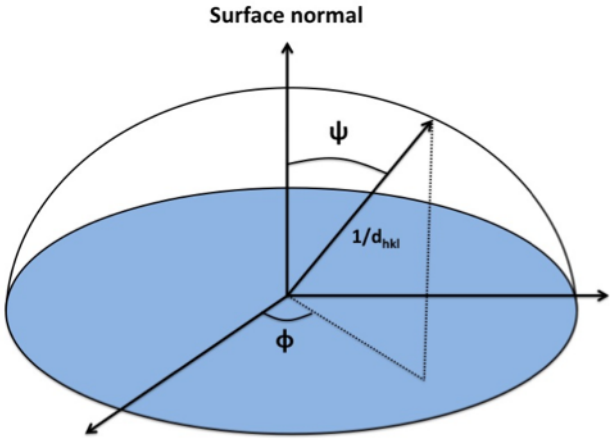

Figure 3.8 Definition of reciprocal space coordinates $1/\ d_{hkl}$, ψ and ϕ associated to a crystalline material sample.

we obtain an angular mapping of orientations of the {hkl} family of planes. By repeating this procedure for different angles of incidence a complete 3D reciprocal space map of the sample may be obtained. It should be mentioned that obtaining a complete map using a point detector takes an extremely long time (few days).

Measuring with a linear detector, one needs to scan only the angles χ and ϕ, as the detector covers a certain range in angle 2θ (certain range in d_{hkl}). This will decrease the measurement time to few hours. However, the trade off will be the angular resolution. A planar detector shortens the measurement time even more by covering a certain range in angles 2θ and χ, while we are scanning the angle ϕ. Using a planar detector is very convenient for quick systematic texture analysis, at the expense of losing some resolution. This loss of resolution may be detrimental for the determination of strain.

A pole figure is an orientation map (angles χ and ϕ) of a certain family of planes {hkl} that is obtained from the 3D reciprocal space map. Figure 3.10 shows random, fiber, axiotaxial, and epitaxial textures and their corresponding pole figures. Now we briefly explain how the pole figures of different selected textures look like. We consider a polycrystalline film that consists of grains with three different textures : randomly oriented grains, fiber texture/axiotaxial grains, and epitaxial ones. The pole figures of randomly oriented grains will show only a constant background with no specific feature with higher intensity, since for a random texture the number of grains in every possible orientation is the same. In a fiber texture/axiotaxial grains, the 1D alignment of a specific plane of the grains with a specific plane of the substrate results in observing circles, arcs, and lines with more intensity on some pole figures. We observe such features in the pole figures of fiber/axiotaxial textures, since the grains have

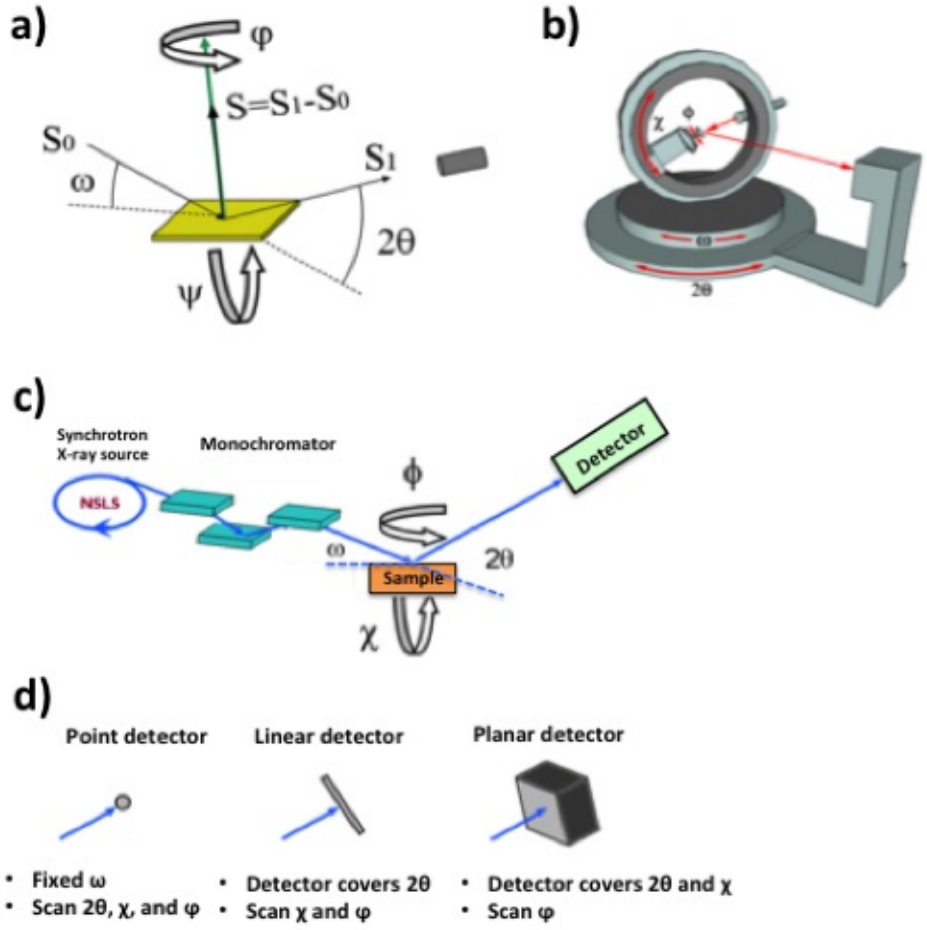

Figure 3.9 Configuration of XRD pole figure measurement. a) Incident (S_0) and diffracted (S_1) beam and their angle with sample's plane, b) geometry of the sample holder and illustration of angles, c) experimental setup to obtain reciprocal space map with a synchrotron source, and d) different types of detectors and their corresponding scan modes.

a rotational degree of freedom about the fiber/axiotaxy axis (1D alignment). Hence, for a specific fiber/axiotaxy axis we observe circles in the pole figure of some planes and arcs and line in some others. Finally, for epitaxial grains that have 2D alignment we observe spots with higher intensities.

Knowing the angular position of different planes of the substrate and studying different pole figures of a sample (position of the bright spots, circles, arcs, and lines) we can determine the epitaxial/axiotaxial orientation of the grains with respect to the substrate. Figure 3.11 shows the position of different planes normal on the reciprocal space map of GaP.

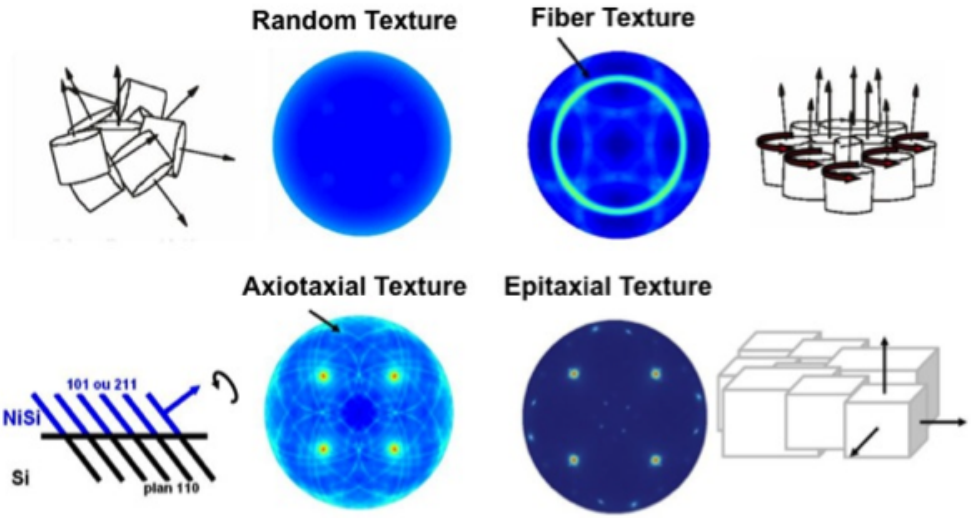

Figure 3.10 Different types of texture and their corresponding pole figures. This figure is taken from (Gaudet, 2011).

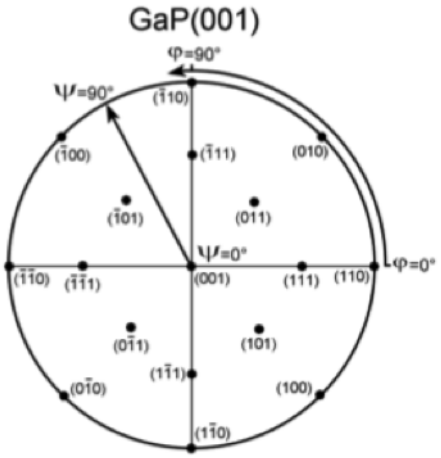

Figure 3.11 Position of different planes normal on the reciprocal space map of GaP. This reciprocal space map is obtained by a projection of a surface in 3D to a plane. The image is taken from (Lambert-Milot, 2012).

A bright spot at a specific ψ and ϕ on a pole figure corresponding to a specific d_{hkl} represents a family of grains, for which the normal to their {hkl} planes makes the angles ψ

and ϕ with the surface normal. Theses grains do not necessarily have the same crystallographic orientations, since they could have a rotational degree of freedom about the normal to that {hkl} plane, i.e. fiber/axiotaxial texture. To verify the grains with the same crystallographic orientation we need to analyze at least two pole figures.

Simon Gaudet has developed a software that facilitates the pole figures analysis (Gaudet, 2011). This software can be found on :`http://code.google.com/p/xrd-texture`. The details on how the software works are presented in Ref. (Gaudet, 2011).

Figure 3.12 shows the MnP (111) pole figure of MnP-650-15 that contains axiotaxial and epitaxial grains. MnP (111) pole figure corresponds to inter-planar spacing of 2.47 Å. The bright spots correspond to the epitaxial alignments, while the arcs indicate axiotaxial texture. Two of the bright spots shown by arrows number 1 and 2 have been selected as an example of epitaxial alignments. These bright spots correspond to : MnP {121} || GaP (100) (arrow 1) and MnP {010} || GaP (100) (arrow 2). The arc shown in the figure corresponds to the axiotaxial texture with axiotaxy axis : MnP (001) || GaP (011). These assigned alignments have been confirmed by studying other pole figures of MnP-650-15, such as MnP (020), MnP (101), and MnP (211).

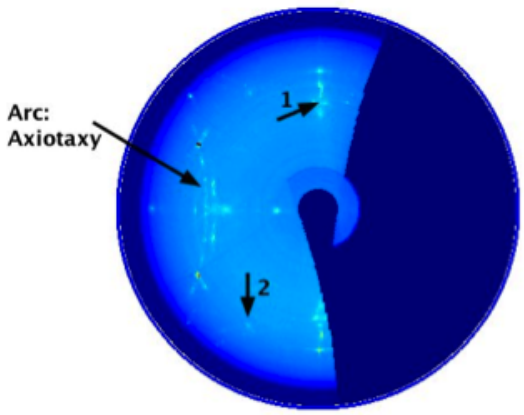

Figure 3.12 MnP (111) Pole figure of MnP-650-15. The blue color shows the lowest intensity and the red shows the highest. The spots with higher intensity correspond to epitaxial grains, while the arc corresponds to axiotaxial grains. The dark blue color on the right side of the pole figure corresponds to the angular portion that has not been measured.

Another piece of information that can be obtained from the pole figures is the relative population of the grains with different crystallographic orientations, the details of which is available in Ref. (Lambert-Milot, 2012). In our samples, The relative population of each orientation family has been obtained from the following procedure : We have chosen the

MnP (211) pole figure of this sample, since the bright spots that correspond to MnP (211) planes of different orientation families do not overlap in this pole figure. Using our pole figure analysis software (Gaudet, 2011), we obtained the XRD spectrum at the angular position of each bright spot. The relative population of each orientation family has been obtained by comparing the area under its corresponding MnP (211) XRD peak.

All the pole figures studies in this thesis have been obtained using the National Synchrotron Light Source (NSLS) (Brookhaven National Laboratory) X20A and X6B beamlines. The wavelength of the X-rays have been selected using Si (111) monochromators to be 1.5406 Åwith $\Delta E/E \approx 0.4\%$ on X20A and 1.050 Åwith $\Delta E/E \approx 0.2\%$ on X6B). A linear and planar detector has been used on X20A and X6B beamlines, respectively. All the samples have been measured by Samuel Lambert-Milot, except for MnP-M17 that hes been measured by Jelle Demeulemeester.

3.4 Vibrating sample magnetometer (VSM)

To study the magnetic properties of our samples, we have used the EV9 magnetometer of Microsense (formerly ADE Technologies) that provides us with magnetic fields in the range -2.2 to 2.2 Tesla and a precision of about 8×10^{-6} A/m (10^{-7} emu) for 300 averaging in the magnetization measurements (0.15 seconds for each measurement point). It also enables us to carry on temperature dependent measurements in the range 77 to 900 K.

Figure 3.13 illustrates the configuration of a typical VSM measurement. The magnetic sample is positioned in the middle of two pole pieces of an electromagnet that provide DC magnetic field. The sample vibrates at a frequency of 75 Hz resulting in a time and space variation of magnetic field generated by its magnetic moment. This varying magnetic field induces a current in two pairs of perpendicular coils that are positioned in plane of the sample (gradiometer configuration). The induced potential difference in the coils (V) is translated into the average magnetic moment (Am^2) after calibrating the system with a known sample (usually a Nickel disk). Knowing the weight or the volume of the sample, the moment is then converted into mass magnetization σ_M ($\mathrm{Am}^2/\mathrm{kg}$) or volume magnetization, M (A/m).

In this thesis we have measured the isoremanent magnetization (IRM) signal to extract the size and magnetic size distribution of magnetic MnP nanoclusters in GaP:MnP samples. The results are presented in Chapter 4. To measure the IRM signal, we started from a demagnetized state of the samples, which had been achieved by heating the sample at 330 K (above its Curie temperature, $T_c \approx 291$ K). We then cooled the samples to a desired temperature, $T = 240, 260$, or 280 K, at zero magnetic field (zero field cooled (ZFC)). At the desired temperature, a magnetic field of $H = 15.9$ kA/m (200 Oe) was applied parallel to the sample's

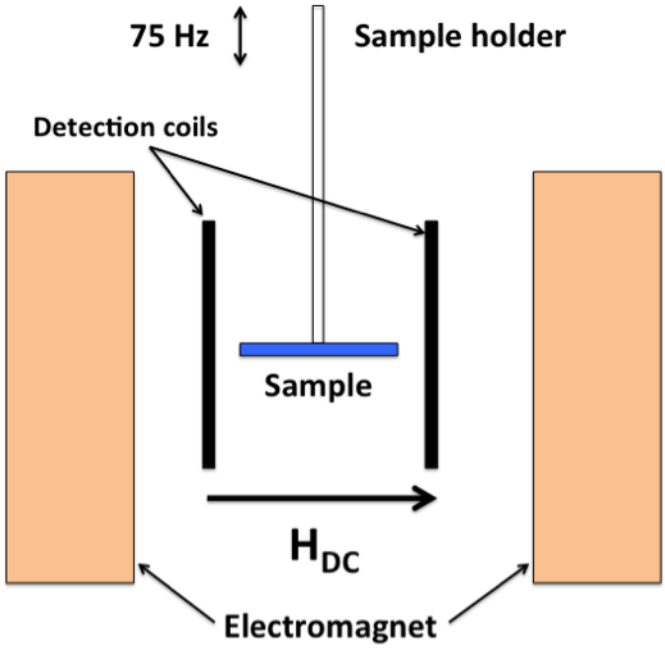

Figure 3.13 Schematic representation of a VSM measurement.

normal (out-of-plane configuration) for $t = 90$ seconds. Finally, we measured the remanent magnetization, $IRM(H, T, t = 90s)$, 90 seconds after we removed the magnetic field, H. We have increased the applied magnetic field by steps of 15.9 kA/m (200 Oe) and repeated this procedure at the same temperature until the IRM signal saturates at a magnetic field H_k, $IRM(H_k, T, t = 90s)$.

We have taken 300 averages for each measurement of the IRM signal, which takes 45 seconds. We then waited another 45 seconds to reach the desired time constant of 90 seconds. We have then increased the magnetic field in steps of 15.9 kA/m (200 Oe) and measured the IRM signal with the same time constants. Figure 3.14 shows the IRM signal (mass magnetization) of GMP-650-45 at 280 K as a function of magnetic field. We see the IRM signal to increase with magnetic field, until it reaches a saturation point.

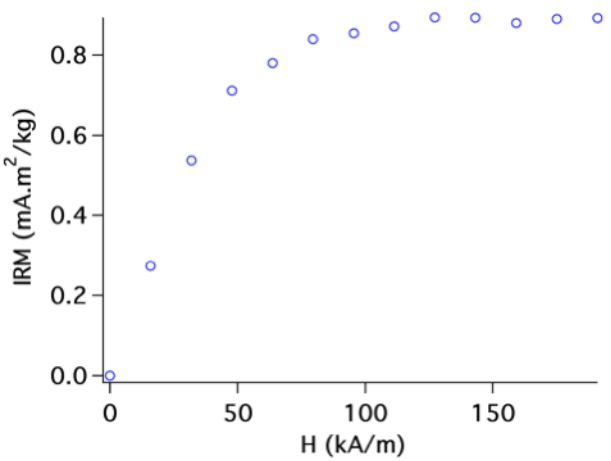

Figure 3.14 The IRM response of GMP-650-45 to the magnetic field (in-plane) applied at $T = 280$ K.

CHAPTER 4

Texture evolution of polycrystalline MnP films grown on GaP (100)

4.1 Introduction

Studying the time evolution of the texture of GaP:MnP epilayers grown at 650 °C by TEM image analysis and XRD pole figures, S. Lambert-Milot *et al.* proposed a qualitative picture to describe the formation of MnP nanoclusters in different families of orientations in GaP:MnP (Lambert-Milot, 2012),(Lambert-Milot *et al.*, 2012). Based on TEM image analysis, they suggested that nucleation and growth of MnP nanoclusters at the beginning of growth affects the growth of GaP that forms at later times around these nanoclusters, such that several GaP facets form during the growth of the epilayer. Presence of such facets consequently affects the orientation of the nanoclusters that form at later growth times, as they provide different GaP surfaces for nucleation of MnP. For example, figure 4.1 presents the cross-sectional TEM micrograph of GMP-650-5, in which we observe nucleation of MnP nanoclusters (shown by white arrows) on GaP (111) facets. MnP nanoclusters with MnP {010} || GaP {111} are an example of an orientation family that is suggested to form on these facets. The proposed growth model is schematically shown in figure 4.2.

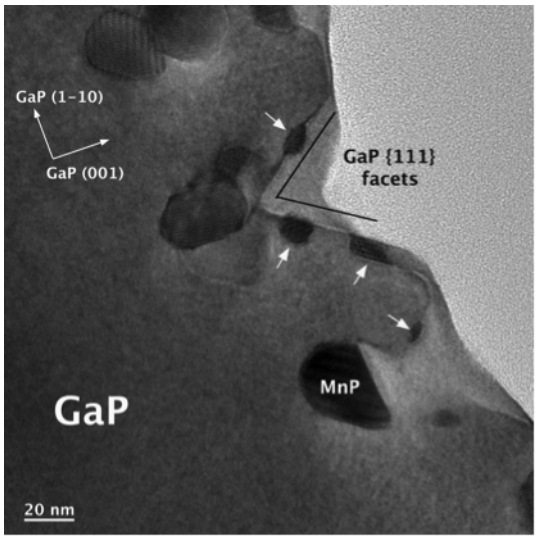

Figure 4.1 a) Cross-sectional TEM micrograph of GMP-650-5, showing the formation of GaP (111) facets. White arrows show the MnP nanoclusters that form on GaP (111) facets.

In order to increase our understanding of the formation of MnP nanoclusters embedded

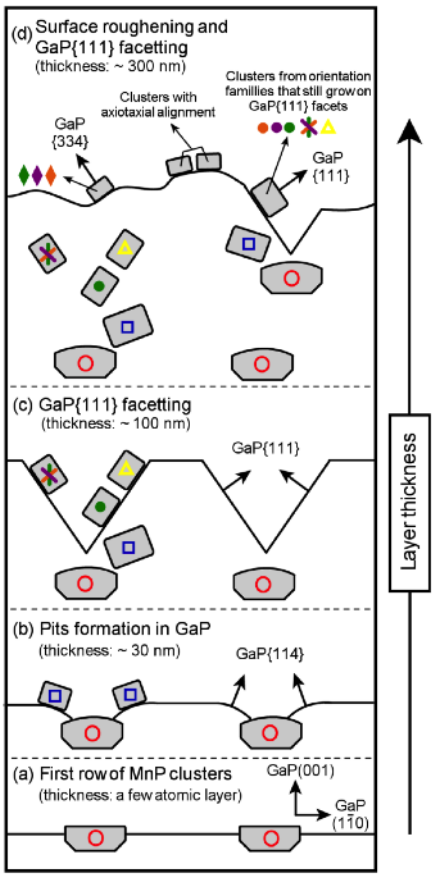

Figure 4.2 Schematic representation of the growth model describing the time evolution of the texture of GaP:MnP epilayers. Symbols with different colors inside the nanoclusters correspond to a specific family of orientation, described in Refs. (Lambert-Milot, 2012),(Lambert-Milot *et al.*, 2012). The image is taken from Ref. (Lambert-Milot, 2012).

in a GaP matrix we selected an apparently less complex system, namely MnP films on GaP, also grown from the vapor phase. Studying the growth time and temperature evolution of the texture of this system enables us to determine the most favorable crystallographic orientations of MnP that form on GaP (100) at different growth temperatures. Comparison of these preferred orientations with those of MnP nanoclusters in GaP:MnP may lead us to understand the role of the GaP matrix on texture selection in GaP:MnP epilayers.

We first study the growth time evolution of the texture of the films grown at 550 °C (MnP-550-1.5, MnP-550-5, MnP-550-15) and 650 °C (MnP-650-5, MnP-650-15, MnP-650-30) by analyzing their SEM and TEM micrographs, ED patterns, and XRD pole figures. The results provide us with information on the formation mechanism of MnP crystals on GaP (100) and their most favorable crystallographic orientations. Then, using the same analysis tools we study the effect of growth temperature on the texture of the films that are grown for

15 minutes in the temperature range $550 - 750\,^{\circ}\mathrm{C}$. We then discuss different aspects of our observations in separate sub-sections in Section 4.4 in more details, propose hypotheses to describe the observed phenomena and provide supplementary results (if necessary) to support our hypotheses. Finally, a semi-quantitative model to describe the formation mechanism and texture selection of MnP films grown on GaP (100) will be presented in Section 4.5.

In Chapter 5, we show that the knowledge of the growth mechanism and texture evolution of MnP films helps us to better understand the formation mechanism and texture evolution of GaP:MnP epilayers. This in turn, exhibits the potential to design different heterostructure, in order to achieve the desired texture.

4.2 Growth time evolution of MnP films grown on GaP (100)

In this section the results of growth time evolution of the texture of MnP films grown at $550\,^{\circ}\mathrm{C}$ and $650\,^{\circ}\mathrm{C}$ will be presented.

4.2.1 MnP films grown at $550\,^{\circ}\mathrm{C}$

Figure 4.3 presents the plan-view SEM micrographs of MnP films grown at $550\,^{\circ}\mathrm{C}$ for 1.5, 5, and 15 minutes. In figure 4.3 (a) we observe the formation of very small (≈ 30 nm) individual crystals on the substrate. The crystals in this sample (MnP-550-1.5) are fairly separated, and as discussed in Chapter 2 (Section 2.2, one can assume that the sample is at the pre-coalescence stage. We observe larger gains in the samples with longer growth times (≈ 60 nm in GMP-550-5 and ≈ 100 nm in GMP-550-15). The coalescence of the crystals occurs in samples with longer growth times (figures 4.3 (b) and 4.3 (c)), in which larger MnP crystals are in contact with each other.

Table 4.1 Average effective diameter and mean effective diameter of MnP crystals grown at $550\,^{\circ}\mathrm{C}$ for different growth times, as well as their standard deviations and aspect ratios.

Sample	**Average effective diameter (nm)**	**Standard deviation (nm)**	**Average aspect ratio**	**lognormal fit Mean effective diameter (nm)**	**lognormal fit Standard deviation (nm)**
MnP-550-1.5	30	4	1.4	30 ± 0.4	0.14
MnP-550-5	58	11	1.7	51 ± 1	0.16
MnP-550-15	95	32	1.7	110	0.32

In table 4.1 we report the "average effective diameter" and "mean effective diameter" of the crystals. The procedure to find the effective diameter is the following : we have found the projected area of 100 crystals (manually) by measuring their widths and lengths using Fiji

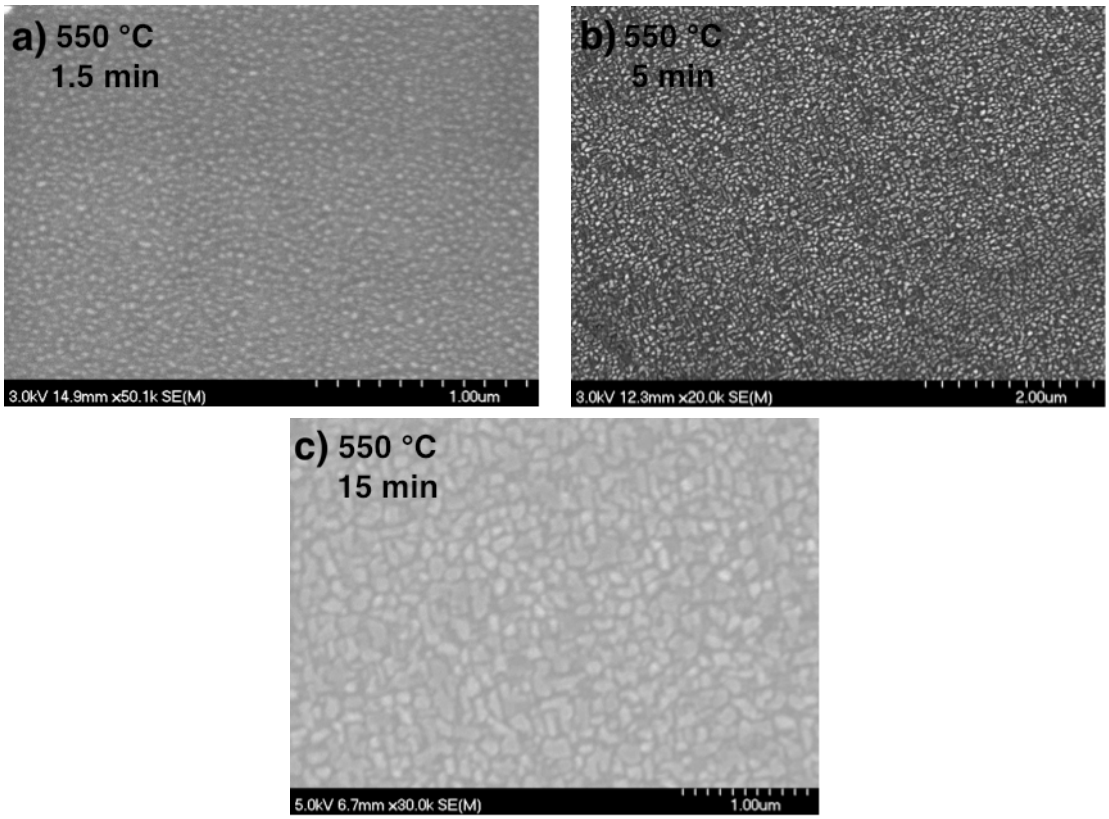

Figure 4.3 Plan view SEM micrographs of a) MnP-550-1.5, b) MnP-550-5, and c) MnP-550-15 showing formation of polycrystalline films. The sample grown for 1.5 min appears to be in the pre-coalescence stage, while the crystals of the samples grown for longer times are in contact with each other and most likely are in the coalescence stage.

software, assuming a rectangular shape. The effective diameter of a crystal is the diameter of a circle that has the same area as the projected area of the (rectangular) crystal. The average effective diameter is the arithmetic mean of the effective diameters of 100 crystals. On the other hand, the mean effective diameter is obtained from the lognormal fit of the effective diameter histogram of the samples. Figure 4.4 shows the size (effective diameter) histogram of these samples and the corresponding lognormal fits, obtained from Igor pro software. The sample grown for the shortest time (MnP-550-1.5) seems to have a unimodal size distribution, which is not the case for the other two, as is evident from the comparison with a lognormal fit. We will further discuss the size distribution of different samples in Section 4.4.

Cross-sectional TEM images of these films, presented in figure 4.5, reveal the endotaxial growth of MnP grains. Endotaxial growth takes place even at an early stage of growth (MnP-550-1.5), as seen in 4.5 (a). We also observe that the endotaxial depths of the grains increases with growth time.

From the cross-sectional TEM images we have extracted the average normal growth rates

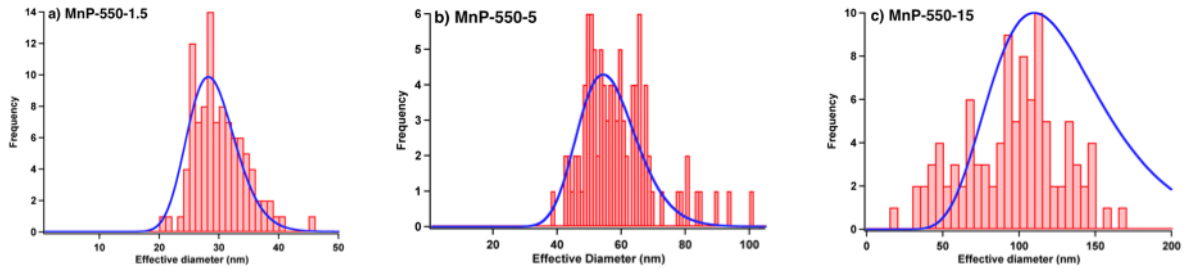

Figure 4.4 Size histogram of a) MnP-550-1.5, b) MnP-550-5, and c) MnP-550-15. The size distribution of MnP-550-1.5 looks unimodal, which is not the case for MnP-550-5 and MnP-550-15, as a comparison with the best lognormal fit (obtained from Igor pro software) indicates.

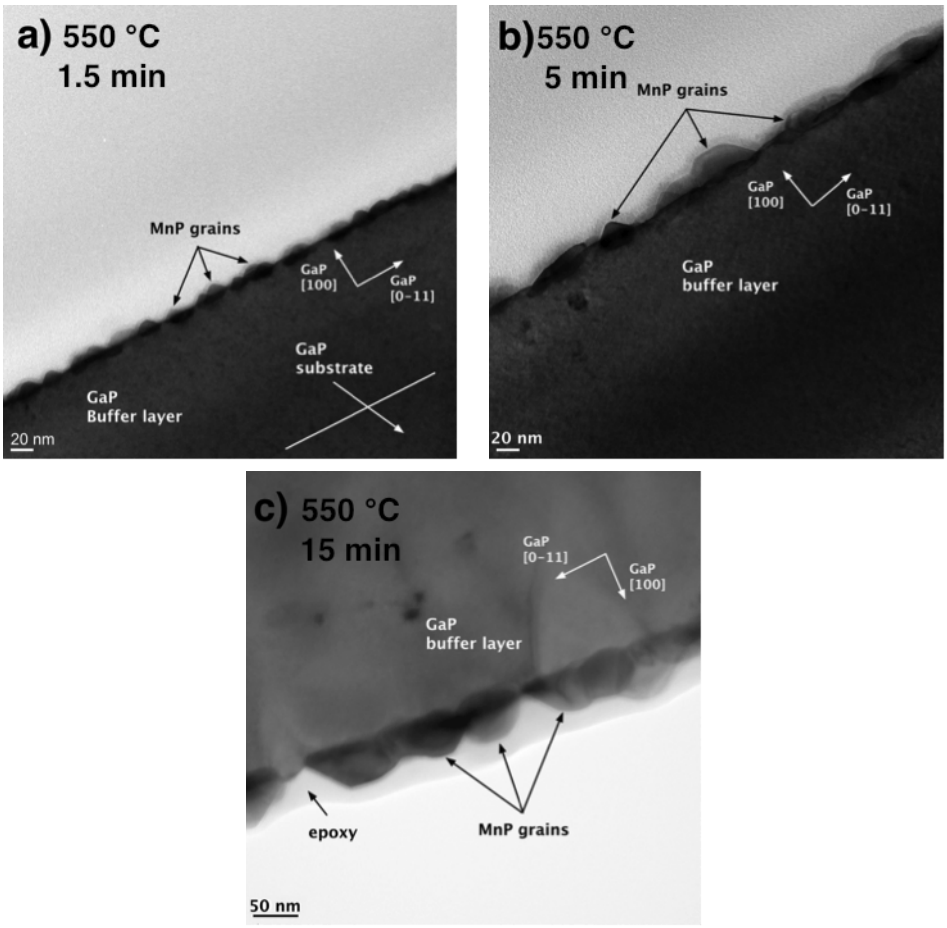

Figure 4.5 Cross-sectional TEM images of a) MnP-550-1.5, b) MnP-550-5, and c) MnP-550-15. The white line in (a) shows the GaP buffer layer/substrate interface. MnP grows endotaxially on GaP, even at an early stage of growth, as shown in (a). We also observe that samples with longer growth times have larger endotaxial depths.

of MnP grains, $R_{\perp}$ (nm/s), by measuring the maximum height of the grains (perpendicular to the GaP surface) that is growing outside GaP (distance above a GaP surface). The average lateral growth rates, $R_{\parallel}$ (nm/s), have been obtained from the average effective diameter of each sample reported in Table 4.1 (column 2). Table 4.2 shows that the average $R_{\parallel}$ is at least twice (at most 5 times) larger than $R_{\perp}$ (will be discussed in Section 4.4).

Table 4.2 Average normal growth rate of the samples grown at 550 °C compared to their lateral growth rates.

Sample	**Average growth height (nm)**	**Standard deviation (nm)**	$R_{\parallel}$ (nm/s)	$R_{\perp}$ (nm/s)	$R_{\parallel}$ / $R_{\perp}$
MnP-550-1.5	8	1.8	0.3	0.09	3.3
MnP-550-5	13	4.0	0.2	0.04	5
MnP-550-15	45	10.8	0.1	0.05	2

Unfortunately, the XRD pole figures of MnP-550-1.5 and MnP-550-5 are not available to statistically analyze their texture. Moreover, obtaining their SAED pattern was impossible due to the very small size of the grains. Hence, to determine the orientation of the crystals we have used the electron diffraction patterns obtained from the Fourier transform of the HR-TEM image of each grain. Figure 4.6 shows an example of the HR-TEM image of an endotaxial grain in MnP-550-1.5 and its corresponding FFT pattern. We have assigned the MnP {121} || GaP (200) alignment to this grain by analyzing its FFT, as shown in 4.6 (b) (the methodology of assigning the alignments is described in Chapter 3, Section 3.2).

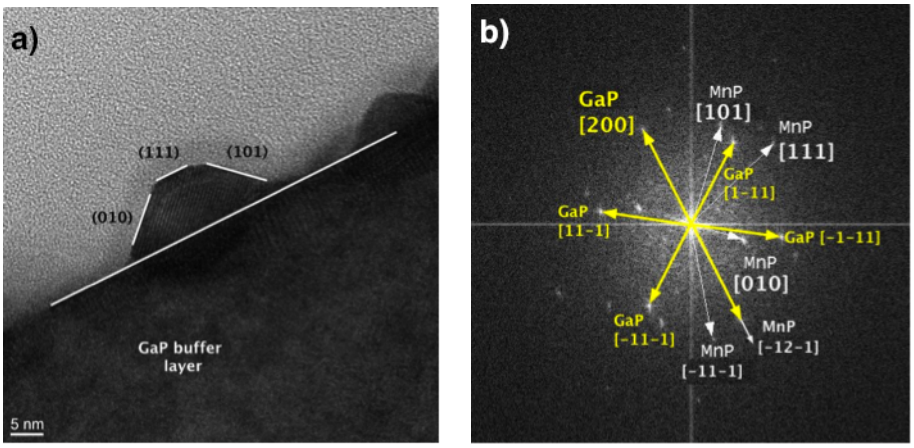

Figure 4.6 a) HR-TEM image of a MnP crystal in MnP-550-1.5 and b) its FFT pattern. Analyzing the FFT pattern (shown in (b)), we assigned the MnP {121} || GaP (200) the alignment to this grains. Moreover, we determined MnP (010), (111), and (101) surface facets, as shown in the HR-TEM image. The long white line shows the surface of the GaP buffer layer ($\approx$ 200 nm thick). We also observe that this crystal partly grew inside the GaP buffer layer.

It should be mentioned that we could not obtain the FFT pattern of some grains that mostly grew inside GaP, since their atomic planes were not clear in the HR-TEM micrograph. Figure 4.7 shows an example of a challenging situation, in which we are not able to determine the crystallographic orientation of a crystal (grains A) from FFT.

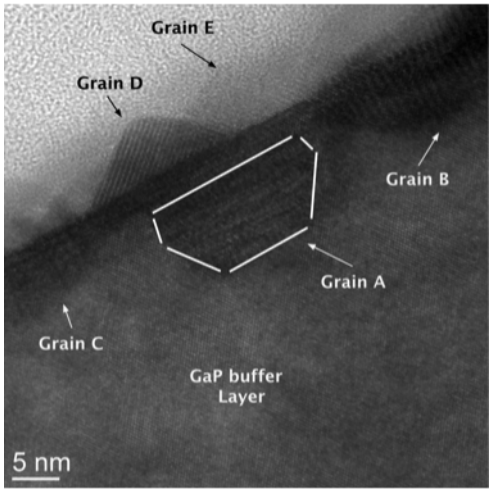

Figure 4.7 HR-TEM image of five MnP grains in MnP-550-1.5. We could not determine the orientation of grain A, since it completely grew inside GaP and we do not clearly observe its planes. Grains D and E have the same alignment, namely MnP {121} || GaP (200).

We also realized, through direct observation, that the shape and orientations of the grains are correlated. For example, trapezoidal shape grains in all the samples have the alignment MnP {121} || GaP (200). Figure 4.8 shows an example of two crystals of MnP-550-5 with MnP {121} || GaP (200) and MnP {110} || GaP (200) that have different shapes and different surface facets.

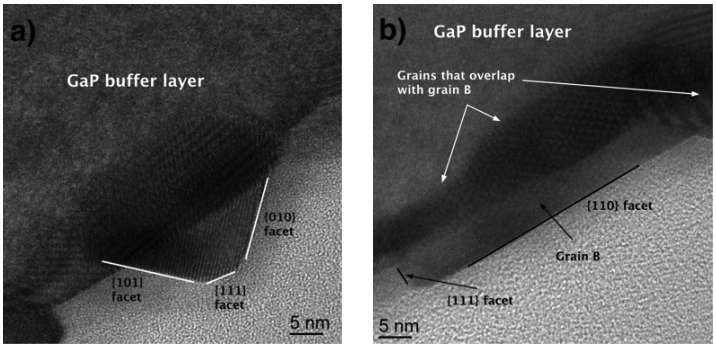

Figure 4.8 a) A trapezoidal crystal in MnP-550-5 with MnP {121} || GaP (200), and b) an elongated crystal in MnP-550-5 with MnP {110} || GaP (200). The two crystals have different surface facets (except for MnP {111} facet).

All of the grains in MnP-550-1.5, to which we were able to assign an alignment using the FFT pattern, have the alignment MnP {121} || GaP (200). However, it is likely that there are other crystals with different orientations. This is inferred from their different shapes, such as grain A in figure 4.7, for which we were not able to determine the alignment. In MnP-550-5, similar to MnP-550-1.5, most of the crystals ($\approx 80\%$) have the alignment MnP {121} || GaP (200). Another orientation that we have observed in this sample is MnP {110} || GaP (200) for elongated grains. Similar to MnP-550-1.5, there were some crystals in MnP-550-5 that were observed with different shapes, for which we could not determine their orientations.

Contrary to MnP-550-1.5 and MnP-550-5, MnP-550-15 has large grains, which made it possible to study its SAED patterns. Similar to MnP-550-1.5 and MnP-550-5, the most observed orientation in this sample determined from SAED patterns analysis is MnP {121} || GaP (200). Moreover, the XRD pole figures of this sample were available, which provides us with systematic information on the crystallographic orientation of all MnP grains (it will be discussed in this section). The above-mentioned orientation had the most intense signal in the pole figures of MnP-550-15. It seems then safe to conclude that this is the most favorable and most stable orientation to form on GaP (100) at this growth temperature. The other orientation that was determined from SAED pattern of this samples is MnP {110} || GaP (200), which has the second most intense signal in the XRD pole figures (Table 4.3).

Figure 4.9 shows MnP (020), (111), and (101) pole figures of MnP-550-15. As described in Chapter 3, a pole figure is an orientation map of a family of planes {hkl} that is obtained from 3D reciprocal space map of the sample. By verifying the angular position (ψ and ϕ) of the bright spots on a {hkl} pole figure, we can determine whether there is an alignment between this family of planes with any GaP planes.

On the pole figures of MnP-550-15 we observe bright spots and partial arcs/lines. The bright spots correspond to epitaxial alignments, while partial arcs/lines correspond to partial axiotaxy or partial fiber texture. Full circles/arcs/lines on a pole figure corresponds to a family of grains that have 1D alignment with the substrate, i.e. {hkl} of the grains || {h′k′l′} of the substrate (fiber/axiotaxy axis). The grains of this family are free to choose any crystallographic orientation, while keeping their 1D alignment (fiber/axiotaxy axis). Hence, we expect to observe full circles, arcs, or lines in the pole figures (e.g. {121} pole figure) of such texture. In MnP-550-15 we only observe a part of a circle, arc, or a line, which means that the grains have a limited degree of freedom for orientation selection, keeping their 1D alignment. This limitation could be due to the strain arising from the lattice mismatch between MnP planes and GaP substrate. The partial axiotaxial texture will be discussed in more details in section 4.4.

Compared to FFT and SAED patterns analysis, XRD pole figure analysis is a much

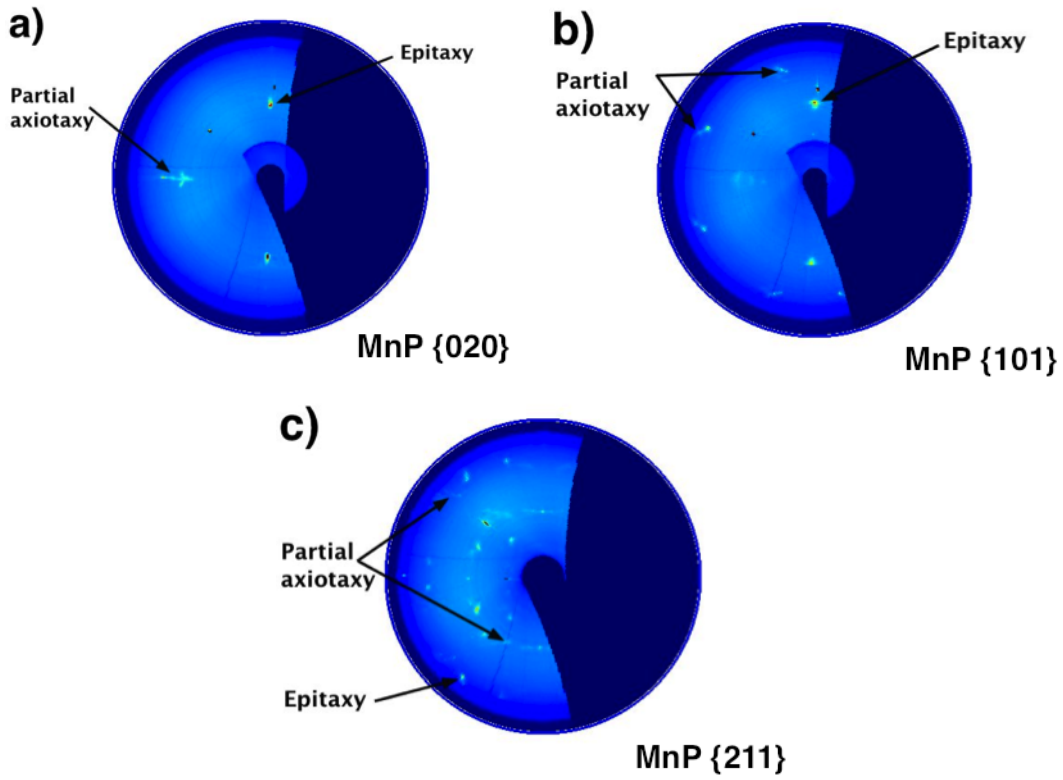

Figure 4.9 Pole figures of MnP-550-15 obtained using a planar detector a) MnP {020}, b) MnP {101}, and c) MnP {211}. The bright spots indicate epitaxial alignments, while partial arcs/lines indicate partial axiotaxy.

more complete technique to *systematically* describe the texture of any given sample. We have identified 10 orientation families (epitaxial alignments) in MnP-550-15 from pole figure analysis, which are listed in table 4.3.

In order to determine these epitaxial alignments, in addition to analyzing the pole figures using the software mentioned in Chapter 3, we have used the information obtained from the SAED pattern of the grains in all MnP films grown on GaP (100) (at different growth temperatures and different growth times). The details of this procedure will be presented in section 4.3. Some orientations are coded following the work of S. Lambert-Milot (Lambert-Milot, 2012) on determining the orientation of MnP nanoclusters in GaP:MnP. This facilitates the comparison of the most favorable orientations in MnP films and nanoclusters, which will be presented in Chapter 5 . The orientation families in table 4.3 are sorted in a decreasing order according to their relative population.

In table 4.3 we also provided the estimated strain in the MnP planes arising from the lattice mismatch between the grain and the substrate at the growth temperature (550 °C). The thermal expansion coefficients of MnP above room temperature are not available in

Table 4.3 Epitaxial alignments of MnP grains in MnP-550-15 obtained from pole figure analysis by decreasing order of population weight. The last columns indicate the least value of strain, respectively calculated for each alignment using equation 4.2, as well as the integers m and n (described in the text).

Code	**Epitaxial alignment**	**Strain** ($e\%$)	(m, n)
Black ellipse	MnP (121) || GaP (100) and MnP (-121) || GaP (31-1)	-5 and 0.008	$(1, 3)$ and $(7, 6)$
Yellow circle	MnP (110) || GaP (100) and MnP {001} || GaP (011)	-2 and 0.1	$(5, 7)$ and $(4, 5)$
Blue square	MnP {110} || GaP (411) and MnP (210) || GaP (100)	-3 and 5	$(3, 1)$ and $(1, 2)$
Red circle	MnP {010} || GaP (100) and MnP {001} || GaP (011)	2 and 0.1	$(1, 1)$ and $(4, 5)$
Lines	MnP {010} || GaP (111) and MnP {001} || GaP (011)	-1 and 0.1	$(5, 3)$ and $(4, 5)$
White square	MnP {111} || GaP (100) and MnP {111} || GaP (111)	-1 and 0.1	$(4, 9)$ and $(7, 9)$
Diamonds	MnP {010} || GaP (433) and MnP {001} || GaP (011)	5 and 0.1	$(6, 1)$ and $(4, 5)$
Not coded	MnP (101) || GaP (100) and MnP (10-1) || GaP (011)	-1 and -0.3	$(1, 2)$ and $(5, 7)$
Not coded	MnP {131} || GaP (0-11) and MnP (10-1) || GaP (011)	3 and -0.3	$(2, 5)$ and $(5, 7)$
Not coded	MnP {121} || GaP (111) and MnP (10-1) || GaP (011)	-1 and 0.1	$(3, 5)$ and $(4, 5)$

the literature. However, following (Lambert-Milot, 2012) we have calculated the lattice parameters of MnP and GaP at the growth temperature using their linear thermal expansion coefficients at room temperature : MnP : $\alpha_a = 2.4 \times 10^{-5}\ K^{-1}$,$\alpha_b = 2.9 \times 10^{-5}\ K^{-1}$ and $\alpha_c = -2.9 \times 10^{-5}\ K^{-1}$ at 300 K (Iwata, 1969) and GaP : $\alpha_{GaP} = 5.9 \times 10^{-6}\ K^{-1}$ at 300 K (Deus *et al.*, 1983). As an example, we show how we calculated a_{MnP} (a-axis of orthorhombic MnP) at the growth temperature :

$$a_{MnP}(T) = a_{MnP}(300K)(1 + \alpha_{MnP}\Delta T) \tag{4.1}$$

where $\Delta T = 823 - 300 = 523$ K. The strain, $e(\%)$, is calculated from :

$$e(\%) = \frac{nd_{MnP} - md_{GaP}}{nd_{MnP}} \times 100 \tag{4.2}$$

where d_{MnP} and d_{GaP} are the d-spacing of the MnP and GaP planes (at the growth temperature) that are aligned, and m and n are positive integers. In Table 4.3, we reported the values of m and n that result in the smallest strain values in each orientation family. The values of strain ($e\%$) are reasonable for epitaxial alignments, yet they do not explain the relative weight in population.

4.2.2 MnP films grown at 650 °C

Plan-view SEM micrographs of the MnP films grown at 650 °C are presented in figure 4.10. These micrographs also show the formation of polycrystalline films, as those grown at 550 °C. The SEM image of MnP-650-5 shows the formation of larger (> 100 nm) and more elongated

grains comparing to the sample grown at 550 °C (MnP-550-5). The MnP grains grow larger in time, and we also see the formation of long rods on top of the primary grains, presented in figure 4.10 (c) for 30 min growth. Table 4.4 summarizes the lateral size of the grains in these samples. The lateral size histogram of the grains, presented in figure 4.11 look multimodal, hence we only report the average effective diameter of the grains. The multimodal lateral size distribution of the grains could attribute to different growth rates of different orientation families. This will be further discussed in Section 4.4.

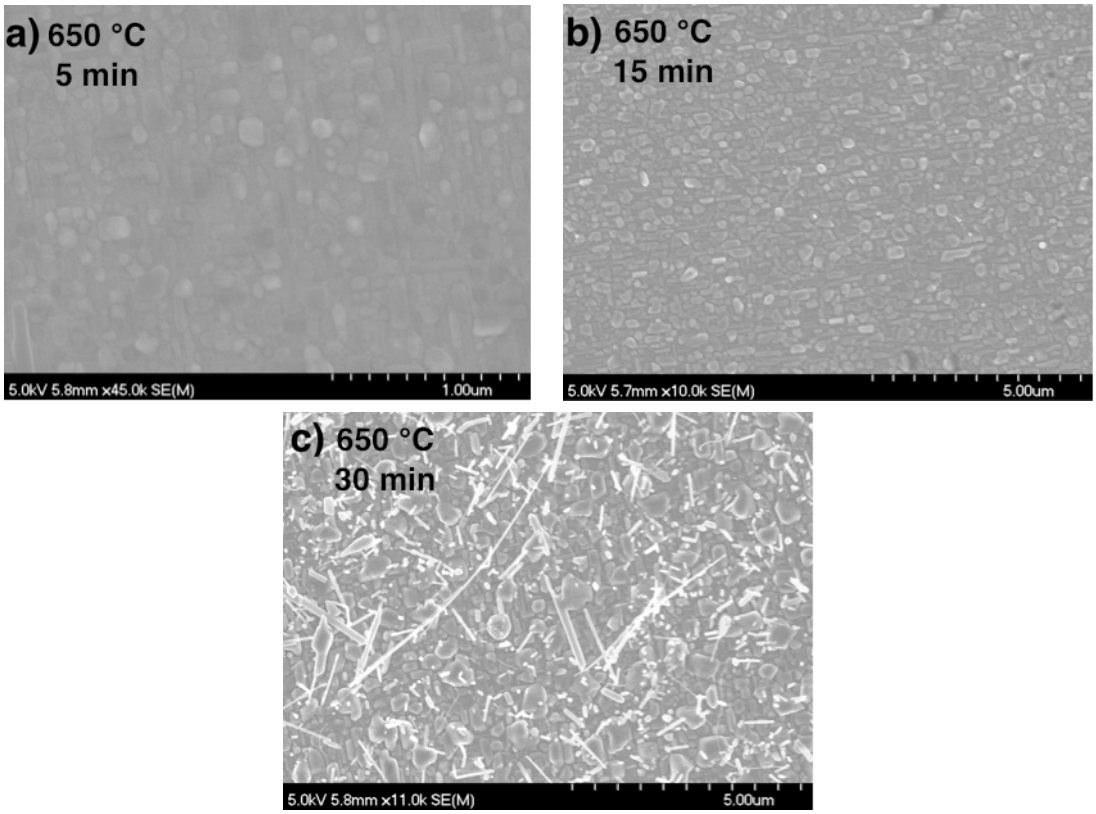

Figure 4.10 Plan view SEM micrographs of a) MnP-650-5, b) MnP-650-15, c) MnP-650-30 show the formation of polycrystalline films, the grains of which grow larger in time. In (c) we observe the formation of long rods (≈ 2 μm) on top of primary grains.

Table 4.4 Average effective diameter of primary MnP grains grown at 650 °C for different growth times, as well as their standard deviations and aspect ratios.

Sample	**Average effective diameter (nm)**	**Standard deviation (nm)**	**Average aspect ratio**
MnP-650-5	121	35	2
MnP-650-15	206	75	2
MnP-650-30	222	111	1

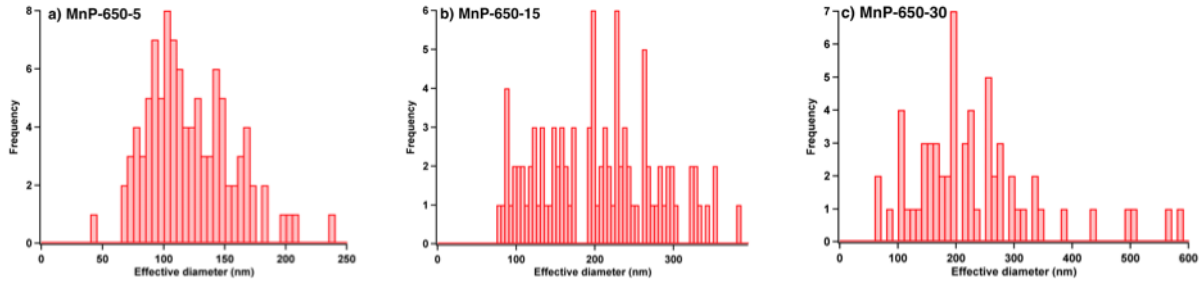

Figure 4.11 Lateral size histograms of primary MnP grains of a) MnP-650-5, b) MnP-650-15, and c) MnP-650-30 show a multimodal distribution.

The cross-sectional TEM images, presented in figure 4.12 reveal the endotaxial growth of MnP grains with different shapes. They also confirm the nucleation and growth of secondary grains on top of the primary ones in the samples that have longer growth times (MnP-650-15 and MnP-650-30) in figures 4.12 (b) and (c), respectively. Figure 4.12 (c) shows that the secondary grains have a tendency to grow as long rods in MnP-650-30.

Nucleation of secondary grains could occur through segregation of impurities on the primary grains, as described by the model presented by Barna and Adamik (Barna et Adamik, 1995) (Chapter 2, Section 2.2). A potential impurity that could segregate on MnP grains is CO, which could be provided by the organometallic precursor of Mn, MCTMn ($(CH_3C_5H_4)Mn(CO)_3$).

From the TEM micrographs, we have determined the average normal growth rate of primary MnP grains. Similar to the samples grown at 550 °C, table 4.5 indicates the at least 2.5 (at most 5.7) times larger lateral growth rate than the normal growth rate.

Table 4.5 Average normal growth rate of the primary grains grown at 650 °C compared to their lateral growth rates.

Sample	**Average growth height (nm)**	**Standard deviation (nm)**	$R_{\parallel}$ (nm/s)	$R_{\perp}$ (nm/s)	$R_{\parallel}$ / $R_{\perp}$
MnP-650-5	20	12.3	0.4	0.07	5.7
MnP-650-15	62	42.2	0.2	0.07	2.9
MnP-650-30	79	59.1	0.1	0.04	2.5

We have determined the crystallographic directions of the long axes of some of the rods that grow on top of the primary grains in MnP-650-30, from their SAED patterns. Figure 4.13 shows three rods and their corresponding SAED patterns. Two of the rods are elongated along MnP [002] direction, while the other one is along MnP [101]. Hence, either MnP has a larger growth rate along these directions or the corresponding planes have the lowest surface energies. We observed the formation of long MnP rods in MnP films grown on glass (presented in Appendix B), as well. Similar to two of the rods in MnP-650-30, the rods obtained from

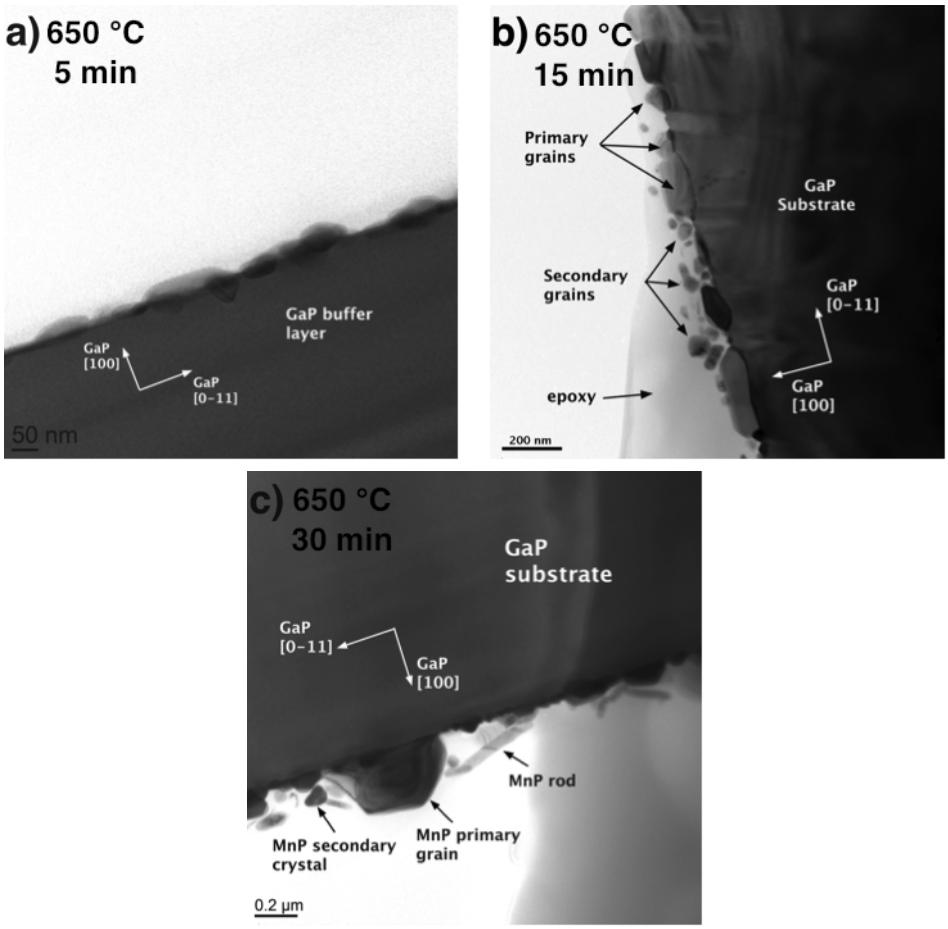

Figure 4.12 Cross-sectional TEM images of a) MnP-650-5, b) MnP-650-15, and c) MnP-650-30, showing the endotaxial growth of the grains. Grains with longer growth times have a larger endotaxial depths. Nucleation and growth of secondary grains is observed in (b) and (c). We infer that secondary grains have a tendency to grow as long rods, as observed in MnP-650-30.

the sample grown on glass have been determined to grow faster along MnP [002] direction.

To determine the orientation of the grains in MnP-650-5 we have used the FFT pattern due to small size of its grains, for MnP-650-30 the SAED pattern, and for MnP-650-15 the SAED pattern combined with the pole figure data. The orientations of the grains at this growth temperature obtained from the FFT and SAED patterns are listed in Table 4.6.

According to FFT and SAED patterns, in these samples we observe 5 more orientation families in addition to the two we observed for MnP grains grown at 550 °C. This implies that either the higher growth temperature (650 °C) favors the formation of these 5 new orientation families, or they already existed in the samples grown at 550 °C but with a relatively low population, such that we missed them in our TEM image and ED pattern analysis.

Pole figure analysis of MnP-550-15 and MnP-650-15 (which will be presented in Sec-

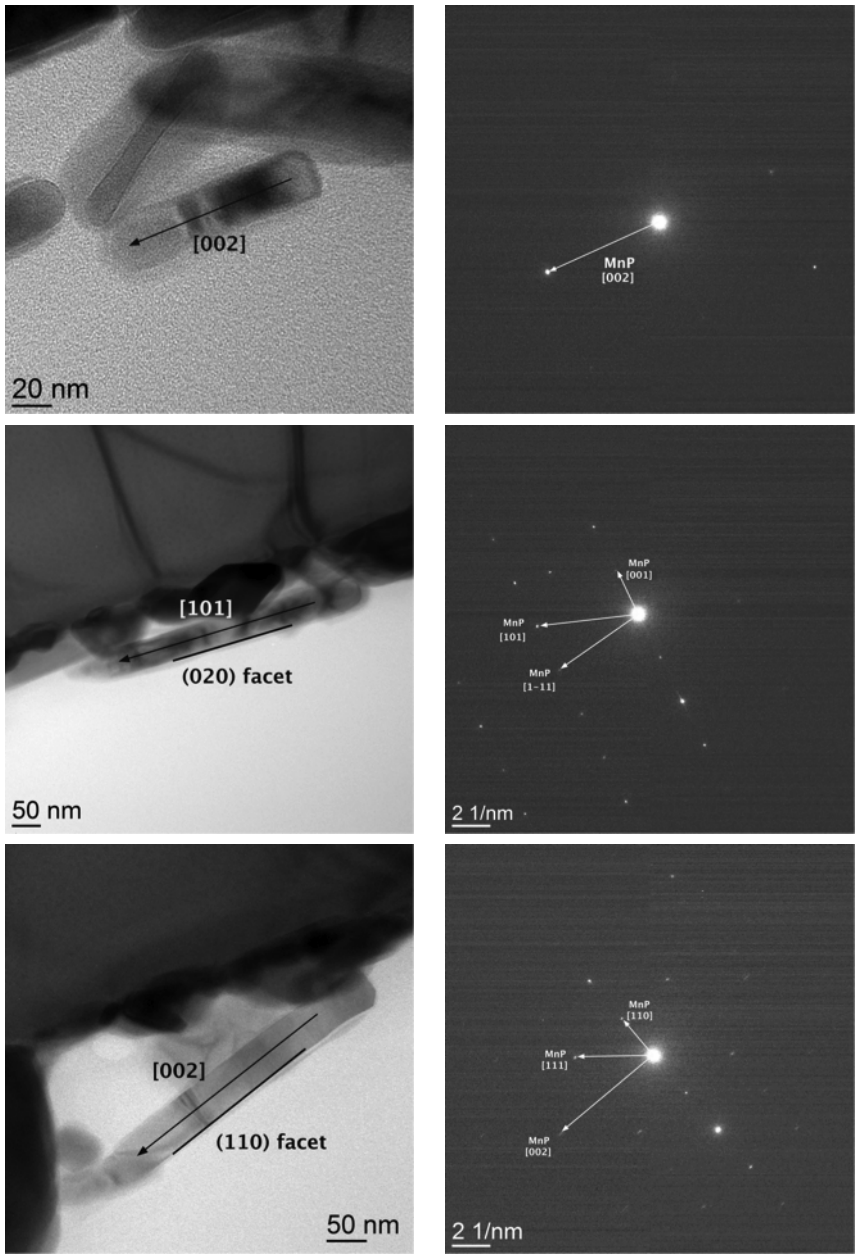

Figure 4.13 TEM micrograph of three nanorods in MnP-650-30 and their corresponding SAED patterns. Two of the nanorods are growing faster in [002] direction, while the other one is elongated along [101].

tion 4.3) clarifies that of the orientation families listed in Table 4.6, MnP {021} || GaP (100) is the only new orientation family (aligned with low-index GaP planes) and the rest already exist in MnP-550-15, but were missed in our ED pattern analysis (due to limited number of grains studied). This emphasizes the importance of studying a statistically large number of grains in order to arrive at a firm conclusion.

Table 4.6 Observed epitaxial alignments of the MnP grains for the three samples grown at 650 °C for the growth times indicated in the table. These orientations are obtained from FFT (MnP-650-5) and SAED patterns (MnP-650-15 and MnP-650-30).

Sample/Orientation	**MnP-650-5**	**MnP-650-15**	**MnP-650-30**	**Strain** (**e**%)	(m, n)
MnP (121) || GaP (100) MnP (-121) || GaP (31-1)	Yes	Yes	Not observed	-1 and 0.07	$(4, 9)$ $(3, 2)$
MnP {111} || GaP (100) MnP {111} || GaP (111)	Not observed	Yes	Yes	-1 and 0.008	$(1, 3)$ $(7, 6)$
MnP {110} || GaP (100)	Not observed	Yes	Yes	-2	$(5, 7)$
MnP {010} || GaP (100)	Yes	Yes	Not observed	1	$(1, 1)$
MnP {121} || GaP (111)	Not observed	Yes	Yes	-1	$(3, 5)$
MnP {010} || GaP (111)	Yes	Yes	Not observed	-2	$(5, 3)$
MnP {021} || GaP (100)	Not observed	Yes	Yes	1	$(3, 8)$

Moreover, the pole figure analysis of MnP-650-15 revealed that we observe more orientation families (bright spots on the pole figure) compared to MnP-550-15. However, we could not determine some of them, as they appear to have alignments with high-index GaP planes. In section 4.3 we will study the pole figures of samples grown at different temperatures in more details.

The values of strain (e%) that we have calculated at this growth temperature are almost the same as the ones reported in table 4.3 for samples grown at 550 °C. This means that either strain does not play a significant role in orientations selection, or the approximated values of the thermal expansion coefficients that we have used to calculate the strain are not reliable.

TEM images of the samples grown at 650 °C, along with their FFT and SAED patterns revealed a larger variety of crystallographic orientations compared to the samples grown at 550 °C. This enabled us to study the endotaxial depths and surface facets of grains with different crystallographic orientation. The results revealed that the endotaxial depths and surface facets varies from one crystallographic orientation family to another. In other words, grains with different crystallographic orientations have different endotaxial depths and different surface facets. Similar to the grains grown at 550 °C we have determined the surface facets of these grains from the ED patterns. In Appendix A , we describe how we measure the endotaxial depth of different grains.

Studying the growth time evolution of the endotaxial depth of grains with different orientations, we observed a direct proportionality between the endotaxial depth and the square root of growth time, which is a strong indication that the mechanism of endotaxial growth is related to a diffusion process. We extracted the diffusion coefficient of Mn in GaP for different

orientation families, as well. The results are presented in Appendix A and will be discussed in Section 4.4.

4.3 Growth temperature evolution of MnP films grown on GaP (100)

Figures 4.14 shows the plan-view SEM micrographs of MnP films grown for 15 minutes in the temperature range $550 - 750\,^{\circ}\mathrm{C}$. The SEM images show that : (1) MnP grows on GaP (100) substrates as polycrystalline films, (2) more elongated grains are observed at higher growth temperatures, and (3) long rods are formed on top of the primary MnP grains at $700\,^{\circ}\mathrm{C}$. We noticed these rods already in growth temperature of $650\,^{\circ}\mathrm{C}$ for a longer growth time (see figure 4.10 (c)).

Tables 4.7 and 4.8 summarize the average size and average growth rates of these samples, indicating at least 2.5 (at most 5.7) times larger average lateral growth rate than average normal growth rate. Similar to the MnP films studied in section 4.2.2, the size histogram of these samples (not shown here) seemed to be multimodal.

The cross-sectional TEM micrographs, presented in figure 4.15, show the endotaxial growth of MnP grains. Secondary grains nucleated on top of the primary ones are observed in MnP-650-15, MnP-700-15, and MnP-750-15. As mentioned before, nucleation of secondary grains is attributed to be due to segregation of impurities (such as CO) on top of primary grains that act as new nucleation sites.

Table 4.7 Average effective diameters of the grains in MnP films grown for 15 minutes at different temperatures.

Sample	**Average effective diameter (nm)**	**Standard deviation (nm)**	**Average aspect ratio**
MnP-550-15	95	32	1.70
MnP-600-15	156	79	1.50
MnP-650-15	206	75	2.1
MnP-700-15	256	87	2.0

Table 4.8 Average normal growth rate of the primary grains grown at different temperatures compared to their lateral growth rates. The sample MnP-750-15 was not available to determine its effective diameter and lateral growth rate from SEM micrographs.

Sample	**Average growth height (nm)**	**Standard deviation (nm)**	$R_{\parallel}$ (nm/s)	$R_{\perp}$ (nm/s)	$R_{\parallel}$ / $R_{\perp}$
MnP-550-15	45	10.8	0.1	0.05	2
MnP-600-15	27	8.9	0.17	0.03	5.7
MnP-650-15	62	42.2	0.2	0.07	2.9
MnP-700-15	55	24.3	0.3	0.06	2.9
MnP-750-15	110	33.3	Not determined	0.12	-

Similar to the samples studied in the previous section, from the TEM images and SAED

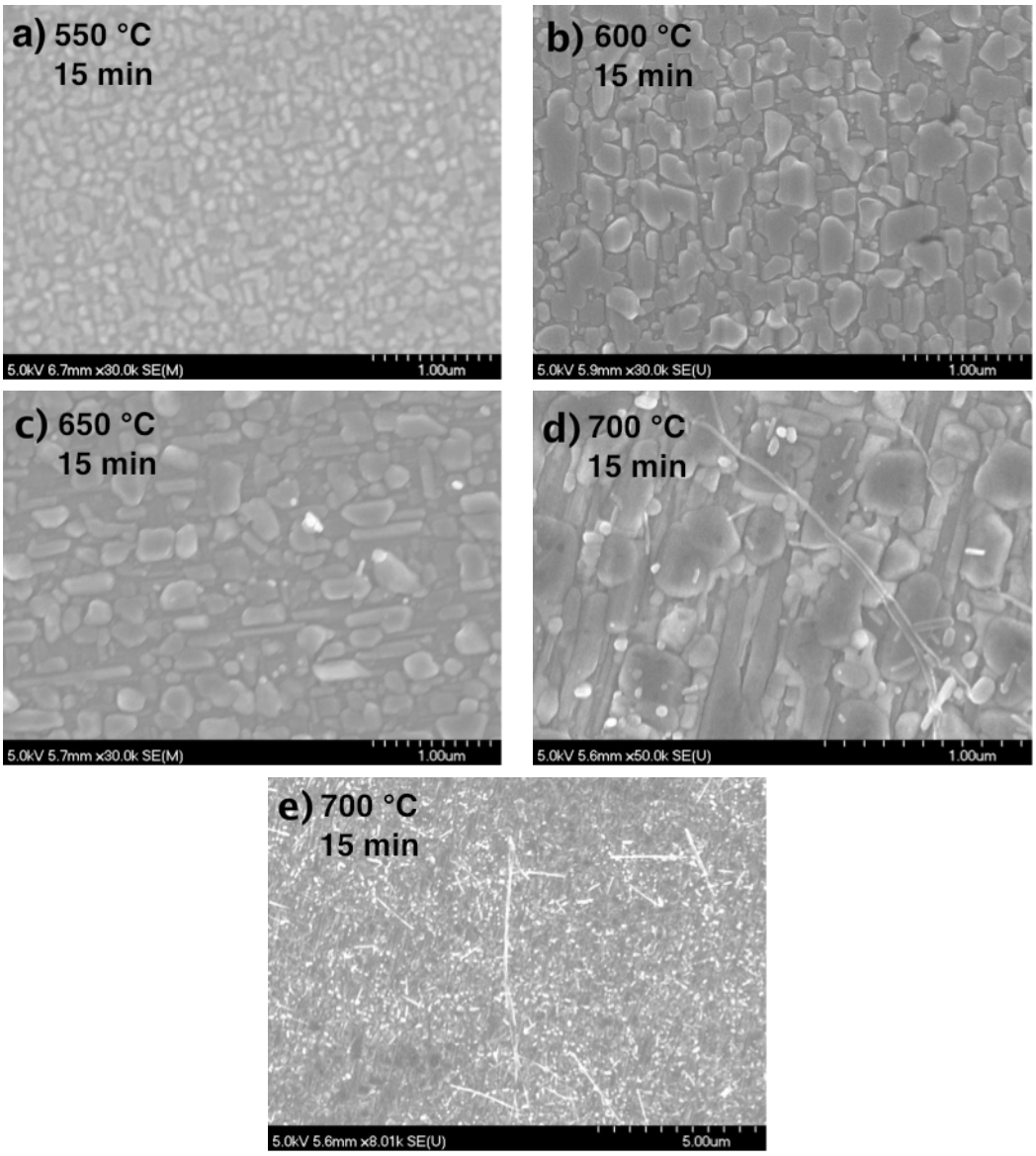

Figure 4.14 Plan view SEM images of MnP films grown at a) 550 °C, b) 600 °C, c) 650 °C, and d) 700 °C. e) Larger area of MnP-700-15, showing formation of very long nanorods.

pattern analysis of each of the samples we realized that the grains with different orientations have different endotaxial depths and different surface facets. By studying the endotaxial depths of the grains grown at different temperatures we provide an estimate of the pre-exponential factor of Mn diffusion in GaP, as well as the activation energy for diffusion. The results are presented in Appendix A and disscussed in Section 4.4.

To study the texture evolution of the films grown at different temperatures we combined the results of the SAED patterns and the XRD pole figures of the samples. Analyzing the SAED patterns of the MnP grains and GaP matrix we have determined the relative orien-

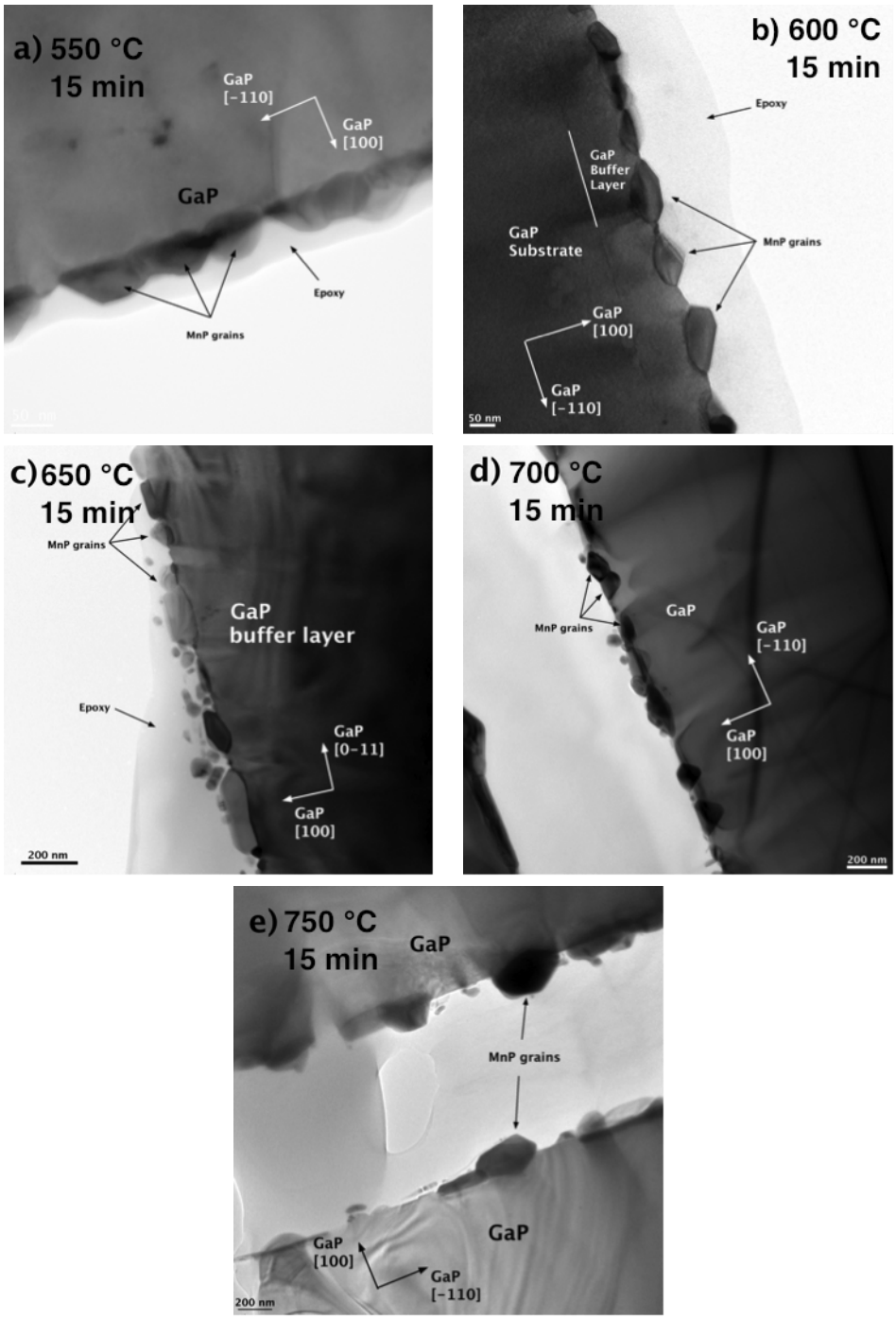

Figure 4.15 Bright field cross-sectional TEM images of MnP films grown for 15 min at a) 550 °C, b) 600 °C, c) 650 °C, and d) 700 °C, and e) 700 °C. The white line in b) shows the GaP substrate/buffer layer interface. Formation of new grains on top of endotaxial primary grains is observed in (c), (d), and (e).

tation of those grains that we observed in the cross-sectional TEM image. The disadvantage of using this methodology is that there is a chance that we miss some families of MnP grain

orientations. To have statistical information regarding the orientation of a much larger number of grains we have studied the XRD pole figures of our samples, which were available to us.

Combining the results of SAED patterns with XRD pole figures provides us with a better understanding and a wider perspective to analyse the texture (crystallographic alignments) of MnP grains with low-index GaP planes. In order to further clarify this, we bring an example.

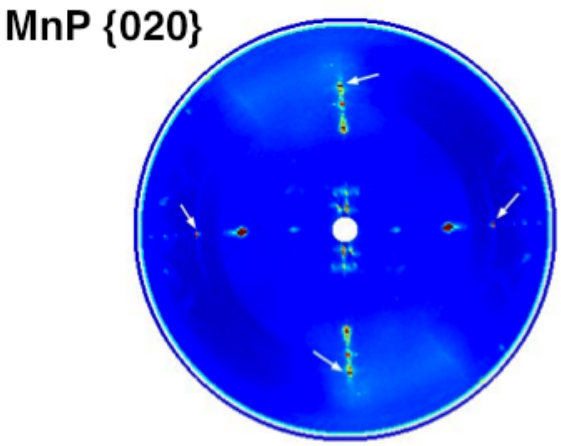

Figure 4.16 MnP 020 pole figure of MnP-650-15. The white arrows show the bright spots located at $\psi = 64$ and $\phi = 0\,^{\circ}$, $90\,^{\circ}$, $180\,^{\circ}$, and $270\,^{\circ}$. These are the angular positions where we expect GaP {233} planes. This pole figure has been obtained using a linear detector.

Figure 4.16 shows the MnP {020} pole figure of MnP-650-15, in which we observe bright spots corresponding to many epitaxial relationships. (We have determined 12 crystallographic orientation families that have alignments with low-index GaP planes for this sample. There are few orientation families that are not determined, since most likely they have alignments with high-index GaP planes). Four of these bright spots, shown by white arrows in figure 4.16 are located at the exact angular positions of GaP {233}. It should be mentioned that we observe bright spots corresponding to this alignment (MnP {020} || GaP {233}) on other pole figures, as well. Using only XRD pole figure analysis to interpret these bright spots, one obtains the alignment MnP {020} || GaP {233} for that family of grains. However, observing few grains in TEM images and finding their orientations using SAED pattern analysis, we realized that the orientation family MnP {111} || GaP {100} also results in a bright spot to appear at the exact same positions on the MnP {020} pole figure. This does not mean that MnP {020} is not in the direction of GaP {233}. It means these grains have the alignment MnP {111} || GaP {100}, for which MnP {020} lies parallel to GaP {233}. The alignment

of MnP grains with the GaP substrate becomes important when one studies the strain and interfacial energies when the grain is forming with that specific alignment.

Figure 4.17 shows MnP {101} and MnP {211} XRD pole figures of the sample MnP-650-15, in which we observe bright spots, as well as bright arcs/line segments. These features indicate that MnP grains have epitaxial alignments, as well as partial axiotaxial alignments. Similar features have been observed in MnP-550-15 and MnP-600-15.

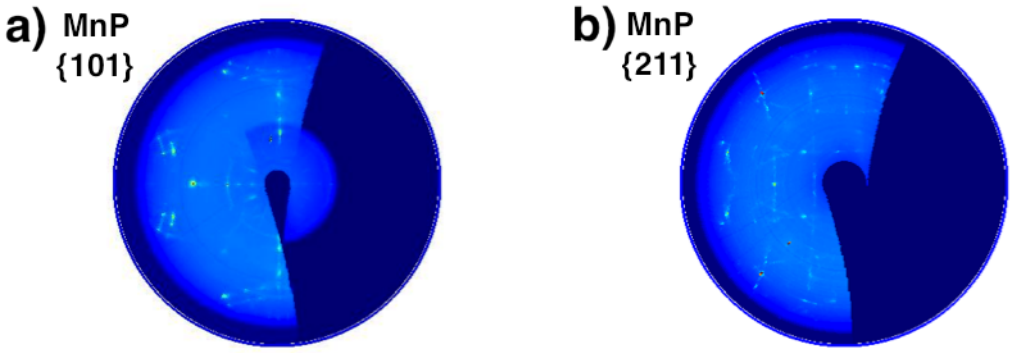

Figure 4.17 MnP {101} and b) MnP {211} pole figures of MnP-650-15. In these pole figures we observe bright spots and bright arcs/line segments that indicate epitaxial and partial axiotaxial alignments. These pole figures have been obtained using a planar detector.

Figure 4.18 shows the MnP {211} pole figures of all the samples grown during 15 minutes and presented in Table 4.8 . The bright spots in MnP {211} pole figures that are shown by white arrows are observed at the exact same angular position with the same intensity in all pole figures of that sample. This means that even on the pole figures that corresponds to none of the GaP or MnP planes (for example d-spacing of 3.20 Å), we also observe these bright spots. Hence they do not correspond to diffraction of any GaP or MnP planes and are assigned to be measurement artifacts.

In all of the pole figures of MnP-700-15 and MnP-750-15 we observe only bright arcs and lines and no bright spots. This indicates that these two samples have only axiotaxial texture.

Our methodology to determine the orientation of a family of grains is the following : For each sample, we have determined the epitaxial alignment of all individual grains that we observed in the TEM images of all of our samples by analyzing their SAED pattern. Then we have verified if each orientation family have a relatively large population to be present on the pole figures of our samples. For a certain orientation that has been observed in SAED pattern, our software enabled us (as described in Chapter 3, Section 3.4) to determine the angular position of all MnP planes and their relative intensities on the pole figures. Hence by studying

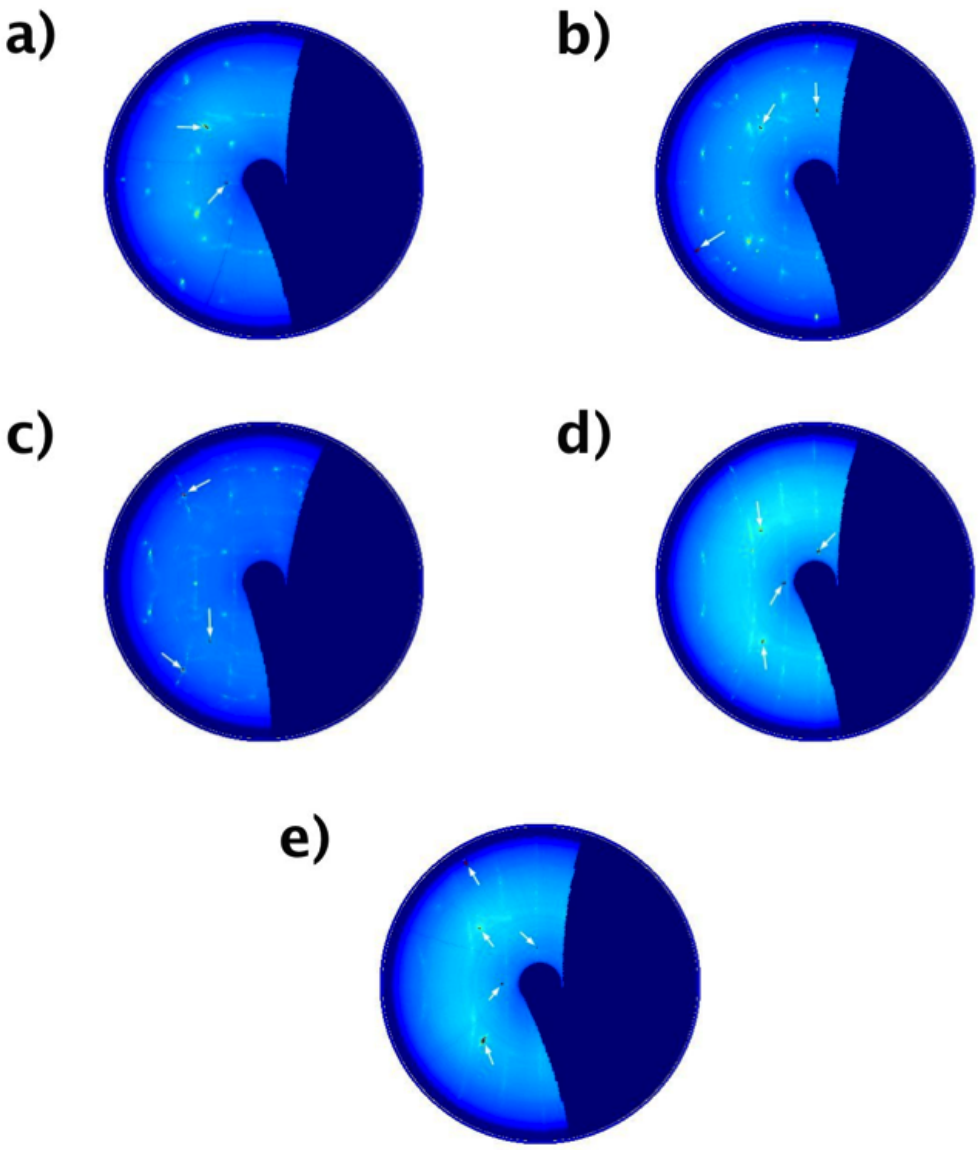

Figure 4.18 MnP {211} pole figures of a) MnP-550-15, b) MnP-600-15, c) MnP-650-15, d) MnP-700-15, e) MnP-750-15. The white arrows show the bright spots due to the artifacts of the experiment. For MnP-700-15 and MnP-750-15 we only see bright arcs and lines that indicate axiotaxial texture, while the other samples have epitaxial and partial axiotaxial textures. The pole figures have been obtained using a planar detector.

at least two different pole figures we can verify if a large enough number of grains have the assigned orientation. Since we observe a limited number of grains in the TEM images, we were not able to determine the orientation of all the bright spots that we observed in the pole figures by this method.

To overcome this problem we have made an assumption. Suppose that we observe the

alignment MnP {111} || GaP (100) in the SAED pattern of a MnP grain in MnP-600-15, for which we also observe bright spots on the pole figures of this sample. Now suppose that we observe some bright spots in at least three pole figures of MnP-550-15 at the exact same angular positions as the bright spots in pole figures of MnP-600-15 corresponding to MnP {111} || GaP (100) alignment, but we do not observe any MnP grains in the TEM images of MnP-550-15 with this alignment. Then we assume that those bright spots in MnP-550-15 correspond to MnP {111} || GaP (100) alignment. Using this assumption, we listed all the observed alignments in SAED patterns of all the samples (grown at the temperature range $(550 - 750\,^{\circ}\mathrm{C})$) and then verified if such alignment exists in each sample for a large number of grains using pole figure analysis.

We have used a notation to distinguish between direct observation of an alignment from SAED pattern of the grains in a sample and borrowing the alignment from another sample. In table 4.9, we marked the former by "↑↑" and the latter by "↑↓". If we directly observe an alignment in the SAED pattern of a grain and we do not observe any bright spots corresponding to this alignment, we realize that this orientation have a small population and mark it as "Not confirmed by pole figures". We were still missing a major epitaxial orientation family (bright spots), according to the pole figures of our samples. We assigned a hypothetical alignment with high-index GaP planes following (Lambert-Milot, 2012), which we found only from the pole figures to this family of grains. This epitaxial orientation, MnP (010) || GaP {433} (in Table 4.9), is marked by "↓↓".

From figure 4.18 and other pole figures not shown here, we realized that as we increase the growth temperature more features (bright spots and bright arcs/lines) appear on the MnP pole figures. The new features (in the pole figures of the sample grown at higher temperature) are observed to be added to the old ones (in the pole figures of the sample grown at lower temperature) along certain paths in the pole figures : specific lines on some pole figures and specific arcs and circles on some others. For example, in figure 4.19 we show MnP {020} and MnP {111} pole figures of MnP-600-15 and MnP-650-15. We see more bright spots and partial arcs on the pole figure of MnP-650-15 than MnP-600-15. We can see that the extra bright spots that we observe on the pole figures of MnP-650-15 are added along certain paths (arcs, lines, circles) in reciprocal space to the pole figure of MnP-600-15. These specific paths, shown in figure 4.20, correspond to axiotaxial/fiber paths, which are identified (using the pole figure analysis software) to have the axiotaxy/fiber axes :

1. **Black/white arcs/lines** : MnP (001) || GaP (011), (01-1)
2. **Pink circle** : MnP (111) || GaP (100) (Fiber axis)
3. **Green/purple lines/arcs** : MnP (10-1) || GaP (011), (01-1)
4. **Yellow circle** : MnP (010) || GaP (100), (-100) (Fiber axis)

Table 4.9 Epitaxial alignments of MnP grains in MnP-550, MnP-600, and MnP-650.

Code	Orientation	MnP-550-15	MnP-600-15	MnP-650-15
White square	MnP {111} || GaP (100) MnP {111} || GaP (111)	↑↓	↑↑	↑↑
Yellow circle	MnP (110) || GaP (100) MnP {001} || GaP (011)	↑↑	↑↓	↑↑
Black ellipse	MnP (121) || GaP (100) MnP (-121) || GaP (31-1)	↑↑	↑↓	↑↓
Red circle	MnP {010} || GaP (100) MnP {001} || GaP (011)	↑↓	↑↓	↑↓
Lines	MnP {010} || GaP (111) MnP {001} || GaP (011)	↑↓	↑↓	↑↑
Blue square	MnP {110} || GaP (411) MnP (210) || GaP (100)	↑↓	↑↓	↑↓
Diamonds	MnP {010} || GaP (433) MnP {001} || GaP (011)	↓↓	↓↓	↓↓
Not coded	MnP (101) || GaP (100) MnP (10-1) || GaP (011)	↑↓	↑↓	↑↓
Not coded (Not confirmed by pole figures)	MnP {131} || GaP (0-11) MnP (10-1) || GaP (011)	↑↑	↑↑	↑↓
Not coded	MnP {121} || GaP (111) MnP (10-1) || GaP (011)	↑↓	↑↑	↑↑
Not coded (Not confirmed by pole figures)	MnP {021} || GaP (100) MnP {(101} || GaP (311)	Not observed	Not observed	↑↑
Not coded (Not confirmed by pole figures)	MnP {010} || GaP (011)	Not observed	↑↑	Not observed

In the MnP (020) pole figure of figure 4.20, we did not show the green/purple lines, as in this pole figure the axiotaxial paths corresponding to MnP (10-1) || GaP (011) axiotaxy axes overlap with those corresponding to MnP (001) || GaP (011) axiotaxy axis (black/white lines).

4.4 Discussion

Studying the growth time and temperature evolution of the texture of MnP thin films grown on GaP (100), we observed a number of phenomena that we will discuss in five sub-sections. Wherever more evidence is required to support a hypothesis or an argument, we present complementary results.

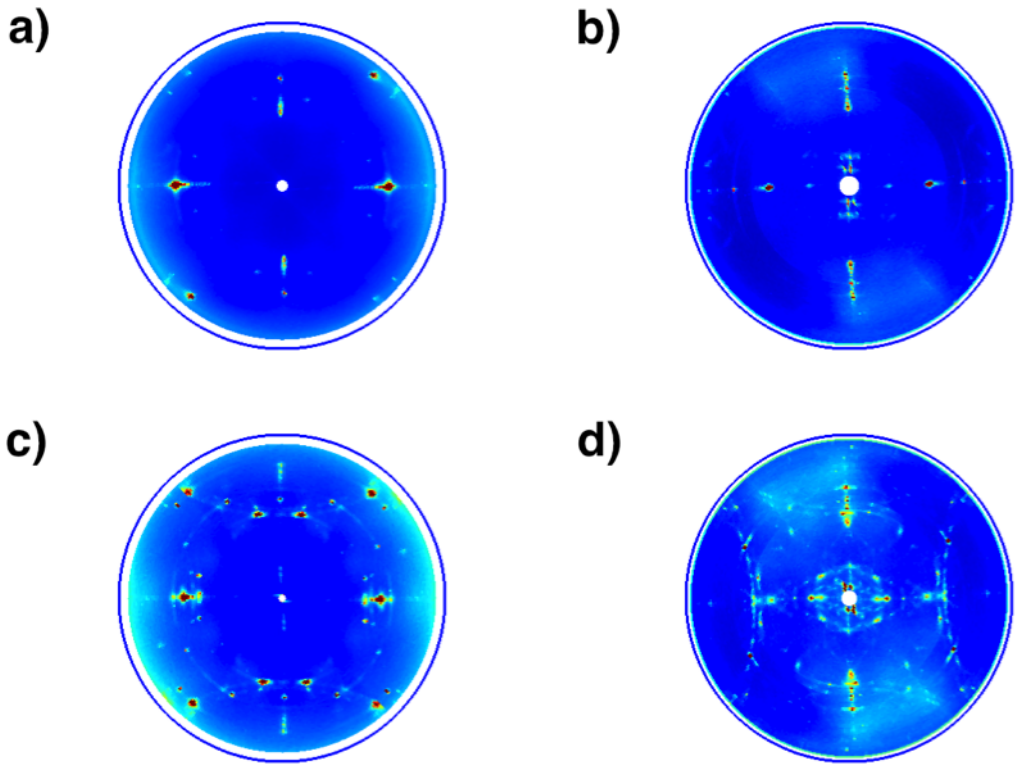

Figure 4.19 MnP (020) pole figures of a) MnP-600-15 and b) MnP-650-15, as well as MnP (111) pole figures of c) MnP-600-15 and d) MnP-650-15. We observe more features on the pole figures of MnP-650-15 than MnP-600-15. The pole figures have been obtained using a linear detector.

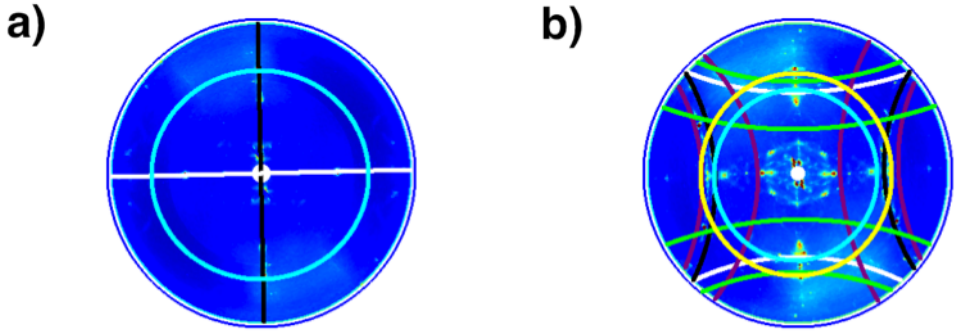

Figure 4.20 Axiotaxial features on a) MnP (020) and b) MnP (111) pole figures of MnP-650-15. The purple/green arcs on MnP (111) pole figure appear as lines on MnP (020) pole figure. As it is described in the text, we do not show the purple/green line in the MnP (020) pole figure.

4.4.1 Crystallographic orientation of MnP grains grown on GaP (100)

By combining the results of ED patterns and XRD-pole figures of the samples we realized that MnP forms on GaP in specific number of epitaxial crystallographic orientations. Moreover, we observed partial axiotaxial features. Studying the growth temperature evolution of the texture (by pole figure analysis) of MnP films grown during 15 minutes (in the temperature range $550 - 750\,^{\circ}\mathrm{C}$) revealed that the partial axiotaxial features become stronger (compared to the epitaxial ones) and more complete as we increase the growth temperature, such that for growth temperatures of $700\,^{\circ}\mathrm{C}$ and $750\,^{\circ}\mathrm{C}$ we only observe axiotaxial texture.

As described in Chapter 2, there are two conditions for an axiotaxial alignment (Detavernier *et al.*, 2003). One is that the d-spacing of the {hkl} plane of the film and that of the {h′k′l′} plane of the substrate are very similar (small strain in the axiotaxy axis). The other one is that the interface remains periodic (meaning that there is no angle between the planes of the substrate and the film at the interafce), which lowers the interfacial energy (Detavernier *et al.*, 2003).

Observing axiotaxial features implies that these two conditions are satisfied in all of our MnP films. However, observing partial axiotaxy indicates that the grains are not completely free to form all possible orientations with a specific 1D alignment (for example axiotaxy axis of MnP {101} || GaP {011}). As we discussed in Chapter 2, the grains will select crystallographic orientations that minimize their energy. To clarify the partial axiotaxial texture we show the SAED patterns of three MnP grains of MnP-600-15 in figure 4.21. In the SAED patterns of these grains, we measured the angles (α_1, α_2, α_3) between three MnP directions (planes) and three GaP directions (planes) : (1) α_1 : MnP [020] with GaP [-11-1], (2) α_2 : MnP [-11-1] with GaP [11-1], and (3) α_3 : MnP [-13-1] with GaP [02-2]. The values of α are reported in table 4.10.

Table 4.10 The angles between MnP [020] with GaP [-11-1] (α_1), MnP [-11-1] with GaP [11-1] (α_2), and MnP [-13-1] with GaP [02-2] (α_3) directions in three MnP grains of MnP-600-15.

Orientation	**MnP (-13-1) || GaP (02-2)**	**MnP (-1-1-1) || GaP (200)**	**MnP (-11-1) || GaP (11-1)**
$\alpha_1(^{\circ})$	3	6	8
$\alpha_2(^{\circ})$	6	3	0.1
$\alpha_3(^{\circ})$	0.3	2	5

These three grains share the MnP [10-1] || GaP [011] alignment (out of plane directions of the SAED patterns shown in figure 4.21). If we follow the SAED patterns of these three grains and the angles α_1, α_2, α_3 (Tble 4.10) from left to right, it looks as if the crystallographic orientation of the grain with MnP (-13-1) || GaP (02-2) alignment (figure 4.21 (a)) is rotating 3° clock-wise about normal to SAED pattern (MnP [10-1] || GaP [011]) and makes the

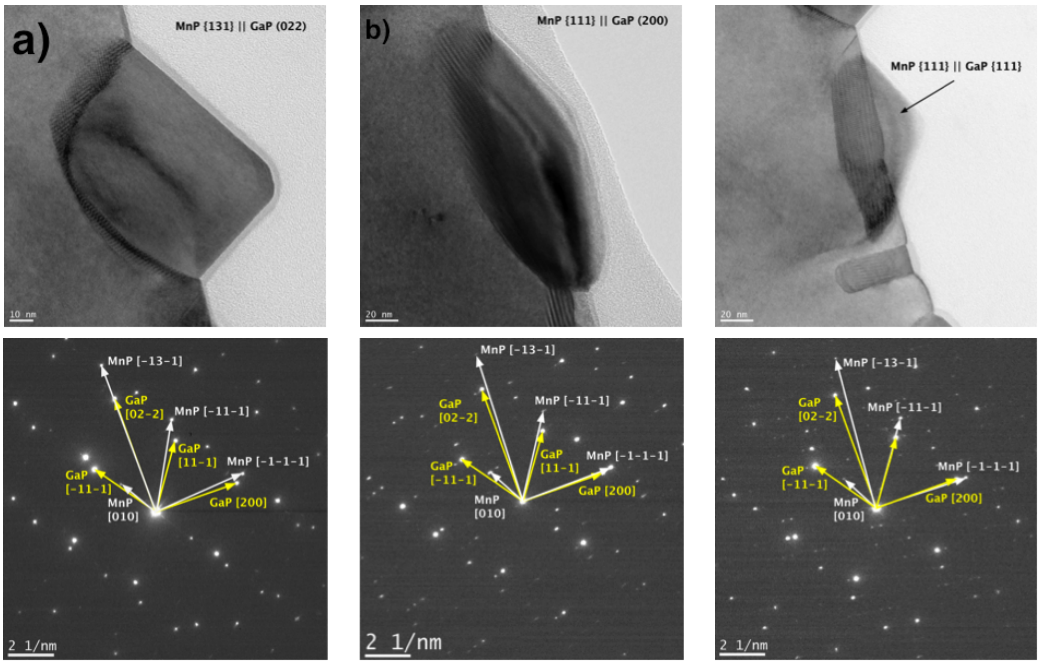

Figure 4.21 SAED pattern of MnP grains with a) MnP (-13-1) || GaP (02-2), b) MnP (-1-1-1) || GaP (200), and c) MnP (-11-1) || GaP (11-1) alignments are shown below their TEM micrographs.

alignment MnP (-1-1-1) || GaP (200) (figure 4.21 (b)) and rotates another 3° clock-wise to make MnP (-11-1) || GaP (11-1) alignment (figure 4.21 (c)). This rotation-like behavior of the grains about an axis results in observing arcs, circles, or lines on the pole figures (if the pole figures are nor measured with good angular resolutions). These features (arcs, lines, or circles) could be a large number of small bright spots on the pole figures that are very close to each other. As an example, in figure 4.22 we show the MnP (020) pole figure of MnP-600-15, taken by the linear detector (more resolution and more intensity compared to the planar detector), in which we see many small bright spots on the pole figure that look like a continuous line. This indicates that the partial axiotaxial texture that we observe in our samples is most likely a combination of many small-populated epitaxial alignments. Nevertheless, these epitaxial orientations share an alignment, which is the axiotaxy axis.

The free surface, interface, and strain energies of the grains vary as a function of temperature. Thus, enhancement of axiotaxial textures at higher growth temperatures suggests that the grains have more degree of freedom to minimize their energy at higher growth temperatures, while keeping their 1D alignment (axiotaxy axis).

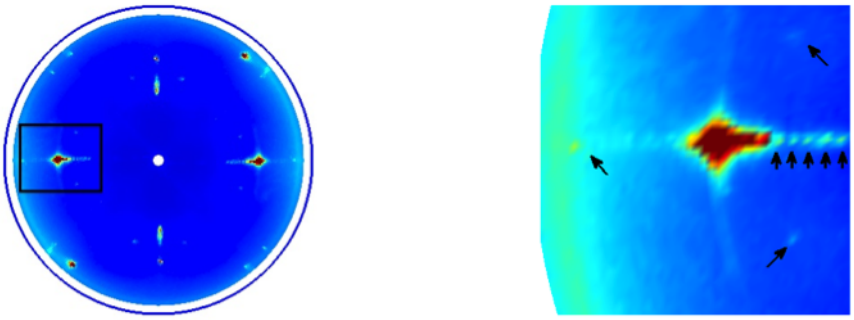

Figure 4.22 Small bright spots that are very close to each other on the MnP (020) of MnP-600-15. The region in the box is enlarged and presented on the right. The black arrows point to some of the bright spots on the seemingly axiotaxial line. This pole figure is obtained by a linear detector.

4.4.2 Free surface facets of MnP grains

As we have pointed out in Section 4.2, MnP grains with different crystallographic orientations have different free surface facets. Formation of surface facets is an indication that the grains have a slower growth rate normal to these surface facets. The slower growth rate leading to the formation of facets could be limited by the (1) kinetics or (2) thermodynamics and energy minimization of the MnP grains. The atomic configurations of different MnP planes can favor larger normal growth rates. For example, a facet plane with more dangling bonds will have a larger prependicular growth rate. This kinetically controlled growth rate is expected to be independent of the grains alignments with the GaP substrate.

Formation of surface facets can also be related with a lower free energies of the corresponding surfaces. If facet formation is thermodynamically controlled, it will depend on the orientation of the grains, as grains with different orientations have different interface/strain energies. In this latter case, we expect to see different surface facets in grains with different orientations, which is what we observe in our samples. Hence, it is likely that the formation of different facets is thermodynamically controlled.

4.4.3 Endotaxial growth of MnP grains on GaP

By studying the growth time evolution of the texture of MnP films grown at 550 °C and 650 °C, we have shown that MnP grains form on GaP (100) through endotaxy, with evidence already present at early stages (90 seconds) of growth (MnP-550-1.5). We have also shown that grains with different crystallographic orientations have different endotaxial depths.

Endotaxial growth increases the contact surface area between GaP and MnP and hence

increases the interface/strain energies. Figure 4.23 schematically shows the contact surface area of a grain grown on top of GaP and a grain that grows endotaxially on GaP. This indicates that MnP grains prefer to increase their interface/strain energies rather than the free surface energy, which implies that the sum of interface and strain energies of MnP/GaP boundary is smaller than the free surface energy of MnP.

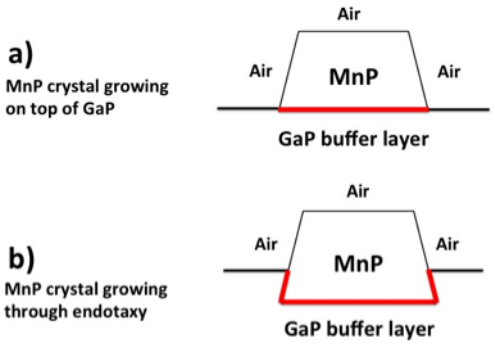

Figure 4.23 Schematic side view of GaP/MnP contact area in a) MnP crystal growing on top of GaP and b) MnP crystal growing partially inside GaP. Red lines show the portion of MnP that is in contact with GaP. This indicates the larger contact area in the case of endotaxial growth.

Figure 4.24 shows two grains of MnP-650-15 as an example of grains with different crystallographic orientation that have different surface facets and different endotaxial depths. The grain with MnP {121} || GaP (200) alignment has an endotaxial depth of 57 nm along GaP <111>, while the grain with MnP {110} || GaP (200) alignment diffuses 27 nm inside GaP along GaP <111>.

4.4.4 Could endotaxial growth favor axiotaxial texture ?

As it was mentioned earlier, the axiotaxial texture dominates at higher growth temperatures. Moreover, MnP grains grown at higher temperatures have larger endotaxial depths.

It is possible that endotaxial growth favors axiotaxial texture. A crystal forming through endotaxy on a substrate has more degree of freedom for orientation selection compared to the one that is only allowed to form on the surface. In the former case, the crystal has the opportunity to access different GaP planes (rather than only the surface planes) to minimize its energy. Hence, it has the possibility to keep one alignment (axiotaxy axis), while selecting an orientation.

Higher growth temperature provides more energy for adatom mobility and enhances the

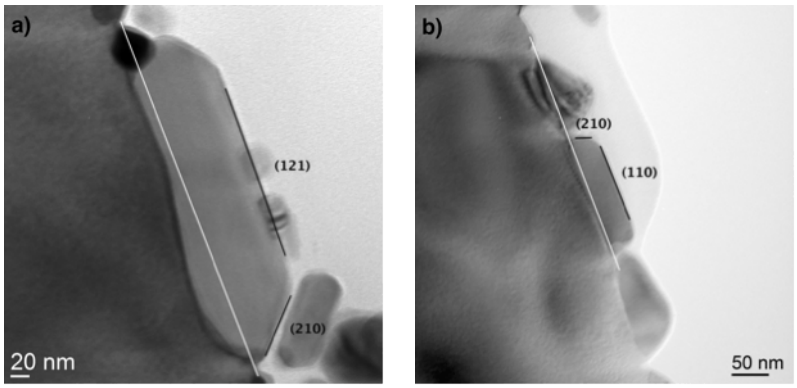

Figure 4.24 Two grains of MnP-650-15 with different orientation that have different facets and different endotaxial depth. a) MnP {121} || GaP (200), endotaxial depth along GaP <111> = 57 nm, and b) MnP {110} || GaP (200) endotaxial depth along GaP <111> = 27 nm. The long white lines show the approximate position of where the surface of GaP buffer layer is deduced to be.

diffusion process. Hence, it favors endotaxial growth. As the endotaxial growth itself favors the axiotaxial texture, we expect to see stronger axiotaxial texture at higher growth temperatures, which is the case for growth of MnP on GaP.

4.4.5 Growth rates

As it was mentioned earlier, the lateral size distribution of MnP grains is not monomodal (figures 4.4 and 4.11). This could be attributed to the fact that our samples contain grains belonging to families with different crystallographic orientations, which could have different growth rates. Each orientation family with a specific growth rate and certain population will contribute to the size histogram of the samlpe, making a multimodal histogram.

The lateral growth rates of the grains calculated from their average effective diameter have been compared to their normal growth rates (normal to GaP (100) plane) (tables 4.2, 4.5, and 4.8). The results show that the lateral growth rate is at least twice larger in the grains than the normal growth rates. It is not very surprising to see a larger lateral growth rate in samples, the grains of which coalescence. Therefore, we only focus on the growth rates of the sample, which is in the pre-coalescence stage, GMP-550-1.5. The average lateral growth rate of the grains of this sample is ≈ 3 times larger than their normal growth rates. This indicates that the system prefers to increase its contact surface area (between GaP and MnP) as the film grows rather than increasing its free surface area. This further confirms that as the volume of the grains becomes larger they prefer to increase their interface/strain energies rather than free surface energy of MnP (the conclusion, which was drawn from endotaxial growth of MnP on GaP). Thus the sum of the interface and strain energies of MnP/GaP

boundary is smaller than free surface energy of MnP.

4.5 Endotaxial growth model

Based on these observations, we propose a semi-quantitative model to describe the endotaxial growth of MnP crystals on GaP substrate. We suggest that the endotaxy mechanism in MnP/GaP is similar to what has been proposed by Braun *et al.* in MnSb/GaSb (Braun *et al.*, 2007) (Chapter 2). The Ga atoms at the MnP/GaP interface diffuse to the surface and are replaced by Mn atoms. There is a possibility that these Ga atoms recombine with P atoms that are present at the surface (during the growth of MnP) and form GaP crystals at the surface. This process is schematically shown in figure 4.25. Figure 4.26 shows an example of a convex GaP surface between two MnP grains observed in MnP-600-15, named as GaP bumps, which supports the recrystallization of GaP at the surface from the out-diffused Ga atoms.

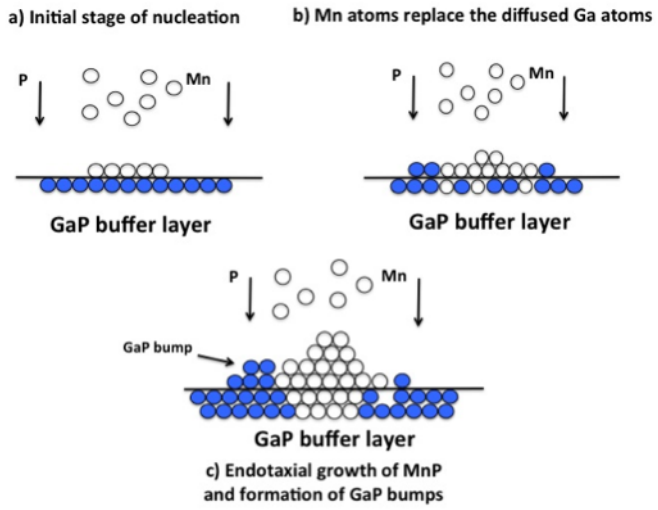

Figure 4.25 a) Initial stage of nucleation of MnP on GaP, b) Mn atoms replacing the Ga atoms that are diffused to the surface, and c) endotaxial growth of MnP crystal and formation of a GaP bump at the surface.

The endotaxial depths of grains with different crystallographic orientations have been studied as a function of growth time. The results show that the endotaxial depth is linearly proportional to the square root of time. This confirms that the endotaxial growth occurs through the diffusion mechanism. In Appendix A, we have extracted the diffusion coefficients and activation energy for diffusion of Mn in GaP along specific GaP crystallographic directions. For the grains grown at 550 °C, 600 °C, and 650 °C we obtained the diffusion co-

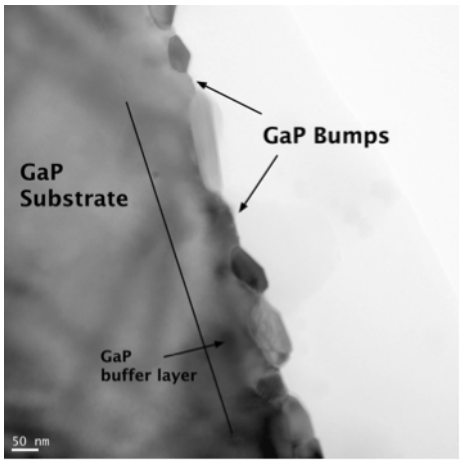

Figure 4.26 Recrystallization of GaP at the surface, possibly from out-diffused Ga atoms in MnP-600-15.

efficients to be of the order of 10^{-14} (cm^2/s) and the activation energy of 0.6 ± 0.2 (eV) (for the orinetation family with MnP {121} || GaP {100} alignment) .

In order to distinguish this diffusion process from bulk diffusion of MnP in GaP, we compared these diffusion coefficients and activation enrgy to the bulk diffusion coefficient of Mn in GaP (order of 10^{-20} to 10^{-17} (cm^2/s) and 4.7 eV) (Kirillov *et al.*, 1980). The results show a much larger (at least two orders of magnitude) diffusion coefficients and much smaller (one order of magnitude) activation energy for Mn diffusion in endotaxial growth of MnP on GaP, indicating either a different or enhanced diffusion process.

Such larger diffusion coefficient is present in MnAs crystals that grow through endotaxy on GaAs (111) substrate (Yatago *et al.*, 2012) (order of 10^{-14} (cm^2/s) at 600 °C), as well. This vale was not reported in Ref. (Yatago *et al.*, 2012), but we extracted an estimate of it from their cross-sectional TEM images. The diffusion coefficient of Mn in GaAs obtained from Ref. (Yatago *et al.*, 2012) is 2 orders of magnitude larger than the diffusion coefficient of Mn in semi insulating GaAs (order of 10^{-16} (cm^2/s) at 680 °C, no data available below 680 °C) (Koskelo *et al.*, 2009). Figure 4.27 compares the orders of magnitude of the diffusion coefficients obtained for interface diffusion of Mn in GaP, with those of bulk Mn diffusion in GaP, interface diffusion of Mn in GaAs, and bulk diffusion of Mn in GaAs.

One possible phenomenon that could explain the much larger diffusion coefficient of Mn in GaP (and GaAs) obtained from the endotaxial growth is the presence of dislocations in GaP buffer layer. These dislocations could act as a diffusion path for Ga to diffuse to the surface. However, this is ruled out, since we observed a dislocation free GaP buffer layer in MnP-600-15 and MnP-650-15. The absence of dislocations has been confirmed from TEM images taken at two different zone axes and three different g vectors, as mentioned in Chapter 3. As an

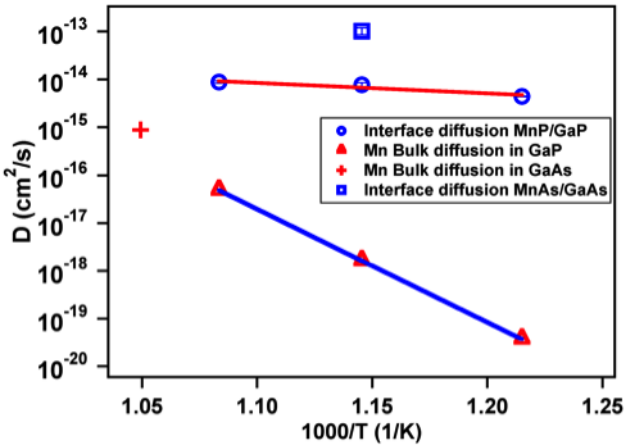

Figure 4.27 Semi-logarithmic graph of the diffusion coefficient (D) as a function of ($1000/T$) for our samples (average of all orientation families) and their corresponding linear fits, compared to Mn bulk diffusion reported in Ref. Kirillov *et al.* (1980). The extracted activation energy (ΔE) and the pre-exponential factor (D_0) in our samples are 0.45 ± 0.14 (eV) and $1.03 \pm 0.99 \times 10^{-11} (cm^2/s)$, respectively, compared to 4.7 (eV) and $2.1 \times 10^9 (cm^2/s)$ reported in Ref. Kirillov *et al.* (1980). The interface and bulk diffusion coefficients of Mn in GaAs are also presented in the graph for comparison.

example, figure 4.28 shows a cross-sectional TEM image of MnP-650-15 taken at GaP [1-12] zone axis along g [1-11], in which there is no dislocations observed.

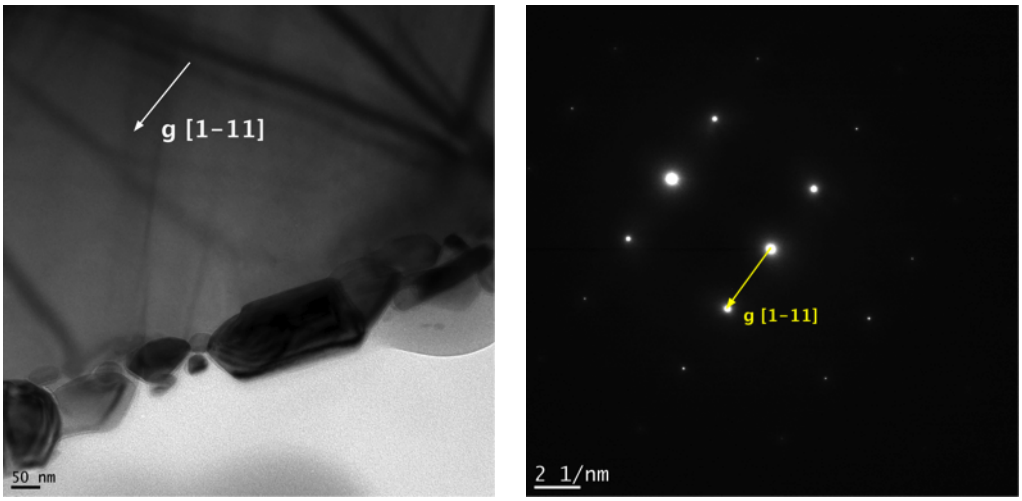

Figure 4.28 Cross-sectional TEM image of MnP-650-15 taken at GaP [1-12] zone axis along g [1-11] and its corresponding diffraction paatern. No dislocations are observed in this image.

Another possible phenomenon that could enhance the out-diffusion of Ga atoms at the MnP/GaP interface could be presence of a large number of vacancies at the interface. Due

to the different crystal structure of MnP (orthorhombic) and GaP (zinc blend) the interface of MnP/GaP might contain a large number of vacancies, through which the Ga atoms could diffuse (self-diffusion of Ga at this interface). As Ga atoms leave their sites to diffuse through these vacancies, Mn atoms replace them (since MnP tends to increase its contact surface area with GaP rather than its free surface area). The Ga atoms that have been replaced by Mn atoms either diffuse inside MnP or diffuse to the surface. The latter is more likely, since as we observed, there is recrystallization of GaP crystals (bumps) at the surface.

CHAPTER 5

Texture of MnP films vs. MnP nanoclusters

In this chapter, we revise the growth model proposed by Lambert-Milot *et al.* ((Lambert-Milot, 2012),(Lambert-Milot *et al.*, 2012)) and describe the texture evolution of GaP:MnP epilayers, taking into account what we learned from endotaxial growth and texture evolution of MnP films. We consider the ripening of the nanolusters, while analysing the texture evolution of the GaP:MnPepilayers, the outcome of which is a better understanding of texture selection in GaP:MnP epilayers, as well as an improvement of the qualitative picture of texture evolution suggested by Lambert-Milot *et al.* ((Lambert-Milot, 2012),(Lambert-Milot *et al.*, 2012)).

Moreover, we study two multilayer samples, GaP/GaP:MnP/GaP (GMP-M10) and GaP/MnP/GaP (MnP-M17), which are designed to further understand the diffusion of Mn in GaP:MnP epilayers. Our results reveal an opportunity to design different heterostructures, in order to achieve the desired texture.

5.1 Texture of GaP:MnP epilayers

In this section, we revise the texture analysis of GaP:MnP epilayers grown at different times and temperatures, and compare their texture to those of MnP thin films. Since Lambert-Milot *et al.* ((Lambert-Milot, 2012),(Lambert-Milot *et al.*, 2012)) studied the epilayers grown at 650 °C (four samples with different growth times) in more details, the focus of this section will be on these samples. We will discuss the results of the comparison in Section 5.3 and provide a qualitative picture for texture development in GaP:MnP epilayers.

Before comparing the texture of the GaP:MnP epilayers with the MnP films, we should mention that we have determined three more orientation families in GaP:MnP epilayers than what has been reported in Refs. (Lambert-Milot, 2012),(Lambert-Milot *et al.*, 2012) :

1. **White square** (MnP {111} || GaP {100}) and (MnP {101} || GaP {011})
2. **Black ellipse** (MnP {121} || GaP {100}) and (MnP {101} || GaP {011})
3. **Yellow circle** (MnP {110} || GaP {100}) and (MnP {001} || GaP {011})

These three orientation families have been determined for MnP films (through analyzing their SAED patterns) and have been confirmed by pole figure analysis. On (at least three) pole figures of GaP:MnP epilayers, we see bright spots at the exact same angular positions and relative intensities that we expect to observe the signature of the above-mentioned three

orientation families. Hence, we have realized that these orientation families were missing in the texture analysis of the epilayers. Since, Lambert-Milot *et al.* determined the crystallographic orientations of MnP nanoclusters using pole figure analysis only ((Lambert-Milot, 2012),(Lambert-Milot *et al.*, 2012)), they missed these three orientation families. This further emphasizes the strength of texture analysis by combining ED patterns and pole figure analysis.

5.1.1 GaP:MnP epilayers grown at 550 °C

According to Ref. ((Lambert-Milot, 2012)), it is not possible to grow epitaxial GaP:MnP at 550 °C. The epilayers grown at this temperature had a very rough surface and could be removed from the substrate by scratching the surface. This has been attributed to the poor crystalline quality of GaP grown at 550 °C ((Lambert-Milot, 2012)). Surfaces of GaP grown at 550 °C show very poor morphology and most successful growth of GaP reported in the literature is done above 700 °C (Stringfellow (1999)).

5.1.2 GaP:MnP epilayer and MnP film grown at 600 °C

As reported in Refs. ((Lambert-Milot, 2012),(Lambert-Milot *et al.*, 2012)), studying the cross-sectional TEM images and XRD pole figures revealed the presence of many structural defects (twins, stacking fault) in the GaP:MnP epilayer grown at this temperature. This has been attributed to the poor crystalline quality of GaP grown at this temperature ((Lambert-Milot, 2012),(Lambert-Milot *et al.*, 2012)). Figure 5.1(a) shows the plan-view SEM image of GaP surface grown at 600 °C, in which we observe bright spots at the surface. These bright spots (unknown surface defects) indicate the poor crystalline quality of the surface. Structural defects (twins, stacking faults)((Lambert-Milot, 2012),(Lambert-Milot *et al.*, 2012)) in GMP-600-45 are shown in figure 5.1(b).

The orientation families of the samples grown at this temperature have been determined by the XRD pole figure analysis combined with SAED patterns. We have identified two orientation families that exist in GMP-600-45 but not in MnP-600-15 :

1. **Dots** (MnP {010} || GaP {211})
2. **Yellow triangles** (MnP {520} || GaP {111})

As it will be discussed in Section 5.3, these two orientation families could be attributed to nucleation and growth of MnP nanoclusters on high-index GaP surfaces (due to the presence of GaP facets during the growth of GaP:MnP epilayers).

The orientation families that exist in MnP-600-15 and not in GMP-600-45 are :

1. **White square** (MnP {111} || GaP {100})

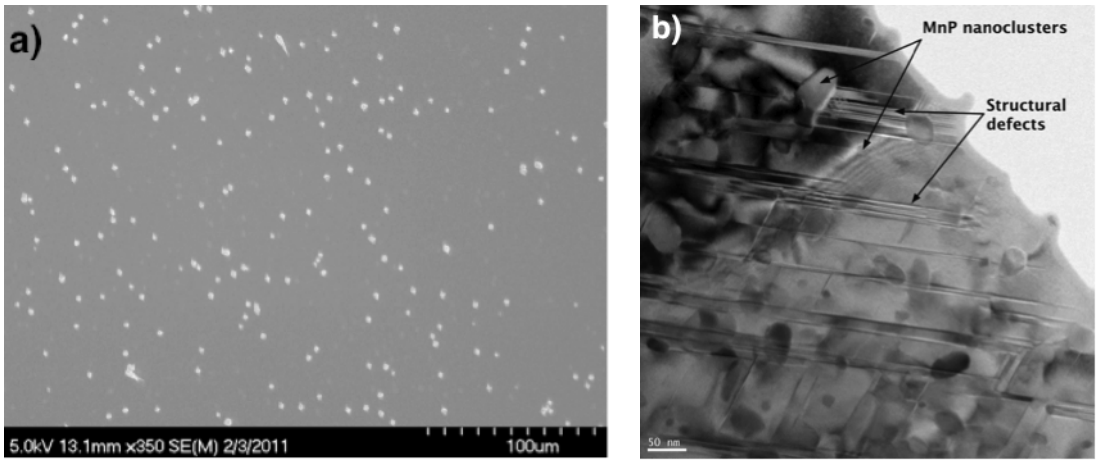

Figure 5.1 a) Plan-view SEM image of GaP grown at 600 °C shows its poor surface quality. b) Presence of many structural defects revealed from the cross-sectional TEM micrograph of GMP-600-45.

2. **Black ellipse** (MnP {121} || GaP {100})
3. MnP {010} || GaP {011}
4. MnP {101} || GaP {100}
5. MnP {131} || GaP {011}

The absence of these orientation families in GMP-600-45 could be attributed to 1) presence of structural defects that affect the texture of the epilayer and 2) the fact that there are fewer number of orientations that survive during growth of MnP nanoclusters in GaP:MnP compared to MnP grains in MnP-600-15. We will discuss the latter in more details in the next section.

5.1.3 GaP:MnP epilayers and MnP films grown at 650 °C

As described in Chapter 4, based on HR-TEM image analysis and pole figure data, S. Lambert-Milot *et al.* presented a qualitative description of the texture evolution in GaP:MnP (see figure4.2) ((Lambert-Milot, 2012),(Lambert-Milot *et al.*, 2012)). They suggested that MnP initially forms in one orientation family on GaP (100), red circle (MnP (010) || GaP (100)). The other orientation families nucleate and grow on different GaP surfaces such as GaP {111} and GaP {411}, due to the formation of these facets at later growth times (figure 4.1 presents an example of MnP nanoclusters that nucleate on GaP {111} surfaces). MnP {110} || GaP {411} (blue square) and MnP {010} || GaP {111} (lines) are two examples of the orientation families that nucleate on GaP {411} and {111} facets, respectively. As the epilayer grows further, more GaP facets and more MnP orientation families appear in the

sample.

However, we have observed both of these orientation families (blue square and lines) in MnP grains that form on GaP (100) (MnP-650-15), for which GaP (100) is initially the only surface that is available for nucleation (no GaP facets in this sample). Hence, MnP selects the same crystallographic orientations to nucleate and grow on different GaP surfaces (in MnP films grown on GaP (100), MnP nucleates on different GaP planes (other than GaP (100)) through endotaxial growth).

Figure 5.2 shows the MnP (020) and MnP (101) pole figures of GMP-650-15 and MnP-650-15. We observe more bright spots and partial arcs in the pole figures of MnP-650-15, which indicates that the grains in MnP-650-15 has a larger degree of freedom to select different crystallographic orientations, while the nanoclusters in GMP-650-15 are limited to form in specific epitaxial orientations.

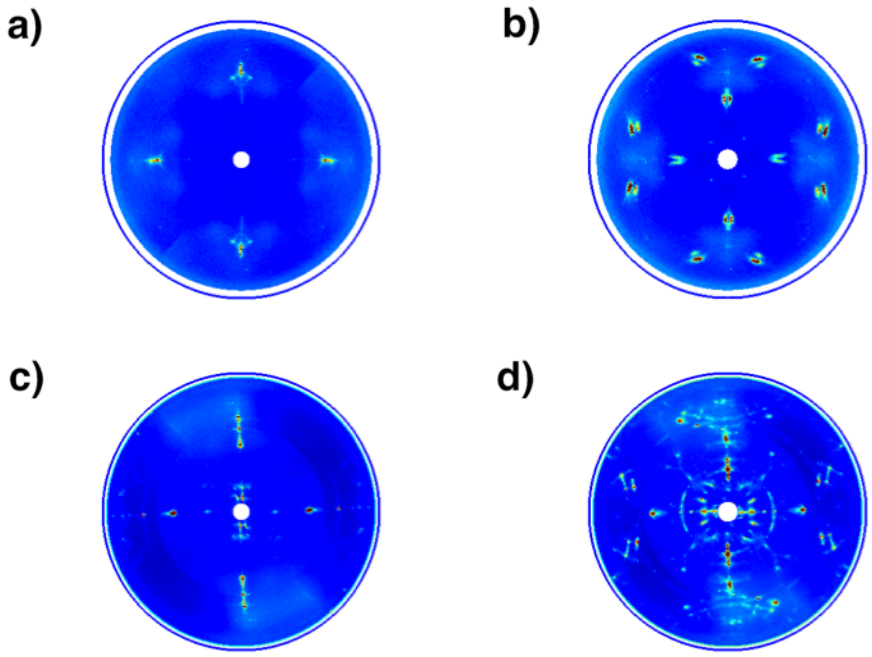

Figure 5.2 a) MnP (020) and b) MnP (101) pole figures of GMP-650-15 (top) compared to c) MnP (020) and d) MnP (101) pole figures of MnP-650-15 (bottom). More bright spots and partial arcs are observed in the pole figures of MnP-650-15, which indicates that there are more epitaxial and partial axiotaxial orientations in this sample compared to GMP-650-15. These pole figures are obtained using a linear detector.

Table 5.1 lists and compares all the orientation families (only the ones that are confirmed by pole figures) that are found in all the samples (GaP:MnP epilayers and MnP film grown at this temperature).

Table 5.1 List of all orientation families (mostly alignments with low-index GaP planes) in the GaP:MnP epilayers and MnP film grown at 650 °C.

Orientation	**GMP-650-1.5**	**GMP-650-5**	**GMP-650-15**	**GMP-650-45**	**MnP-650-15**
Black ellipse MnP (121) || GaP (100)	No	No	Yes	Yes	Yes
Yellow circle MnP (110) || GaP (100)	No	Yes	Yes	Yes	Yes
Blue square MnP {110} || GaP (411)	Yes	Yes	Yes	Yes	Yes
Red circle MnP {010} || GaP (100)	Yes	Yes	Yes	Yes	Yes
Lines MnP {010} || GaP (111)	No	Yes	Yes	Yes	Yes
White square MnP {111} || GaP (100)	No	Yes	Yes	Yes	Yes
Diamonds MnP {010} || GaP (433)	No	Yes	Yes	Yes	Yes
Not coded MnP (101) || GaP (100)	No	No	No	No	Yes
Not coded MnP {131} || GaP (0-11)	No	No	No	No	Yes
Not coded MnP {121} || GaP (111)	No	No	No	No	Yes

According to table 5.1, seven orientation families are in common in thicker epilayers (grown during 15 and 45 minutes) and MnP-650-15 : red circle, blue square, lines, diamonds, white square, black ellipse, and yellow circle.

The orientation families that exist in GMP-650-15 and GMP-650-45 and are missing in MnP-650-15 are :

1. MnP {010} || GaP {211} (dots in Refs. ((Lambert-Milot, 2012),(Lambert-Milot *et al.*, 2012)))

2. MnP {520} || GaP {111} (triangles in Refs. ((Lambert-Milot, 2012),(Lambert-Milot *et al.*, 2012)))

A possible explanation could be that these two orientation families nucleate on high-index GaP surfaces (GaP facets) in GaP:MnP epilayers, which are not accessible in MnP-650-15 through endotaxial growth.

On the other hand there are more orientation families that exist in MnP-650-15 and not in GaP:MnP epilayers, some of which are not determined since they have alignments with high-index GaP planes. The ones that are determined by combining the pole figures and SAED patterns are :
1. MnP {101} || GaP (100)
2. MnP {131} || GaP (011)
3. MnP {121} || GaP (111)

5.1.4 Samples grown at 700 °C

Many structural defects have been observed in GMP-700-45 ((Lambert-Milot, 2012), (Lambert-Milot *et al.*, 2012)). This sample shows more axiotaxial features as compared to the other epilayers (more degree of freedom to rotate about the axiotaxy axes (Lambert-Milot, 2012), (Lambert-Milot *et al.*, 2012)), but still shows strong epitaxial alignments. MnP-700-15 showed only axiotaxial texture and no epitaxial alignments. This suggests that at higher growth temperatures the nanoclusters (similar to grains) have a larger degree of freedom for orientation selection, yet the excess strain/interfacial energies in the nanoclusters compared to the grains limits the axiotaxial texture formation.

5.2 Multilayer samples

In this section, we study the texture of two heterostructure systems, GaP/GaP:MnP/GaP (period =10) and GaP/MnP/GaP (period = 17), to verify the significance of Mn diffusion in GaP and ripening of nanoclusters in texture developement of GaP:MnP epilayers. We expect to see the trace of Mn in GaP spacer layers in these two heterostructures, if Mn diffusion in GaP is significant.

5.2.1 GMP-M10 (GaP/GaP:MnP/GaP (period =10))

Figure 5.3 shows the cross-sectional TEM images of GMP-M10. The growth time of each layer has been set to obtain 30 ± 5 nm of GaP:MnP sandwiched between two 60 nm GaP spacer layers (total of 300 nm GaP:MnP) (for details of growth procedure see Section 3.1). The TEM images show that MnP nanoclusters form even in the GaP spacer layers (where we do not expect to see them). This indicates enough Mn diffusion inside GaP to form nanoclusters. These nanoclusters have a mean effective diameter of 18.5 ± 0.5 nm.

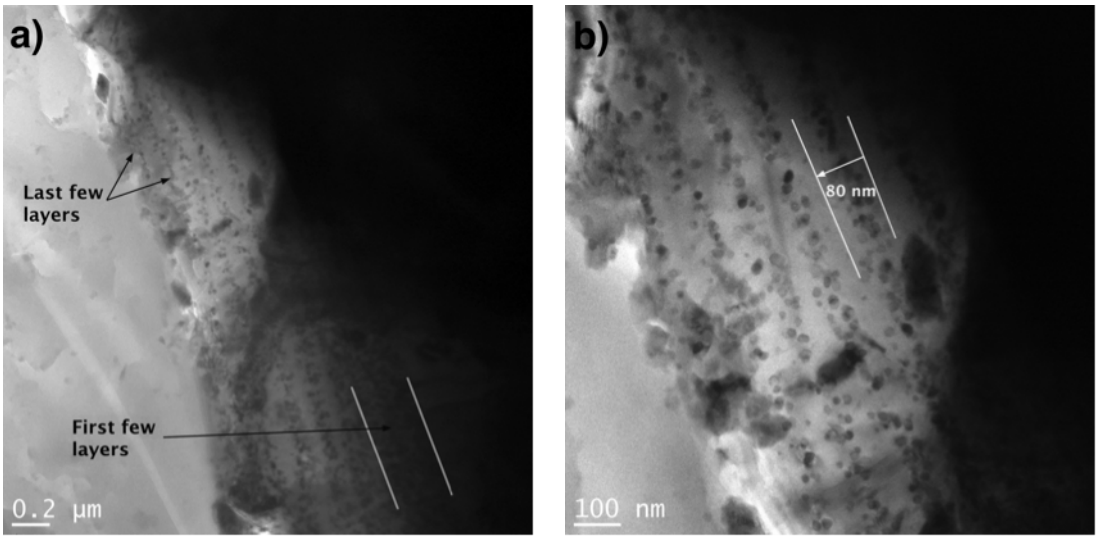

Figure 5.3 Cross-sectional TEM images of GMP-M10. In (a) we see that the spacing between the first few layers is much less than that of the last layers, which indicates more Mn diffusion in GaP for the first few layers. In (b), at higher resolution, we highlight a 80 nm thick layer containing MnP nanoclusters, while the growth time should contain the nanoclusters to a 30 ± 5 nm thick layer.

In figure 5.3 (a), we observe that the thickness of the layers containing the nanoclusters decreases as we move away from the substrate. In figure 5.3 (b), at higher resolution we show a layer containing MnP nanoclusters with a thickness of 80 nm, while the growth time has been adjusted to obtain nanoclusters only within a 30 nm thick layer. This implies the diffusion of Mn in GaP during growth. Since the first few layers have been formed at earlier growth times, the Mn atoms in these layers have more time to diffuse inside GaP. Hence, the Mn diffusion length is larger in the first few layers compared to the last ones. Therefore, the spacing between the first few effective GaP:MnP layers is much less than that of the last layers.

By studying the thickness of GaP:MnP layers as a function of their formation time, we provide an estimate of the diffusion coefficient of Mn in GaP in this heterogeneous epilayer. It should be mentioned that the quality of the samples prepared for cross sectional TEM imaging did not allow us to study the thickness of more than four layers. Figure 5.4 presents the graph of the square of the diffusion length as a function of time, which shows a roughly linear behavior. The diffusion length is the difference between the actual thickness of each layer (measured from TEM) and the expected one (30 ± 5, as reported for the thickness of GMP-650-1.5 ((Lambert-Milot, 2012),(Lambert-Milot *et al.*, 2012)). The slope of the fitted line gives us the diffusion coefficient of Mn in GaP to be $4.0 \pm 0.3 \times 10^{-15}$ (cm^2/s).

The diffusion coefficient thus obtained is one order of magnitude smaller than the one

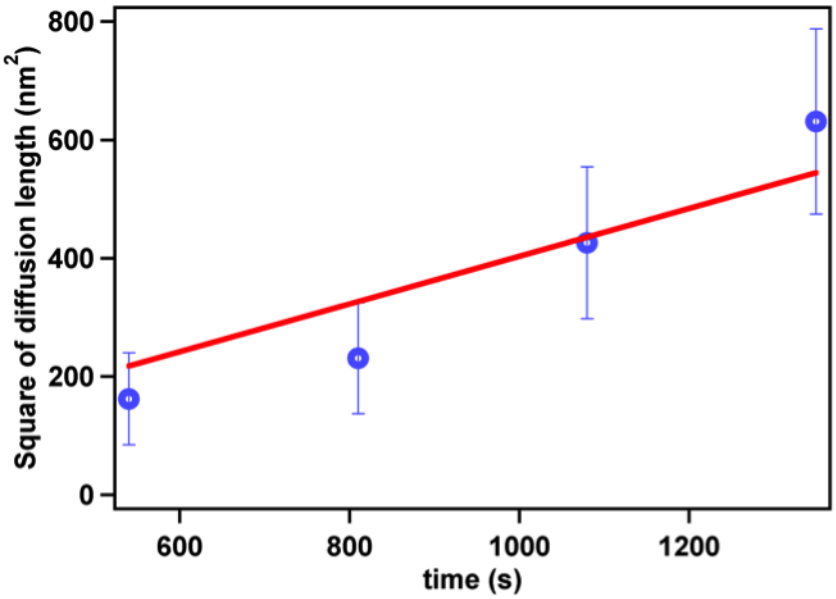

Figure 5.4 Square of the diffusion length as a function of time in GMP-M10. The slope of the line represents the diffusion coefficient of Mn in GaP to be $4.0 \pm 0.3 \times 10^{-15}$ (cm^2/s). The error bars are roughly estimated.

obtained for the endotaxial growth in Chapter 4, while it is two orders of magnitude larger than the reported value of the bulk diffusion coefficient of Mn in GaP (Kirillov *et al.* (1980)). The enhanced bulk diffusion of Mn in GaP in this heterogeneous sample is expected due to the structural defects present in the GaP spacer layers, which are grown on GaP:MnP. These structural defects are already enhanced in the poor morphology, which has been obtained in a 60 nm GaP layer grown at 650 °C on 30 nm GaP:MnP layer containing nanoclusters (grown at 650 °C), as shown in figure 5.5.

5.2.2 MnP-M17 (GaP/MnP/GaP (period = 17))

Figure 5.6 shows the cross-sectional TEM images of MnP-M17. The growth times of the MnP and GaP layers have been set to obtain 3 nm of MnP film sandwiched between two 50 nm GaP spacer layers (total of 51 nm MnP). The TEM images reveal formation of MnP nanoclusters inside GaP rather than formation of 17 layers of MnP thin films. This confirms the rather larger Mn diffusion in GaP during growth.

Very close to the surface of GaP buffer layer (figure 5.6 (b)), we observe formation of many large MnP nanoclusters (mean effective diameter = 41 ± 4.5 nm) compared to the other parts of the sample (average effective diameter = 16 ± 0.4 nm) (figure 5.6 (c)). Similar to GMP-M10, this can be attributed to the larger diffusion length of Mn in GaP closer to

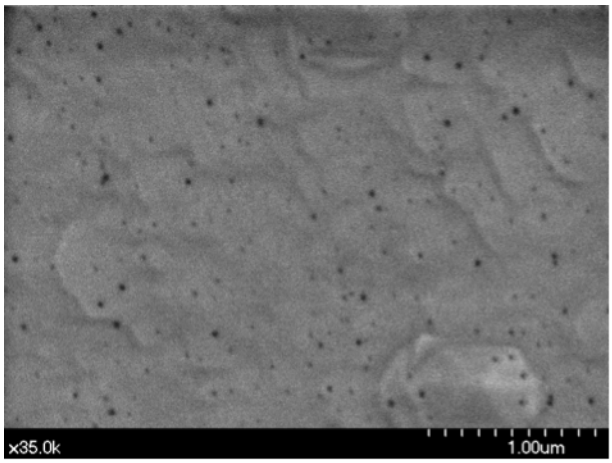

Figure 5.5 Plan-view SEM image of a GaP layer (60 nm) grown at 650 °C that has been grown on a 30 nm GaP:MnP layer (grown at 650 °C). The dark spots are the GaP surface pits. These pits are also observed in cross-sectional TEM images of GMP-650-1.5 in (Lambert-Milot, 2012),(Lambert-Milot *et al.*, 2012).

the MnP/GaP buffer layer interface (because of a longer diffusion time).

We also observed different contrast in the TEM images at different parts of the sample (figure 5.6 (c)). If we assume that we are examining a specimen of homogeneous thickness, this can be interpreted as the formation of GaP crystals having different crystallographic orientations. This interpretation is further confirmed by ED patterns and XRD pole figures of this sample.

Figure 5.7 shows the ED pattern of the film, as well as GaP (100) and GaP (111) XRD pole figures. Presence of many bright spots that almost form a circle in the ED pattern and many bright spots on the pole figure of GaP (100) and (111) implies that GaP forms in many different crystallographic orientations. On the pole figures, the yellow arrows show the expected positions of the bright spots corresponding to GaP (100) and (111) planes of the substrate. Some GaP crystals that grow with different crystallographic orientations on the GaP substrate are marked as an example with red and white arrows on the pole figures (which will be further discussed in figure 5.8).

Figure 5.8 shows the MnP (020) and MnP (101) pole figures of this sample. The white and red arrows on MnP (020) pole figure correspond to (020) planes of the nanoclusters that form on the GaP crystals, which are marked by the white and red arrows in figure 5.7.

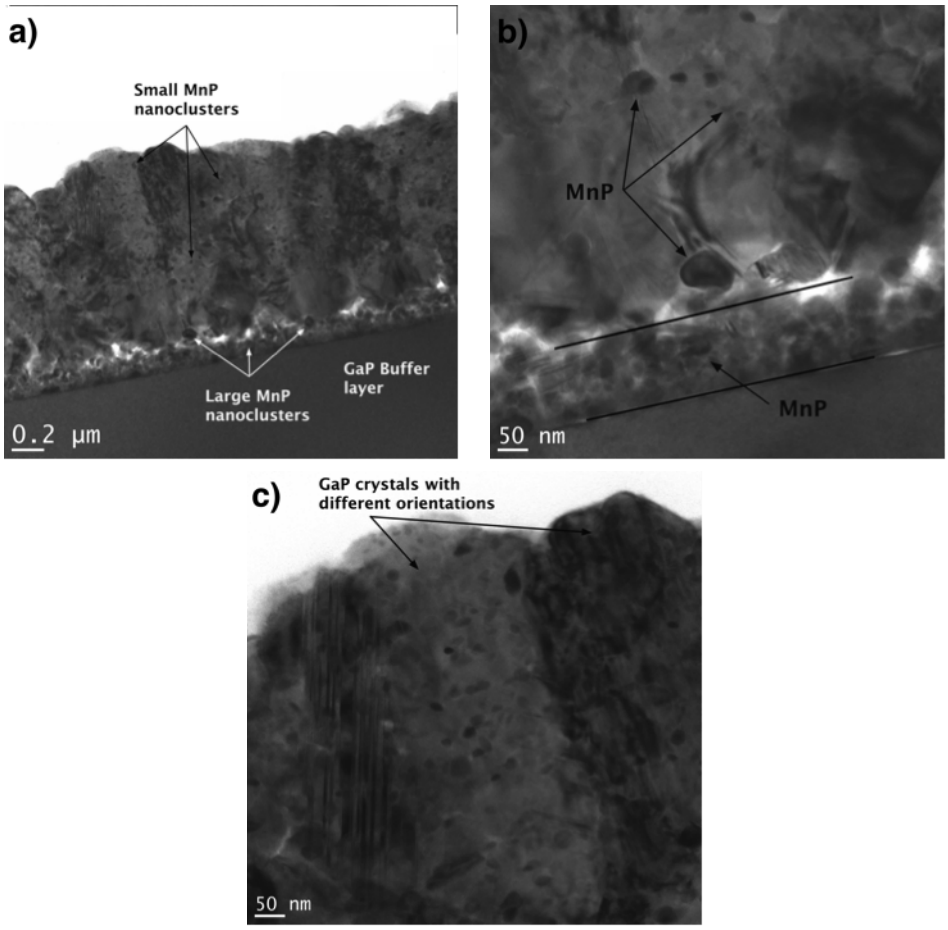

Figure 5.6 Cross-sectional TEM images of MnP-M17, a sample grown at 650 °C (GaP) and 550 °C (MnP) to nominally have 17 periods of 3 nm MnP and 50 nm GaP. We observe formation of larger nanoclusters close to the buffer layer/epilayer interface. We also observe formation of GaP with different crystallographic orientations and structural defects in this sample.

5.3 Discussion

To understand why we observe more epitaxial and axiotaxial orientations in MnP films than in GaP:MnP epilayers we should consider the texture development during the nucleation, growth, and ripening of MnP nanoclusters in GaP:MnP. Since we observed significant Mn diffusion in GaP spacer layers of multilayer samples, we consider the ripening process of the nanoclusters (which was ignored in the work of Lambert-Milot *et al.* ((Lambert-Milot, 2012),(Lambert-Milot *et al.*, 2012))) in discussing the texture development of GaP:MnP epilayers.

It is likely that the nucleation and initial growth mechanism of MnP nanoclusters in GaP:MnP are similar to those of MnP crystals on GaP. Hence, the endotaxial growth model

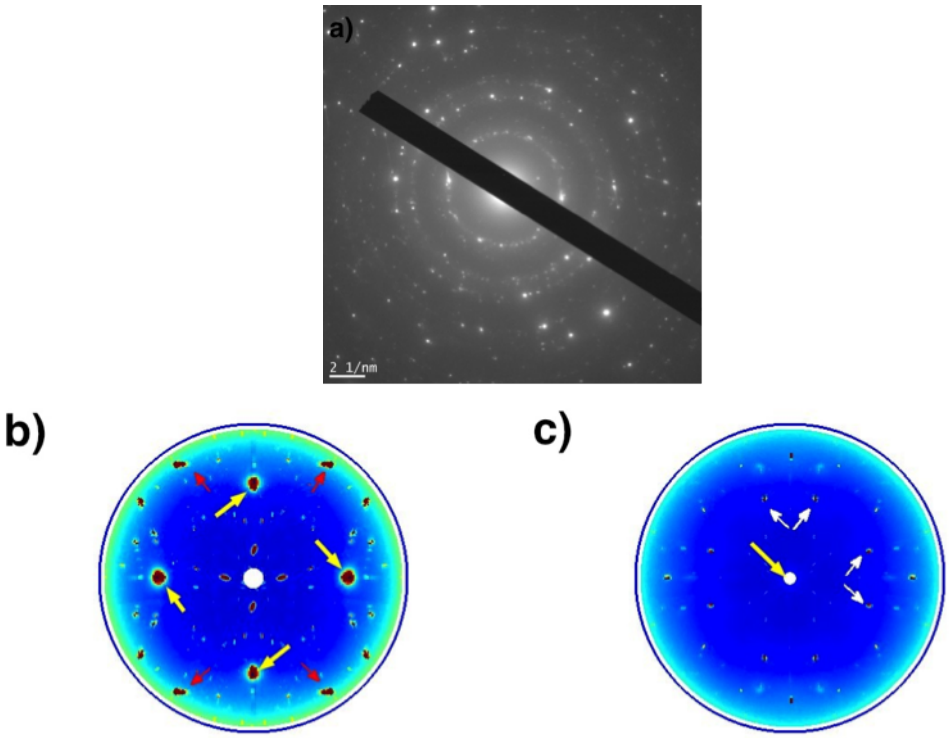

Figure 5.7 a) ED pattern, b) GaP (111), and c) GaP (200) pole figures of MnP-M17. The presence of many bright spots on the ED pattern and pole figures suggest that in this sample GaP crystals grow with different crystallographic orientations. The yellow arrows show the expected angular positions of GaP (111) and (200) planes of the substrate. The red and white arrows correspond to angular positions of GaP (111) and (200) planes of some GaP crystals that are differently oriented than the substrate, on which MnP nanoclusters nucleate (will be presented in figure 6.11). These pole figures are obtained using a linear detector.

that has been presented in Chapter 4 could be applied to nucleation and initial stage of growth of MnP nanoclusters in GaP. The difference between the growth of MnP grains on GaP and MnP nanoclusters in GaP:MnP epilayers is that in addition to Mn and P adatoms that are provided from the gas phase in the growth of MnP films, Ga adatoms are also present at the surface and incorporate to the growth of GaP:MnP epilayers.

Now we consider the effect of GaP growth along with MnP nanoclusters on the texture development of GaP:MnP. Consider a MnP crystal that nucleates on GaP (100) with orientation MnP (hkl) || GaP (h′k′l′). As this crystal grows, it lowers its energy by balancing its free surface energy (different surface facets), and strain/interfacial energies (through endotaxial growth)). Grains with different crystallographic orientations lower their energy through different endotaxial depths and formation of different surface facets.

Now consider the same crystal growing within a GaP (100) epitaxial matrix with the same

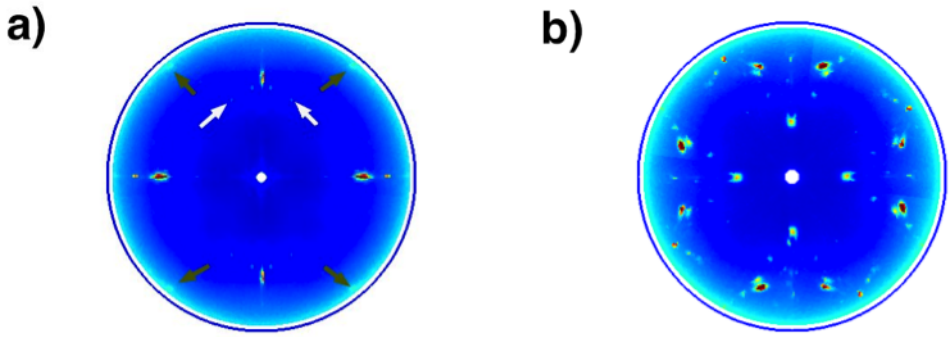

Figure 5.8 a) MnP (020) and b) MnP (101) pole figures of MnP-M17. The white and red arrows in a) correspond to MnP {020} || GaP {100} (red circle) and MnP {020} || GaP {111} (lines) alignments for the nanoclusters that form on GaP crystals with different orientation than the substrate. The pole figures are obtained using a linear detector.

crystallographic orientation MnP (hkl) || GaP (h′k′l′) and same size. Figure 5.9 illustrates the MnP crystals (nanoclusters) that are embedded in the GaP matrix compared to the MnP crystal that is formed endotaxially on GaP (both structure are grown at 650 °C for 90 seconds). The strain/interface energies of these crystals (nanoclusters) are larger than those of MnP crystal grown on GaP (in MnP film) due to their larger contact surface area with GaP and larger number of GaP/MnP interfaces.

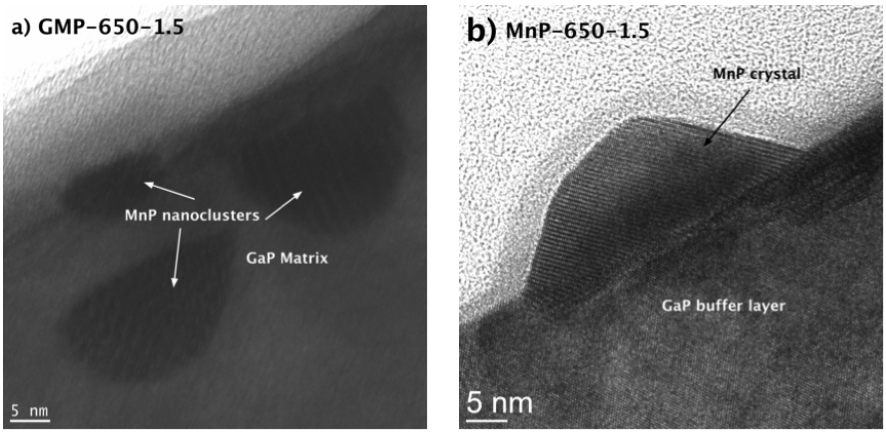

Figure 5.9 a) MnP nanoclusters embedded in GaP (GMP-650-1.5) compared to b) MnP crystal grown endotaxially on GaP (GMP-650-1.5).

It is likely that MnP nanoclusters initially nucleate in the same families of orientations in GaP:MnP and on GaP (MnP films), but some of the orientation families do not survive in GaP:MnP due to their higher interface/strain energies. These nanoclusters will disappear during the ripening process, while the grains that have lower interfacial/strain energies

grow larger. Figure 5.10 is the schematic representation of the suggested ripening process in GaP:MnP epilayers.

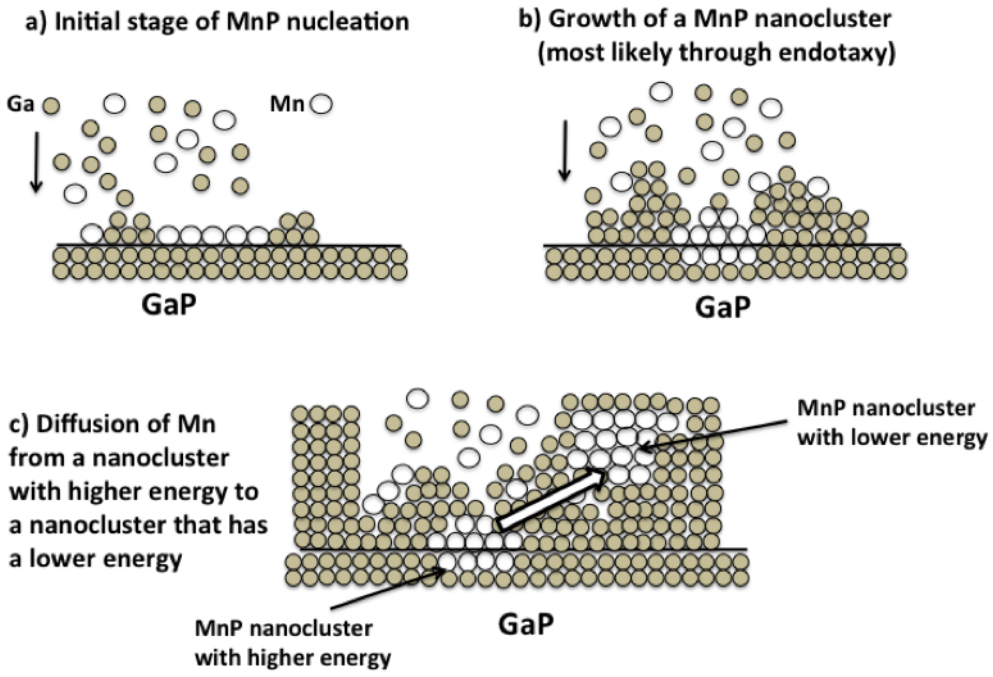

Figure 5.10 Schematic representation of the ripening process in GaP:MnP. a) Initial stage of nucleation of a nanocluster. b) As the nanocluster grows, it ends up surrounded by GaP due to larger growth rate of GaP. c) When this nanocluster is completely buried in GaP, Mn atoms of this nanocluster may diffuse towards a neighboring nanocluster with lower energy (shown by the block arrow). In this representation we do not show the P atoms.

Now, we present a qualitative description of the time evolution of the texture of GaP:MnP epilayers grown at 650 °C. The most favorable orientation families that form on GaP (100) are the red circle and the blue square families, as observed in GMP-650-1.5. It is possible that other orientation families also form along with these two orientation families, but with a small population that cannot be detected in the XRD pole figures. As the epilayer grows, some of these orientations that have a lower energy will grow at the expense of the others (the ripening process). These orientation families that survive in GaP:MnP are the lines, diamonds (Refs. [(Lambert-Milot, 2012),(Lambert-Milot *et al.*, 2012)]), white square, black ellipse, and yellow circle. As we observe these orientation families in MnP films grown on GaP (100), we suggest that the texture selection in GaP:MnP epilayers, similar to MnP films, occurs through the process of endotaxial growth.

There are two orientation families observed in GaP:MnP, the dots and the yellow triangles,

which we already suggested that they possibly nucleate on high-index GaP GaP planes (GaP facets) that are not accessible to MnP grains during endotaxoial growth. These are all the epitaxial orientations that were observed in GaP:MnP epilayers. The orientation families that do not survive during the ripening process are the three "not coded" orientation families listed in table 5.1 (and also the orientations in MnP films that correspond to alignments with high-index GaP planes, which could not be determined in this work).

Partial axiotaxy is also observed in GaP:MnP epilayers ((Lambert-Milot, 2012),(Lambert-Milot *et al.*, 2012))). The degree of freedom to select different crystallographic orientations while keeping the 1D alignments (the axiotaxy axes) is very limited for the nanoclusters. As mentioned earlier, this corresponds to the fact that the nanoclusters are surrounded by GaP and the excess interfacial/strain energies in the nanoclusters limits the degree of partial axiotaxy in GaP:MnP epilayers compared to MnP films.

The signature of Mn diffusion in GaP has been found in GaP spacer layers in GMP-M10. The length of Mn diffusion has been observed to decrease, as we move away from the substrate. It is likely that the same phenomenon occurs in the growth of GaP:MnP epilayers, for example in GMP-650-45. If so, then the first layers have more time to exchange material compared to the last layers. Therefore, the degree of ripening will gradually change with the thickness of the epilayer. Hence, we expect that the population of each orientation family in the epilayers change with growth time.

In order to have an epilayer, in which MnP nanoclusters in specific orientation families have a homogeneous distribution, one possible way could be to control the Mn diffusion in GaP by growing an epilayer, in which we alter the concentration of Mn in the gas phase as a function of time. This way less MnP nanoclusters, which will be more distant from one another, form at the earlier stages of growth. Thus the material exchange between them will be less.

Mn diffusion in GaP was further confirmed in MnP-M17, were we observed formation of MnP nanoclusters in GaP rather than multilayer GaP/MnP thin films. We tentatively propose the process of formation of MnP nanoclusters in this sample. First small MnP crystals grow on GaP (potentially through endotaxy, similar to MnP-550-1.5). Then GaP is deposited on these crystals, most likely with a poor quality (and many structural defects, similar to what we have seen in figure 5.5). As MnP crystals are sandwitched between GaP layers, their interface/strain energies increase. Presence of structural defects, shown in figure 5.6(c), could enhance the Mn diffusion inside GaP. There is a chance that the diffused Mn atoms nucleate in the GaP spacer layer. If the size of this newly formed nucleus exceeds the critical size, it will be thermodynamically stable and grows as a MnP crystal inside GaP (MnP nanocluster). If the energy of the newly formed nanocluster is smaller than the neighboring MnP grains

initially formed on GaP, then it is more favorable to have nanoclusters embedded in GaP rather than crystals in a multilayer film. Figure 5.11 shows a schematic representation of nanocluster formation in MnP multilayers.

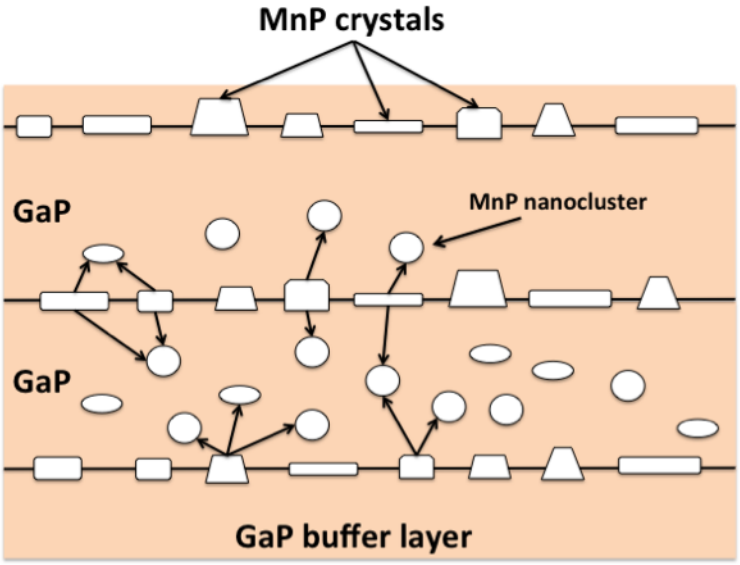

Figure 5.11 Schematic representation of nucleation of MnP nanocluster in MnP-M17 (only three MnP layers are shown). The arrows show the direction of Mn diffusion from the crystals to the nanoclusters, that potentially occurs through structural defects present in this sample.

5.4 Summary

In this chapter we compared the orientation families of MnP grains in MnP films with those of MnP nanoclusters formed in GaP:MnP epilayers (studied in Refs. (Lambert-Milot, 2012),(Lambert-Milot *et al.*, 2012)). By combining the results of SAED pattern analysis of MnP films and pole figure analysis of GaP:MnP epilayers we have found three orientation families in the epilayers that were missed in Refs. (Lambert-Milot, 2012),(Lambert-Milot *et al.*, 2012)). This confirms the strength of combining these methods in analyzing the texture.

We have found two orientation families that form in the epilayers (except for GMP-650-1.5), but not in the films : MnP {520} || GaP {111} (yellow triangles in Refs. ((Lambert-Milot, 2012),(Lambert-Milot *et al.*, 2012))) and MnP {020} || GaP {211} (dots in Refs. [(Lambert-Milot, 2012),(Lambert-Milot *et al.*, 2012)]). We attributed these orientation families to nucleate on high-index GaP surfaces, due to the formation of different GaP facets during the

growth of GaP:MnP epilayers ((Lambert-Milot, 2012),(Lambert-Milot *et al.*, 2012)). The other orientation families observed in the GaP:MnP epilayers also form in the MnP films grown on GaP (100).

We also observed more epitaxial orientation families and axiotaxial alignments in the MnP films than in the GaP:MnP epilayers and multilayer. We suggested that the texture selection of the MnP nanoclusters is very similar to MnP crystals grown on GaP (100) at the initial stage of growth, but the excess interface/strain energies in the buried crystals (nanoclusters) limits the further growth of those orientation families and axiotaxial features. The nanoclusters of these orientation families have been suggested to disappear during the ripening of the sample, a process which has not been considered in the work of Lambert-Milot *et al.* ((Lambert-Milot, 2012),(Lambert-Milot *et al.*, 2012)).

In the multilayer samples GMP-M10 and MnP-M17 we observed a larger diffusion of Mn in GaP. The diffusion coefficient of Mn inside GaP in GMP-M10 has been estimated to be $4.0 \pm 0.3 \times 10^{-15}$ (cm^2/s) at 650 °C, which is two orders of magnitude larger than the reported value in Ref. (Kirillov *et al.* (1980)). This enhanced diffusion has been attributed to be due to larger concentration of structural defects in GaP layers that are grown on GaP:MnP layers of GMP-M10.

In MnP-M17 we observed the formation of nanoclusters rather than the expected multilayer films. This has been attributed to the potential enhanced diffusion of Mn through many structural defects in this sample.

These observations bring us one step closer to understand the texture selection and development in heterogeneous magnetic semiconductors, and clarifies how challenging it would be to control the texture.

CHAPTER 6

Extracting the magnetic size distribution of an assembly of ferromagnetic/superparamagnetic nanoparticles using magnetometry

6.1 Introduction

As it has been mentioned in Chapter 1, C. Lacroix Lacroix (2010) extracted the magnetic size of MnP nanoclusters in GaP:MnP epilayers by modeling their magnetic hysteresis loop, assuming a lognormal size distribution. His model relied on the assumption that the nanoclusters were single magnetic domains, exhibiting coherent magnetic reversal. His results showed a 50% difference between the magnetic size and physical size of the nanoclusters obtained from TEM image analysis Lambert-Milot (2012). In this chapter, we propose an alternative approach to extract the magnetic size distribution and we discuss the discrepancies between magnetic and TEM results.

TEM images have been widely used to determine the size distribution of magnetic nanoparticles, as well as their mean size and standard deviation. Measuring the dimensions of a large number of particles, one can build the size histogram of the system and fit it with some known mathematical functions (most frequently a log-normal) to obtain the size distribution and its relevant parameters. However, in some cases this technique seems to be limited and results in extracting inaccurate information. Two such limitations of TEM analysis involve the chemical nature and the shape of particles. For example :

1) A system that contains nanoparticles consisting of atoms A and B, which are in different phases, e.g. AB and A_xB_y. In this case, when counting the nanoparticles and measuring their dimensions from the TEM image, one counts and measures the dimensions of both AB and A_xB_y nanoparticles. This leads to inaccurate information, since A_xB_y nanoparticles might have a completely different mean size and size distribution than AB nanoparticles, as well as different magnetic properties.

2) A system that contains elongated nanoparticles. In this case, TEM images provide us with information regarding the projected area of the nanoparticles. The information regarding their third (in depth) dimension, must be assumed, leading to some degree of uncertainty in estimating the volume of the nanoparticles. Likewise, elongated nanoparticles with different orientations have different projected areas in the image, possibly distorting the size distribution. For instance, an ideal system containing elongated ellipsoidal nanoparticles with exactly same dimensions, which are spatially randomly oriented, will lead to a broad size distribution

of particles of different shape, ranging from spheres to elongated ellipsoids.

Using the magnetic properties of the nanoparticles to obtain their size distribution enables one to overcome some of the limitations of and to complement the TEM image analysis to some extent. El-Hilo and O'Grady El-Hilo et O'Grady (1990) presented a model that targets the magnetic properties of assemblies of ferromagnetic and superparamagnetic nanoparticles to extract their magnetic size distribution. By magnetic size, we mean the volume of a nanoparticle that is magnetically active. In their model, El-Hilo and O'Grady took into account the size distribution of nanoparticles in the equation that describes the thermoremanent magnetization (TRM) of randomly distributed (orientation) identical nanoparticles (in shape and size) proposed earlier by Tholence and Tournier Tholence et Tournier (1974). The TRM signal is the remanent magnetization of a sample measured at a specific temperature, after cooling it from above its Curie temperature (T_c) in the presence of a specific magnetic field. It is possible to determine the blocking temperature distribution of the nanoparticles from the shape of the derivative of TRM with respect to temperature, $d(TRM)/d(T)$. Due to Néel magnetic moment relaxation theory, the blocking temperature distribution is directly proportional to the size distribution of nanoparticles. Hence, one can determine the size distribution function from the blocking temperature distribution. However, their model assumes temperature independent saturation magnetization, which is not justified, especially in our case. Moreover, Néel theory is based on particles with uniaxial magnetic anisotropy, whereas our system is constituted of particles with orthorhombic anisotropy.

In this chapter we propose an alternative method for obtaining the magnetic size histogram of an assembly of oriented single domain ferromagnetic and superparamagnetic nanoparticles, whose magnetic moment reverses by coherent rotation. We show how, using our method, by measuring the magnetic field dependence of isoremanent magnetization (IRM) response at a fixed temperature and considering thermally activated magnetization reversal process, we may construct the magnetic size histogram of the nanoparticles.

The method is applied to epitaxially grown GaP films, containing epitaxial (MnP) nanoclusters, GaP:MnP. The magnetic size distribution and mean magnetic size of the nanoclusters are then extracted. In addition to possessing interesting magnetic functionalities Monette *et al.* (2010), Monette *et al.* (2012), GaP:MnP, combines the two cases addressed above, which embody the deficiencies of TEM image analyses : it contains elongated ferromagnetic and superparamagnetic MnP (with a bulk Curie temperature of 291.5 K) and anti-ferromagnetic Mn_2P nanoclusters (whose Néel temperature is $\approx$ 100 K) Lambert-Milot *et al.* (2012). This technique could be applied to any similar systems, which contain oriented magnetic nanoparticles which reverse by coherent rotation.

6.2 Theoretical background

We first introduce the concept of thermally activated magnetization reversal of the nanoparticles. Consider the simple case of an assembly of N non-interacting single domain magnetically uniform nanoparticles of volume V, all with uniaxial magnetic anisotropy, exhibiting coherent rotation magnetization reversal. By coherent rotation we mean that each particle behave as a "macrospin" with a constant magnetic moment, but with variable orientation.

For simplicity, we initially assume that the direction of the easy axis of magnetization of all the nanoparticles is along the z-direction. Then, in the absence of an external magnetic field ($H_0 = 0$) at absolute temperature $T = 0$ K, the magnetic moment (macro spin) of half of the nanoparticles is expected to be in the positive z-direction, whose state is represented by ($\uparrow$) (up-state) and the other half in the negative z-direction, ($\downarrow$) (down-state). These states represent the minima of the magnetic energy. At $H_0 = 0$, there is an energy barrier for magnetization reversal, ΔE, due to magnetic anisotropy. Figure 6.1 schematically shows the energy barrier between these two states, in the absence of applied magnetic field.

In what follows, we will consider two situations : (1) demagnetization of the system as a function of time in the absence of applied magnetic field, and (2) remagnetization of the system as a function of time in the presence of applied magnetic field.

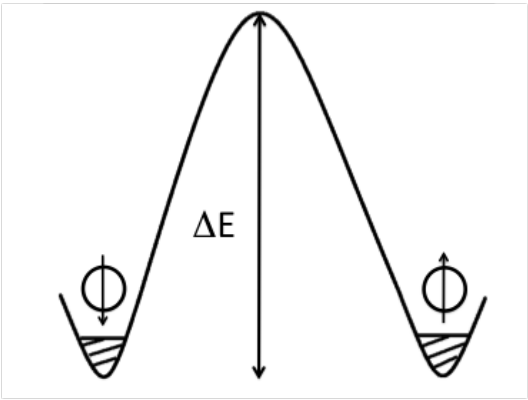

Figure 6.1 Magnetic energy of the system (vertical) as a function of the angle with respect to the z-axis (horizontal). The minima of magnetic energy in the absence of external magnetic field ($H_0 = 0$) are at -180° and 0°, corresponding to ($\downarrow$) and ($\uparrow$), respectively.

6.2.1 Demagnetization in the absence of applied magnetic field

Let us assume that the population of the two states are initially unbalanced, such that there are n^+ particles in ($\uparrow$) and n^- particles in ($\downarrow$) ($N = n^+ + n^-$). At $H_0 = 0$, at a specific

temperature T the nanoparticles in each state will gradually reverse their magnetic moment toward equilibrium (demagnetized state) with a relaxation time, τ. According to Néel Néel (1949), the relaxation time is given by

$$\tau(\Delta E, T) = f_0^{-1} \exp\left(\frac{\Delta E}{k_B T}\right), \tag{6.1}$$

where k_B is the Boltzmann constant, and f_0 is the reversal attempt frequency, which is usually taken to be in the range 10^9 to 10^{10} s^{-1} Dormann *et al.* (1997).
The rate of change of the population of each state is Dormann *et al.* (1997)

$$\frac{dn^+}{dt} = \frac{n^-}{2\tau} - \frac{n^+}{2\tau}, \tag{6.2}$$

$$\frac{dn^-}{dt} = \frac{n^+}{2\tau} - \frac{n^-}{2\tau}. \tag{6.3}$$

The total magnetic moment of the system, m_{tot}, is proportional to the difference in the number of particles in the two states, $n = n^+ - n^-$

$$m_{tot} = M_s V n, \tag{6.4}$$

where V is the volume of nanoparticles and M_s is the magnetization per unit volume of one nanoparticle at temperature T. Subtracting the two differential equations in Eqs. (6.2) and (6.3) yields an equation for $n(t)$, which is found to decay exponentially with time

$$n(t) = n(0) e^{-\frac{t}{\tau(\Delta E, T)}}. \tag{6.5}$$

Then from Eqs. (6.4) and (6.5) the total magnetic moment (demagnetization) of the system as a function of time is found to be

$$m_{tot}(\Delta E, T, t) = M_s(T) V n(0) e^{-\frac{t}{\tau(\Delta E, T)}}. \tag{6.6}$$

Eq. 6.6 tells us that the magnetic moment of the system exhibit an exponential decay as a function of time, with a characteristic relaxation depending on energy barrier and temperature. If the two states are equally populated initially, the total magnetic moment of the system will be zero, since $n(0) = 0$.

6.2.2 Remagnetization in the presence of applied magnetic field

In the presence of an applied magnetic field the magnetic energy of the system, as well as its minima will change. If we apply a magnetic field, H_0, along the easy axis in the positive z-direction, at temperature $T_0 < T_C$ to a sample, the energy barrier for magnetic moment reversal of the nanoparticles in the ($\downarrow$) and ($\uparrow$) will be (Ref. (Cullity et Graham, 2011), page 387)

$$\begin{aligned} \Delta E_{\downarrow\uparrow} &= \Delta E \left[1 - \frac{\mu_0 H_0 M_s(T)}{2\Delta E}\right]^2, \\ \Delta E_{\uparrow\downarrow} &= \Delta E \left[1 + \frac{\mu_0 H_0 M_s(T)}{2\Delta E}\right]^2, \end{aligned} \tag{6.7}$$

where μ_0 is the permeability of free space. $\Delta E_{\uparrow\downarrow}$ and $\Delta E_{\downarrow\uparrow}$ are illustrated in figure 6.2. In this case the nanoparticles in ($\uparrow$) face an increased reversal energy barrier and are in the deep minimum energy state, while the nanoparticles in ($\downarrow$) are in the shallow minimum energy state. Figure 6.2 shows the deep and shallow minima of the magnetic energy in the presence of applied magnetic field H_0, as well as the population of each state at two different times. The asymmetry of the energy barrier results in unequal reversal rates of the two states of particles, and consequently a change in the relative population of each state.

Now if we assume that there are initially $n^+(0)$ particles in ($\uparrow$) and $n^-(0)$ particles in ($\downarrow$) ($N = n^+ + n^-$ and $n(0) = n^+(0) - n^-(0)$), the rate of change of populations will be Dormann *et al.* (1997)

$$\frac{dn^+}{dt} = \frac{n^-}{\tau^-} - \frac{n+}{\tau^+}, \tag{6.8}$$

$$\frac{dn^-}{dt} = \frac{n^+}{\tau^+} - \frac{n-}{\tau^-}, \tag{6.9}$$

where

$$\tau^+ = f_0^{-1} \exp\left(\frac{\Delta E_{\uparrow\downarrow}}{k_B T}\right), \tag{6.10}$$

$$\tau^- = f_0^{-1} \exp\left(\frac{\Delta E_{\downarrow\uparrow}}{k_B T}\right). \tag{6.11}$$

By subtracting Eqs. (6.8) and (6.9) and rearranging the terms, we find an equation for the time evolution of n

$$\frac{dn}{dt} = \frac{NP - n}{\tau}, \tag{6.12}$$

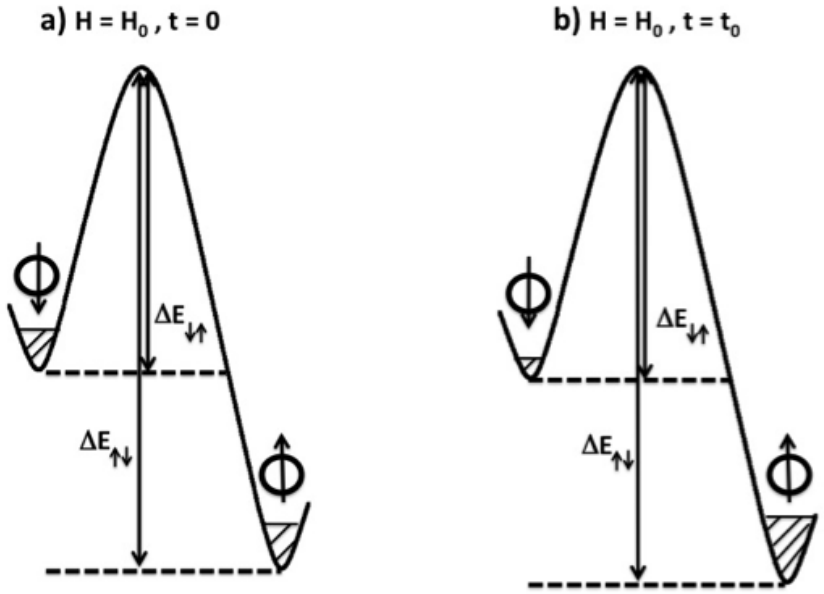

Figure 6.2 Schematic diagrams of the magnetic energy and its deep and shallow minima in applied field H_0. The figure shows the change in populations of (↑) and (↓) a) right after the field is applied and b) some time (t_0) after it is applied.

where

$$P(\Delta E, H_0, T) = \frac{\tau^+ - \tau^-}{\tau^+ + \tau^-}, \tag{6.13}$$

and

$$\frac{1}{\tau(\Delta E, H_0, T)} = \frac{1}{\tau^+} + \frac{1}{\tau^-}. \tag{6.14}$$

Solving Eq. (6.12), we obtain

$$n(t) = \left[[n(0) - NP]e^{\frac{-t}{\tau}} + NP\right]. \tag{6.15}$$

Comparing Eqs. (6.15) and (6.5) indicates that P is the fraction of nanoparticles that will be in the (↑) state, as $t \to \infty$. This occurs due to the asymmetry of the energy barrier, as seen by the nanoparticles in the (↑) and (↓) states. Using Eq. 6.4 we can describe the total magnetic moment (remagnetization) of the system

$$m_{tot}(t, H_0, T) = M_s(T)V\left[(n(0) - NP)e^{\frac{-t}{\tau}} + NP\right], \tag{6.16}$$

or more explicitly

$$m_{tot}(t, H_0, T) = M_s(T)VN\left[(\frac{n^+ - n^-}{n^+ + n^-} - \frac{\tau^+ - \tau^-}{\tau^+ + \tau^-})e^{\frac{-t}{\tau}} + \frac{\tau^+ - \tau^-}{\tau^+ + \tau^-}\right], \tag{6.17}$$

which can also be presented more compactly as

$$m_{tot}(t, H_0, T) = m_\infty + (m_0 - m_\infty)e^{\frac{-t}{\tau}}. \tag{6.18}$$

In Eq. 6.18, $m_0 = M_sVn(0)$ is the initial total magnetic moment of the system and $m_\infty = M_sVNP$ is the total magnetic moment of the system as $t \to \infty$ (thermal equilibrium). By introducing $m_{sat} = M_sVN$ as the total magnetic moment of the system when all the nanoparticles are aligned at a given temperature, we will have $m_\infty = m_{sat}P$. As calculated by substituting Eq. (6.7) into Eqs. (6.10) and (6.11) and then into Eq. (6.13), the fraction of the moment accumulation as $t \to \infty$ can be written as

$$P(\Delta E, H_0, T) = \frac{\tau^+ - \tau^-}{\tau^+ + \tau^-} = tanh\left[\frac{\mu_0 M_s V H_0}{k_B T}\right]. \tag{6.19}$$

For the range of parameters used in this work (will be presented in Section 6.3), we obtain $\frac{\mu_0 M_s V H_0}{k_B T} \approx 10$, which gives $P \approx 1$.

6.2.3 Volume distribution of particles

Now consider a system containing an ensemble of nanoparticles with an energy barrier distribution $f(\Delta E)$, where $\int_0^\infty f(\Delta E)dE = 1$. $f(\Delta E)dE$ is the fraction of nanoparticles that face an energy barrier distribution between ΔE and $\Delta E + dE$. Then, the total magnetic moment of the system in the remagnetization condition will change to

$$m_{tot}(t) = m_{sat}\int_0^\infty [(\frac{n(0)}{N} - P)e^{-\frac{t}{\tau(\Delta E)}} + P]f(\Delta E)dE. \tag{6.20}$$

The magnetic moment in the demagnetization condition can be found by substituting $H_0 = 0$ in Eq. (6.19), yielding $P = 0$ in Eq. (6.20).

Now, assuming a coherent magnetic moment reversal for the nanoparticles, their reversal energy barriers will be directly proportional to their volume

$$\Delta E = K(T)V, \tag{6.21}$$

where $K(T)$ is the temperature dependent magnetic anisotropy constant (J/m^3), assumed to be the same for all nanoparticles (typical values on the order of $10^5 - 10^6$ J/m^3 for our materials). We further assume that the volume distribution of particles is $f(V)$, where $\int_{V_1}^{V_2} f(V)dV$ is the probability that a particle has a volume $V_1 \leq V \leq V_2$. Following this assumption, the magnetic moment of the system in the remagnetization conditions, for a given T_0 and H_0, is given by

$$m_{tot}(t) = M_s \int_0^{\infty} [(n(0) - NP)e^{-\frac{t}{\tau(V)}} + NP]Vf(V)dV, \tag{6.22}$$

which is also valid for demagnetization, provided we set $P = 0$. The exponential term in Eq. (6.22) is extremely sensitive to volume at $t \approx \tau(V)$. Figure 6.3 illustrates the rapid change of $\tau(V)$ and $exp(-\frac{t}{\tau(V)})$ at $t \approx \tau(V)$ for different time intervals, during which the magnetic field is applied (t = 1 s, 90 s, and 1 day) for MnP nanoclusters embedded in GaP:MnP epilayer grown at 650 °C during 45 minutes. For figure 6.3 (a), $\tau(V)$ has been calculated using Eqs. (6.14) and (6.7), but with energy barrier that is calculated, as explained in Section 6.3.

The energy barrier density of the nanoclusters has been calculated at 260 K at zero applied field and the values of the magnetocrystalline anisotropies and of M_s, reported in Table 6.1, are taken from Ref. Lacroix (2010) (the calculations are addressed in Section 6.3).

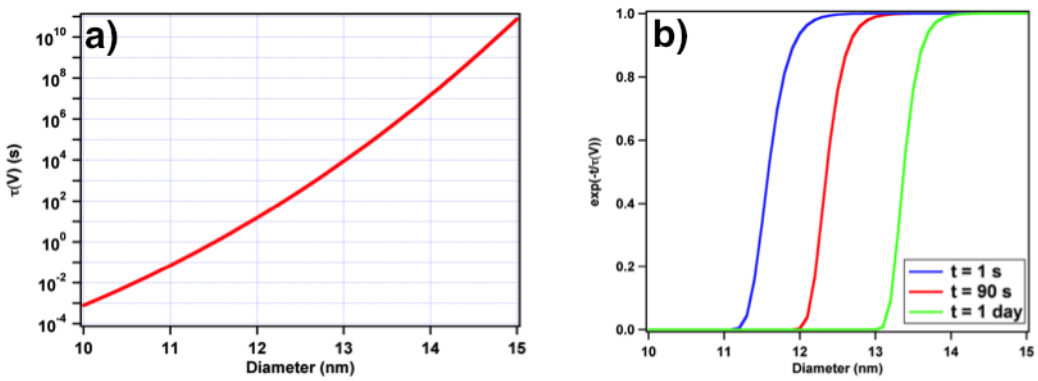

Figure 6.3 a) Rapid variation of $\tau(V)$ as a function of the diameter of MnP nanoclusters in GMP-650-45 and b) rapid variation of the exponential term in Eq. (6.22) as a function of the diameter of the nanoclusters, for different time constants (t = 1 s, 90 s, and 1 day). The exponential term could be fairly approximated with a step function. The energy barrier density of the clusters has been calculated at 260 K at zero applied field. The diameter has been calculated assuming spherical nanoclusters.

Based on figure 6.3, it is reasonable to simplify Eq. (6.22) by approximating the exponen-

Table 6.1 Anisotropy fields and saturation magnetization of GaP:MnP at different temperatures Lacroix (2010).

	T = 240 K	**T = 260 K**	**T = 280 K**
H_{a1} (MA/m)	2.5	2.2	1.8
H_{a2} (MA/m)	0.78	0.7	0.65
M_s (kA/m)	313	283	228

tial function with a step function : for $t/\tau(V_c) > 1$ it has a value of zero and for $t/\tau(V_c) < 1$ it has a value of 1, where V_c is the volume of the nanoparticle for which $t = \tau(V_c)$. Using Eqs. (6.7), (6.10), (6.11), and (6.14), we can find V_c by solving

$$\frac{1}{t} = \frac{1}{f_0^{-1}\exp\left(\frac{KV_c}{k_BT}(1+h)^2\right)} + \frac{1}{f_0^{-1}\exp\left(\frac{KV_c}{k_BT}(1-h)^2\right)} \tag{6.23}$$

where $h = \frac{H_0}{H_K}$ and $H_K = \frac{2K}{\mu_0 M_s}$. Defining $V_0 = \frac{k_BT}{2K}$ and rearranging Eq. (6.23), we obtain

$$\frac{V_c}{V_0}(\frac{1+h^2}{2}) = ln(f_0 t) + ln\left[2cosh(\frac{V_c}{V_0}h)\right]. \tag{6.24}$$

Considering the typical values of V_0 (for our samples $\approx 10^{-27}$ nm^3), h (≈ 0.1), and V_c (assuming to be $\approx 10^{-24}$ nm^3 for a nanoparticle with radius 10 nm), we obtain $\frac{V_c}{V_0}h \gg 1$ and consequently

$$\lim_{\frac{V_c}{V_0}h\to+\infty} ln\left[2cosh(\frac{V_c}{V_0}h)\right] = \frac{V_c}{V_0}h, \tag{6.25}$$

which results in

$$V_c(h,T,t) = \frac{2V_0}{(1-h)^2}ln(f_0 t). \tag{6.26}$$

Figure 6.3 indicates that V_c slightly changes as we change the time interval (t), during which the magnetic field is applied. For example, as we change t from 1 second to 1 day, d_c changes from ≈ 11.5 to ≈ 13.5 (d_c is the critical diameter of the nanoparticle for which $t = \tau(d_c)$).

If we replace $exp(-\frac{t}{\tau(V)})$ by the step function in Eq. (6.22), we obtain

$$m_{tot}(t) = \int_0^{V_c} M_s NPVf(V)dV + \int_{V_c}^{\infty} M_s n(0)Vf(V)dV. \tag{6.27}$$

Taking $P = 1$ (which was justified earlier) we obtain

$$m_{tot}(t) = \int_0^{V_c} M_s NV f(V)dV + \int_{V_c}^{\infty} M_s n(0) V f(V)dV, \tag{6.28}$$

which can also be presented as

$$m_{tot}(t) = \frac{n(0)}{N} \int_0^{\infty} M_s NV f(V)dV + (1 - \frac{n(0)}{N}) \int_0^{V_c} M_s NV f(V)dV, \tag{6.29}$$

or equivalently

$$m_{tot}(t) = m_{tot}(0) + [m_{sat} - m_{tot}(0)] \frac{\int_0^{V_c} V f(V)dV}{\int_0^{\infty} V f(V)dV}. \tag{6.30}$$

If we apply a magnetic field to a demagnetized sample, in which the ($\uparrow$) and ($\downarrow$) states are equally populated initially ($n(0) = 0$), after a time t we will measure the total magnetic moment to be

$$m_{tot}(t) = \int_0^{V_c} M_s NV f(V)dV, \tag{6.31}$$

which is the sum of the magnetic moments of the nanoparticles with volume $V \leq V_c$.

Now if we remove this magnetic field, we will have $\tau^+ = \tau^-$, hence $P = 0$ (from Eq. (6.13). If we measure the total magnetic moment of the sample at a time t' after suppressing the field, using Eq. (6.27) we obtain

$$m_{tot}(t') = \int_{V_{sp}}^{\infty} M_s n(t) V f(V)dV, \tag{6.32}$$

which could be written as

$$m_{tot}(t') = \int_0^{\infty} M_s n(t) V f(V)dV - \int_0^{V_{sp}} M_s n(t) V f(V)dV, \tag{6.33}$$

or

$$m_{tot}(t') = m_{tot}(t) - \int_0^{V_{sp}} M_s n(t) V f(V) dV, \tag{6.34}$$

where

$$V_{sp}(t', T) = 2V_0 ln(t' f_0). \tag{6.35}$$

The second term in Eq : (6.34) is the demagnetization due to the nanoparticles that are in *superparamagnetic* state.

6.3 Description of the method

In this section we describe our method for extracting the magnetic size distribution of fine particles from IRM measurements. The IRM signal is the total magnetic moment of the system, which is measured $t^{'}$ seconds after suppressing the magnetic field H_0, which was applied during t seconds to the demagnetized sample (described in Section 3.4).

Figure 6.4 shows the change of total magnetic moment, the temperature, and the applied magnetic field as a function of time. To measure the IRM signal of the system, we first increase the temperature of the sample from room temperature (RT) to a temperature above its Curie temperature, T_c, to destroy its magnetic history. Then we decrease it to the desired temperature, T_1, below T_c. This process is known as zero-field cooling (ZFC). We keep the temperature constant for the rest of an experiment. Then (at time t_1) we apply the magnetic field, H_1, during $t = t_2 - t_1$ and then remove it (at time t_2). Since we will not focus on the effect of rate of change of magnetic field on magnetization, we assume that the magnetic field increases from 0 to H_1 instantly (and so does the temperature). After suppressing the magnetic field, we wait $t^{'} = t_3 - t_2$ and then measure the magnetic moment (at time t_3).

When we increase the temperature above T_c at $H_0 = 0$, the average magnetic moment is zero (from time t_0 to t_1). Then we cool the sample to T_1 from t_0 to t_1 keeping the external field $H_0 = 0$. Then by applying a magnetic field H_1 (at time t_1) we alter the magnetic moment reversal energy barriers for the nanoparticles in ($\uparrow$) and ($\downarrow$).

We wait for $t = t_2 - t_1$, after which we remove the magnetic field. During this time interval, the total magnetic moment of the system, $m_{tot}(H_1)$ (shown in figure 6.4) is the sum of the

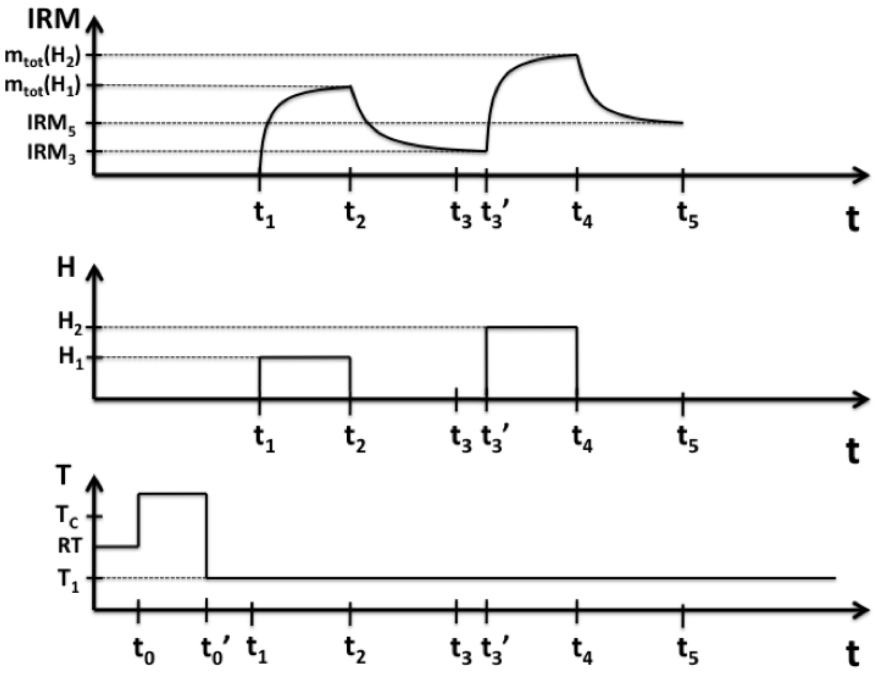

Figure 6.4 Isoremanent magnetization, temperature of experiment, and applied magnetic field as a function of time during ZFC process and IRM measurement.

magnetic moment of nanoparticles with $V \leq V_c(H_1, t, T)$ (Eq. (6.31))

$$m_{tot}(H_1, t, T) = \int_0^{V_c(H_1,t,T)} M_s N V f(V) dV, \tag{6.36}$$

which can also be presented as

$$m_{tot}(H_1, t, T) = \int_0^{\infty} M_s n(t) V f(V) dV = \frac{n(t)}{N} \int_0^{\infty} M_s N V f(V) dV = \frac{n(t)}{N} m_{sat}. \tag{6.37}$$

From Eq. (6.37) we obtain

$$n(t) = \frac{N}{m_{sat}} m_{tot}(H_1, t, T) = \frac{N}{m_{sat}} \int_0^{V_c(H_1,t,T)} M_s N V f(V) dV. \tag{6.38}$$

After we remove the magnetic field the nanoparticles in ($\uparrow$) and ($\downarrow$) will face the same energy barrier ($P = 0$). The total magnetic moment of the system measured after a time

$t^{'} = t_3 - t_2$, $IRM(H_1, t', T)$ (IRM_3 in Fig. 6.4), is described by (Eq. (6.34))

$$IRM(H_1, t', T) = \int_{V_{sp}}^{\infty} M_s n(t) V' f(V') dV'. \tag{6.39}$$

Substituting Eq. (6.38) into Eq. (6.39) we obtain :

$$IRM(H_1, t', T) = \frac{M_s^2}{m_{sat}} \int_0^{V_c(H_1,t,T)} VNf(V) \left[\int_{V_{sp}}^{\infty} NV' f(V') dV' \right] dV, \tag{6.40}$$

which could be written as

$$IRM(H_1, t', T) = m_{sat} \left[\frac{\int_0^{V_c(H_1,t,T)} VNf(V)dV}{\int_0^{\infty} VNf(V)dV} \right] \left[\frac{\int_{V_{sp}}^{\infty} VNf(V)dV}{\int_0^{\infty} VNf(V)dV} \right]. \tag{6.41}$$

Taking

$$g(V_c(H_1, t, T)) = \left[\frac{\int_0^{V_c(H_1,t,T)} VNf(V)dV}{\int_0^{\infty} VNf(V)dV} \right], \tag{6.42}$$

to be the fraction of the nanoparticles with $V \leq V_c(H_1, t, T)$ and

$$1 - g(V_{sp}) = \left[\frac{\int_{V_{sp}}^{\infty} VNf(V)dV}{\int_0^{\infty} VNf(V)dV} \right], \tag{6.43}$$

we obtain

$$g(V_c(H_1, t, T)) = \frac{IRM(H_1, t', T)}{m_{sat}[1 - g(V_{sp})]}. \tag{6.44}$$

If we apply a large magnetic field ($H \to \infty$) to saturate the system, and measure the isore-

manent magnetization after time interval t', we obtain

$$IRM(\infty, t', T) = \int_{V_{sp}}^{\infty} VNf(V)dV, \tag{6.45}$$

which can be written as

$$IRM(\infty, t', T) = \int_{0}^{\infty} VNf(V)dV - \int_{0}^{V_{sp}} VNf(V)dV = m_{sat}(1 - g(V_{sp})). \tag{6.46}$$

Replacing Eq. (6.46) into Eq. (6.44) we obtain the fraction of the nanoparticles with $V \leq V_c(H_1, t, T)$

$$g(V_c(H_1, t, T)) = \frac{IRM(H_1, t', T)}{IRM(\infty, t', T)}. \tag{6.47}$$

$IRM(H_1, t', T)$ and $IRM(\infty, t', T)$ in Eq. (6.47) are both measured experimentally (isoremanent magnetization), thus we can determine $g(V_c(H_1, t, T))$.

If we repeat this procedure with applied magnetic field, H_2 (applied for $t = t_4 - t_3$, and measure the total magnetic moment after $t' = t_5 - t_4$, $IRM(H_2, t', T)$ (IRM_5 in figure 6.4), we can determine $g(V_c(H_2, t, T))$ experimentally

$$g(V_c(H_2, t, T)) = \frac{IRM(H_2, t', T)}{IRM(\infty, t', T)}. \tag{6.48}$$

which is the fraction of the nanoparticles with $V \leq V_c(H_2, t, T)$. By subtracting $g(V_c(H_1, t, T))$ from $g(V_c(H_2, t, T))$ we can obtain the fraction of the nanoparticles with $V_c(H_1, t, T) \leq V \leq V_c(H_2, t, T)$.

$$g(V_c(H_2, t, T)) - g(V_c(H_1, t, T)) = \frac{IRM(H_2, t', T) - IRM(H_1, t', T)}{IRM(\infty, t', T)}. \tag{6.49}$$

At fixed temperature, by determining the relative difference in consecutive IRM signals from the magnetic field dependence of the IRM response (IRM vs. H) we can obtain the fraction of the nanoparticles within different volume ranges. This allows us to build the magnetic size histogram of the nanoparticles and extract the magnetic size distribution function, as well as the mean magnetic size and standard deviation of the nanoparticles.

6.4 Application of the method to GaP:MnP

In this section, we apply the method described in the previous section to determine the magnetic size distribution of elongated single domain Lacroix (2010) MnP nanoclusters embedded in GaP matrices grown on GaP (100) substrate. We first verify the consistency of our method, by comparing the magnetic size distribution of GMP-650-45 obtained at three different temperatures, $T = 240, 260$, and 280 K (T_c of MnP is ≈ 291 K). The method will be further validated by simulating the magnetic hysteresis curve of GMP-650-45 at $T = 240$ K, using the magnetic size distribution obtained for this sample. Finally, we compare the magnetic size distributions of GaP:MnP epilayers grown at 600°C (GMP-600-45), 650°C (GMP-650-45), and 700°C (GMP-700-45) with those obtained from TEM image analysis.

6.4.1 Magnetic size distribution of GaP:MnP

Figure 6.5 presents the cross-sectional TEM image of GMP-650-45, showing the nanoclusters in the GaP matrix. XRD pole figure analysis of the samples confirmed the presence of Mn_2P in GMP-650-45 and GMP-700-45, but not in GMP-600-45 Lambert-Milot (2012). Since Mn_2P is antiferromagnetic with a Néel temperature of 100 K, it does not contribute to the magnetic moment signal that we measured at the temperatures reported in this section.

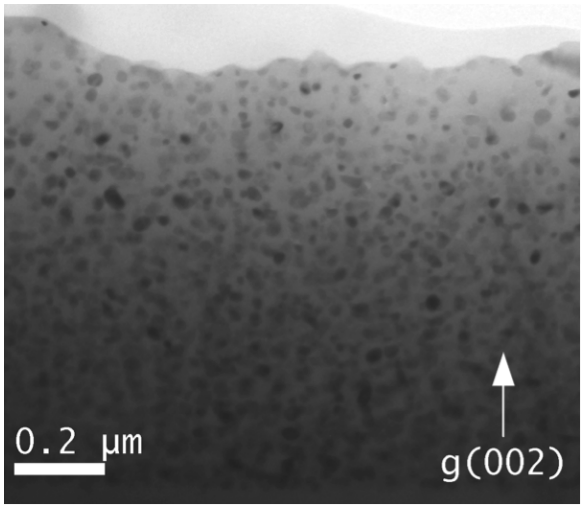

Figure 6.5 Bright field cross-sectional TEM image of GaP:MnP grown at 650°C.

To apply our method for GaP:MnP system we have made some assumptions :
(1) Based on the size range of the nanoclusters obtained from TEM analysis (13-88 nm), calculation show that they are likely to be single domain Lacroix (2010), and we assume that the nanoclusters exhibit coherent rotation magnetization reversal.

(2) We assume that the nanoclusters are non-interacting, since the magnetocrystalline anisotropy energy of the nanoclusters has been determined to be much larger than the dipole-dipole interaction energy Lacroix (2010). Other anisotropy terms such as surface anisotropy, shape anisotropy, and magneto-elastic anisotropy may also have a small contribution to the total measured anisotropy. anisotropy Lacroix (2010).
(3) We also assume that all clusters have the same saturation magnetization (the value for bulk MnP Lacroix (2010), Huber Jr et Ridgley (1964)) and the same anisotropy constants.
(4) Finally, we assume that the orthorhombic the energy barrier for magnetic moment reversal of the MnP nanoclusters is directly proportional to their volume, thus the energy density for magnetic moment reversal of a nanocluster is assumed to be : $\Delta\varepsilon = \frac{\Delta E}{V}$. $\Delta\varepsilon$ is equivalent to an effective K in Eq. (6.21).

The anisotropy constants of orthorhombic MnP nanoclusters have been extracted from the hysteresis curves of the samples obtained at different temperatures Lacroix (2010). The resulting anisotropy fields, $H_{a_i} = \frac{2K_i}{\mu_0 M_s}(i = 1, 2)$, and the magnetic saturation at three different temperatures are presented in Table 6.1.

Angle dependent ferromagnetic resonance studies Lacroix (2010), in agreement with the results of XRD pole figure analyses Lambert-Milot (2012) have determined the epitaxial orientations of the nanoclusters with respect to GaP matrix. Since the easy axis of magnetization of MnP is along its c-axis (with $a > b > c$ convention) and we are interested in the magnetic properties of our samples, we categorized the nanoclusters in six different magnetic orientation families, O_1 to O_6. The nanoclusters in a family of orientation (e.g. O_1) have their c-axis along the same direction. Figure 6.6 represents the directions of MnP c-axis of six families of orientations with respect to GaP [100].

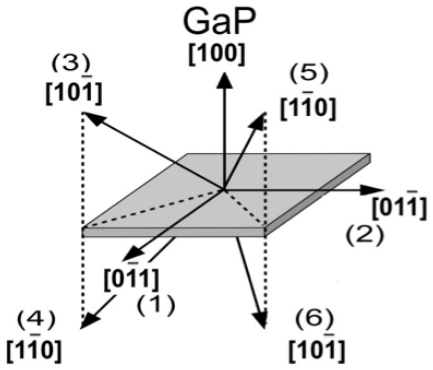

Figure 6.6 Easy axes of magnetization (c-axis) of MnP nanoclusters with respect to GaP [100].

To apply our method on this system according to figure 6.6, we should apply the magnetic

field in the direction of GaP [100] and measure the isoremanent magnetization of the system in the direction of surface normal (GaP [100]). This way, orientation families O_1 and O_2 will not contribute to the remanent signal. Moreover, orientation families O_3 to O_6 will be equivalent, since their easy axis of magnetization makes an angle of 45° with the surface normal. This enables us to determine the size distribution of the clusters in orientation families O_3 to O_6 and then generalize it for the whole system, assuming that all orientation families have the same size distribution.

Now we need to determine the limits of the integral (critical volumes) using Eq. (6.26) (by taking $t = t' = 90$ s, as described in Chapter 3, Section 3.4). To do so, we first need to find the reversal energy barrier density at different applied magnetic fields. Considering a biaxial magnetic anisotropy for orthorhombic MnP, the magneic energy density of a MnP nanocluster at an applied magnetic field H_0 (schematically shown in figure 6.7) can be found from Lacroix (2010)

$$\begin{aligned}\epsilon = &-M_s H_0[sin\theta sin\theta_H cos(\phi - \phi_H) + cos\theta cos\theta_H], \\ &+ \sum_{m=1}^{2} K_i[sin\theta sin\theta_{ci} cos(\phi - \phi_{ci}) + cos\theta cos\theta_{ci}]^2. \end{aligned} \tag{6.50}$$

The saturation magnetization, M_s, and anisotropy constant, $K_i = \frac{\mu_0 M_s}{2} H_{ai}$ have been obtained from Table 6.1.

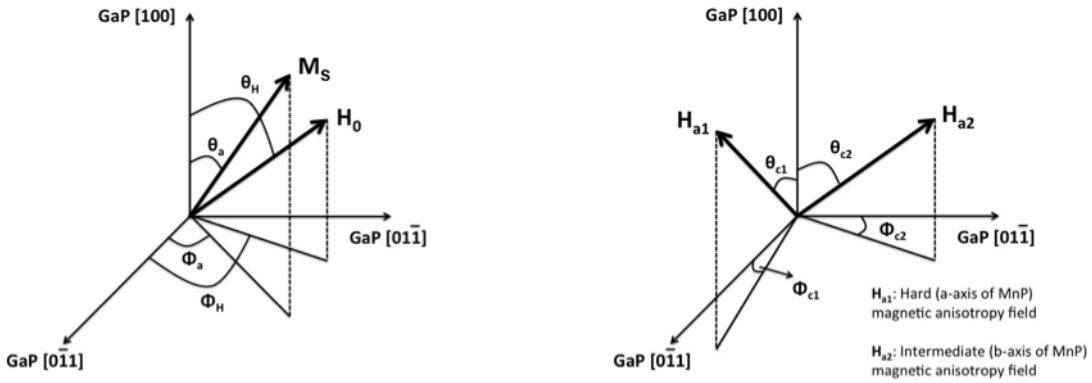

Figure 6.7 Magnetic field H_0 applied at an arbitrary angle θ_H with respect to GaP [100]. The Hard (a-axis of MnP) and intermediate (b-axis of MnP) anisotropy fields of a MnP (orthorhombic with convention a > b > c) nanocluster are also shown in the figure.

To measure the IRM response of our samples, we applied the magnetic field along GaP [100], hence $\theta_H = \phi_H = 0$ (orientation families O_1 and O_2 do not contribute to the remanent signal). The angles θ_{ci} and ϕ_{ci} for orientations O_3 to O_6 are presented in Table 6.2.

Table 6.2 The angles θ_{ci} and ϕ_{ci} for orientations O_3 to O_6 Lacroix (2010).

Angle	O_3	O_4	O_5	O_6
θ_{c1}	35.3	144.7	114.1	65.9
θ_{c2}	125.3	54.7	54.7	54.7
ϕ_{c1}	90	90	71.6	108.43
ϕ_{c2}	90	90	0	0

Figures 6.8 and 6.9 show the energy density minima, maximum, and saddle point for GMP-650-45, at $H_0 = 0$ and $H_0 = 159kA/m(2000Oe)$ in the 3D and contour graph of energy density. To plot the energy density as a function of angle we have used the values of the magnetocrystalline anisotropy constants and saturation magnetization from Table 6.1. The energy density of MnP as a function of θ_a and ϕ_a has been described in more detail in Ref. Lacroix (2010).

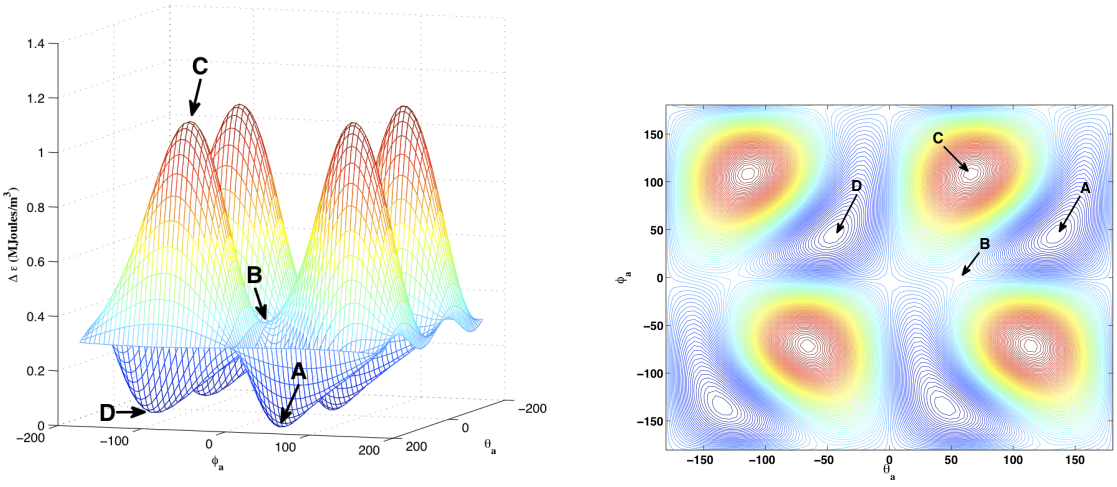

Figure 6.8 a) 3D representation of the magnetic energy density of GaP:MnP at $H_0 = 0$. Points A, D, B, and C represent local minima, saddle point, and maximum of the energy density, respectively. b) Contour graph of the magnetic energy density of GaP:MnP at $H_0 = 0$. The points A, B, C, D are the same as shown in part (a). The blue color represents the lowest and the red color indicates the highest value of the energy density.

The minima (A) and (D) in figures 6.8 and 6.9 are equivalent to $(\uparrow)$ and $(\downarrow)$ described earlier in this chapter. For the magnetic moment reversal process, we suggest the route $A \rightarrow B \rightarrow D$ in figure 6.9. Since the reversal energy barrier for this route is smallest, it will be the favorable route for magnetization reversal. The minima of energy have been found numerically using the function "fminunc" of MATLAB, which finds the local minima of a

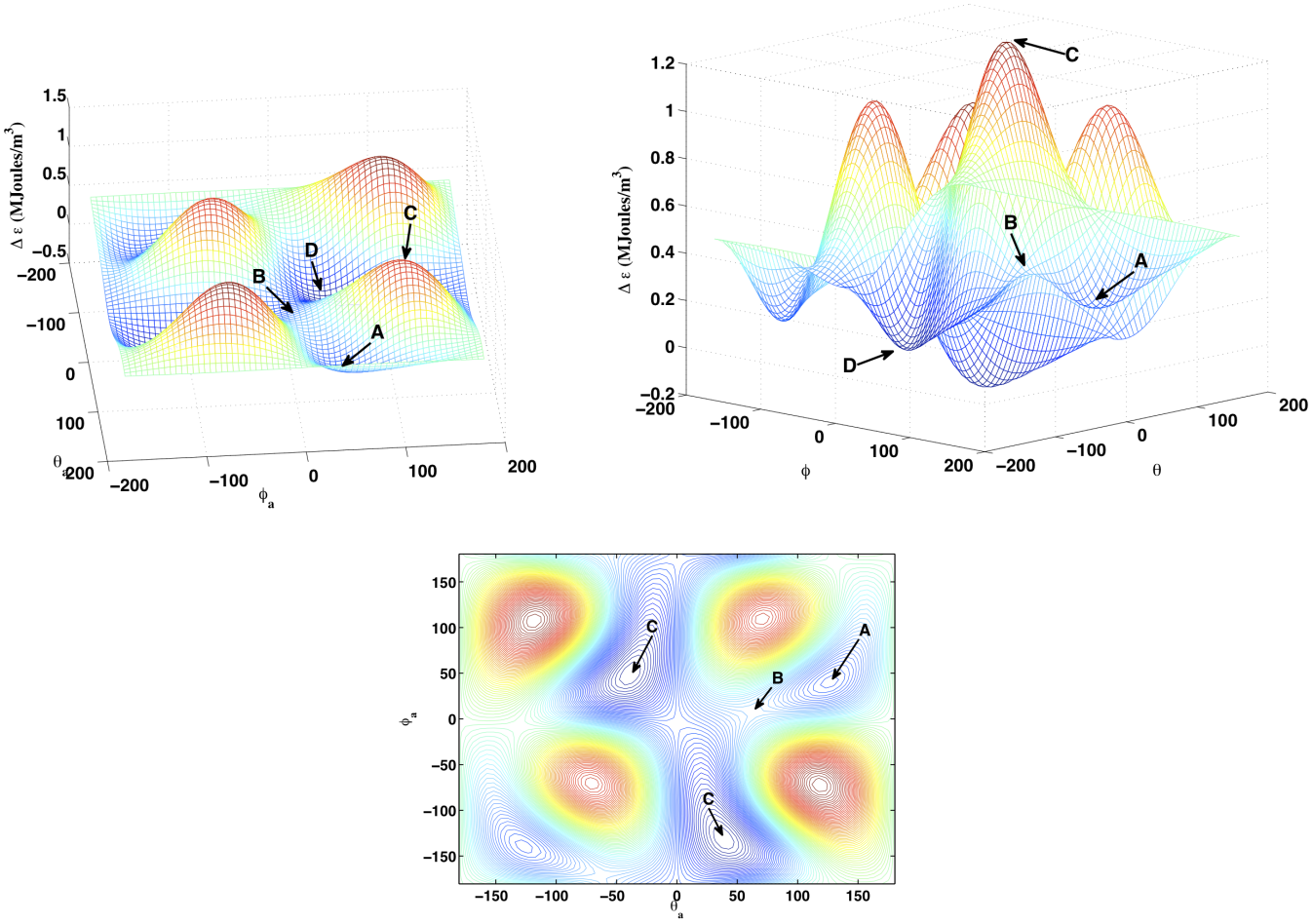

Figure 6.9 3D representation of the magnetic energy density of GaP:MnP at $H_0 = 159kA/m(2000Oe)$. Points A, D, B, and C represent the local minima, saddle point, and maximum of the energy density, respectively. b) Same graph as in (a), but from a different point of view. c) Contour graph of the magnetic energy density of GaP:MnP at $H_0 = 159kA/m(2000Oe)$.

multivariable function, and the saddle points have been found from the contour graphs.

After the energy density barriers at different applied magnetic fields were determined ($\Delta\varepsilon_{\downarrow\uparrow}$), the critical volumes, $V_c(H, t, T)$, were found using Eq. (6.26).

6.4.2 Validation of the method

Figure 6.10 shows the IRM response of GMP-650-45 obtained at T = 280 K at different applied magnetic fields.

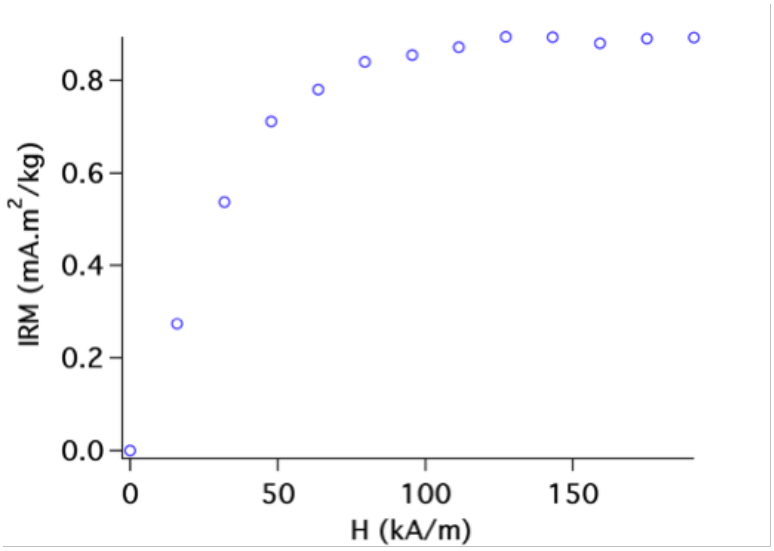

Figure 6.10 The IRM response of GMP-650-45 at T = 280 K.

$$f(V) = \frac{1}{V\sigma\sqrt{2\pi}} exp(-\frac{(lnV-\mu)^2}{2\sigma^2}),$$
$$\text{with} \qquad m_p = exp(\mu + \frac{\sigma^2}{2}), \tag{6.51}$$
$$\text{and} \qquad s = exp(\mu + \frac{\sigma^2}{2})\sqrt{exp(\sigma^2)-1}.$$

We have extracted the fraction of the nanoparticles in different volume ranges from figure 6.10 using Eq. (6.49). Figure 6.11 shows the magnetic size histogram and the corresponding lognormal fit of GMP-650-45 at 240, 260, and 280 K. The lognormal function, described in Eq. (6.51), in which m_p and s are the mean size and standard deviation of the lognormal distribution, was found to provide reasonably good fits to the magnetic size histograms. Table 6.3 compares the mean magnetic diameter and standard deviation of the nanoclusters at these three temperatures. The result shows that the parameters obtained at three different temperatures are fairly similar (within 10% of error).

Table 6.3 Extracted parameters from the lognormal fit of magnetic size histogram of GMP-650-45 obtained at 240, 260, and 280 K.

Temperature (K)	**Apparent mean magnetic diameter (nm)**	**Standard deviation(nm)**
240	11.8	0.08
260	12.2	1.1
280	13.2	0.05

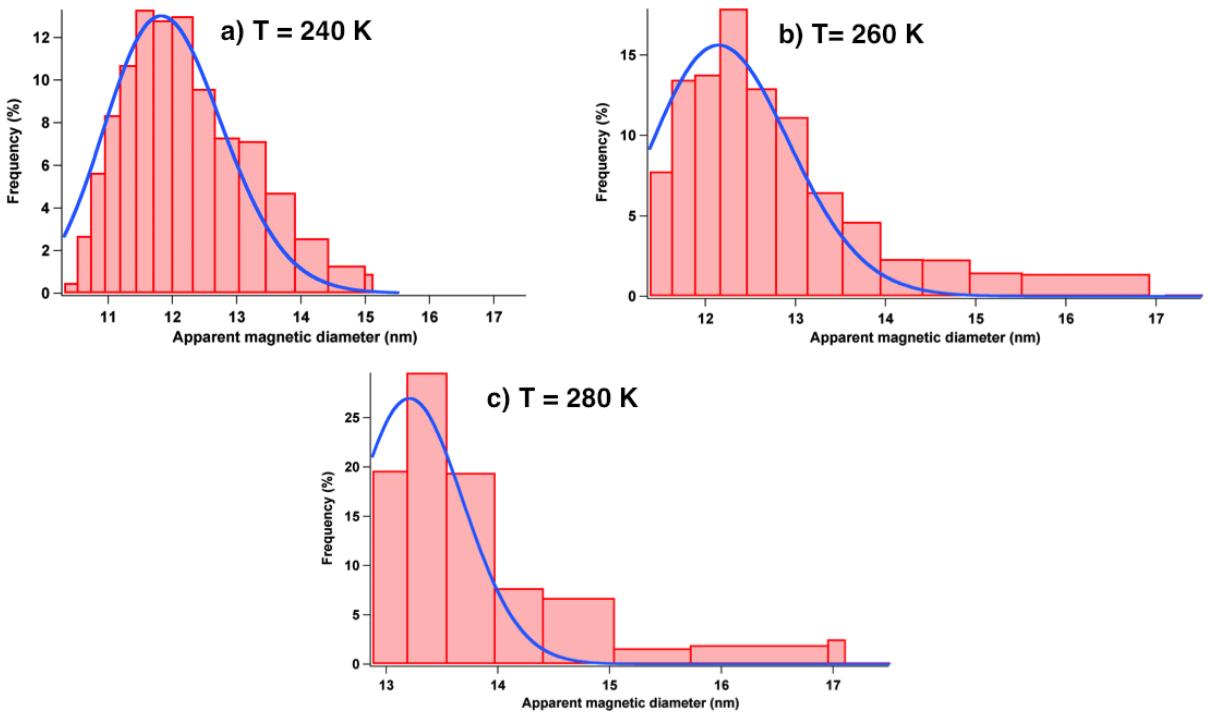

Figure 6.11 The magnetic size histogram of GMP-650-45 and its lognormal fit obtained at a) 240 K, b) 260 K, and c) 280 K.

The difference in the parameters reported in Table 6.3 could be attributed to the uncertainty in extracting the anisotropy fields and magnetic saturation at different temperatures (which was not quantified in Ref. Lacroix (2010)).

To further validate our model, we have simulated the hysteresis curve of GMP-650-45 at 240 K following Lacroix (2010), assuming a lognormal distribution with the mean magnetic size and standard deviation reported in Table 6.3. The simulation is done based on calculating the magnetization of the system at different applied magnetic fields, considering thermal fluctuation. The magnetization at different magnetic fields has been found from the volume fraction of the nanoparticles that contribute to the signal (as disscussed in Section 6.3). The result, presented in figure 6.12, shows excellent agreement between experiment and model.

6.4.3 Magnetic size distribution of GaP:MnP grown at different temperatures

Figure 6.13 shows the magnetic size histogram of our three GaP:MnP, as well as the size histogram obtained from TEM, which are fitted with lognormal function. In Table 6.4 the mean size and standard deviation extracted from the fits are compared to those obtained from TEM analyses. the apparent magnetic diameter (reported in Table 6.4) has been calculated,

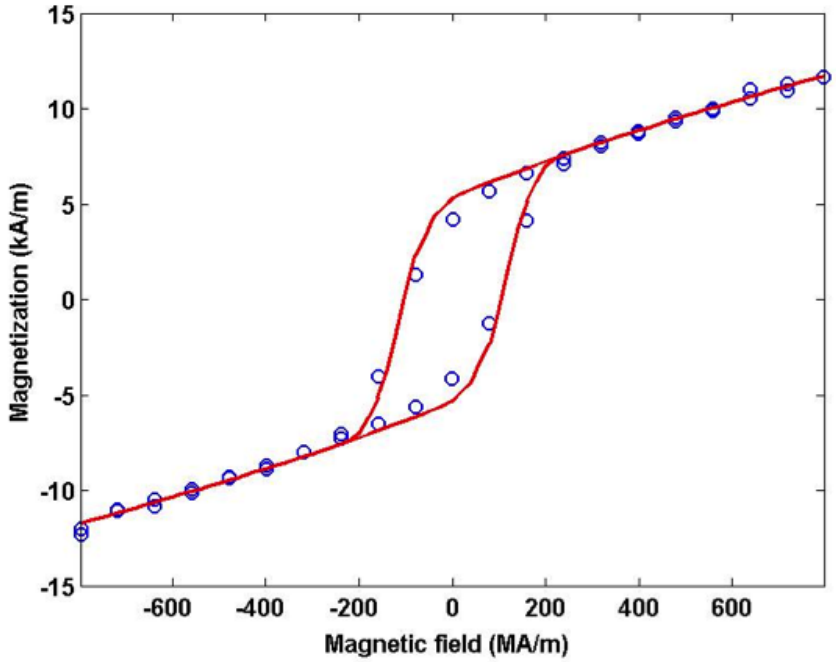

Figure 6.12 Magnetic hysteresis curve of GMP-650-45 obtained at 240 K, while the magnetic field was applied parallel to sample's normal (GaP [100]). The blue dots show the experimental data and the red line shows the result of simulation using the parameters presented in Table 6.3.

assuming spherical nanoclusters.

Table 6.4 Mean effective diameter (m) and standard deviation (s) extracted from the lognormal fit of the magnetic size histogram and TEM size histogram.

	Magnetic size histogram		**TEM size histogram**	
Sample	**m (nm)**	**s (nm)**	**m (nm)**	**s (nm)**
GMP-600-45	13.0	0.07	16.9	0.56
GMP-650-45	13.2	0.05	22.6	0.41
GMP-700-45	13.5	0.15	26.2	0.42

Table 6.4 shows that the mean magnetic sizes of MnP nanoclusters are fairly similar and significantly smaller than the mean physical size of the nanoclusters obtained from TEM image. We also realize that the difference (%) of magnetic size and physical size increases with growth temperature, from $\approx$ 23% smaller magnetic size in GMP-600-45 to $\approx$ 48% smaller magnetic size in GMP-700-45. As the volume (%) of Mn_2P in the epilayers increases at higher growth temperatures Lambert-Milot (2012), the larger difference (%) at higher growth temperatures implies that Mn_2P nanoparticles are possibly larger than MnP nanoclusters.

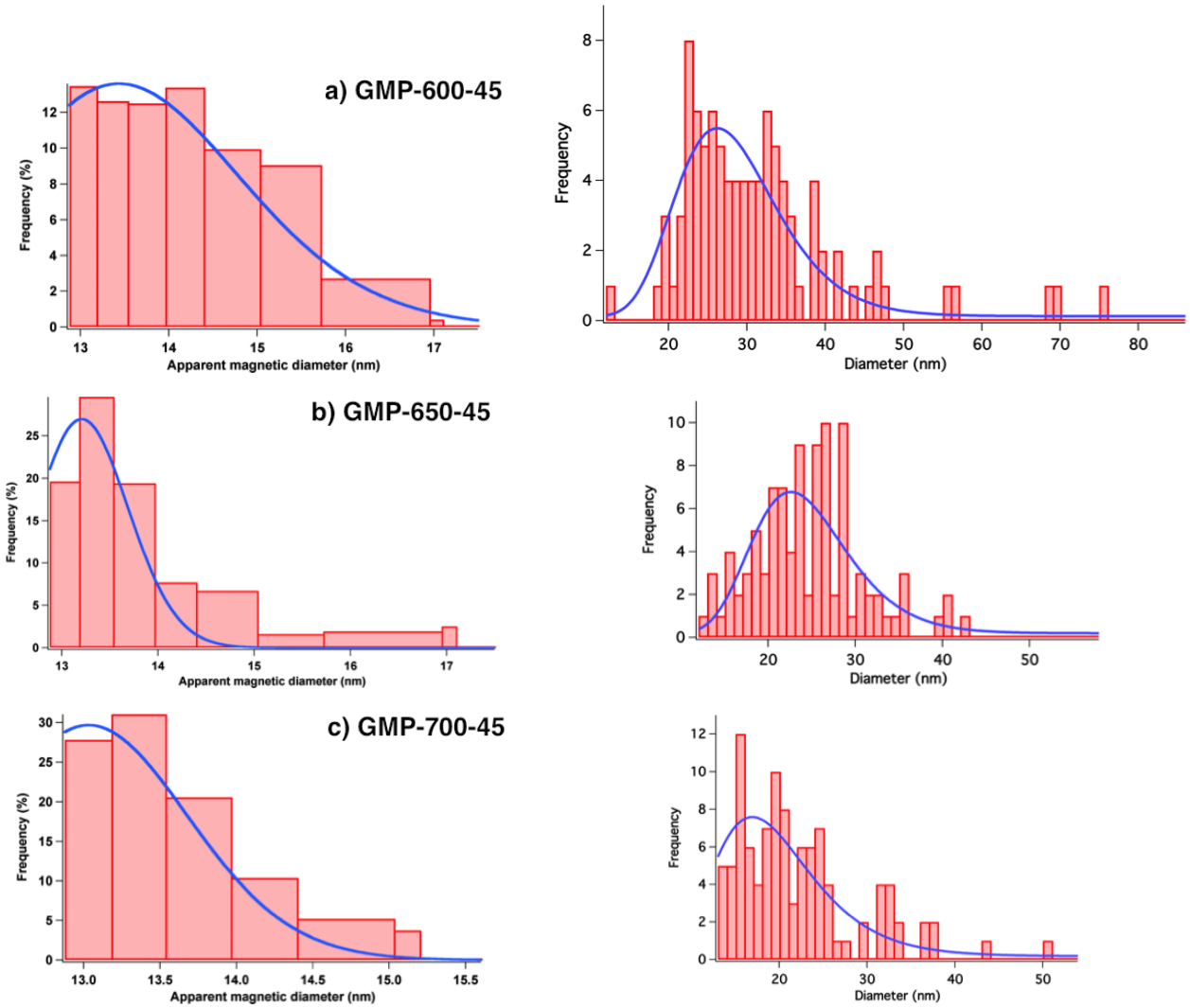

Figure 6.13 Magnetic size histogram obtained at T = 280 K (left) vs. physical size histogram (right) of a) GMP-600-45, b) GMP-650-45, and c) GMP-700-45.

6.4.4 Discussion

We have proposed a very simple technique to determine the magnetic size distribution of assembly of non-interacting oriented single domain ferromagnetic and superparamagnetic nanoparticles with coherent rotation magnetization reversal. We measured the isoremanent magnetization at different magnetic fields to construct the magnetic size histogram. The advantage of this technique is that the measurements are short and simple to perform, and unlike the model that has been widely used in the literature Tholence et Tournier (1974), it can be applied to systems with temperature dependent saturation magnetization ; however it can only be applied to systems containing nanoparticles with known orientation distribution.

To develop our method, we have made three simplifications, which will be discussed here.

(1) In Eq. (6.19) we have simplified the *tanh* function and obtained $P = 1$, which is valid for the range of parameters used in this work.

(2) To evaluate V_c (Eq. (6.24)), we simplified the *cosh* function in Eq. (6.25). Since Eq. (6.24) does not have an analytic solution, this simplification cannot be quantitatively justified. However, based on the typical order of magnitude of the parameters used in this work, it is a reasonable simplification.

(3) We have simplified the exponential term in Eq. (6.22) by a step function, base on figure 6.3. Since, similar to case (2), Eq. (6.22) does not have an analytic solution, this simplification cannot be further justified quantitatively. However, since the exponential term drastically changes as the critical diameter changes less than 1 nm (see figure 6.3), it is a reasonable simplification.

Now we discuss the validity of the assumptions that we have made to adapt our method to GaP:MnP epilayers, in order of their importance :

(1) Following C. Lacroix Lacroix (2010), we assumed that MnP nanoclusters exhibit coherent magnetization reversal with an energy barrier that is directly proportional to the volume of the nanocluters ($\Delta E = \Delta\varepsilon V$). As it was mentioned earlier, the magnetocrystalline anisotropy has been considered as the major magnetic anisotropy term for MnP nanoclusters Lacroix (2010). However, C. Lacroix Lacroix (2010) points out that of the other anisotropy terms (surface and magneto-elastic anisotropies, as well as inter-particle interaction), which were not considered in his work, the surface anisotropy is more significant. As the surface effects become more significant for nanoclusters with smaller sizes, we expect to have a distribution of energy barrier for magnetization reversal in our samples, which is not necessarily linearly proportional to the volume of nanoclusters. Further investigation of the size dependent energy barrier for magnetization reversal, which potentially could be provided through electron holography studies on individual nanoclusters, could improve the method presented in this chapter. It should be mentioned that even if energy barrier for magnetization reversal is independent of the volume of the naoclusters, there could be other magnetic reversal mechanisms with smaller energy barrier, such as curling or buckling (Cullity et Graham, 2011). This would result in underestimating the volume of the nanoclusters.

(2) We assumed that all MnP nanoparticles have the same saturation magnetization as bulk MnP. It is possible that the magnetic saturation of the nanocluters is less than that of MnP bulk (for example due to surface effects), which will affect our calculations to determine the energy barrier for magnetization reversal, and consequently the mean magnetic size of nanoclusters.

(3) We assumed that MnP nanoclusters are single domain nanoparticle, based on the

evidence (size range of nanoparticles) obtained from Refs. Lambert-Milot (2012), which has been justified in Ref. Lacroix (2010).

(4) We have applied our method, which has been developed for nanoparticles with uniaxial anisotropy, to MnP nanoclusters with orthorhombic anisoropy, by considering an effective magnetic anisotropy. While this looks reasonable, it is quite an extension of Né el's original work on single domain nanoparticles with uniaxial anisotropy.

Hence, the first two assumptions could have an effect on the obtained results (an example will be provided shortly), while the third one has a less significant effect.

We have validated our method by applying it on GMP-650-45 at three different temperatures. The results show a self consistency of the method, within $\approx 10\%$ error. We have also simulated the magnetic hysteresis curve of GMP-650-45 by calculating the magnetization of the system at different applied magnetic fields, which was found to have excellent agreement with experimental data. This indicates that magnetic volume distribution (or at least the energy barrier distribution for magnetization reversal) is consistent with magnetometric results.

Then we applied our technique to GaP:MnP epilayers grown at three different temperatures. The results showed fairly the same magnetic size for MnP nanoclusters in these three samples, which was significantly smaller compared to physical size of the nanoclusters, obtained from TEM image analysis. Obtaining smaller magnetic size for nanoclusters could attribute to several factors :

(1) An important factor to consider is when measuring the size of the nanoclusters in the TEM micrographs, we measure the dimensions of both MnP and Mn_2P nanoclusters. Hence, the mean physical diameter reported in Table 6.4 is actually the mean diameter of the mixture of MnP and Mn_2P nanoclusters. If Mn_2P nanoclusters have a different size or size distribution, the size histogram of MnP nanoclusters will be definitely different from what has been presented in figure 6.13. This factor becomes more significant at higher growth temperatures since according to Ref. Lambert-Milot (2012), the presence of Mn_2P becomes more significant (not quantified in Ref. Lambert-Milot (2012)) at higher growth temperatures. As it has been mentioned earlier, the difference (%) between the magnetic size and the physical size increases with growth temperature, which could correspond to stronger presence of Mn_2P at higher growth temperatures.

(2) Another factor that could affect our calculations is the values we have used to calculate the energy barrier density (as mentioned earlier). For example, we have used the saturation magnetization per unit volume of bulk MnP in our model to calculate the magnetic moment reversal energy barrier. If the saturation magnetization of the nanoclusters is smaller than that of bulk MnP, it results in obtaining smaller energy barrier density. For instance, in

GMP-650-45, if we apply a magnetic field of 32 kA/m at T = 280 K and use the M_s of bulk MnP we determine the mean magnetic diameter to be d_p = 13.2 nm. Now if we use a M_s that is 20% less than that of bulk MnP we determine the mean magnetic diameter to be d_p = 14.2 nm, and a M_s that is 50% smaller results in obtaining a diameter of d_p = 16.7 nm.

(3) Presence of a magnetic dead layer could also alter our results. A few monolayers of MnP close to the surface of the nanoclusters might be magnetically frozen due to the enhanced surface and interface effects at nanoscale. Presence of magnetic dead layer in MnP nanoclusters results in obtaining smaller magnetic size than physical size. Moreover, nanoclusters with a magnetic dead layer could have a smaller saturation magnetization per unit volume. For instance, 1 nm of magnetic dead layer on a 14 nm nanocluster results in obtaining a 20% smaller saturation magnetization per unit volume, which in turn affects the calculated energy barriers for magnetization reversal (see point (2) for effect of magnetic saturation on the mean magnetic size).

In order to improve the method presented in this chapter, the first step is to verify how the energy barrier for magnetization reversal and saturation magnetization changes as a function of nanoclusters size. Hopefully this information could be provided by electron holography studies of individual MnP nanoclusters.

CHAPTER 7

Conclusion

This final chapter summarizes the results of my investigations on the structural and magnetic properties of MnP films and nanocrystals embedded in GaP:MnP epilayers. The objectives of the work were to 1) understand the orientation selection mechanism and texture development of MnP nanocrystals in GaP:MnP epilayers by studying the texture of a related, yet simpler material system, namely MnP thin films grown on GaP, and 2) develop a method to determine the magnetic size distribution of magnetic nanoparticles in order to verify the difference between the apparent magnetic size and the physical size of MnP nanoclusters in GaP:MnP layers reported in Ref. Lacroix (2010).

7.1 Summary of the work and principal contributions

In this section, we provide a brief summary of this work and discuss its principal contributions. Our focus will be on the results of Chapters 4, 5, 6 on the texture evolution of MnP films, epilayers, and multilayers, as well as the determination of the magnetic size distribution of MnP nanoclusters.

7.1.1 Texture selection in MnP films, nanocrystals, and multilayers

We have studied the growth time and temperature evolution of the texture of MnP thin films grown on GaP (100) to determine the most favorable orientations that form and survive on GaP. Our results showed that : 1) all MnP grains (observed in cross-sectional TEM images) form through endotaxy on GaP (100) ; 2) grains with different orientations have different endotaxial depths and different surface facets ; 3) combining the results of SAED pattern and XRD pole figures strengthens the texture analysis ; 4) MnP films have epitaxial and partial axiotaxial texture ; and 5) the axiotaxial texture becomes dominant at higher growth temperatures.

Based on the above-mentioned observations, we proposed a semi-quantitative model to describe the endotaxial growth. Following Braun *et. al* Braun *et al.* (2007) we assumed that the mechanism of endotaxial growth takes place through out-diffusion of Ga atoms. Measuring the endotaxial depths of different MnP grains, we have extracted the diffusion coefficient of Mn in GaP. Our results showed a much larger (at least 3 order of magnitude larger) diffusion coefficients compared to bulk diffusion of Mn in GaP and self-diffusion of Ga in GaP. We ruled

out the role of dislocations in enhancing the diffusion in our samples, since we did not observe any dislocations in the cross-sectional TEM images. Since this enhanced diffusion occurs at the MnP/GaP interface, we suggested it to be due to the presence of a large number of vacancies at the interface (due to different crystal structures of MnP and GaP).

The dominance of axiotaxial texture at higher growth temperatures has been attributed to the lower MnP/GaP interface and strain energies at higher temperatures. Minimizing both the strain and the interface energies are the requirements for having an axiotaxial texture.

Comparing the texture of MnP films with GaP:MnP epilayers grown at different temperatures and different growth times, we realized that : 1) there are more epitaxial orientation families in MnP films than in epilayers ; 2) MnP films have more degree of freedom to form partial axiotaxial texture ; 3) there are two orientation families that exist in the thick epilayers and not in the films (all other orientations that exist in the epilayers also exist in the films).

Observing more orientation families in MnP films than the epilayers has been attributed to the fact that the interface/strain energies of a MnP nanocluster, which is embedded in a GaP matrix, are higher than those of a MnP grain on GaP with the same orientation. This leads to the survival of more orientation families and more degree of freedom to form axiotaxial texture in MnP films.

Observing the same orientation families in the films and epilayers (the ones that are in common) suggests that the driving force for the nucleation and growth of the MnP nanoclusters and grains is the same. The two orientation families that are observed in the epilayers but not in the films have been attributed to nucleating and grow on high-index GaP surfaces (GaP facets in GaP:MnP).

Significant Mn diffusion in GaP, has been observed in the multilayer structures, GaP/GaP:MnP/GaP (nominally 10 periods) and GaP/MnP/GaP (17 periods). By studying the thickness of GaP:MnP layers in GMP-M10 as a function of their formation time, we extracted the diffusion coefficient of Mn in GaP, which was found to be two orders of magnitude larger than what has been reported for Mn diffusion in bulk GaP in (Kirillov *et al.* (1980)). This enhanced diffusion has been attributed to occur due to the presence of structural defects in this sample.

In the GaP/MnP/GaP multilayers we observed that MnP diffuses inside GaP to form nanoclusters rather than formation of a multilayer MnP/GaP films. We suggested this to be due to Mn diffusion in GaP, which occurs through many structural defects observed in this sample. Realizing the significance of Mn diffusion in GaP, we considered the ripening of MnP nanoclusters (which was ignored in Refs. ((Lambert-Milot, 2012),(Lambert-Milot *et al.*, 2012)) to provided a qualitative picture of texture development in GaP:MnP epilayers.

The novelty of this work (Chapters 4 and 5) is : (1) We combined the results of SAED pattern and XRD pole figures to determine the texture of the films and epilayers. We have shown that using each of these techniques alone to analyze the texture may result in obtaining insufficient information on the texture ; (2) We have proposed a semi-quantitative model to describe the endotaxial growth of MnP on GaP (100) and reported the enhanced diffusion at the interface, probably caused by the presence of vacancies ; (3) Considering the ripening of MnP nanoclusters GaP:MnP/GaP, we provided a qualitative picture to describe the texture selection and development of the GaP:MnP/GaP epilayers.

7.1.2 Magnetic size distribution of MnP nanoclusters in GaP:MnP

As discussed in Chapter 6, there was a clear need to find a simple way to determine the magnetic size distribution of an assembly of ferromagnetic/superparamagnetic nanoparticles. We have used the concept of thermally activated magnetization reversal process to analyze the IRM response of the system at different magnetic fields. Our proposed simple method enables one to build the magnetic size histogram of oriented single domain nanoparticles, from which one can extract their magnetic size distribution, as well as the mean magnetic size and standard deviation. The novelty of the proposed model is the simplicity of extracting the desired information, as well as the short time to carry out the experiments. Moreover, it can be applied to any system containing oriented single domain nanoparticles with coherent rotation.

Applying this method to MnP nanoclusters in GaP:MnP epilayers, we realized that the magnetic size of the nanoclusters is much smaller than their physical size obtained from TEM image analysis, similar to what has been reported in Ref. (Lacroix (2010)). Aside from the limitations of TEM image analysis, which were addressed in Chapter 6, we attributed the difference in the magnetic and physical size of the nanoclusters to be due to : (1) presence of Mn_2P in the epilayers, which affects the TEM image analysis to obtain the physical size histogram of MnP (but does not contribute in determining the magnetic size of the nanoclusters ; (2) smaller saturation magnetization of the MnP nanoclusters compared to bulk MnP (which has been used in the model) and possible non-coherent rotation magnetization reversal ; (3) the simplifying assumptions we have made to apply the method to orthorhombic MnP nanoclusters in GaP:MnP epilayers and (4) the potential presence of magnetic dead layer in the nanoclusters.

The consistency of the model has been validated by extracting the magnetic size of the nanoclusters from the experiments performed at three different temperatures. The three extracted magnetic sizes were approximately the same (within 10% error). Moreover, using the extracted magnetic size distribution and mean magnetic size and standard deviation we

have successfully modeled the magnetic hysteresis of an epilayer, which is another indication that the method is consistent. However, consistency does not mean absence of systematic errors.

7.2 Suggestions for future work

As it has been mentioned in Chapter 1, MnP thin films grown on GaP have been chosen as a model system to understand the texture selection in heterogeneous semiconductors (such as GaP:MnP). In this section we provide few suggestions that could improve our state of knowledge on the formation mechanism of MnP on GaP, in addition to designing of novel structures.

7.2.1 Energy terms and enhanced diffusion of Mn in GaP

We have shown the endotaxial growth of MnP on GaP to be limited by a diffusion process. This process occurs most likely through the out-diffusion of Ga at MnP/GaP interface. For this process, we have found a diffusion coefficient (for Mn diffusion in GaP) that is at least three orders of magnitude larger than bulk diffusion of Mn in GaP. Since the GaP buffer layer was dislocation free, we attributed this enhanced diffusion to occur through a potentially large number of vacancies at the GaP/MnP interface. To further investigate this, knowing the crysal structure of MnP and GaP and the crystallographic orientations of MnP crystals on GaP, one can estimate the number of vacancies at different GaP/MnP interfaces and compare it to the number of vacancies in bulk GaP. This analysis is the first step to understand the interface diffusion process.

Moreover, there are few pieces of information that are missing in the literature, such as the values of free surface energy of MnP, GaP/MnP interfacial energies, and lattice parameters on MnP at the growth temperature (to calculate the strain at the growth temperature). These values could help us to provide a quantitative picture of the competing energy terms that favor the nucleation of a crystal with a specific crystallographic orientation. The first step could be to estimate the free surface and interface energies by calculating the density of atoms at the free surface and interface and the number of dangling bonds. This way one can have an idea about the relative energies of different free surfaces and interfaces. The lattice parameters of MnP at higher temperatures could be obtained from XRD measurements.

7.2.2 Controlling the texture

We have also pointed out that as a result of this diffusion we will have a inhomogeneous distribution of the population of MnP nanoclusters in different orientation families in

GaP:MnP epilayers. The inhomogeneity of the population of the nanoclusters in different orientations may be undesirable for magneto-optical applications. As we mentioned in the first chapter, the magnitude of the Faraday rotation differs when the light interacts with nanoclusters with different orientations. Hence, the value of the Faraday rotation will change as the light passes through the epilayer.

In order to obtain a homogeneous distribution, we can control the level of the ripening in the epilayer by altering the Mn concentration during the growth. We can introduce a small amount of Mn at the beginning of growth. This way we will have a small number of nanoclusters nucleating on GaP, which have a larger distance with each other (compared to nanoclusters forming at later growth times). As the epilayer grows, the Mn will diffuse inside GaP from one cluster to another. During this process the nanoclusters that have a lower energy will grow at the expense of the others. Due to the small number of nanoclusters and the larger distance between them, this process will be slow.

As we increase the amount of Mn during the growth, we will have more nanoclusters that nucleate on GaP with a smaller distance compared to the ones that formed earlier. The process of ripening in this generation of nanoclusters will be faster, but we can have the same amount of material exchange between the nanoclusters of the two generations (the ones that formed earlier and the ones that formed later on), as the first generation have a longer time to exchange material. This will lead us to grow an epilayer, in which the population of the nanoclusters in different orientation families grows (or decay) with the same rate, resulting in a homogeneous distribution of the population of nanoclusters in different orientation families.

Another suggestion to control the texture is the growth of GaP/GaP:MnP/GaP multilayers, in which we alter the concentration of Mn and/or the thickness of the GaP spacers. The advantage of this approach over the one proposed earlier in this section is that we can avoid the nucleation and growth of some orientations that grow on different GaP facets (that form in the epilayer), such as what has been referred to dots and yellow triangles in this thesis.

In order to design such structures one needs to know the diffusion coefficient of Mn in GaP at different temperatures. In Appendix A we have reported the values of the diffusion coefficient and activation energy of Mn diffusion in GaP obtained from endotaxial depths of MnP grains in GaP. However, a systematic experimental procedure can be designed to have a better estimate of the desired parameters. For example, we can grow very thin layers of MnP on GaP followed by GaP cap layers with different thicknesses. We can then anneal the samples for different times at different temperatures. We expect to see MnP nanoclusters inside the GaP buffer layer and GaP cap layer (similar to the 17 period multilayer sample analyzed). By measuring the diffusion depth of Mn in GaP we can estimate its diffusion

coefficients and activation energies.

7.2.3 Magnetic properties of an individual MnP nanocluster studied by electron holography

Electron holography has the potential to provide us with information on the magnetic behavior of individual MnP nanoclusters. The most important information to us that may be provided using this technique is to verify the assumptions we have made in Chapter 6 to adapt our method to GaP:MnP epilayers : (1) coherent rotation magnetization reversal process, and (2) size independent saturation magnetization of MnP nanoclusters.

We may also be able to verify whether there is any magnetic dead layer on the nanoclusters by studying the magnetization and thickness profiles at different locations in GaP:MnP samples.

Moreover, there is a possibility (depending on the sensitivity of the technique) to obtain the magnetic anisotropy of individual MnP nanoclusters (or grains) by obtaining their angle dependent magnetization response through tilting the sample.

Furthermore, temperature dependent measurements allows us to study the magnetization response of individual nanoclusters (or grains) as we approch their Curie temperature. This way we can study the effect of size of the nanoclusters on their Curie temperature.
This project has been initiated and is in process in collaboration with professor Karen Kavanagh at Simon Fraser University.

REFERENCES

AKINAGA, H., DE BOECK, J., BORGHS, G., MIYANISHI, S., ASAMITSU, A., VAN ROY, W., TOMIOKA, Y. et KUO, L. (1998). Negative magnetoresistance in GaAs with magnetic MnAs nanoclusters. *Applied physics letters*, 72, 3368–3370.

AKINAGA, H., MIYANISHI, S., TANAKA, K., VAN ROY, W. et ONODERA, K. (2000). Magneto-optical properties and the potential application of GaAs with magnetic MnAs nanoclusters. *Applied Physics Letters*, 76, 97–99.

ANDO, K., CHIBA, A. et TANOUE, H. (1998). Uniaxial magnetic anisotropy of submicron MnAs ferromagnets in GaAs semiconductors. *Applied physics letters*, 73, 387–389.

BARNA, P. B. et ADAMIK, M. (1995). Growth mechanisms of polycrystalline thin films. *Science and Technology of Thin Films, edited by FC Matacotta and G. Ottaviani, World Scientific*.

BENNETT, P., HE, Z., SMITH, D. J. et ROSS, F. (2011). Endotaxial silicide nanowires : A review. *Thin Solid Films*, 519, 8434–8440.

BONEV, I. (1972). On the terminology of the phenomena of mutual crystal orientation. *Acta Crystallographica Section A : Crystal Physics, Diffraction, Theoretical and General Crystallography*, 28, 508–512.

BRAUN, W., TRAMPERT, A., KAGANER, V. M., JENICHEN, B., SATAPATHY, D. K. et PLOOG, K. H. (2007). Endotaxy of MnSb into GaSb. *Journal of Crystal Growth*, 301, 50–53.

BUCSA, I., COCHRANE, R. et ROORDA, S. (2009). Segregation and formation of Mnp particles during rapid thermal annealing of Mn-implanted InP and GaP. *Journal of Applied Physics*, 106, 013914–013914.

COUTO, O., BRASIL, M., IIKAWA, F., GILES, C., ADRIANO, C., BORTOLETO, J., PUDENZI, M., GUTIERREZ, H. et DANILOV, I. (2005). Ferromagnetic nanoclusters formed by Mn implantation in GaAs. *Applied Physics Letters*, 86, 071906–071906.

COVA, P., MASUT, R., CURRIE, J., BENSAADA, A., LEONELLI, R. et TRAN, C. A. (1991). Effet des paramètres de croissance sur les couches épitaxiales d'InP obtenues par MOCVD (metal-organic chemical vapor deposition) à basse pression. *Canadian Journal of Physics*, 69, 412–421.

CULLITY, B. D. et GRAHAM, C. D. (2011). *Introduction to magnetic materials*. John Wiley & Sons.

DÄWERITZ, L. (2006). Interplay of stress and magnetic properties in epitaxial MnAs films. *Reports on Progress in Physics*, 69, 2581.

DE BOECK, J., OESTERHOLT, R., VAN ESCH, A., BENDER, H., BRUYNSERAEDE, C., VAN HOOF, C. et BORGHS, G. (1996). Nanometer-scale magnetic MnAs particles in GaAs grown by molecular beam epitaxy. *Applied physics letters*, 68, 2744–2746.

DETAVERNIER, C., ÖZCAN, A., JORDAN-SWEET, J., STACH, E., TERSOFF, J., ROSS, F. et LAVOIE, C. (2003). An off-normal fibre-like texture in thin films on single-crystal substrates. *Nature*, 426, 641–645.

DEUS, P., VOLAND, U. et SCHNEIDER, H. (1983). Thermal expansion of GaP within 20 to 300 K. *physica status solidi (a)*, 80, K29–K32.

DIETL, T. (1994). Handbook on semiconductors. *Vol. 3bNorth-Holland, Amsterdam*, 1251.

DORMANN, J., FIORANI, D. et TRONC, E. (1997). Magnetic relaxation in fine-particle systems. *Advances in Chemical Physics, Volume 98*, 283–494.

EGERTON, R. F. (2005). *Physical principles of electron microscopy : an introduction to TEM, SEM, and AEM*. Springer.

EL-HILO, M. et O'GRADY, K. (1990). Components of magnetisation of a fine particle system. *Magnetics, IEEE Transactions on*, 26, 1807–1809.

FATHAUER, R., GEORGE, T. et PIKE, W. (1992). Co diffusion and growth of buried single-crystal CoSi2 in Si (111) by endotaxy. *Journal of applied physics*, 72, 1874–1878.

FURDYNA, J. K. (1988). Diluted magnetic semiconductors. *Journal of Applied Physics*, 64, R29–R64.

GAJ, J., GINTER, J. et GAŁĄZKA, R. (1978). Exchange interaction of manganese 3d5 states with band electrons in Cd1- xMnxTe. *physica status solidi (b)*, 89, 655–662.

GAUDET, S. (2011). *L'impact de la texture sur la Reaction en phase solide du Ni avec le Si*. Thèse de doctorat, École Polytechnique de Montréal.

HARTMAN, P. et PERDOK, W. (1955). On the relations between structure and morphology of crystals. I. *Acta Crystallographica*, 8, 49–52.

HARTMANN, T., LAMPALZER, M., KLAR, P., STOLZ, W., HEIMBRODT, W., VON NIDDA, H.-A. K., LOIDL, A. et SVISTOV, L. (2002). Ferromagnetic resonance studies of (Ga, Mn) As with MnAs clusters. *Physica E : Low-dimensional Systems and Nanostructures*, 13, 572–576.

HATFIELD, S. A. (2006). *Heteroepitaxial growth of MnSb on III-V semiconductor substrates*. Thèse de doctorat, University of Warwick.

HEIMBRODT, W. et KLAR, P. J. (2005). Magnetic interactions in granular paramagnetic-ferromagnetic GaAs : Mn/MnAs hybrids. *Local-Moment Ferromagnets*, Springer. 167–184.

HUBER JR, E. et RIDGLEY, D. (1964). Magnetic properties of a single crystal of manganese phosphide. *Physical Review*, 135, A1033.

IGUCHI, H., HARA, S., MOTOHISA, J. et FUKUI, T. (2008). Metal-organic vapor phase epitaxial growth condition dependences of MnAs nanocluster formation on GaInAs (111) A surfaces. *Japanese Journal of Applied Physics*, 47, 3253.

ILEGEMS, M., PANISH, M. et ARTHUR, J. (1974). Phase equilibria and vapor pressures in the Ga+P system. *The Journal of Chemical Thermodynamics*, 6, 157–177.

IWATA, N. (1969). Magnetic properties of MnP. *Journal of Science of the hiroshima University*, 33, 1–21.

JACZYŃSKI, M., KOSSUT, J. et GAŁĄZKA, R. (1978). Influence of exchange interaction on the quantum transport phenomena in Hg1- xMnxTe. *physica status solidi (b)*, 88, 73–85.

KIRILLOV, V., PRIBYLOV, N., REMBEZA, S. et SPIRIN, A. (1980). Charge states and diffusion of manganese in gallium phosphide. *SOV. PHYS. SOL. ST.*, 22, 1945–1947.

KOSKELO, O., RÄISÄNEN, J., TUOMISTO, F., SADOWSKI, J. *ET AL.* (2009). The effect of a material growth technique on ion-implanted Mn diffusion in GaAs. *Semiconductor Science and Technology*, 24, 045011.

LACROIX, C. (2010). *Propriétés magnétiques de nanoagrégats ferromagnétiques encastrés dans une épicouche semi-conductrice.*

LAMBERT-MILOT, S. (2012). *Synthèse et caractérisation structurale d'épicouches hétérogènes semi-conductrices/ferromagnétiques : le cas d'agrégats de MnP encastrés dans une matrice de GaP.* Thèse de doctorat, École Polytechnique de Montréal.

LAMBERT-MILOT, S., GAUDET, S., LACROIX, C., MÉNARD, D., MASUT, R. A., LAVOIE, C. et DESJARDINS, P. (2012). MnP nanoclusters embedded in GaP epitaxial films grown by organometallic vapor-phase epitaxy : A reciprocal space mapping and transmission electron microscopy study. *Journal of Vacuum Science & Technology A : Vacuum, Surfaces, and Films*, 30, 061510–061510.

LAMBERT-MILOT, S., LACROIX, C., MÉNARD, D., MASUT, R., DESJARDINS, P., GARCIA-HERNANDEZ, M. et DE ANDRES, A. (2008). Metal-organic vapor phase epitaxy of crystallographically oriented MnP magnetic nanoclusters embedded in GaP (001). *Journal of Applied Physics*, 104, 083501–083501.

LAMPALZER, M., VOLZ, K., TREUTMANN, W., NAU, S., TORUNSKI, T., MEGGES, K., LORBERTH, J. et STOLZ, W. (2003). Overgrowth experiments of ferromagnetic (MnGa) As-cluster layers by MOVPE. *Journal of crystal growth*, 248, 474–478.

MACDONALD, A., SCHIFFER, P. et SAMARTH, N. (2005). Ferromagnetic semiconductors : moving beyond (Ga, Mn) As. *Nature Materials*, 4, 195–202.

MAHATO, J., DAS, D., JULURI, R., BATABYAL, R., ROY, A., SATYAM, P. et DEV, B. (2012). Nanodot to nanowire : A strain-driven shape transition in self-organized endotaxial CoSi2 on Si (100). *Applied Physics Letters*, 100, 263117–263117.

MAUGER, A. et GODART, C. (1986). The magnetic, optical, and transport properties of representatives of a class of magnetic semiconductors : The europium chalcogenides. *Physics Reports*, 141, 51–176.

MONETTE, G., LACROIX, C., LAMBERT-MILOT, S., BOUCHER, V., MÉNARD, D. et FRANCOEUR, S. (2010). Giant magneto-optical Faraday effect in GaP epilayers containing MnP magnetic nanoclusters. *Journal of Applied Physics*, 107, 09A949–09A949.

MONETTE, G., NATEGHI, N., MASUT, R. A., FRANCOEUR, S. et MÉNARD, D. (2012). Plasmonic enhancement of the magneto-optical response of MnP nanoclusters embedded in GaP epilayers. *Physical Review B*, 86, 245312.

MORENO, M., TRAMPERT, A., JENICHEN, B., DAWERITZ, L. et PLOOG, K. (2002). Correlation of structure and magnetism in GaAs with embedded Mn (Ga) As magnetic nanoclusters. *Journal of applied physics*, 92, 4672–4677.

NÉEL, L. (1949). Théorie du traînage magnétique des ferromagnétiques en grains fins avec applications aux terres cuites. *Ann. géophys*, 5, 99–136.

OHNO, H. (1998). Making nonmagnetic semiconductors ferromagnetic. *science*, 281, 951–956.

OHNO, H. (1999). Properties of ferromagnetic III-V semiconductors. *Journal of magnetism and magnetic materials*, 200, 110–129.

PARK, J., KOO, B., YOON, K. Y., HWANG, Y., KANG, M., PARK, J.-G. et HYEON, T. (2005). Generalized synthesis of metal phosphide nanorods via thermal decomposition of continuously delivered metal-phosphine complexes using a syringe pump. *Journal of the American Chemical Society*, 127, 8433–8440.

PRISTOVSEK, M., PHILIPPOU, A., RÄHMER, B. et RICHTER, W. (2008). Properties of InMnP (001) grown by MOVPE. *Journal of Crystal Growth*, 310, 4046–4049.

SCHMIDT, N. (2011). *Ètude sur la transition de phase ferromagnètic/paramagnètic de nanoagrègates de MnP*. Thèse de doctorat, École Polytechnique de Montréal.

SHIMIZU, H., MIYAMURA, M. et TANAKA, M. (2001). Magneto-optical properties of a GaAs : MnAs hybrid structure sandwiched by GaAs/AlAs distributed Bragg reflectors : Enhanced magneto-optical effect and theoretical analysis. *Applied Physics Letters*, 78, 1523–1525.

STRINGFELLOW, G. B. (1999). *Organometallic vapor-phase epitaxy : theory and practice*. Academic Press.

TERSOFF, J. et TROMP, R. (1993). Shape transition in growth of strained islands : Spontaneous formation of quantum wires. *Physical review letters*, 70, 2782.

THIO, T. et SOLIN, S. (1998). Giant magnetoresistance enhancement in inhomogeneous semiconductors. *Applied physics letters*, 72, 3497–3499.

THOLENCE, J. et TOURNIER, R. (1974). Susceptibility and remanent magnetization of a spin glass. *Le Journal de Physique Colloques*, 35, C4–229.

THOMPSON, C. V. et CAREL, R. (1995). Texture development in polycrystalline thin films. *Materials Science and Engineering : B*, 32, 211–219.

WELLMANN, P., GARCIA, J. M., FENG, J.-L. et PETROFF, P. M. (1997). Formation of nanoscale ferromagnetic MnAs crystallites in low-temperature grown GaAs. *Applied physics letters*, 71, 2532–2534.

WELLMANN, P., GARCIA, J. M., FENG, J.-L. et PETROFF, P. M. (1998). Giant magnetoresistance in a low-temperature GaAs/MnAs nanoscale ferromagnet hybrid structure. *Applied physics letters*, 73, 3291–3293.

YATAGO, M., IGUCHI, H., SAKITA, S. et HARA, S. (2012). Growth and characterization of MnAs nanoclusters embedded in GaAs nanowires by metal–organic vapor phase epitaxy. *Japanese Journal of Applied Physics*, 51.

YE, S. (2005). *Magneto-transport in (Ga, Mn) As-based alloys and hybrids*. Thèse de doctorat, Universitätsbibliothek Marburg.

YE, S., KLAR, P., HARTMANN, T., HEIMBRODT, W., LAMPALZER, M., NAU, S., TORUNSKI, T., STOLZ, W., KURZ, T., KRUG VON NIDDA, H.-A. *ET AL.* (2003). Anisotropy of the magnetotransport in (Ga, Mn) As/MnAs paramagnetic-ferromagnetic hybrid structures. *Applied physics letters*, 83, 3927–3929.

YULDASHEV, S. U., SHON, Y., KWON, Y., FU, D., KIM, D., KIM, H., KANG, T. et FAN, X. (2001). Enhanced positive magnetoresistance effect in GaAs with nanoscale magnetic clusters. *Journal of Applied Physics*, 90, 3004–3006.

ANNEXE A

Mn diffusion in GaP

In this appendix we extract the diffusion coefficient of Mn in GaP by studying the time evolution of endotaxial depths of MnP grains (in MnP films) with different crystallographic orientations. The endotaxial depth along different GaP directions has been measured from cross-sectional TEM images of the grains. We have measured the endotaxial depth of different grains along four directions : GaP [11-1], GaP [-11-1], GaP [100], and GaP [31-1]. By studying the endotaxial depths of different grains along the above mentioned directions we found the relationship : $d_{[-11-1]} \approx d_{[11-1]}$, $d_{[11-1]}/d_{[100]} \approx 1.7$, and $d_{[100]}/d_{[31-1]} \approx 1.1$, where d represents the endotaxial depth and its index shows the GaP direction along which the depth were measured, *i.e.* $d_{[100]}$ is the diffusion depth of Mn in GaP along GaP [100]. The relationships that we found are in agreement with what we expect from the projection of the endotaxial depth along different directions. The angles between GaP [100] and GaP [11-1] and between GaP [100] and GaP [31-1] are 54.7 ° and 25.2 °, respectively. Hence, we expect to have $d_{[11-1]}/d_{[100]} = 1/\cos(54.7\,^\circ) = 1.7$ and $d_{[100]}/d_{[31-1]} = 1/cos(25.2\,^\circ) = 1.1$.

To determine the diffusion coefficient of Mn in GaP we have chosen the maximum average endotaxial depth along GaP [11-1] and [-11-1] directions, *i.e.* $d_{<111>} = (d_{[-11-1]} + d_{[11-1]})/2$. The diffusion coefficient of Mn in GaP along other GaP directions is correlated with the angle between GaP [11-1] and the direction of interest. For example, $D_{[100]} = D_{<11-1>}/\cos(54.7\,^\circ)$, where $D_{[100]}$ is the diffusion coefficient of Mn in GaP along GaP [100] direction.

Figure A.1 shows an example of a grain and its maximum endotaxial depths measured along GaP [100] and GaP [-11-1]. Table A.1 shows the measured maximum endotaxial depths of MnP grains with orientation MnP 121 || GaP (200) grown at 550 °C. This maximum depth corresponds to Mn diffusion in the GaP <111> direction, d<111>. The measurement errors reported in this appendix are the standard deviations.

Figure A.2 shows the graph of the square of the average maximum depth ($d^2_{<111>}$) as a function of time (s) for the MnP films grown at 550 °C. The result revealed a linear proportionality between the endotaxial depth and the square root of growth time. This confirms the hypothesis that the endotaxial growth occurs through the diffusion process. Using the diffusion equation $d = \sqrt{Dt}$, from the slope of the line in figure A.2 we have determined the diffusion coefficient of Mn in GaP along [11-1] direction for grains with MnP {121} || GaP (200) alignment to be $D_{<111>} = 1.24 \pm 0.028 \times 10^{-14}(cm^2/s)$. This value is 6 orders of magnitude larger than the one obtained from Ref. Kirillov *et al.* (1980), $D = 3.69 \times 10^{-20}(cm^2/s)$.

Of course this value is different for the grains with different crystallographic orientations due to their different endotaxial depths. We only report the diffusion coefficient for the grains with MnP {121} || GaP (100) at this growth temperature since this is the most observed orientation.

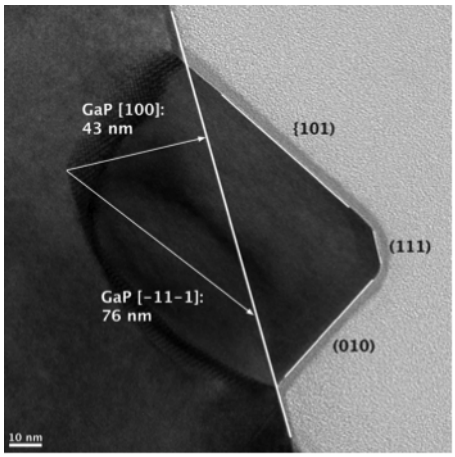

Figure A.1 A grain in MnP-600 with MnP {131} || GaP (111) alignment. The long white line shows the expected GaP surface prior to growth of MnP. For this grain we measured $d_{[100]} = 43$ nm and $d_{[-11-1]} = 76$ nm.

Table A.1 Average maximum depth of Mn diffusion in GaP <11-1>, d<111>, for MnP grains grown at 550 °C with MnP {121} || GaP {100}.

Sample	**MnP-550-1.5**	**MnP-550-5**	**MnP-550-15**
$\mathbf{d_{<111>}(nm)}$	9.5 ± 1.0	18.7 ± 3.3	33.5 ± 5.7

Table A.2 summarizes the average maximum in-diffusion depths (nm) and diffusion coefficient, $D_{<111>}$, of grains with different orientations grown at 650 °C. The diffusion coefficients are obtained from the slope of the graphs presented in figure A.3. The values of the $D_{<111>}$ obtained for different orientations are at least 3 orders of magnitude larger than what has been reported in Ref. Kirillov *et al.* (1980) at 650 °C, $D = 4.81 \times 10^{-17}(cm^2/s)$.

Studying the diffusion coefficient of samples grown at different temperatures, using the equation ($D = D_0 exp(-\Delta E/k_B T)$ (k_B is the Boltzmann constant), we give an estimate of the pre-exponential factor (D_0) and the activation energy (ΔE_{Diff}) for grains with MnP {121} || GaP (100). Table A.3 shows the diffusion coefficient of Mn in GaP <111> at different temperatures. The diffusion coefficient at 600 °C is calculated from the endotaxial depth of only one grain. The values of $D_{<111>}$ reported in table A.3 correspond to samples grown below the congruent temperature of GaP, which is reported to be $960 \pm 20K$ Ilegems *et al.*

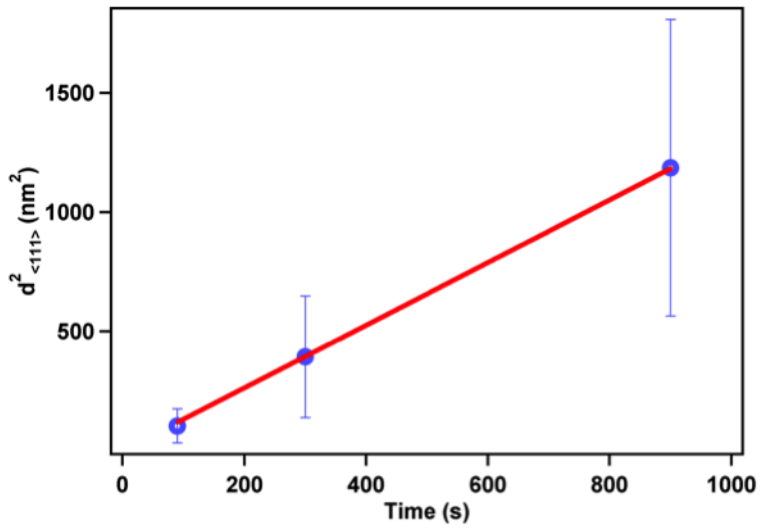

Figure A.2 Square of the diffusion depth ($d^2_{<111>}$) of MnP grains grown at with MnP {121} || GaP (100) in GaP along <111> direction as a function of growth time (t). The slope of the line reveals the diffusion coefficient of $D_{<111>} = 1.31 \pm 0.012 \times 10^{-14}(cm^2/s)$.

Table A.2 $d_{<111>}$ (nm) and the obtained diffusion coefficients ($D_{<111>}$) of Mn in GaP. The data presented without error are obtained from only one grain. The diffusion coefficient for MnP {111} || GaP (100) is obtained from four grains of MnP-650-15, using the diffusion equation $d = \sqrt{Dt}$, where d is the average in-diffusion depth of Mn and t is the growth time.

Orientation/Sample	**MnP-650-5**	**MnP-650-15**	**MnP-650-30**	**D$_{<111>}$(cm^2/s)**
MnP {010} || GaP (111)	22.5 ± 3.5	34.6 ± 1.7	-	$1.4 \pm 8.4 \times 10^{-14}$
MnP {111} || GaP (100)	-	53.3 ± 2.7	-	$3.2 \pm 0.33 \times 10^{-14}$
MnP {121} || GaP (100)	38	55	-	$3.8 \pm 0.26 \times 10^{-14}$
MnP {110} || GaP (100)	49	69	-	$2.6 \pm 0.17 \times 10^{-14}$

(1974). At the congruent temperature P atoms will evaporate from the surface, which affects the diffusion of Mn in GaP. Figure A.4 shows the graph of the natural logarithm of diffusion coefficient as a function of inverse of growth temperature. The slope of the graph leads us to extract the activation energy and the intercept with the vertical axis results in finding D_0.

Table A.3 Diffusion coefficient of Mn in GaP along <111> at different growth temperatures below the congruent temperature of GaP.

Growth T(°C)	**550**	**600**	**650**
D$_{<111>}$(cm^2/s)	$1.31 \pm 0.012 \times 10^{-14}$	2.15×10^{-14}	$3.80 \pm 0.26 \times 10^{-14}$

We have obtained $\Delta E_{Diff} = 0.6 \pm 0.2$ (eV) and $D_0 = (2.7 \pm 2.6) \times 10^{-10}(cm^2/s)$ for Mn diffusion in GaP [11-1] in grains with {121} || GaP (100). The uncertainty of the reported

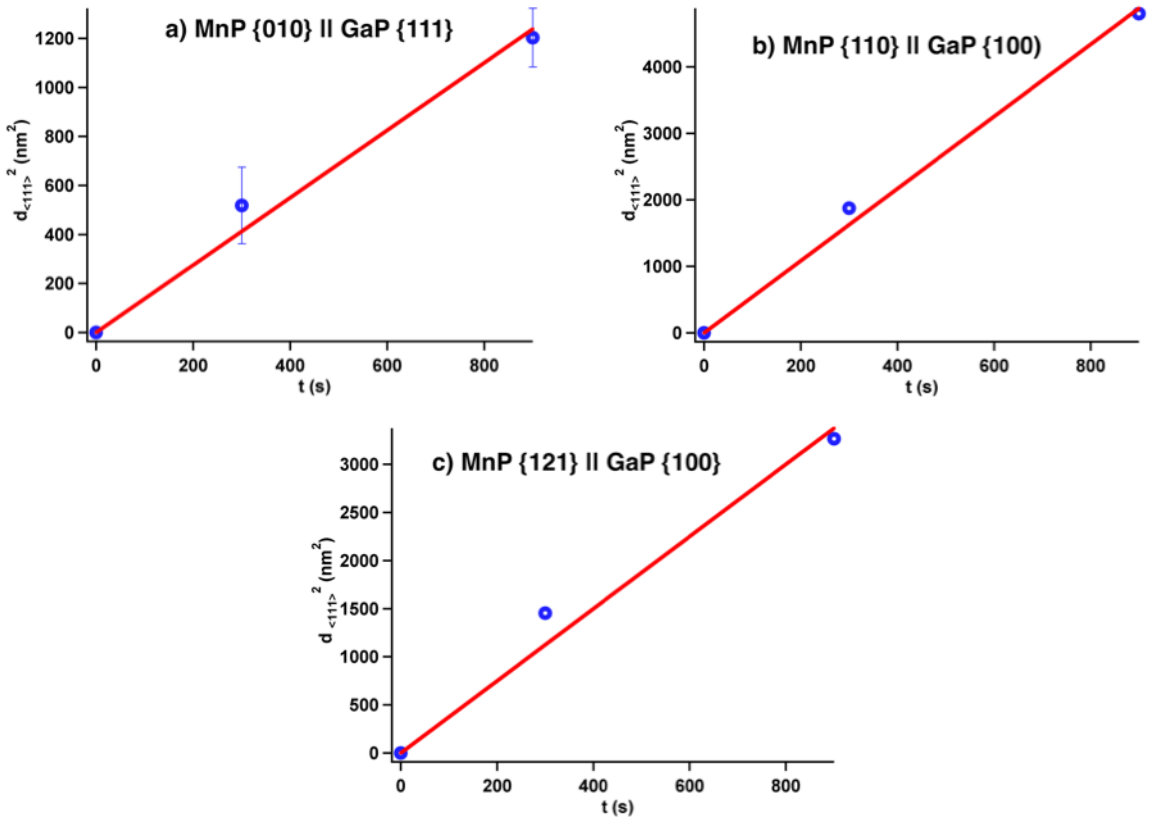

Figure A.3 $d_{<111>}$ as a function of growth time for a) MnP {010} || GaP (111) ($D_{<111>} = 1.4 \times 10^{-14} \pm 8.4 \times 10^{-16} (cm^2/s)$), b) MnP {110} || GaP (200) ($D_{<111>} = 2.6 \times 10^{-14} \pm 1.7 \times 10^{-15} (cm^2/s)$), and c) MnP {121} || GaP (200) ($D_{<111>} = 3.8 \times 10^{-14} \pm 2.6 \times 10^{-15} (cm^2/s)$). Since we only had two data points, we added the point (0, 0) and assured the fitted line, the slope of which represents $D_{<111>}$, is passing through the origin. The data points that are presented with no error bars are obtained from only one grain.

values are relatively high and the fit is not fairly linear (which will be discussed shortly), but they give us a sense of order of magnitude. The values reported in Ref. Kirillov *et al.* (1980) are $\Delta E_{Diff} = 4.7$ (eV) and $D_0 = 2.1 \times 10^9 (cm^2/s)$.

In order to have more statistics on the reported values, we chose to study the average endotaxial depths of the grains (at least 20 grains) of our sample as a function of growth time and temperature, and this along GaP [100] direction (as an alternative). In order to determine the rate of this suggested diffusion controlled process, we have studied the growth time evolution of the endotaxial depths of MnP grains grown at 550 °C and 650 °C. Table A.4 reports the average endotaxial depths of MnP grains with different crystallographic orientations along GaP [100] grown at 550 °C and 650 °C. Figure A.5 shows the endotaxial depths of MnP grains grown at 550 °C and 650 °C as a function of growth time.

Our results show a slightly smaller diffusion coefficients than what has been reported for

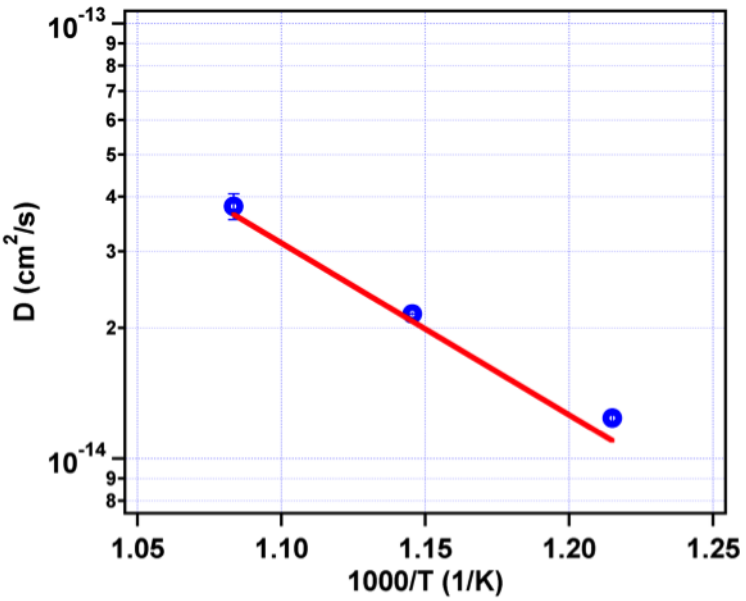

Figure A.4 Semi-logarithmic graph of D as a function of $(1/T)$. The extracted activation energy and pre-exponential factor from the linear fit are $(\Delta E_{Diff}) = 0.6 \pm 0.2$ (eV) and $(D_0 = 2.7 \pm 2.6) \times 10^{-10}(cm^2/s)$.

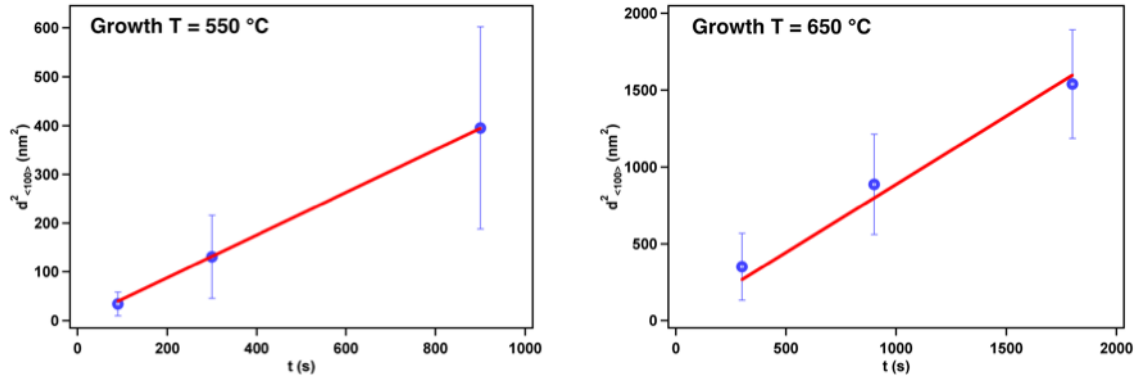

Figure A.5 The square of endotaxial depths as a function of growth time for MnP grains grown at 550 °C and 650 °C. The linear behavior confirms that endotaxial growth is a diffusion-controlled process. The slope of the lines provide the diffusion coefficients to be $4.4 \pm 0.04 \times 10^{-15}(cm^2/s)$ and $8.9 \pm 0.47 \times 10^{-15}(cm^2/s)$ for the growth temperatures 550 °C and 650 °C, respectively.

the specific orientation families studied earlier along GaP <111>, since (1) the endotaxial depths is expected to be larger ($\sqrt{3}$ times) along GaP <111> than GaP <100>, and (2) the averaging on all the orientation families might slightly affect the endotaxial depths.

For growth temperature 550 °C, comparing the diffusion coefficient of MnP {121} || GaP (100) along GaP <111> with the average diffusion coefficient along GaP <100>, we obtain

$D_{<111>}/D_{100} = 2.8$, which is larger than $\sqrt{3}$. Hence, it seems safe to conclude that the other orientation families in this sample have a smaller endotaxial depth (in average).

For the samples grown at 650 °C, comparing the average diffusion coefficient of the four orientation families reported in Table A.2 (along GaP <111>) to the average (most likely over more orientation families) diffusion coefficient (along GaP <100>), we obtain $D_{<111>}/D_{100} = 3.1$, which is larger than $\sqrt{3}$. Hence again, it seems safe to conclude that the other orientation families have a smaller endotaxial depths.

Table A.4 Average maximum endotaxial depth of MnP in GaP along GaP [100], d, for MnP grains grown at 550 °C and 650 °C.

Sample	**MnP-550-1.5**	**MnP-550-5**	**MnP-550-15**	**MnP-650-5**	**MnP-650-15**	**MnP-650-30**
d (nm)	5.5 ± 0.6	10.8 ± 1.9	19.3 ± 3.3	17.9 ± 1.8	29.3 ± 1.7	39.0 ± 1.7

We also provide an estimate of the pre-exponential factor (D_0) and the activation energy (ΔE) for Mn diffusion in GaP by studying the growth temperature evolution of the diffusion coefficients ($D = D_0 e^{(-\Delta E/k_B T)}$ where k_B is the Boltzmann constant and T is the growth temperature). Figure A.6 shows the semi-logarithmic graph of the diffusion coefficient as a function of inverse of growth temperature. This graph does not show a fairly linear behavior, however the slope and the intercept with the vertical axis of the fitted line could provide an estimate of the order of magnitude of the activation energy (found to be $\Delta E = 0.45 \pm 0.14$ eV) and the pre-exponential factor ($D_0 = 1.03 \pm 0.99 \times 10^{-11} (cm^2/s)$).

To describe the not fairly linear behavior of the graphs presented in figure A.6, we consider the effect of lateral growth of MnP grains on the endotaxial depth. At higher growth temperatures and/or longer growth times the film becomes almost continuous, which can prevent the out-diffusion of Ga atoms. We have quantified the coverage% of our samples by image analysis of the plan-view SEM micrographs using Fiji software. Figure A.7 shows an example of our image analysis on MnP-550-15. Table A.5 compares the portion of the GaP substrate that is covered by MnP films grown at different growth temperatures for 15 minutes. According to table A.5, the substrate is almost covered by the film at higher growth temperatures (94% at 650 °C).

Hence, following the assumption that the Mn atoms replace the out-diffused Ga atoms, we expect the endotaxial depths (and diffusion coefficient) to reach a saturation point at higher growth temperatures and/or longer growth times. This can be seen in figures A.5 and A.6 for the diffusion coefficients of GMP-650-30 (completely covered) and GMP-650-15 (94% covered), which seem to be less than what we expect from the diffusion law (linear fit).

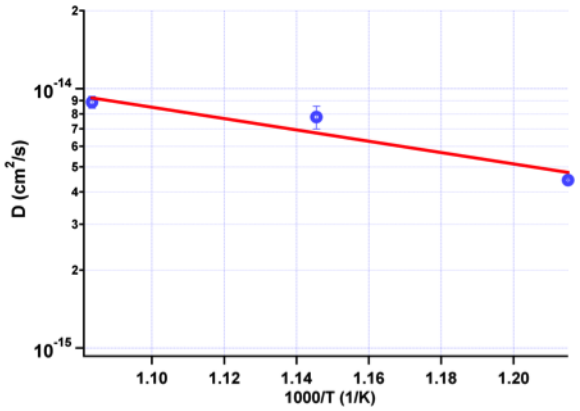

Figure A.6 Semi-logarithmic graph of the diffusion coefficient (D) as a function of ($1000/T$) for our samples and their corresponding linear fits, compared to Mn bulk diffusion reported in Ref. Kirillov *et al.* (1980). The extracted activation energy (ΔE) and the pre-exponential factor (D_0) in our samples are 0.45 ± 0.14 (eV) and $1.03 \pm 0.99 \times 10^{-11} (cm^2/s)$, respectively, compared to 0.45 (eV) and $2.1 \times 10^9 (cm^2/s)$ reported in Ref. Kirillov *et al.* (1980). The interface and bulk diffusion coefficients of Mn in GaAs are also presented in the graph for comparison.

Table A.5 Portion of the GaP substrate, which is covered by MnP films grown at different temperatures for 15 minutes.

Sample	**MnP-550-15**	**MnP-600-15**	**MnP-650-15**
Coverage (%)	72	83	94

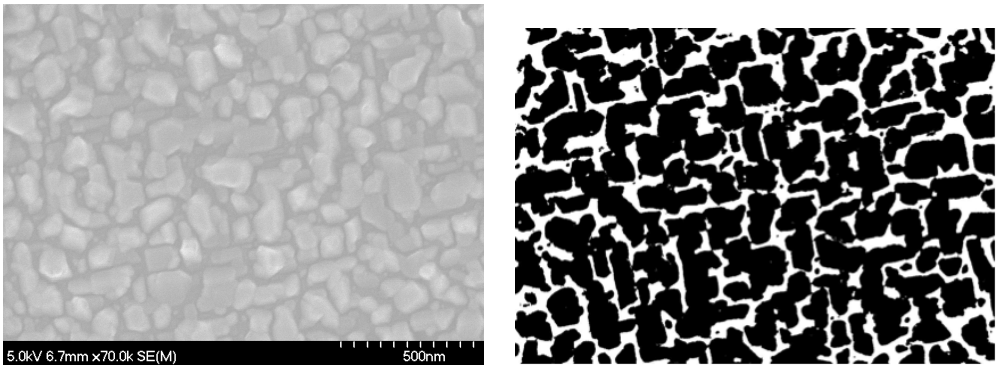

Figure A.7 Image analysis of the plan-view SEM micrograph of MnP-550-15. Dark shows the deposited film, while bright represents the substrate. For this sample the film covers 72% of the substrate.

ANNEXE B

Structural, magnetic, and magneto-optical properties of MnP films grown on glass substrate

We have grown MnP films on glass in order to 1) compare the magneto-optical properties of MnP thin films to MnP clusters in GaP :MnP Monette *et al.* (2012), and 2) to obtain MnP nanoparticles using laser ablation technique Schmidt (2011). The MnP nanoparticles obtained using this technique were embedded in polystyrene and their magnetic properties has been compared to MnP nanoclusters embedded in GaP (GaP :MnP) (Schmidt (2011)). The objective of this study was to understand the effect of strain in MnP nanoclusters (induced from the matrix) on their magnetic properties. The details of this study can be found in Ref. (Schmidt (2011)).

Structural properties

Figure B.1 shows plan-view SEM images of MnP-G550-15 and MnP-G550-60 film grown on glass 550 °C for 15 min and 60 min, respectively. These samples showed a mirror like surface. We observe formation of a polycrystalline film at this growth temperature, with average effective grain size $d_p = 79 \pm 4$ nm (MnP-G550-15) and $d_p = 236 \pm 13$ nm (MnP-G550-60) and average aspect ratios of $AR = 1.46 \pm 0.04$ (MnP-G550-15) and $AR = 1.53 \pm 0.05$ (MnP-G550-60). This gives the lateral growth rates of 5.3 ± 0.3 and 3.9 ± 0.2 nm/min for MnP-G550-15 and MnP-G550-60, respectively. Figure B.2 shows the cross-sectional SEM image of MnP-G550-60, from which we determined the growth rate of MnP on glass at 550 °C to be almost 7 nm/min.

GMP-G600-60 had a very rough surface and we could completely remove the deposited film from the substrate by scratching its surface. Figure B.3 shows the plan-view SEM image of the sample and the plan-view TEM image of the powder obtained from the sample. For TEM imaging, we put the powder obtained from scratching the surface directly on a 200 mesh copper grids, which was coated by 10-30 Åof a polymer followed by 10-50 nm of amorphous carbon. The TEM image shows mostly long rods in the powder obtained from the sample. We believe that these long rods nucleated as secondary grains on top of the primary ones and grew faster in a specific direction, similar to what we observed in MnP-650-30 and MnP-700-15 and (Chapter 4, figures 4.12 and 4.14).

We have studied the SAED pattern of some of these long rods to verify whether they have

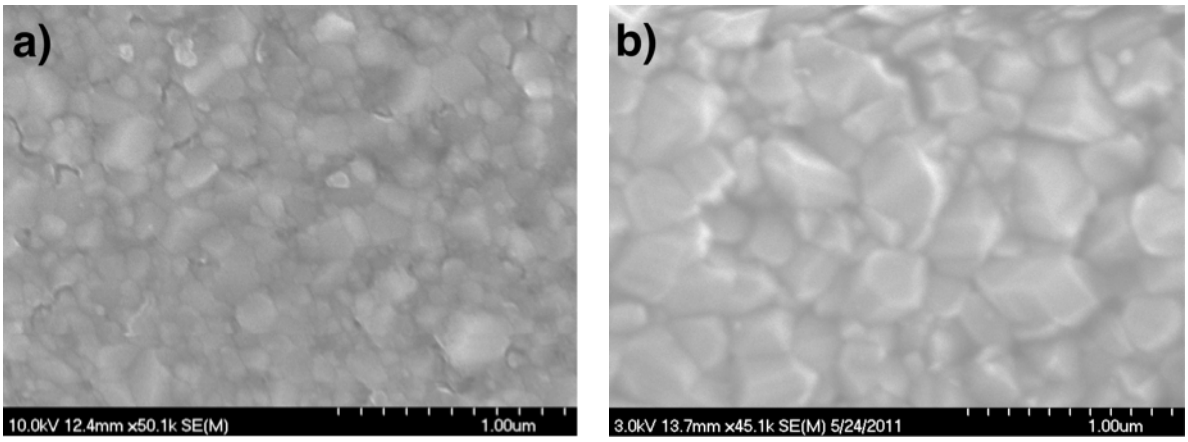

Figure B.1 Plan-view SEM images of MnP films grown on glass at a) MnP-G550-15 and b) MnP-G550-60 show formation of polycrystalline films.

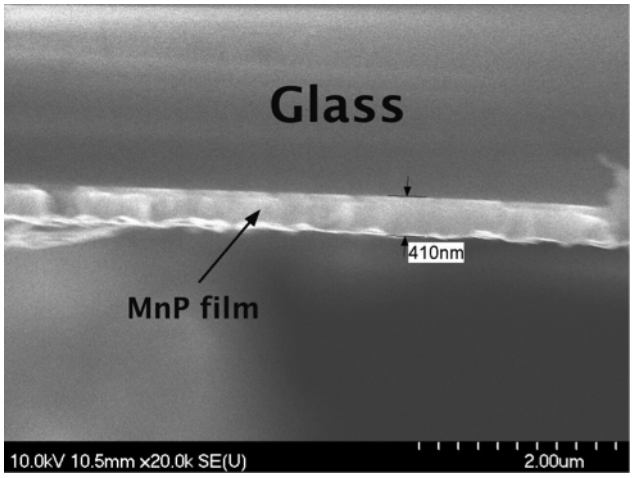

Figure B.2 Cross-sectional SEM image of MnP-G550-60 showing the thickness of the film to be 410 nm. The growth rate has been calculated to be almost 7 nm/min.

a preferential growth direction. Our results, in agreement with results of Park *et al.* Park *et al.* (2005), show that MnP has a larger growth rate along its c-axis (taking the convention a > b > c). Figure B.4 shows the plan view TEM image and the SAED pattern of one of the nanorods.

Magnetic properties

Figure B.5 shows the magnetic hysteresis curve of MnP-G600-60, which confirms the ferromagnetic behavior of the film. The hysteresis curve is obtained by applying the magnetic field parallel to the sample's surface (in-plane). The in-plane IRM response as a function of

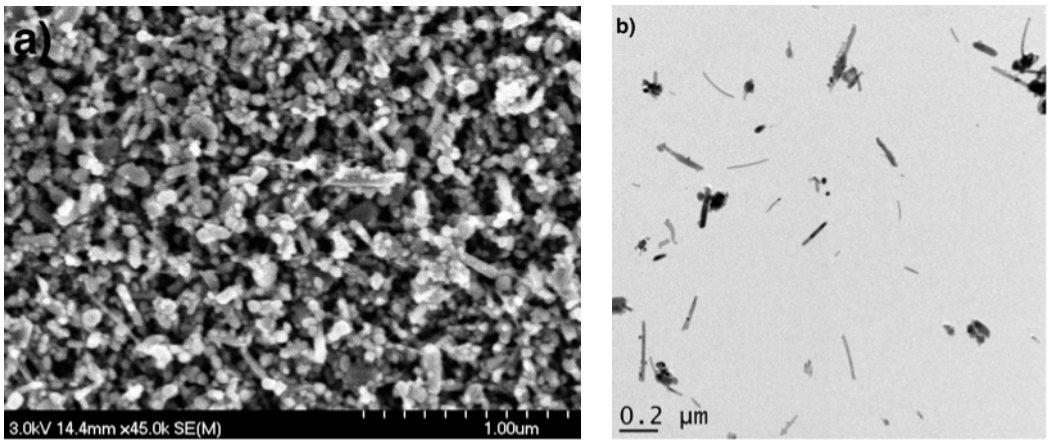

Figure B.3 a) Plan view SEM image of the MnP-G600-60 and b) Plan view TEM micrograph of the powder obtained from this sample.

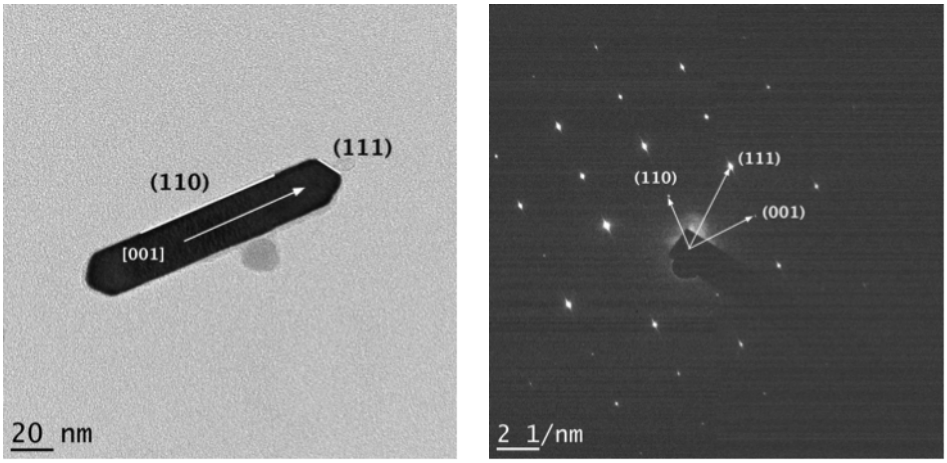

Figure B.4 Plan view TEM image of an elongated MnP nanoparticle obtained from MnP-G600-60 powder and its SAED pattern. It shows that MnP grows faster in [001] direction. We also observe (110) and (111) surface facets.

temperature shows a Curie temperature of 292 ± 1 K, which has been reported for MnP Huber Jr et Ridgley (1964). Here by Curie temperature we mean the temperature at which the sample shows no remanent magnetization. Prior to measuring the IRM signal, we increased the sample's temperature up to a certain point above its Curie temperature. Then we cooled it down to the desired temperature in the absence of applied magnetic field (ZFC). We then applied a magnetic field of 1590 kA/m (20 kOe) parallel to the surface of the demagnetized sample and measured the magnetization right after removing the field. We repeated this procedure prior to measuring the IRM signal at each temperature.

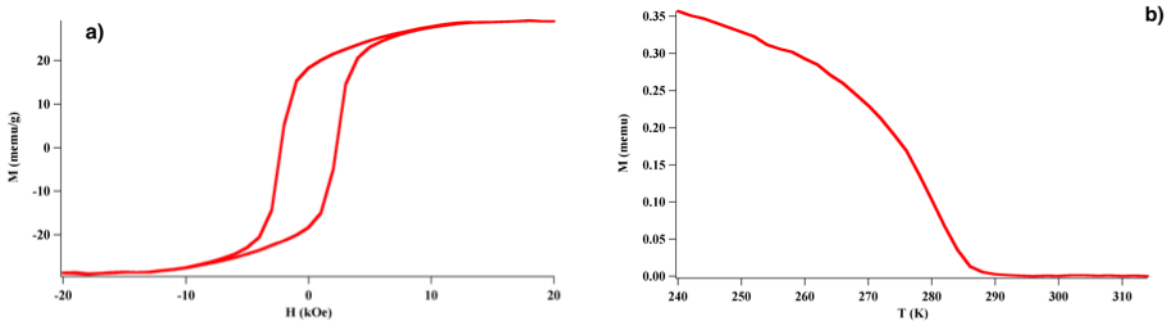

Figure B.5 a) Magnetic hysteresis curve of MnP-G600-60 at 240 K indicating ferromagnetic ordering. b) Temperature evolution of the IRM signal of MnP-G600-60 indicating a Curie temperature of 292 ± 1 K.

Magneto-optical properties

Figure B.6 shows the Faraday rotation of MnP-550-15 as a function of magnetic field at 1.89 eV, as well as its magnetic hysteresis curve. For these measurements the magnetic field has been applied perpendicular to the sample surface (out of plane configuration) Monette *et al.* (2012). The Verdet constant at 1.89 eV has been calculated from the linear slope of θ_f vs. magnetic field at the coercive field to be 1.14 °/ T Monette *et al.* (2012). Using the film thickness of approximately 100 nm (determined from growth rate of almost 7 nm/min and 15 minutes of growth), the value of Verdet constant will be 11400 °/ T mm, which is 3 orders of magnitude larger than commercially available garnets Monette *et al.* (2012). The absorption coefficient of MnP-G550-15 has been calculated at 1.89 eV to be 21.6 μm^{-1} Monette *et al.* (2012), which is relatively high for industrial applications.

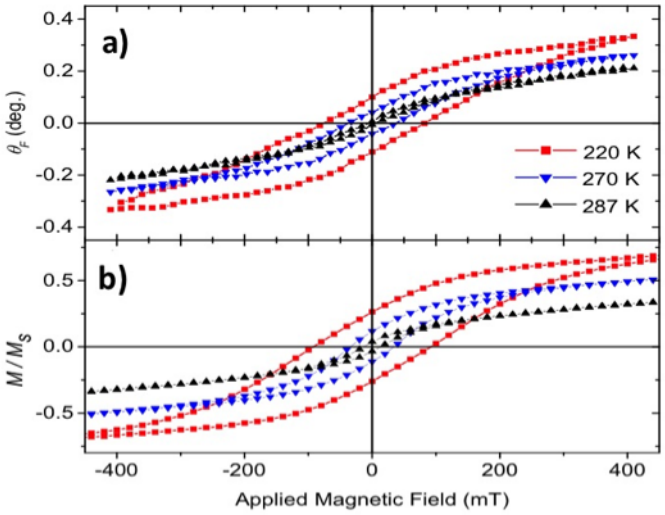

Figure B.6 a) Faraday rotation θ_f of MnP-G550-15 at 1.89 eV as a function of magnetic field at different temperatures. b) Magnetic hysteresis curve of MnP-G550-15 at different temperatures.